Constraints on the use of long-chain diols as environmental proxies

Marijke W. de Bar

This research has been funded by the European Research Council (ERC) under the European Union's Seventh Framework Program (FP7/2007-2013) ERC grant agreement [339206] to S.S.

ISBN: 978-94-6332-471-7

Printed by GVO drukkers & vormgevers, Ede, The Netherlands.

Constraints on the use of long-chain diols as environmental proxies

Mogelijkheden in het toepassen van langeketendiolen als milieu-proxy's

(met een samenvatting in het Nederlands)

PROEFSCHRIFT

ter verkrijging van de graad van doctor aan de
Universiteit Utrecht op gezag van de
rector magnificus, prof. dr. H.R.B.M. Kummeling,
ingevolge het besluit van het college voor promoties
in het openbaar te verdedigen op

dinsdag 21 mei 2019 des ochtends te 10.30 uur

door

Marijke Wilhelmina de Bar

geboren op vrijdag 22 maart 1991

te Doetinchem

Promotoren: Prof. dr. ir. S. Schouten

Prof. dr. ir. J.S. Sinninghe Damsté

CONTENTS

Chapter 1

Introduction

1.1 Past climate reconstruction

Anthropogenic input of greenhouse gases into the atmosphere has resulted in a global warming effect (Intergovernmental Panel on Climate Change, IPCC 2014). To predict the future impact of global warming on Earth's climate in terms of temperature, sea level rise, droughts, storms and floods, we depend on climate models, in particular general circulation models. Validation and testing of these models is only possible by applying them to appropriate time slices in the past to "predict in retrospect" past climate changes. However, this means that we need real data of past climate changes. Historical instrumental data only extend back to the last century, and thus comprise only a very short time slice of Earth's climate history, and moreover, include the influence of human activity on Earth's climate. To go further back in time, we have to rely on so-called climate archives. Examples of such archives are tree rings, ice cores, speleothems and terrestrial, lacustrine and marine sediments. The latter is one of the most used climate archives, because marine sediments provide the longest and most continuous climate records. They contain well-preserved entities which can provide information on the environmental conditions under which the sediments were deposited. These entities are called 'climate proxies' and can be divided into two types, i.e., biological and chemical proxies. Biological proxies comprise a wide range of fossilized remains of (extinct) organisms such as the frequently studied benthic and planktonic foraminifera, diatoms, dinoflagellate cysts, corals and mollusks. Changing fossilized assemblages reflect changing paleo-environmental and paleoclimatic conditions, thus enabling paleoclimatic reconstructions. Besides preserved fossil remains of (marine) organisms, pollen and spores are also considered biological proxies, being derived from higher plants. These plant remains can end up in marine sediments due to wind or river transport, providing information of past vegetation, and thus, climate change.

Next to biological assemblages, chemical properties of fossilized organisms can provide information on past climate change and are referred to as chemical proxies. For instance, the isotopic and elemental composition of foraminiferal shells (calcium carbonate) and diatom shells (silicon dioxide) reflect the chemistry of the seawater in which the organism proliferated. One of the most frequently used robust chemical proxies is based on the stable oxygen isotopic composition ($\delta^{18}O$) of foraminiferal calcite. This calcite is formed from calcium and bicarbonate ions in seawater:

$$Ca^{2+}(aq)+2HCO_3^-(aq) \rightleftarrows CaCO_3(s)+CO_2(aq)+H_2O \quad (1)$$

Upon evaporation of seawater, relatively more water with the light oxygen isotope (^{16}O) evaporates, leaving behind seawater enriched in the heavier isotope (^{18}O). During glacial periods when ice caps build up, this light isotope is captured in ice sheets, leaving the seawater relatively enriched in ^{18}O. This enrichment is reflected in the foraminiferal carbonate, thus, the $\delta^{18}O$ of the carbonate is a reflection of this value in the seawater. Furthermore, the fractionation of the oxygen isotopes during carbonate precipitation is dependent on temperature (Urey, 1947). Accordingly, foraminiferal $\delta^{18}O$ can be used to infer past temperature variations, where benthic foraminiferal $\delta^{18}O$ reflects bottom water temperature, and planktonic foraminiferal $\delta^{18}O$ reflects sea surface temperature (SST). However, over long-term timescales (10^4–10^5 years), foraminiferal $\delta^{18}O$ is in fact a proxy for ice volume changes. Therefore, in calculating past seawater temperature based on foraminiferal $\delta^{18}O$, a correction must be applied to account for the seawater $\delta^{18}O$. Several $\delta^{18}O$-temperature calibrations have been proposed (see Bemis et al. (1998) for an overview). One of the most used transfer functions for cold water and benthics is the polynomial equation of Kim and O'Neil (1997):

$$T\,(°C) = 16.1 - 4.64 \times (\delta^{18}O_{calcite} - \delta^{18}O_{seawater}) + 0.09 \times (\delta^{18}O_{calcite} - \delta^{18}O_{seawater})^2 \quad (2)$$

The most well-known record based on foraminiferal $\delta^{18}O$ is the full Cenozoic record published by Zachos et al. (2008; Fig. 1), a record determined by bottom water temperature and ice volume variations on Earth. As shown by this record, the Late Cretaceous to Early Eocene was a period of warm climates and it is often referred to as the "greenhouse world" associated with high CO_2 concentrations (e.g., Anagnostou et al., 2016; Bijl et al., 2009; Foster et al., 2017; O'Brien et al., 2017). In fact, during the Early Eocene (ca. 55–52 Ma) there were a series of hyperthermals, short term events of carbon dioxide and methane releases from the ocean into the atmosphere leading to rapid global warming. The Paleocene-Eocene Thermal Maximum (PETM; ca. 56 Ma) is one of the most studied hyperthermals (e.g., Sluijs et al., 2006) as it is considered a potential analog for the present ongoing climate change associated with massive carbon input into ocean and atmosphere, leading to global warming and ocean acidification (e.g., Dickens et al., 1997).

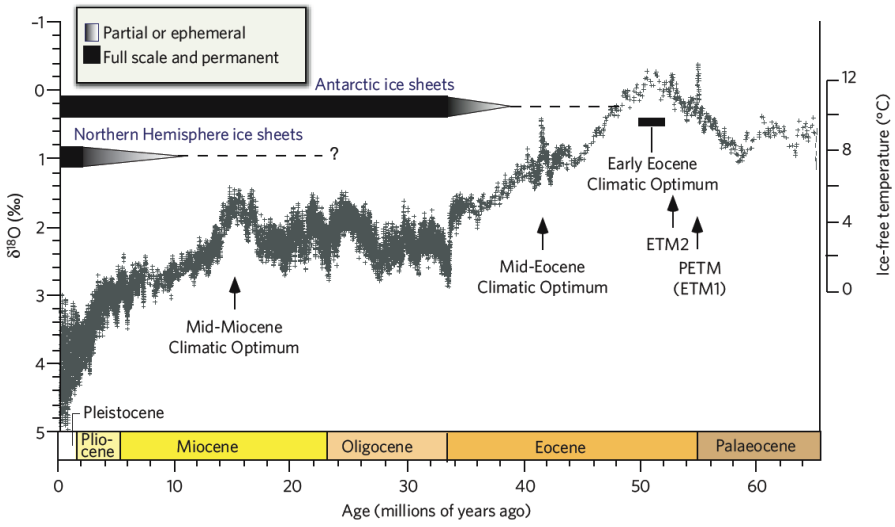

Fig. 1 Global climate variations for the last 65 million years based on a compilation of benthic foraminiferal oxygen isotope records (proxy discussed below) from Deep Sea Drilling Project and Ocean Drilling Program sites. Highlighted are several warming events. Figure adapted from Zachos et al. (2008).

Another widely used foraminiferal proxy for reconstructing past seawater temperature is the Mg/Ca ratio of the calcite shell (Nürnberg et al., 1996; Rosenthal et al., 1997). Whereas these isotopic and elemental measurements are typically referred to as 'inorganic proxies', another type of chemical proxies is based on biomarkers ('organic proxies'). Since lipids are relatively well preserved in the sedimentary records, most molecular chemical proxies are based on lipid biomarkers, organic compounds characteristic for a specific organism, a group of organisms, or a biogeochemical process. These lipids were originally biosynthesized by living organisms (for instance the cell membrane lipids), which after death, sink to the seafloor and disintegrate releasing the relatively stable lipid molecules to be incorporated in the sediment.

Several lipid biomarker-based proxies, in particular for SST reconstructions, have been proposed over the last decades. Below I shortly discuss the currently applied temperature proxies based on the ratio of related individual lipids occurring in sediments.

1.2 Lipid temperature proxies

Long-chain alkenones are lipid biomarkers biosynthesized by haptophyte algae living as phototrophs in the upper euphotic zone of the ocean. These algae biosynthesize long-chain alkenones with different degrees of unsaturation depending on growth temperature (Marlowe et al., 1984a; Brassell et al., 1986; Prahl and Wakeham, 1987). The higher the growth temperature, the higher the relative abundance of the di-unsaturated C_{37} alkenone, and the lower the temperature, the higher the relative abundance of the tri-unsaturated C_{37} alkenone. This temperature dependence is expressed by the $U^{K'}_{37}$ index, ranging from 0 to 1 (Prahl and Wakeham, 1987):

$$U^{K'}_{37} = [C_{37:2} \text{ alkenone}]/[C_{37:2}+C_{37:3} \text{ alkenones}] \quad (3)$$

The relationship between alkenones and temperature was initially defined by Brassell et al. (1986) as the U^{K}_{37} (without prime), which included the tetra-unsaturated C_{37} alkenone in the denominator. However, this compound was excluded in the simplified index of Prahl and Wakeham (1987) as it did not improve the empirical correlation with SST. Further studies focused on the calibration of the $U^{K'}_{37}$ index by means of algal cultures at different temperatures, and by comparison of sediment trap suspended particulate matter and surface sediments $U^{K'}_{37}$ data with the temperature of the overlying water (see Herbert, 2003 for review). One of the most applied temperature calibrations was developed by Müller et al. (1998):

$$SST = (U^{K'}_{37}–0.044)/0.033 \quad (4)$$

Its application is limited to the last ca. 55 Myr, due to the absence of tri-unsaturated C_{37} alkenones in older sediments (Brassell, 2014 and references cited therein). Moreover, additional research has shown that this proxy can be compromised by lateral transport (Ohkouchi et al., 2002; Mollenhauer et al., 2008; Kim et al., 2009b) and post-depositional oxic degradation (Hoefs et al., 1998). Reliable applications of the proxy are limited to SSTs up to 29 °C (Müller et al., 1998; Conte et al., 2006), although a recently proposed Bayesian calibration extended this limit to 29.6 °C (Tierney and Tingley, 2018).

Another lipid paleotemperature proxy is called the TEX_{86}, based on isoprenoidal glycerol dialkyl glycerol tetraethers (GDGTs; Schouten et al., 2002; 2013). These GDGTs are membrane lipids of archaea (Koga and Morii, 2007; Schouten et al., 2013b and references cited therein), and are mainly produced by the phylum Thaumarchaeota in the marine environment (Schouten et al., 2013b). These archaea produce GDGTs with 0 to 3 cyclopentyl moieties (GDGT-0 to -3) and crenarchaeol (cren) with 4 cyclopentyl moieties and one cyclohexyl moiety (Schouten et al., 2002; Sinninghe Damsté et al., 2002). The TEX_{86} is based on GDGT-1, -2, -3 and an isomer of crenarchaeol (cren´):

$$TEX_{86} = [\text{GDGT-2}+\text{GDGT-3}+\text{cren´}]/[\text{GDGT-1}+\text{GDGT-2}+\text{GDGT-3}+\text{cren´}] \quad (5)$$

Kim et al. (2010) proposed two modified indices called the TEX_{86}^{L} and TEX_{86}^{H}. The first index excludes the crenarchaeol isomer, as well as GDGT-3 from the numerator, making the index better applicable for subpolar Southern Ocean sediments. The TEX_{86}^{H}, suitable for global SST reconstructions except for the subpolar regions, is a logarithmic function of the TEX_{86} and correlates best with SST when subpolar data were excluded. Moreover, core-top data from the Red Sea were removed, since the TEX_{86} appeared to behave differently in this region when compared to other parts of the oceans. The relationship with SST is as follows:

$$SST = 68.4 \times \log(TEX_{86}^{H}) + 38.6 \quad (6)$$

Since Thaumarachaeota occur throughout the whole water column (e.g., Karner et al., 2001), the TEX_{86} often reflects subsurface temperatures (e.g., Huguet et al., 2007; Kim et al., 2012a; 2012b; 2015; Schouten et al., 2013b; Chen et al., 2014; Wuchter et al., 2006b; Tierney et al., 2007). This has led to different interpretations of TEX_{86} based temperatures in the literature (see Zhang and Liu, 2018 for review). GDGTs are present in sediments as far back as the middle Jurassic (Jenkyns et al., 2012) making their application wider than the $U_{37}^{K'}$ index. Moreover, the TEX_{86} seems to be less affected by diagenesis (Schouten et al., 2004; Kim et al., 2009c), and can reconstruct temperatures > 30 °C, although this should be done with caution (e.g., Schouten et al., 2003; Tierney and Tingley, 2014 and references cited therein). It has been shown, however, that the TEX_{86} can be greatly affected by the contribution of soil-derived isoprenoid GDGTs in coastal areas. This problem can be overcome by assessing the so-called BIT index, a ratio of branched GDGTs, which are derived from terrestrial soils and are not produced in the marine environment, and the marine-derived crenarchaeol (Hopmans et al., 2004). Weijers et al. (2006; 2009) showed that the TEX_{86} should not be applied when the BIT index > 0.3.

As discussed above, all temperature proxies have different advantages but also suffer from uncertainties. Because these uncertainties are proxy-specific, reconstructions of past seawater temperature are ideally based on more than one proxy in order to increase the reliability of the records. Accordingly, additional temperature proxies are desired. Over the last years, long-chain diols have gained interest as paleoenvironmental proxies. Different diol proxies have been proposed, including a new SST proxy based on long-chain 1,13-and 1,15-diols, called the Long chain Diol Index (LDI). This promising proxy and long-chain diols in general as potential paleoenvironmental indicators are the subject of this thesis.

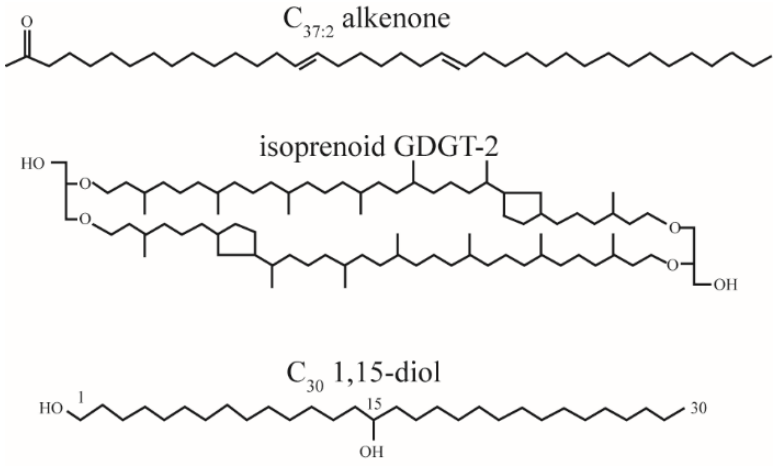

Fig. 2 Examples of molecular structures of lipids used for three organic paleotemperature proxies, i.e., a di-unsaturated C_{37} alkenone, isoprenoid GDGT-2, and a C_{30} 1,15-diol, respectively.

1.3 Distribution and sources of long-chain diols

Long-chain alkyl diols (hereafter referred to as long-chain diols, LCDs or diols) are lipids consisting of long, unbranched alkyl chains with two alcohol groups at C1 and a mid-chain position (de Leeuw et al., 1981; Versteegh et al., 1997; Volkman et al., 1992). The first report of LCDs in the natural environment by de Leeuw et al. (1981) showed their presence in sediments of the Black Sea. Since then, they have been observed in various marine settings (e.g., Smith et al., 1983; ten Haven et al., 1992; ten Haven and Rullkötter, 1991; Yamamoto et al., 1996; Versteegh et al., 1997; 2000; Pearson et al., 2001; van Soelen et al., 2010; Willmott et a., 2010; Rampen et al., 2007; 2008; 2012; Naafs et al., 2012) and lacustrine regimes (e.g., Robinson et al., 1986; Cranwell et al., 1987; Huang et al., 1995; Xu et al., 2007; Shimokawara et al., 2010; Castañeda et al., 2011; Romero-Viana et al., 2012; Villanueva et al., 2014). The most frequently detected diols have even-numbered chain lengths between C_{28} and C_{32}, and alcohol moieties at the 1,13, 1,14, and 1,15 positions (e.g., Rampen et al., 2014a). After the first observation in the Black Sea, long-chain diols were identified in the Baltic Sea during a cyanobacterial bloom of *Aphanizomenon flos-aquae*. The authors therefore proposed that cyanobacteria produced these diols (Morris and Brassell, 1988). However, long-chain diols were not detected in cultures of *A. flos-aquae* or other cyanobacteria (de Leeuw et al., 1992). In contrast, they were identified in cultures of the Eustigmatophyte algae *Nannochloropsis* (e.g., Volkman et al., 1992; Gelin et al., 1996; 1997a; 1997b). However, the LCD distributions in these Eustigmatophytes, often characterized by a dominant C_{32} 1,15-diol (e.g., Volkman et al., 1992; Méjanelle et al., 2003;

Rampen et al., 2014b), are different from distributions observed in the marine environment generally characterized by a dominant C_{30} diol (e.g., Versteegh et al., 1997; 2000; Rampen et al., 2012; 2014b; Fig. 2). The role of Eustigmatophytes as LCD producers in the ocean is therefore uncertain. It is, however, noteworthy that LCD distributions in lacustrine environments (Rampen et al., 2014b) are similar to those in Eustigmatophyte algae. Three fresh water Eustigmatophyte species, *Vischeria punctata*, *Vischeria helvetica* and *Eustigmatos vischeri*, were shown to produce long-chain diols (Volkman et al., 1999a). In addition, Villanueva et al. (2014) observed correlations between LCD concentrations in Lake Challa (East Africa) and 18S rRNA gene copies of (yet unknown) Eustigmatophyte algae, further confirming that Eustigmatophytes are potential producers of long-chain diols in lacustrine environments. It is thought that these long-chain diols occur as building blocks of highly aliphatic non-hydrolysable macromolecules, called algaenans, which are part of the cell wall of Eustigmatophytes (de Leeuw et al., 1981; Tegelaar et al., 1989; Gelin et al., 1997a; Volkman et al., 1998).

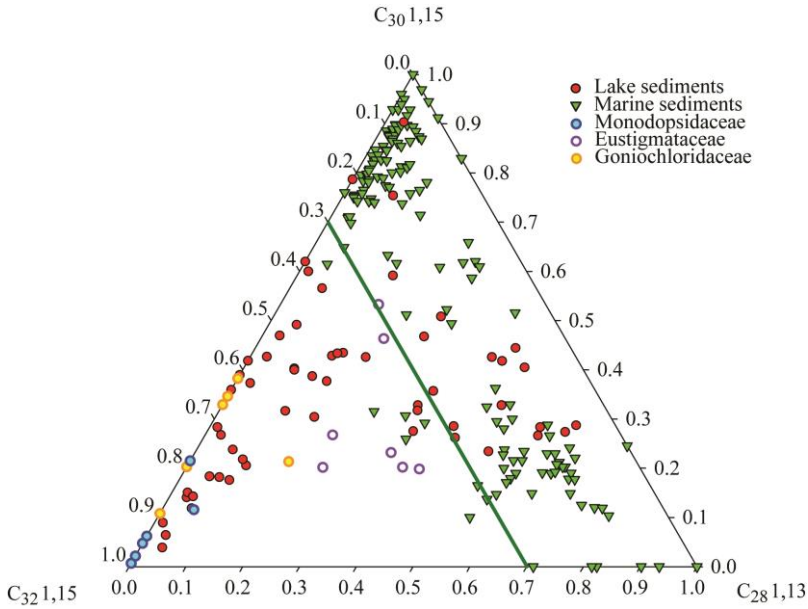

Fig. 3 Ternary diagram showing the relative abundances of the C_{30} and C_{32} 1,15-diol and the C_{28} 1,13-diol from *Eustigmatophyte* cultures (*Monodopsidaceae*, *Eustigmataceae* and *Goniochloridaceae*), lake and marine surface sediments, adopted from Rampen et al. (2014b). The green line indicates a relative abundance for the C_{32} 1,15-diol of 30 %, which is the maximum observed for most marine sediments.

In addition to the 1,13- and 1,15-diols, 1,14-diols are frequently encountered in marine sediments (e.g., Willmott et al., 2010; Rampen et al., 2008; 2009). Both saturated and mono-unsaturated C_{28} and C_{30} 1,14-diols have been identified in *Proboscia* diatoms (Sinninghe Damsté et al., 2003; Rampen et al., 2007). Furthermore, saturated C_{28}, C_{30} and C_{32} 1,14-diols have been identified in the marine heterokont alga *Apedinella radians* (Rampen et al., 2011). Sediment trap studies in the Arabian Sea confirmed that *Proboscia* diatoms are a likely source of 1,14-diols in the marine environment, especially in upwelling regions (Rampen et al., 2007; 2008), whereas the role of *Apedinella* as 1,14-diol producer in the ocean remains uncertain.

1.4 Long-chain diols as paleotemperature proxy

In 2012, Rampen and others evaluated the distribution of 1,13- and 1,15-diols in 209 globally distributed marine surface sediments to determine which environmental factors influence these distributions. The fractional abundances (i.e., the abundances of the individual diols versus the summed 1,13- and 1,15-diol abundances) of the C_{28} 1,13- and C_{30} 1,13-diols showed negative correlations with the annual mean SST and the C_{30} 1,15-diol showed a strong positive relationship with SST. The variation of the fractional abundance of the C_{30} 1,15-diol with SST is largest, ranging from 0 to 1 (R^2 = 0.95), whereas the negative correlation of the C_{28} and C_{30} 1,13-diols with SST range between 0 and 0.69 (R^2 = 0.88) and 0 and 0.55 (R^2 = 0.80), respectively. Consequently, the temperature relationship, named the Long chain Diol Index (LDI), was defined as follows:

$$LDI = [C_{30}\ 1,15\text{-diol}]/[C_{28}\ 1,13\text{-diol}+C_{30}\ 1,13\text{-diol}+C_{30}\ 1,15\text{-diol}] \quad (7)$$

This ratio shows a strong positive linear correlation with annual mean SST, described by the following function:

$$SST = (LDI–0.095)/0.033 \qquad (R^2 = 0.97;\ n = 161) \quad (8)$$

This temperature proxy covers a temperature range of -3 to 27 °C. The calibration error is 2.0 °C, which is larger when compared to the $U^{K'}_{37}$ (1.5 °C) but smaller than that of the TEX^{H}_{86} (2.5 °C).

The fractional abundance of the C_{32} 1,15-diol, ranging between 0 and 0.33, did not show a relationship with SST, and was therefore not included in the LDI calibration. The best correlation with annual mean SST was observed for the upper 30 m of the water column, whereas quality of correlation decreased with greater depths. This indicates that C_{28} and C_{30} 1,13- and 1,15-diols used in the LDI are produced by phototrophic algae living in the upper

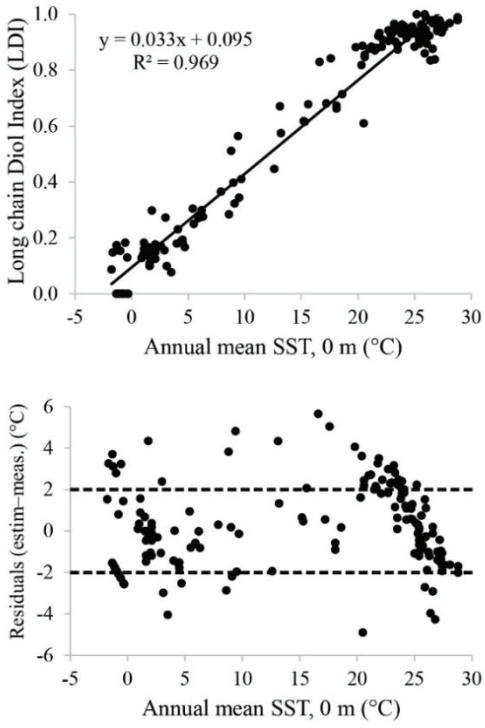

Fig. 4 **(a)** LDI core-top calibration where LDI values of marine surface samples are plotted vs. annual mean sea surface temperature (World Ocean Atlas, 2001). **(b)** Annual mean SST vs. the residual temperature errors (i.e. LDI temperature – measured SST); the dashed lines reflect the standard deviation, i.e., the calibration error of 2.0 °C (Rampen et al., 2012).

mixed layers (euphotic zone) of the ocean. Furthermore, correlation of the LDI values with monthly and seasonal SSTs was highest in late summer and early autumn, suggesting that the diol producers mainly thrive during the warmest months. Rampen et al. (2014b) also tested the LDI in surface sediments of 62 lakes as a proxy for the temperature of the surface waters. They concluded that the correlation with temperature was weak probably due to different Eustigmatophyte producers, each synthesizing different LCD distributions. This clearly indicates that the applicability of the LDI is limited to the marine environment.

The first down-core applications of the LDI revealed highly promising results (Rampen et al., 2012; Naafs et al., 2012; Lopes dos Santos et al., 2013; Smith et al., 2013; Rodrigo-Gámiz et al., 2014) when compared to a large range of other palaeo-SST proxies (Fig. 5). Moreover, the 1,13- and 1,15-diols used for the LDI have been observed in sediments from the Miocene (Ahmed et al., 2000) and the Cretaceous-Tertiary boundary (Yamamoto et al., 1996), indicating that the LDI might be applicable up to 66 Ma.

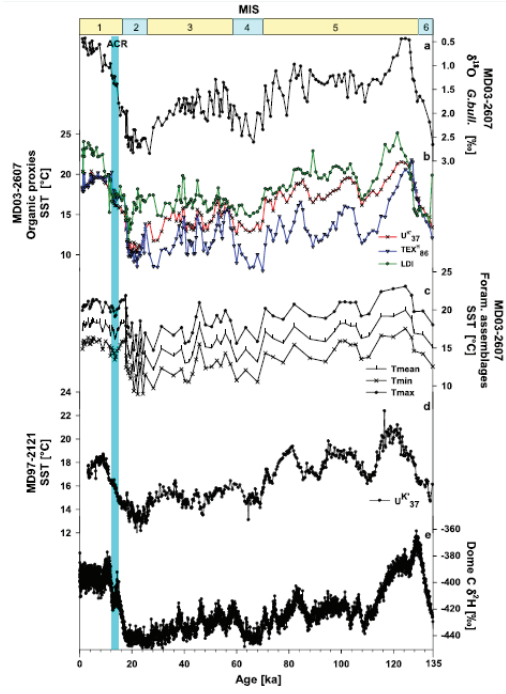

Fig. 5 Example of a down-core application of the LDI over the last 135 kyrs (Lopes dos Santos et al., 2013). The figure shows sediment records from core MD03-2607 (south of Australia). **(a)** Planktonic stable oxygen isotope record ($\delta^{18}O$) (Lopes dos Santos et al., 2012). **(b)** Organic proxy temperature records (LDI in green, TEX_{86}^{H} in blue and $U_{37}^{K'}$ in red). **(c)** Temperature reconstructions based on foraminiferal assemblages. **(d)** $U_{37}^{K'}$ of core MD97-2121 (east of New Zealand). **(e)** Deuterium isotope record from the EPICA ice core, as a proxy for air temperature in Antarctica. Figure adapted from Lopes dos Santos et al. (2013).

1.5 LCDs as upwelling proxy

1,14-diols have been identified in *Proboscia alata*, *P. indica* and *P. inermis* (Sinninghe Damsté et al., 2003; Rampen et al., 2007). *Proboscia* diatoms are generally associated with upwelling (i.e., high nutrient) areas (Hernández-Becerril, 1995; Lange et al., 1998; Koning et al., 2001; Smith, 2001) and it was therefore proposed that their lipids, i.e. 1,14-diols, might be useful indicators of upwelling conditions (Sinninghe Damsté et al., 2003). This was confirmed by sediment trap studies in the Arabian Sea (Rampen et al., 2007; 2008). Consequently Diol Index 1 was introduced as proxy for upwelling in the Arabian Sea, associated with the Southwest Monsoon (Rampen et al., 2008):

$$\text{Diol Index 1} = [C_{28}+C_{30}\ 1,14\text{-diol}]/[C_{28}+C_{30}\ 1,14\text{-diol}+C_{30}\ 1,15\text{-diol}] \quad (9)$$

A following study in the Western Bransfield Basin (Antarctica) carried out by Willmott and others in 2010 also identified relatively high abundances of 1,14-diols, but low concentrations of the C_{30} 1,15-diol, whereas 1,13-diols were more abundant. Consequently, Willmott et al. (2010) defined Diol Index 2 as indicator of upwelling in the Western Bransfield Basin:

$$\text{Diol Index 2} = [C_{28}+C_{30}\ 1,14\text{-diol}]/[C_{28}+C_{30}\ 1,14\text{-diol}+C_{28}+C_{30}\ 1,13\text{-diol}] \quad (10)$$

These Diol Indices have been applied in the Arabian Sea, Equatorial Pacific, Benguela Upwelling System, offshore Australia and the Mediterranean (Rampen et al., 2008, Seki et al., 2012, Pancost et al., 2009, Lopes dos Santos et al., 2012 and Nieto-Moreno et al., 2015, respectively). Based on these and other studies their applicability as upwelling tracers is however uncertain. For instance, studies have related *Proboscia* diatoms to stratified instead of upwelling conditions (e.g., Fernández and Bode, 1994), and although *Proboscia* is often reported in upwelling regions, the specific conditions are often described as early or pre-upwelling, post-bloom and/or oceanic side of the upwelling lens (references in Table 1 of Rampen et al., 2014a). Moreover, Contreras et al. (2010) reported high abundances of the C_{28} 1,14-diol in the Peruvian upwelling system during the Last Interglacial and related this to water column stratification. Hence, application of Diol Indices 1 and -2 at this stage is debatable and likely depends on local factors affecting *Proboscia* ecology.

1.6 Objectives and outline

As indicated above, many investigations have shown that long-chain diols occur ubiquitously in the marine environment, both spatially and temporally, and can serve as useful indicators of certain environmental conditions, i.e., seawater temperature and possibly upwelling conditions. However, many uncertainties still exist, in particular associated with factors such as the unknown marine biological source(s) of the LDI diols, the seasonality and habitat depth of the LCD producers, the effects of preservation and diagenesis, and the impact of fluvial input. These shortcomings in our knowledge of the environmental distribution of LCDs negatively impact the reliability of the proxies and complicates climate reconstructions based on long-chain diols. Also, so far studies focusing on different methods for the analysis of LCDs are lacking. Accordingly, the aim of the first part of this thesis (chapters 2 and 3) is to develop a better understanding of the biochemical role of LCDs, as well as to evaluate and compare different methods for the analysis of diols. Furthermore, in order to further calibrate the proxies against environmentaltemperatures (LDI) and upwelling and productivity indicators (Diol Index), we analyzed core-tops as well as sediment trap samples (chapters 4 – 6). Lastly, we applied the proxies down-core, thereby studying their potential as proxies on a glacial-interglacial timescale, as well as over the last 90 Myrs (chapters 7 and 8).

In **Chapter two** several chromatographic methods to analyze long-chain diols, as well as long-chain alkenones and GDGTs, are compared and evaluated. The traditional methods used for long-chain diols and alkenones, i.e., gas chromatography (GC)–flame ionization detection (FID) and GC– mass spectrometry (GC-MS) using selected ion monitoring (SIM) were evaluated and compared with newly developed methods. We developed a GC-MS/MS method using multiple reaction monitoring (MRM) for the analysis of diols, and two liquid chromatography-mass spectrometric (LC-MS) methods, i.e., ultra-high performance LC (UHPLC) nominal mass MS in SIM mode and UHPLC with high resolution MS (HRMS), to simultaneously analyze diols, alkenones and GDGTs. We

compared the methods in terms of detection and quantification limits, and reproducibility, by serial dilutions of culture extracts. For alkenones, both UHPLC-MS using SIM and UHPLC-HRMS were 2 to 3 orders of magnitude more sensitive as compared to GC-FID. For diols, the lowest quantification limit was obtained using MRM, though authentic standards are needed to quantify the LCDs. The HRMS method revealed a similar quantification limit as the traditional GC-MS method, and best reproducibility. However, the UHPLC nominal mass MS method was more than one order of magnitude less sensitive. In summary, the UHPLC-HRMS is an excellent method for the simultaneous determination of the LDI, $U_{37}^{K'}$ and TEX_{86}, but standards are needed for quantification and the determination of relative response factors.

Chapter three reports on the impact of different culture conditions on the production and composition of long-chain diols in *Nannochloropsis*. The culture conditions included variations in light irradiance, salinity, nitrogen depletion, desiccation, oxidative stress and cold shock. All experiments revealed relatively similar LCD concentrations which suggests that they are not storage lipids, but support the hypothesis that they act as building blocks of the algaenan in the cell wall. Abundances of C_{30} 13 and C_{32} 15 hydroxy fatty acids, which are potential precursors of LCDs, correlate with those of the C_{14} and C_{16} fatty acids, conform with the idea that long-chain hydroxy fatty acids form after hydroxylation and elongation of shorter fatty acids.

Chapter four describes the analysis of sediment traps from five tropical sites (Cariaco Basin, tropical Atlantic, Mozambique Channel) to evaluate seasonal imprints in the concentrations and fluxes of long-chain diols, and the LDI proxy and Diol Index. Quantification of diols in sediment traps from the Atlantic, and underlying surface sediments showed that generally less than 2 % of the LCDs from the water column is preserved in the sediment. However, despite significant degradation, LDI-derived temperatures are very similar for the sediment traps and seafloor sediments, and correspond with annual mean SST. In the Cariaco Basin, the LDI shows a clear seasonal signal, linked to seasonal upwelling, with LDI-temperatures associated with water depths of up to ca. 30 m during summer stratification, and surface temperatures during winter with shoaling of the thermo- and nutricline. In the Atlantic and Mozambique Channel, minimal seasonal LDI-variations are observed, which at least in the Mozambique Channel is probably caused by resuspension due to eddy migration. Good agreement between primary production rates (driven by upwelling) and the Diol Index in the Cariaco Basin suggests that the Diol Index is an excellent upwelling indicator in this area.

The global LDI core-top calibration was extended and reevaluated in **Chapter five**. In total, 597 globally distributed marine surface sediments were considered, revealing a similar relation with annual mean SST as the original calibration, but with increased scatter (R^2 = 0.82). We evaluated the impact of fresh water (e.g., river runoff) on the LDI, and observed that core-tops in brackish/fresh water regions showed substantial deviations in LDI-derived temperatures as compared to the calibration line. Exclusion of core-tops with

salinities below 32 substantially decreased the amount of scatter in the calibration ($R^2 = 0.86$). Additionally, we identified core-tops which showed unusual LCD distributions, all revealing LDI-temperatures significantly lower when compared to that predicted by the calibration. These distributions are characterized by relatively high 1,12-diols and $C_{27} - C_{30}$ hydroxy fatty acids, typical biomarkers for *Proboscia* diatoms, and thus indicative of *Proboscia* production. Exclusion of core-tops with high 1,12-diol abundances also substantially improved the LDI relation with SST ($R^2 = 0.88$). The final LDI-temperature transfer function is highly similar to the original calibration of Rampen et al. (2012), but with a larger calibration error of 3 °C.

Chapter six presents a core-top study along the Portuguese margin, influenced by upwelling and fluvial input. Marine suspended particulate matter (SPM) as well as SPM from the Tagus River was analyzed. We observed elevated abundances of the C_{32} 1,15-diol in the surface sediments in the river mouths of the Douro and Tagus Rivers, and its fractional abundance correlated strongly with the BIT index, a proxy for riverine continental input (Hopmans et al., 2004). Moreover, we noted an even higher fractional abundances of the C_{32} 1,15-diol in the river SPM, suggesting that this diol derives from rivers, and might be a suitable tracer of river outflow. The LDI temperatures agreed relatively well with satellite SST offshore, but was substantially lower in front of the Tagus and Sado rivers, suggesting that river runoff compromises the LDI. The Diol Index was high along the northern part of the coast, likely linked to coastal upwelling. A substantial difference in the stable carbon isotopic composition (3.8 ‰) of the $C_{30:1}$ and $C_{28:0}$ 1,14-diol suggests different sources for these 1,14-diols.

Chapter seven reports on the application of the long-chain diol proxies down-core, over the last 150 kyrs, at ODP site 1234, offshore Chile. The LDI co-varies with the TEX_{86}^{H}, $U_{37}^{K'}$, and planktonic $\delta^{18}O$, implying that the LDI reflects past SST variations at this site. The Diol Index, as well as a recently proposed nutrient proxy based on 1,14-diols (Nutrient Diol Index; NDI; Gal et al., 2018) shows significant differences with other proxies indicative of phytoplankton productivity, i.e., TOC, C_{37} alkenone, dinosterol and loliolide accumulation rates, and diatom counts. Where most proxies suggest a peak in upwelling intensity and primary productivity around 100 ka, the Diol Index and the NDI reveal a minimum around this time, and peak before and after the upwelling event. This suggests that the Diol Index and NDI should perhaps be more considered as proxies for *Proboscia* productivity, rather than upwelling conditions or nutrient concentrations.

Finally, in **Chapter eight** changes in long-chain alkenone, diol and GDGT distributions in sediments from the Bass River core (New Jersey, USA) over the last ca. 90 Myrs are described. GDGT distributions remained fairly similar, showing distributions which are comparable to modern-day distributions, suggesting that the TEX_{86} can be applied up to 90 Ma. Late Cretaceous sediments reveal the presence of an unusual $C_{40:2}$ alkenone, suggesting different ancestors. The long-chain diol distributions show a clear change through

time, with dominant C_{30} and C_{32} 1,15-diols in the youngest intervals, up to the Miocene/Oligocene, and dominant C_{28} 1,12- and C_{26} 1,13-diols in the older sediments (Eocene-Cretaceous). The LDI could be calculated up to ca. 50 Ma but disagrees with other paleotemperature records, suggesting that the unknown producers of the C_{28} 1,12-diol and C_{26} 1,13-diols between 33 and 91 Ma may have impacted the LDI.

In summary, the results described in this thesis show that even though the long-chain diol proxies, i.e. the LDI and Diol Index, have great value, there are several factors compromising the proxies spatially and temporarily. The Diol Index is in some regions an excellent indicator of upwelling intensity. However, since the index is based on lipids produced by *Proboscia* diatoms, it is in fact an indicator of *Proboscia* productivity. Whether the proxy tracks upwelling variations or not is dependent on the ecological dynamics in the region, since the abundance of *Proboscia* is controlled by several environmental factors (e.g., nutrient availability, competition with other phytoplankton). The LDI shows a strong correlation with SST and applications down-core have proven its potential as SST proxy. However, the proxy can be compromised by diol production of *Proboscia* diatoms and by freshwater input. Regional core-top studies can assess such local factors. Moreover, more studies are needed to assess the applicability of the LDI throughout the Cenozoic as first results show that unknown producers of diols may cause a bias. Most importantly, future research should aim at identification of the marine biological sources to understand the biochemical function of long-chain diols.

Chapter 2

Development and comparison of chromatographic methods for the analysis of long-chain diols and alkenones in biological materials and sediment

Marijke W. de Bar, Ellen C. Hopmans, Monique Verweij, Denise J.C. Dorhout, Jaap S. Sinninghe Damsté and Stefan Schouten

Journal of Chromatography A 1521 (2017)

DOI: 10.1016/j.chroma.2017.09.037

Abstract

We have compared and assessed the suitability of several chromatographic methods for the analysis of long-chain alkenones and long-chain diols and the associated paleotemperature proxies ($U^{K'}_{37}$ and LDI). We evaluated the traditional methods for the analysis of the $U^{K'}_{37}$ and the LDI, gas chromatography (GC) - flame ionization detection (FID) and GC mass spectrometry (MS) using selected ion monitoring (SIM), respectively, and developed a new method using GC-MS/MS in multiple reaction monitoring mode (MRM) for the analysis of long-chain diols as well as a method for automatic silylation of diols using a robot autosampler. Finally, we evaluated liquid chromatography (LC) methods to simultaneously measure the $U^{K'}_{37}$ and the LDI, using ultra high performance LC (UHPLC) with low (nominal mass) resolution MS in SIM mode, and UHPLC with high resolution MS (HRMS). Detection and quantification limits and reproducibility were assessed by means of serial dilutions of culture extracts. Automated silylation by robot autosampler showed similar reproducibility as off-line silylation while substantially decreasing sample preparation time. The novel MRM method had a slightly lower limit of quantification (LOQ; i.e. 0.3 pg C_{28} 1,13-diol injected on-column) than the traditional method (0.5 pg) and improved reproducibility while allowing more unambiguous identification of LCDs in complex matrices. For diols, UHPLC-MS using SIM had the highest LOQ (i.e. 15 pg) and a comparable reproducibility as GC-MS. UHPLC-HRMS had a LOQ of ca. 1.5 pg, and an improved reproducibility for diol analysis. For alkenone analysis, both UHPLC-HRMS and UHPLC-MS using SIM were 2-3 orders of magnitude more sensitive (LOQ ca. 20 and 2 pg $C_{37:2}$ alkenone injected on-column, respectively) than GC-FID (LOD ca. 3 ng), with a similar reproducibility of the $U^{K'}_{37}$ index. Hence, UHPLC-HRMS allows simultaneous analysis of the $U^{K'}_{37}$ and LDI at an increased sensitivity. In addition, it allows simultaneous measurement of TEX_{86}, a temperature proxy based on the isoprenoid glycerol dialkyl glycerol tetraethers. This reduces the preparation

time by excluding the need of derivatization and separation of the ketone (containing the long-chain alkenones) and polar fractions (containing the long-chain diols and GDGTs). However, synthetic standards are required to fully assess the accuracy of the new methods for determination of the LDI and $U_{37}^{K'}$.

1. Introduction

Future climate conditions can be better assessed if we have knowledge of past climate and oceanic responses to past climate perturbations. The reconstruction of past temperatures is one of the main goals for paleoceanographers as temperature is an important boundary condition for identifying the processes and mechanisms responsible for past climate changes. Two organic proxies, the TEX_{86} based on glycerol dialkyl glycerol tetraethers (GDGTs) (Schouten et al., 2002) and $U_{37}^{K'}$, based on long-chain alkenones (LCAs) (Brassell et al., 1986) (Fig. 1) have been developed, and are now commonly applied in reconstructing past sea water temperatures. Recently, a new index has been proposed, the Long chain Diol Index (LDI) (Rampen et al., 2012), based on the distribution of specific long-chain diols (LCDs) occurring in marine sediments (Fig. 1) (Volkman et al., 1992; Versteegh et al., 1997), likely derived from eustigmatophyte algae. Thus, it is now possible to use a multiproxy approach using three independent organic proxies to constrain past seawater temperatures. This is often preferred as every proxy has its limitations, and therefore the comparison between different proxies can shed more light on these shortcomings, and result in better constrained temperature reconstructions.

The traditional method for the analysis of LCAs is gas chromatography-flame ionization detection (GC-FID) (Herbert, 2003). Although this method separates and quantifies LCAs satisfactorily, there are disadvantages such as the co-elution of long-chain alkenoates and adsorption effects (Villanueva and Grimalt, 1997; Grimalt et al., 2001), and studies have therefore focused on e.g. sample clean up (Villanueva et al., 1997), different GC stationary phases (Longo et al., 2013), multidimensional GC (Xu et al., 2001) and new detection methods such as GC-chemical ionization mass spectrometry (GC-CI-MS) (Rossell-Melé et al., 1995; Chaler et al., 2000), GC-electron ionization MS (GC-EI-MS) in selected ion monitoring (SIM) mode (Rontani et al., 2006b), and GC time-of-flight MS (GC-TOF-MS) (Hefter, 2008). Two studies have evaluated the possibility to analyze LCAs by means of liquid chromatography (LC)-MS. Schwab et al. (2009) presented a semi-preparative normal phase high pressure LC-MS (NP-HPLC-MS) protocol for purifying C_{37} and C_{38} LCAs and Becker et al. (2015) proposed a method for the quantitation of the C_{37} and C_{38} LCAs using LC-qTOF- high resolution MS (LC-qTOF-HRMS). Despite all these developments, LCA analysis by means of GC-FID is still the most preferred method as the instrumentation is relatively cheap and easy to use, and the chromatographical separation and the sensitivity is generally sufficient.

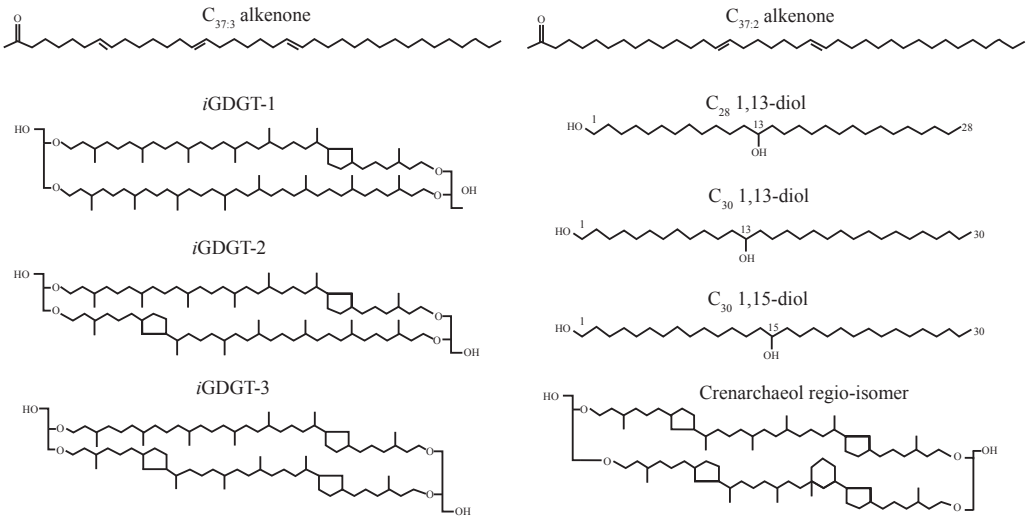

Fig. 1 Structures of some long-chain alkenones, isoprenoid GDGTs and long-chain diols.

GDGTs, which are used for the TEX_{86} index, are analyzed by normal phase high performance liquid chromatography coupled to atmospheric pressure chemical ionization mass spectrometry (NP-UHPLC-APCI-MS), and were initially quantified in full scan (*m/z* 950-1450) by peak integration of the $[M+H]^+$ and $[M+H]^+$+1 (protonated molecule and isotope peak) (Hopmans et al., 2000; Schouten et al., 2002; Escala et al., 2009). Presently, GDGTs are analyzed by SIM of the protonated molecules $[M+H]^+$ (Schouten et al., 2007). In 2013, a new HPLC protocol using reversed phase (RP) combined with electrospray ionization (ESI) MS was proposed for the analysis of GDGTs, enabling comprehensive analysis of intact polar lipid (IPL) and core GDGTs (Zhu et al., 2013). Becker et al. (2013) proposed a new method with improved chromatography for the isoprenoid core GDGTs, using two UHPLC BEH HILIC amide columns in tandem. Recently, improved NP separation of core GDGTs was achieved using two UHPLC silica columns in series, in combination with the APCI-MS detection method (Hopmans et al., 2016).

Finally, LCDs are commonly analyzed by GC-MS of their silylated derivatives and quantified using SIM (Rampen et al., 2012). GC separates the diols based on chain lengths but not on mid-chain alcohol position. MS analysis, however, allows identification of the specific mid-chain isomers based on fragment ions formed by cleavage adjacent to the OTMSi groups (silylated hydroxyl groups) and quantification is achieved by SIM analysis of these specific fragment ions (Versteegh et al., 2997; Rampen et al., 2012). The contributions of these selected ion fragments to the total ion counts for the different LCDs is taken into account and corrected for. Unfortunately, LCD analysis requires substantial work up time because of derivatization, and injection of silylated polar fractions of sediment extracts often

results in major build-up of column contamination, limiting sample throughput. Recently, it was shown that diols can also be analyzed by UHPLC-HRMS in which diols are separated on the basis of their mid-chain alcohol position rather than on chain length (Becker et al., 2015). Analysis of LCDs by LC-MS offers several advantages, i.e. no derivatization is needed, therefore contamination by silylation reagents is avoided, and sample preparation is less time consuming. Another advantage of this approach is that other lipids used as proxies for past climate conditions can be measured simultaneously, i.e. GDGTs for the TEX_{86} temperature proxy, and LCAs used in the $U^{K'}_{37}$ index, substantially improving sample throughput. However, an UHPLC-HRMS is relatively expensive and therefore not readily available in paleoclimate geochemical labs. Furthermore, it is not clear how well the sensitivity and accuracy of LCD and LCA analysis on an UHPLC-HRMS compares with that of the more traditional GC-MS and GC-FID, respectively.

Here we evaluated different analytical methods for the identification and quantification of lipids for paleotemperature assessment (see Table 1 for overview). The ideal method would be one that allows the simultaneous analysis of multiple proxies, i.e. the TEX_{86}, $U^{K'}_{37}$ and LDI, i.e. UHPLC-HRMS (Becker et al., 2015). However, since most paleoclimate geochemical labs have less advanced MS equipment, we have evaluated this approach using both low (nominal mass) resolution MS and HRMS. In addition, we developed a novel method for diol analysis using GC-MS/MS in multiple reaction monitoring (MRM) mode and compare this with the UHPLC-MS and traditional GC-SIM methods. Furthermore, we developed an automated silylation procedure using a robot autosampler to minimize preparation time for GC-analyses.

	GC	**GC-MS**	**UHPLC-MS**	**GC-MS/MS**	**UHPLC-HRMS**
Diols		SIM *	SIM	MRM	Full scan
Alkenones	FID *		SIM		Full scan

Table 1 Analytical methods evaluated for the analysis of long-chain diols and long-chain alkenones. The traditional methods are indicated with an asterisk (*), i.e., GC-MS using single ion monitoring (SIM) for long-chain diols, and GC-FID for long-chain alkenones.

2. Experimental section

2.1 Samples and extraction

2.1.1 Long-chain diols

LCDs were extracted from *Nannochloropsis oculata* biomass (Reed Mariculture, Inc., San Jose, USA). After freeze-drying, the biomass (46.9 g dry weight) was saponified (following de Leeuw et al., 1983 and Rodrigo-Gámiz et al., 2015) by refluxing for 1 h with 1 N potassium hydroxide (KOH) in methanol (MeOH) (96 %). Subsequently, 2 N hydrochloric acid (HCl)/MeOH (1:1, vol./vol.) was added to obtain a pH of 3. The extract was then transferred to a separatory funnel filled with bidistilled water. The residue was washed with MeOH/H_2O (1:1, vol./vol.), MeOH (two times) and dichloromethane (DCM) (three times), and these solvents were pipetted in the separatory funnel. The DCM layer was collected in a round-bottom flask. The solvent was removed by rotary evaporation. Subsequently, water was removed from the total lipid extract (TLE) over anhydrous Na_2SO_4 using a Pasteur pipette, and the TLE was dried down under N_2. The TLEs were separated by column chromatography, for which activated (for 2 h at 150 °C) Al_2O_3 was used as stationary phase, using 3 column volumes DCM and DCM/MeOH (95:5, vol./vol.) as eluents to yield the apolar and polar fractions, respectively. Prior to GC-MS analysis, aliquots of the polar fraction were silylated by means of addition of BSTFA (N,O-bis(trimethylsilyl)trifluoroacetamide) and pyridine, and heating of the sample at 60 °C for 20 min. For GC-MS/MS analysis the polar fraction was silylated by a robotic autosampler (see below). In case of LC-MS analysis, an aliquot of the polar fraction was re-dissolved in hexane/isopropanol (99:1, vol./vol.), and filtered over a 0.45 μm PTFE filter. For quantification purposes we added a C_{22} 7,16-diol internal standard (31.0 μg) to the polar fractions (MolPort SIA, Latvia).

A selected set of sediment extracts and one river suspended particulate matter (SPM) sample with a range of LDI values were analyzed on GC-MS/MS in MRM mode and GC-MS in SIM mode. These samples derive from the Iberian Atlantic margin and the Tagus river, collected during the PACEMAKER 64PE332 cruise with the R/V Pelagia in 2011 (Zell et al., 2014; 2015). Furthermore, to evaluate the simultaneous analysis of LCDs, LCAs and isoprenoid GDGTs by means of UHPLC-HRMS, we also analyzed a lipid extract from a sediment sample derived from sediment core 434G (252.5 cm) (Alboran Sea, latitude: 36´12.313N, longitude: 4´18.735W; depth: 1108 mbsl, sample interval: 231.25–232.75 cm) recovered during the TTR-17 cruise with the R/V Professor Logachev (Rodrigo-Gámiz et al., 2014). All samples were extracted by means of accelerated solvent extraction (ASE) and polar fractions were obtained by column chromatography as described previously by Rodrigo-Gámiz et al. (2014) for the Alboran Sea and Zell et al. (2014; 2015) for the Iberian Atlantic margin and Tagus river.

The LDI was calculated according to Rampen et al. (2012):

$$LDI = [C_{30}\ 1,15\text{-diol}]/[C_{28}\ 1,13\text{-diol}+C_{30}\ 1,13\text{-diol}+C_{30}\ 1,15\text{-diol}] \quad (1)$$

Sea surface temperature (SST) is calculated from the LDI index based on the following relation:

$$LDI = 0.033\times SST+0.095 \qquad (R^2 = 0.969;\ n = 161) \quad (2)$$

2.1.2 Long chain alkenones

LCAs were extracted from freeze-dried *Emiliani huxleyi* biomass obtained by collecting washed out cells from a continuous culture. The biomass was extracted by sonication using DCM/MeOH (2:1, vol./vol.) according to Chivall et al. (2014). The TLE was separated over activated Al_2O_3, using 4 column volumes of *n*-hexane/DCM (9:1, vol./vol.), *n*-hexane/DCM (1:1, vol./vol.) and 3 column volumes of DCM/MeOH (1:1, vol./vol.) as eluents to yield the apolar, ketone and polar fractions, respectively. The fraction was dissolved in ethyl acetate prior to analysis on GC-FID, and in hexane/isopropanol (99:1, vol./vol.), and filtered over a 0.45 µm PTFE filter prior to injection on LC-MS. For quantification purposes, a 10-nonadecanone ($C_{19:0}$ ketone; 300.8 µg; Aldrich Chemical Company, Inc., USA) internal standard was added to the extract.

The $U^{K'}_{37}$ index as described by Prahl and Wakeham (1987) was calculated:

$$U^{K'}_{37} = [C_{37:2}\ \text{alkenone}]/[C_{37:2}+C_{37:3}\ \text{alkenones}] \quad (3)$$

The $U^{K'}_{37}$ values were converted to SST using the following equation (Müller et al., 1998):

$$SST = (U^{K'}_{37}-0.044)/0.033 \qquad (R^2 = 0.958;\ n = 370) \quad (4)$$

2.2 Instrumentation

2.2.1 GC-FID

GC-FID analysis of LCAs was performed using an Agilent 6890N GC with FID and mounted with a 50 m fused silica column (diameter 0.32 mm) coated with CP Sil-5 (thickness 0.12 µm) (e.g. Rodrigo-Gámiz et al., 2015). Helium was used as carrier gas. The oven program started at 70 °C upon injection, and T was subsequently increased by 20 °C per minute to 200 °C, and finally by 3 °C per minute until 320 °C. The final temperature of 320 °C was held for 30 min. A constant pressure of 100 kPa was maintained and samples were injected on-column. The alkenone fraction of the *E. huxleyi* extract, containing LCAs, was serially diluted to assess the limit of detection and quantitation (LOD and LOQ), and these dilutions were measured in duplicate.

2.2.2 GC-MS

GC-MS analysis of LCDs present in silylated polar fractions was carried out on an Agilent 7890B gas chromatograph coupled to a Agilent 5977A mass spectrometer. Samples were dissolved in ethyl acetate and injected at 70 °C. The oven temperature was programmed to 130 °C by 20 °C min^{-1}, and subsequently to 320 °C by 4 °C min^{-1}; this temperature was held for 25 min. The GC was equipped with an on-column injector and fused silica column (25 m × 0.32 mm) coated with CP Sil-5 (film thickness 0.12 µm). Helium was used as carrier gas at a constant flow of 2 mL min^{-1}. The mass spectrometer operated with an ionization energy of 70 eV and a cycle time of 1.9 s. The temperature of the ion source was 250 °C, and of the interface 320 °C. The injection volume was 1 µL. The LCDs were identified by means of the characteristic fragmentation spectra in full scan mode, using a *m*/*z* range of 50–800 (Versteegh et al., 1997). Quantification of the different diol isomers was achieved by selective ion monitoring (SIM) mode scanning of the characteristic fragment ions, i.e. *m*/*z* 299, 313, 327, 341 and 355, with a gain factor of 3 and a dwell time of 100 ms. The runtime was 75.5 min. Serial dilutions of polar fraction of the *N. oculata* extract were analyzed in full scan and SIM mode in triplicate.

2.2.3 GC-MS/MS

GC-MS/MS analysis of LCDs was performed on an Agilent 7890B GC system interfaced to a 7000 C / Triple Quadrupole MS, in multiple reaction monitoring (MRM) mode. An Agilent 7693 robotic autosampler was used to silylate the polar fractions. For this purpose, a small aliquot of the polar fraction was transferred into an autosampler vial with a 250 µL insert and the solvent was evaporated using nitrogen. Firstly, 10 µL pyridine was added, after which the sample was shaken at 2500 rpm for 5 × 5 sec. Subsequently, 10 µL BSTFA was added, and the sample was shaken again at 2500 rpm for 5 × 5 sec. The sample was then heated at 60 °C for 20 min, after which the sample was kept at room temperature for 10 min. Next, 100 µL ethyl acetate was added and the sample was shaken at 3000 rpm for 5 × 10 sec, left for 30 sec, and again shaken at 3000 rpm for 5 × 10 sec. Subsequently, 0.5 µL out of 120 µL was injected on-column. Oven program, column, carrier gas and MS settings were the same as for GC-MS described above, apart from the interface temperature which was 330 °C and a runtime of 60.5 min (kept for solely 10 min at 320 °C). Serial dilutions of the *N. oculata* fractions were analyzed in SIM and MRM mode in triplicate. The environmental samples deriving from the Iberian margin, to assess the relationship between SIM and MRM derived LDI values, were analyzed once.

2.2.4 NP-UHPLC-APCI-MS

NP-UHPLC-APCI-MS analysis of LCDs and LCAs was performed using an Agilent 1260 UHPLC, equipped with automatic injector, coupled to a 6130 Agilent single quadrupole

MSD with HP Chemstation software. The method has been previously been described by Hopmans et al. (2016) for the analysis of GDGTs. Briefly, separation of LCDs and LCAs was achieved using 2 silica BEH HILIC columns in series (150 mm × 2.1 mm; 1.7 µm; Waters Acquity), kept at 25 °C. The compounds were eluted isocratically with 82 % A and 18 % B for 25 min, followed by a gradient to 35 % B in 25 min and 100 % B, kept for 20 min, where A = hexane and B = hexane/isopropanol (90:10, vol./vol.). Flow rate was kept constant at 0.2 mL min^{-1}. Maximum pressure during analysis was 400 bar. The total run time was 102 min followed by 20 min re-equilibration, for LCDs. For LCAs the total run time was shortened to 26 min, i.e. using solely isocratic elution, however, in case of multi-proxy analysis, a total run time of 102 minutes is needed. Conditions for the APCI-MS were as follows: nebulizer pressure 60 psi, vaporizer temperature 400 °C, drying gas (N_2) flow 6 L min^{-1} and temperature 200 °C, capillary voltage -3kV, corona 5 µA. Initially detection of diols was achieved by monitoring *m*/*z* 375 to 525. In general, a 10 µL injection volume was used. For determination of LOD and LOQ, serial dilutions of both the *N. oculata* and *E. huxleyi* fractions were analyzed in triplicate in SIM mode. For the LCDs the $[M+H]^+$–18 ions with *m*/*z* 409 (C_{28}), 437 (C_{30}), 451 (C_{31}), 465 (C_{32}), 493 (C_{34}) and 521 (C_{36}) were integrated, whereas for the $C_{37:2}$ and $C_{37:3}$ LCAs the $[M+H]^+$ protonated molecule traces were integrated, i.e. *m*/*z* 531 and 529, respectively.

2.2.5 UHPLC-HRMS

UHPLC- high resolution MS (HRMS) was performed using an Ultimate 3000 RS UHPLC equipped with thermostatted auto-injector and column compartment coupled to a Q Exactive (Quadrupole Orbitrap hybrid MS) MS equipped with ion max source with APCI probe (Thermo Fisher Scientific, USA). The Q Exactive was calibrated within a mass accuracy range of 1 ppm using the Thermo Scientific Pierce LTQ Velos ESI Positive Ion Calibration Solution (containing a mixture of caffeine, MRFA, Ultramark 1621, and N-butylamine in an acetonitrilemethanol-acetic solution). The positive-ion APCI settings were as follows: capillary temperature 275°C, sheath gas (N_2) 50 arbitrary units (AU); auxiliary gas (N_2) 5 AU, corona current 4.5 µA, APCI heater temperature 275 °C and S-lens 50 V. Separation was achieved using the identical chromatographic conditions as described above for the UHPLC-single quadrupole MS measurements.

Detection of LCDs, LCAs and GDGTs was achieved in positive ion mode by scanning *m*/*z* 400–1450 with a resolution of 17,500 ppm mimicking the resolution of a typical TOF MS. Quantifications were done by integrating mass chromatograms (smoothed with Gaussian factor 7) within 20 ppm mass accuracy of the protonated molecules (LCAs and GDGTs) or the protonated molecules after loss of water ($[M+H]^+ – H_2O$) in case of LCDs. Serial dilutions of both the *N. oculata* and *E. huxleyi* fractions were analyzed in triplicate.
To determine the elution order of the LCD isomers on the UHPLC-MS, LCD isomers of the *Nannochloropsis oculata* culture were isolated by separation on the Agilent 1260 UHPLC with identical chromatography (2 × BEH HILIC Si; Hopmans et al., 2013) as described

above, and subsequent collection of half minute intervals by an ISCO Foxy Jr. fraction collector. The solvent in the collection vials within the diol time window (15–30 min) were evaporated under N_2, the fractions were silylated and analyzed by GC-MS.

3. Results and discussion

3.1 Development and evaluation of different methods for the analysis of LCDs

The traditional method for quantification of LCDs, as well as computation of the LDI, is single quadrupole GC-MS using SIM, as introduced by Rampen et al. (2012). We developed a new method, using triple quadrupole GC-MS/MS using MRM to improve selectivity compared to SIM detection. Moreover, we developed a method for the automatic silylation of polar fractions using a robot autosampler to increase sample throughput. Additionally, a multi-proxy analytical method using UHPLC-HRMS modified from Becker et al. (2015) was evaluated in terms of sensitivity. Besides UHPLC-HRMS, we also analyzed LCDs using UHPLC- single quadrupole MS in SIM mode (see Table 1 for overview of methods). For both approaches the UHPLC chromatographic protocol according to Hopmans et al. (2016) (i.e., 2 × BEH HILIC Si) was used. Below, we will first discuss the development of automated silylation combined with MRM analysis using triple quadrupole GC-MS/MS, followed by the analysis of diols on UHPLC-HRMS and UHPLC-MS.

3.1.1 Automated silylation

Traditionally, polar fractions are silylated manually in the laboratory prior to injection by addition of two silylation reagents (pyridine and BSTFA) and heating for >20 min, followed by the addition of the injection solvent (mostly ethyl acetate). Here, a robot autosampler was used for automatic silylation of the polar fractions, meaning that during a sequence of analyses each fraction is derivatised during the analysis of the prior sample. This is a major advantage in case of large sample sets, saving substantial work-up time, and ensuring that compounds are derivatised freshly at the time of analysis. The most important parameter to optimize was mixing efficiency, i.e. the combination of mixing time and mixing speed (rpm), to ensure complete mixing of the derivatizing reagents pyridine and BSTFA with the injection solvent ethyl acetate in the 205 µL insert vials. For this purpose, several aliquots of the *N. oculata* extract were automatically silylated and after addition of solvent, shaken at different mixing speeds for different durations. Comparisons of the resulting diol peak areas showed that the largest diol peak areas were obtained with a mixing time and speed of 5 × 10 s at 3000 rpm, which was done twice with a 30 s pause in between. Subsequently, we compared the overall yield of diol derivatization of automatic silylation with manual silylation by derivatization and analysis of the C_{22} 7,16-diol standard (in quintuplicate). The difference in peak area between manual silylation and robot silylation (ca. $1.1e^8$ and $9.6e^7$, respectively) is statistically not significant (two-tailed t-test *p*-value = 0.10) and the

reproducibility of both derivatization methods is highly comparable: 9.4 % and 9.7 %. This confirms the robustness of the automated silylation method.

3.1.2 MRM analysis using triple quadrupole GC-MS/MS

We developed methodology for the detection of LCDs using MRM. For a reliable identification we used two MRM transitions: one to quantify the diol (quantifier) and another to confirm the identity of the diol (qualifier). For the first MRM transition (quantification), we selected the ions *m*/*z* 299 (e.g., C_{28} 1,14), 313 (e.g., C_{28} 1,13; C_{30} 1,15) , 327 (e.g., C_{30} 1,14) and 341 (e.g., C_{30} 1,13) as parent ions (Table 2), as these are the most dominant ions produced during electron ionization, and commonly used in GC-MS SIM analysis of diols (Versteegh et al., 1997; Rampen et al., 2012). We examined their MS^2 product spectra after collision induced dissociation with helium and nitrogen. The resulting MS^2 fragmentation spectra reveal *m*/*z* 73 as the dominant fragment as well as *m*/*z* 103 as characteristic product ions for all parent ions, representing the $[TMSi]^+$ and $[CH_2OTMSi]^+$ groups, respectively (see Fig. 2b for *m*/*z* 313 as parent ion for the C_{30} 1,15-diol). Although *m*/*z* 73 is much more abundant than *m*/*z* 103 ion, the latter is more characteristic for LCDs as it is mostly derived from the midchain TMSi group and consequently this ion was selected in MS^2 as the product ion for all LCD parent ions. The collision energy was optimized for maximum yield of the *m*/*z* 103 product ion for each individual LCD (Table 2). The parent ions selected in MS^1 for the second transition (qualification), are the more minor fragments generated from the opposite α-cleavage of the mid-chain silylated alcohol group (see Fig. 2), corresponding to *m*/*z* 359, 373 and 387 for the 1,13, 1,14 and 1,15 diols (Versteegh et al., 1997). In the MS^2 spectrum of these qualifier ions, one of the major fragments is m/z 109 (C_8H_{13}), which was selected as the product ion. Also for this product ion, the collision energy for the production of this fragment was optimized for maximum yield (Table 2).

Compound	Precursor ion	Product ion	Collision energy (eV)
Quantifier ions			
C_{28} 1,14	299	103	14
C_{28} 1,13; C_{30} 1,15	313	103	16
C_{30} 1,14	327	103	16
C_{30} 1,13; C_{32} 1,15	341	103	20
Qualifier ions			
C_{28} 1,13; C_{30} 1,13	359	109	10
C_{28} 1,14; C_{30} 1,14	373	109	10
C_{30} 1,15; C_{32} 1,15	387	109	10

Table 2 MRM transitions and the optimal collision energies used for the analysis of different long-chain diols.

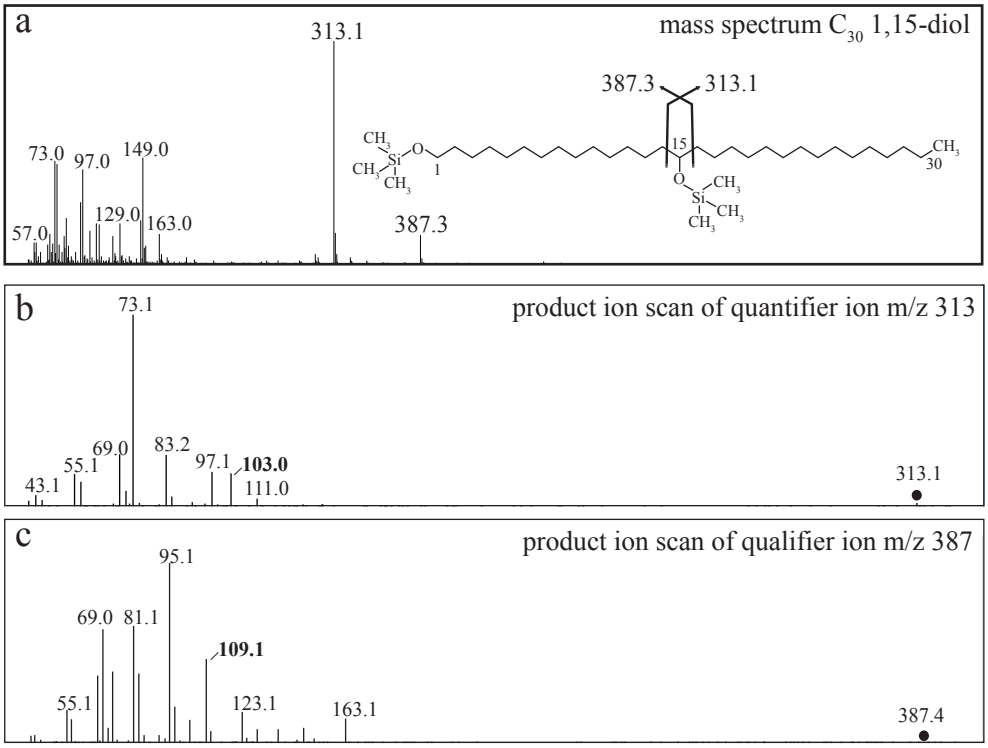

Fig. 2 Panel 2a shows the mass spectrum (MS^1) of the silylated C_{30} 1,15-diol and the typical fragmentations adjacent to the OTMSi group are indicated, resulting in the characteristic product ions with *m/z* 313 and 387. The MS^2 product ions scans of the characteristic mass fragments with *m/z* 313 (quantifier ion) and 387 (qualifier ion) are shown in panel 2b and 2c, respectively. The product ions selected in the second stage of mass filtering (*m/z* 103 and 109) are in bold.

3.1.3 NP-UHPLC-(HR)MS

Becker et al. (2015) showed the possibility of a multi-proxy analysis using UHPLC-MS. We tested this approach using normal phase chromatography of Hopmans et al. (2016) as it has been shown that it results in an improved chromatographic resolution for GDGTs. First we performed a full scan analysis (using single quad MS) to verify the dominant formation of the $[M+H]^+$–18.0 Da (loss of water) for the LCDs over the $[M+H]^+$ after APCI as described by Becker et al. (2015). The LCDs eluted in a time window of 16 to 24 min (Fig. 3b). The elution order of the various diols was confirmed by analyzing collected 30 s effluent fractions with GC-MS. This showed that the normal phase UHPLC method of Hopmans et al. (2016) (2 silica BEH HILIC columns) also results in the separation of LCDs based on the mid-chain position of the hydroxyl group, as observed earlier by Becker et al. (2015) (2 amide BEH HILIC columns).

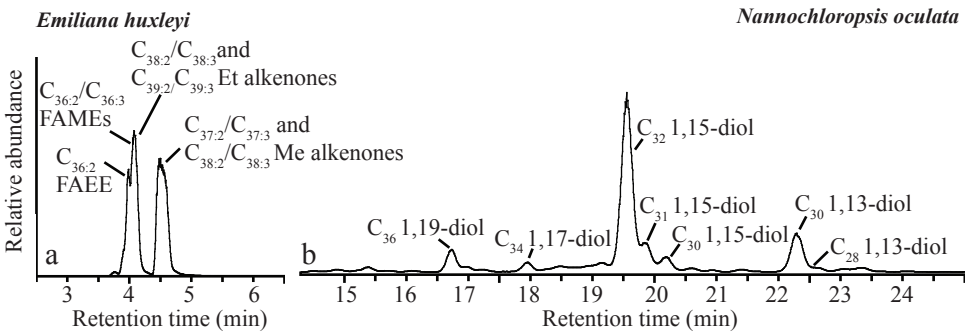

Fig. 3 Partial total ion currents of the *E. huxleyi* (panel a) and *N. oculata* fractions (panel b) analyzed by UHPLC-HRMS (*m/z* 400–1450). Me = methyl; Et = ethyl; FAME = fatty acid methyl ester; FAEE = fatty acid ethyl ester.

3.2 Comparison of LCD analysis methods

We compared five different methods for the quantitation of LCDs: single quadrupole GC-MS using SIM, triple quadrupole GC-MS/MS in SIM mode using the 3rd quadrupole only, triple quadrupole GC-MS/MS using MRM, single quadrupole UHPLC-MS using SIM and Orbitrap UHPLC-HRMS set at a resolution of 17,500 (Table 1). The latter resolution is somewhat lower compared to the 27,000 used by Becker et al. (2015) but in the range of typical LC-TOF-MS equipment which are less expensive.

3.2.1 LOD and LOQ

We determined the limit of detection (LOD) (signal-to-noise ratio (S/N) of > 2) of the C_{28} 1,13-diol (as this was the lowest abundant LCD in the culture extract) and the limit of quantitation (LOQ) of the LDI by repeated analysis of serial dilutions of an extract of *N. oculata* biomass as there are currently no synthetic standards of naturally occurring C_{28}-C_{32} LCDs available. The dominant LCDs present in the *N. oculata* extract are the C_{28} 1,13-, C_{30} 1,13- and 1,15-, C_{31} 1,15-, C_{32} 1,15-, C_{34} 1,17- and the C_{36} 1,19-diol. In order to determine the abundance of the C_{28} 1,13-diol in the extract we added a known amount of a C_{22} 7,16-diol synthetic standard and analyzed the extract by GC-MS in SIM mode. The C_{28} 1,13-diol and C_{22} 7,16-diol were quantified by integrating mass traces *m/z* 313 and *m/z* 187, respectively. A correction of 27 % and 16 % for the C_{22} 7,16- and C_{28} 1,13-diol, respectively, was applied for the contributions of these fragment ions to the total ion counts. The LOQ is defined as the amount of the C_{28} 1,13-diol at which the LDI index significantly deviated from the average LDI determined at higher concentrations.

In Fig. 4 the LDI values versus different amounts of C_{28} 1,13-diol injected are shown for the different methods. The lowest LOD was obtained by MRM analysis, corresponding to ca.

0.05 pg C_{28} 1,13-diol injected on-column. However, the LDI value at this LOD is significantly different from the values at higher concentrations (two-tailed t-test *p*-value << 0.05) and therefore we define the LOQ for the LDI as ca. 0.3 pg LCD injected on-column based on the first higher concentration injected. The LOD and LOQ were slightly higher for SIM analysis on both the single quadrupole MS or the triple quad MS with LODs and LOQs of ca. 0.5 pg C_{28} 1,13-diol injected on-column (Fig. 4). The slightly improved LOD and LOQ of the MRM method compared to a SIM approach is probably due to the elimination of non-targeted compounds and background. This is further demonstrated by the analysis of an environmental sample (Tagus River SPM, Portuguese margin; Zell et al., 2015; de Bar et al., 2016) using MRM (Fig. 5) revealing considerably improved signal-to-noise ratios compared to SIM. The LOD obtained for Orbitrap UHPLC-HRMS is higher than that of both MRM and SIM analysis using GC-MS, being around ca. 1.5 pg C_{28} 1,13-diol injected on-column (Fig. 4). Since at this concentration the LDI is significantly different from the LDI at higher concentrations (two-tailed t-test *p*-value < 0.05), the LOQ is defined as ca. 3 pg C_{28} 1,13-diol injected on-column. This LOQ is in the same order of magnitude as reported by Becker et al. (2015) for LC-qToF-MS ("<10 pg"). However, we observed substantial variations in LOD/LOQ for our triplicate measurements due to variability in background signals, probably due to differences in solvent batches used as mobile phase. Single quadrupole UHPLC-MS reveals a LOD, as well as LOQ, of around ca. 15 pg C_{28} 1,13-diol, i.e. a lower sensitivity compared to GC-MS and UHPLC-HRMS.

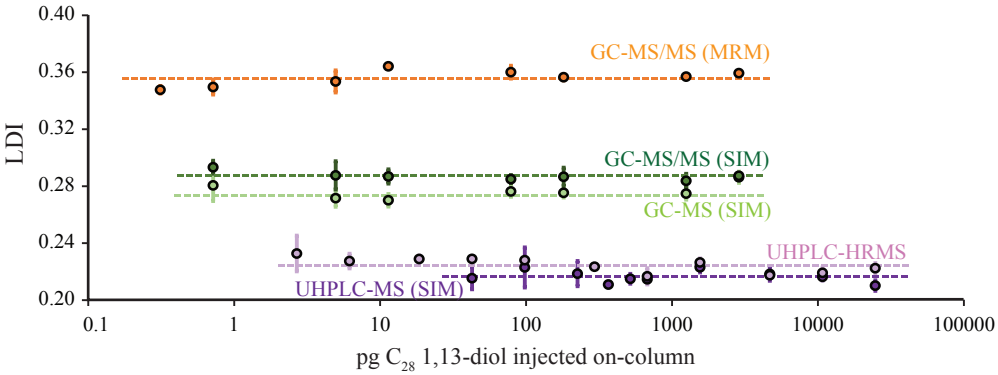

Fig. 4 LDI values versus the amounts of C_{28} 1,13-diol injected on-column for different methods (GC-MS/MS using MRM, GC-MS using SIM for two different MS detectors (dark green = 7000 C GC/MS Triple Quad and light green = Agilent 5977A MS), Orbitrap UHPLC-HRMS and UHPLC-MS using SIM. LCDs were extracted from a *Nannochloropsis oculata* culture. The error bars reflect ± 1σ standard deviation from triplicate measurements; when not visible, the error bars are smaller than the symbol size.

3.2.2 Reproducibility and linearity

The reproducibility of the LDI index was, as observed for the sensitivity, better for GC-MS MRM (±0.0030, n = 24 when solely data above LOQ is considered; reproducibility visualized as error bars in Fig. 4), compared to reproducibility's of ±0.0052 (n = 21) and ±0.0049 (n = 21) we obtained on the single and triple quadrupole GC-MS systems in SIM mode, respectively. The reproducibility of the LDI on UHPLC-HRMS was ±0.0027 (n = 30 above LOQ), similar to the MRM method on GC-MS and better than the single and triple quad GC-MS(/MS) in SIM mode. The reproducibility on UHPLC-MS was ±0.0053 (n = 30). The responses (peak area versus amount of C_{28} 1,13-diol (pmol) injected on-column) were linear for all methods over the measured decades (Table 3).

3.2.3 Comparison of LDI values

We compared the LDI values of the *N. oculata* extract obtained by the five different analysis methods and only considered data above the LOQ (Fig. 6). For the commonly used SIM analysis the LDI was 0.276±0.0052 and 0.287±0.0049 for the single and triple quadrupole MS, respectively, which is statistically different. In fact, all LDI values obtained by the different methods are significantly different from each other (two-tailed t-test *p*-value << 0.05 for all methods). The average LDI values for UHPLC-MS and UHPLC-HRMS are quite similar with values of 0.216±0.0053 and 0.224±0.0027, respectively. Hence, whereas the difference in LDI between the single and triple quadrupole GC-MS was solely 0.011, and the

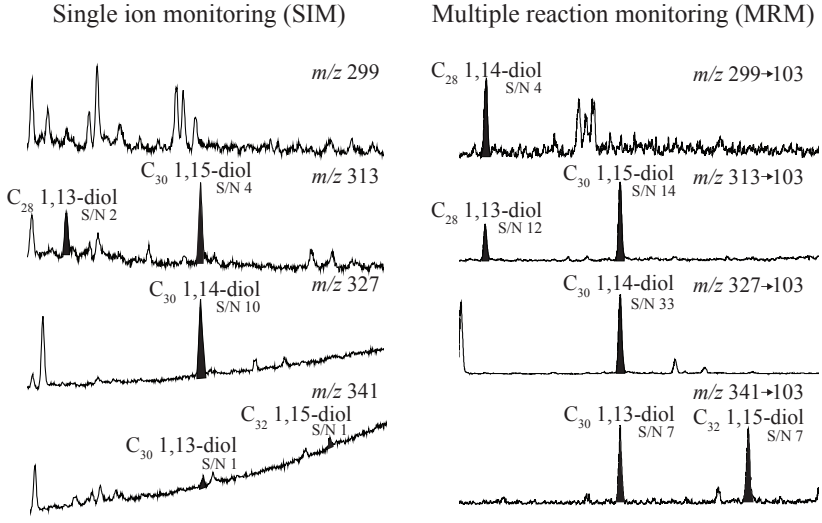

Fig. 5 SIM and MRM chromatograms (left and right) of a sediment sample deriving from the Portuguese margin (Zell et al., 2015; de Bar et al., 2016). As identification in MRM mode is based upon the presence of two target ions, selectivity is improved.

Proxy/ compound	Method	LOD	LOQ	Reproducibility	*n*	R^2
LDI/	GC-MS (SIM)	~0.5 pg	~0.5 pg	±0.0052	21	0.9943
C_{28} 1,13-diol	GC-MS/MS (SIM)	~0.5 pg	~0.5 pg	±0.0049	21	0.9984
	GC-MS/MS (MRM)	~0.05 pg	~0.3 pg	±0.0030	27	0.9993
	UHPLC-MS (SIM)	~15 pg	~15 pg	±0.0053	30	0.9945
	UHPLC-HRMS	~1.5 pg	~3 pg	±0.0027	33	0.9983
$U_{37}^{K'}$/	UHPLC-MS (SIM)	~1 pg	~2 pg	±0.0032	36	0.9972
$C_{37:2}$ alkenone	UHPLC-HRMS	~2 pg	~20 pg	±0.0021	30	0.9946

Table 3 Reproducibility for the LDI and $U_{37}^{K'}$ indices and LOD and LOQ for detection of the compounds used in the indices for the different methods, as well as linear regression data in terms of number of fractions analyzed (*n*; above LOD) and the R^2 describing the peak area response as function of the amount of the C_{28} 1,13-diol/$C_{37:2}$ alkenone (pmol) injected on-column.

difference between UHPLC low (nominal mass) resolution MS and HRMS 0.007, the average difference between GC-MS and UHPLC is the largest at 0.062. Becker et al. (2015) analyzed a sample set with LDI values varying between 0.58 and 0.98 on GC-MS, and showed that the linear relationship was close to the 1:1 line, but the mean Δ_{LDI} between GC and LC was ± 0.03. Hence, in spite of the almost 1:1 relationship, there is a clear difference in absolute LDI values derived from UHPLC and GC-MS. Accordingly, standards are required to monitor the relative responses of the LDI LCDs on LC-MS.

The MRM method reveals an average LDI value of 0.36 for the *N. oculata* extract, i.e., significantly higher than the LDI values in SIM method (Fig. 6). For further comparison, we measured the LDI in MRM and SIM in a number of environmental samples from the Iberian Atlantic margin (Zell et al., 2014; 2015; de Bar et al., 2016). The resulting LDI values show a strong linear correlation (Fig. 7; $R^2 = 0.99$; slope = 0.84). However, note that this relation is not 1:1, with LDI values derived from MRM being generally higher than those from SIM for lower LDI values. This is not unexpected, as the relative peak areas of the LCDs are different in the MRM compared to SIM due to the different fragment yields of *m*/*z* 103 from the target ions (*m*/*z* 299, 313, 327 and 341). Hence, because of these different responses as compared to SIM, authentic LCDs standards will be required to assess the response of the individual LCDs, posing a severe limitation on this MRM method.

3.3 Comparison of methods for LCA analysis

Though many studies have focused on different methods for the analysis of LCAs, the most applied method is still GC-FID due to the relative simplicity of the method, the sufficient

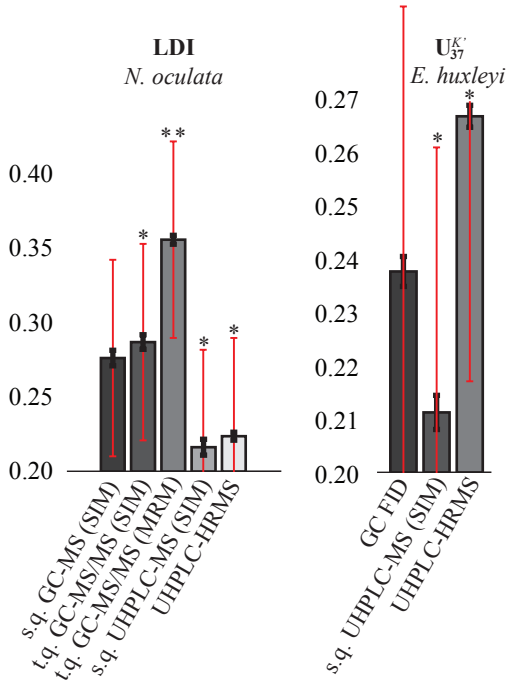

Fig. 6 Average LDI and $U_{37}^{K'}$ values for the *N. oculata* and *E. huxleyi* culture, respectively, obtained using the different methods. The black error bars reflect reproducibility; the red error bars represent the calibration errors (2 °C for LDI; 1,5 °C for $U_{37}^{K'}$). All proxy values are significantly different from each other, as well as from the values obtained by the traditional methods (GC-MS for LDI, GC FID for $U_{37}^{K'}$; * = *p*-value < 0.005; ** = difference is larger than calibration error). S.q. = single quadrupole; t.q. = triple quadrupole.

sensitivity and chromatographic separation and the consistency in $U_{37}^{K'}$ results between different laboratories (Rosell-Melé et al., 2001). However, the recently proposed UHPLC-HRMS approach of Becker et al. (2015) offers the key advantage of the potential analysis of LCAs simultaneously with other biomarkers used in paleothermometry (i.e. GDGTs and LCDs). Similar to Becker et al. (2015), the NP chromatography of Hopmans et al. (2016) allows the computation of the LDI. However, the applicability of this UHPLC method for the determination of the $U_{37}^{K'}$ index needs to be investigated. We therefore also determined LOQ and LOD for LCAs, using the identical chromatography as for the LCDs (2 × BEH HILIC Si; Hopmans et al., 2016), combined with HRMS and low (nominal mass) resolution MS using SIM, and compare this with the traditional GC-FID method.

3.3.1 NP-UHPLC-(HR)MS

We analyzed the ketone fraction of an extract of the coccolithophorid alga *E. huxleyi*. This fraction mainly contains the $C_{37:3}$, $C_{37:2}$, $C_{38:3}$, $C_{38:2}$, $C_{39:3}$ and $C_{39:2}$ LCAs, $C_{36:2}$ fatty acid ethyl ester and $C_{36:3}$ and $C_{36:2}$ fatty acid methyl esters. The dominant ions for the $C_{37:2}$ and $C_{37:3}$ LCAs formed with APCI ionization are the $[M+H]^+$ protonated molecules (Becker et al., 2015). Similar to the separation of the LCDs, the application of the NP-UHPLC (Hopmans

et al., 2016) method results in LCA separation based on the position of the carbonyl group, and not the chain length (as obtained using GC); i.e., the ethyl and methyl LCAs are separated, but the $C_{37:2}$ and $C_{37:3}$ methyl LCAs (used in the $U^{K'}_{37}$) co-elute with a retention time of 4-5 min (Fig. 3a). In contrast, the chromatographic protocol of Becker et al. (2013) results in the chromatographic separation of the C_{37} LCAs. The C_{38} and C_{39} ethyl ketones, as well as the di- and tri-unsaturated C_{36} fatty acid methyl esters and $C_{36:2}$ fatty acid ethyl ester elute before the $C_{37:2}$ and $C_{37:3}$ Me ketones (3.5 - 4.5 min; Fig. 3a). Because of the co-elution of all C_{37} LCAs, the $^{13}C_2$ isotopic peak of the $C_{37:3}$ LCA (i.e. the second isotope peak which has the same *m/z* value as the $C_{37:2}$ LCA) contributes to the monoisotopic peak of the $C_{37:2}$ LCA, and thus the peak area of the $C_{37:2}$ LCA requires correction in order to quantify the $U^{K'}_{37}$. The fractional abundance of this $^{13}C_2$ isotopic peak is 7.79 % of the monoisotopomer (theoretically determined). Consequently, when quantifying co-eluting C_{37} LCAs or calculating the $U^{K'}_{37}$ index on single quadrupole UHPLC-MS using SIM or UHPLC-HRMS, the peak area of the $C_{37:2}$ LCA has to be corrected by subtracting 0.0779 ×area$_{C37:3}$ from the peak area of the $C_{37:2}$ LCA. In this culture, we did not detect the $C_{37:4}$ LCA. However, when present (normally produced under low temperatures or in freshwater environments; Prahl et al., 1988), its $^{13}C_2$ peak would in turn contribute to the area of the $C_{37:3}$ LCA. This contribution would be the same, and hence, also the correction.

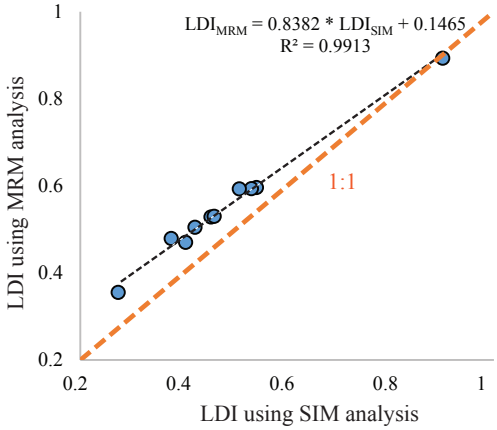

Fig. 7 Cross-plot of LDI values determined by GC-MS using SIM (Agilent 5977A mass spectrometer) and GC-MS/MS using MRM (7000 C GC/MS Triple Quad). The orange dashed line represents the 1:1 line.

3.3.2 LOD and LOQ

We used a serially diluted *E. huxleyi* alkenone fraction in order to determine the LOD of the $C_{37:2}$ LCA and the LOQ of the $U^{K'}_{37}$ for the different methods. To quantify the amount of $C_{37:2}$ LCAs in the *E. huxleyi* alkenone fraction, we added 10-nonadecanone ($C_{19:0}$ ketone) as standard and analyzed the extract by GC-FID assuming equal response factors for the LCAs and 10-nonadecanone. For GC-FID, a LOD of ca. 3 ng $C_{37:2}$ LCA injected on-column was

evident (Fig. 8), in agreement with detection limits of 5 to 10 ng previously reported (Villanueva and Grimalt, 1997). The LOD for both the UHPLC-MS and UHPLC-HRMS is ca. 1 pg and ca. 2 pg LCA injected on-column, respectively, 3 orders of magnitude lower than for GC-FID. Based on significant deviation of the $U_{37}^{K'}$ values (two-tailed t-test *p*-value < 0.05) for the lowest amounts injected, as compared to the average $U_{37}^{K'}$ calculated from the higher concentrations (Fig. 8), we define LOQs of the $U_{37}^{K'}$ index of ca. 2 and ca. 20 pg C_{37} LCA injected on-column for UHPLC-MS and UHPLC-HRMS, respectively.

3.3.3 Reproducibility and linearity

The reproducibility of the $U_{37}^{K'}$ (above LOQ) on the single quadrupole UHPLC-MS was ±0.0032 (n = 33) and ±0.0021 (n = 24) on the UHPLC-HRMS which is similar to that obtained for GC-FID (±0.0028; n = 6). The responses (peak area versus amount of $C_{37:2}$ alkenone (pmol) injected on-column) were linear for both methods (Table 3). This contrast the results of chemical ionization MS in a GC/MS method (GC-IC-MS) for quantitation of LCAs which has shown a substantial non-linear response (Chaler et al., 2003). However, these authors have analyzed higher amounts C_{37} LCAs, i.e., up to ca. 160 ng injected on-column, whereas we have analyzed between ca. 0.4 pg and 4 ng, and Becker et al. (2015) between 10 pg and 10 ng.

3.3.4 Comparison of $U_{37}^{K'}$ values

The average $U_{37}^{K'}$ value calculated for the *E. huxleyi* culture fraction on GC-FID is 0.238±0.0028, whereas on single quadrupole UHPLC-MS and UHPLC-HRMS we obtain values of 0.211±0.0032 and 0.267±0.0021, respectively, i.e. there is a significant difference (two-tailed t-test *p*-value << 0.05) between both UHPLC low (nominal mass) resolution MS and HRMS and GC-FID of 0.026 and 0.029, respectively (Fig. 6). Becker et al. (2015) showed that $U_{37}^{K'}$ values obtained by GC-FID and LC-MS reveal almost a 1:1 relationship, suggesting the suitability of LC-MS for the measurement of the $U_{37}^{K'}$ index. This contrasts, for example, with the findings of Hefter (2008), who observed different relative linear responses for the $C_{37:2}$ and $C_{37:3}$ LCAs leading to different $U_{37}^{K'}$ values for a GC-TOF-MS method as compared to GC-FID. However, as for LCDs, standards are required to monitor the relative responses of the $U_{37}^{K'}$ LCAs on LC-MS.

3.4 Multi-proxy versus individual proxy analysis

As pointed out by Becker et al. (2015), a major advantage of using LC-MS for determination of organic proxies is the simultaneous analysis, i.e. the TEX_{86}, $U_{37}^{K'}$ and LDI can be determined in a single run. Fig. 9 shows an example of an environmental sample analyzed

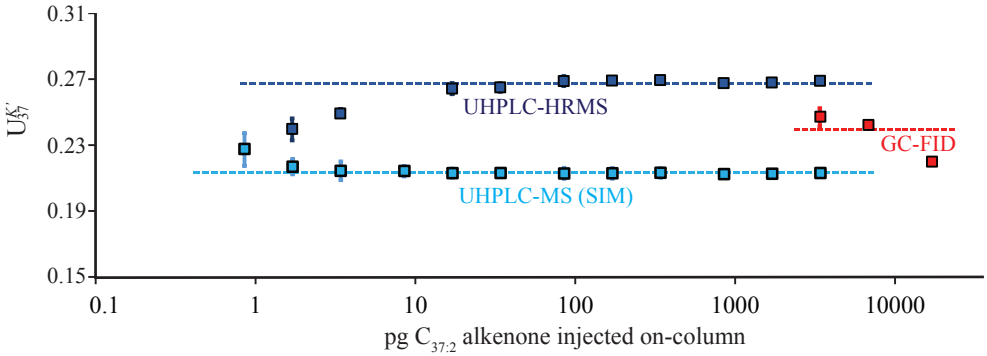

Fig. 8 $U^{K'}_{37}$ values versus the amounts of $C_{37:2}$ alkenone injected on-column for different methods (UHPLC-HRMS, UHPLC-MS and GC-FID). LCAs were extracted from an *Emiliana huxleyi* culture. The dotted lines represent the average $U^{K'}_{37}$ values within the linear response ranges. The error bars reflect ± 1σ standard deviation from triplicate measurements for UHPLC and duplicates for GC; when not visible, the error bars are smaller than the symbol size.

for LCDs, LCAs and GDGTs on the Orbitrap NP-UHPLC-HRMS. This method results in the elution of the isoprenoid GDGTs and LCDs in the same retention window (between ca. 16 and 30 min). Our results show that for LCDs, the LOD and LOQ for UHPLC-HRMS (with a resolution of typical TOF MS) is similar to the conventional GC-MS SIM method, while for LCAs the LOD and LOQ are more than two orders of magnitude lower as compared to GC-FID. Hence, in this sense UHPLC-HRMS seems highly suitable for the simultaneous analysis of GDGTs, LCAs and LCDs. Additionally, since HRMS operates in full scan mode, it allows for identification of other compounds, in contrast to SIM methods. Although the analysis time (ca. 1.7 h) is similar to those of the other methods, the significantly reduced sample preparation time, i.e. no need for silylation of LCDs, and separation of alkenone and polar (GDGTs and LCDs) fractions, allows a substantial increased sample throughput. However, a UHPLC-HRMS is relatively expensive, and not available in all paleoclimate labs in contrast to GC-FID and GC-MS instruments. Another alternative, UHPLC low (nominal mass) resolution MS, which is an increasingly used instrument in geochemical labs (Schouten et al., 2013b), has an LOQ for LCDs that is an order of magnitude higher as compared to GC-MS, making this method less suitable, as LCDs are often present in trace amounts in environmental samples.

With respect to the UHPLC methods, we chose to use the NP-UHPLC chromatographic method according to Hopmans et al. (2016), as the resolution between several critical pairs of GDGTs is highest using this method (Hopmans et al., 2016). However, this two UHPLC silica column method does not result in chromatographic separation of the $C_{37:2}$ and $C_{37:3}$ LCAs and the isomers are only partially separated in mass, requiring an isotope contribution

correction. In contrast, the protocol of Becker et al. (2013) does result in the chromatographical separation of the C_{37} LCAs, but has lesser separation for several critical pairs of GDGTs (Hopmans et al., 2016). Hence, both protocols can be considered equally suitable for multi-proxy analysis.

Although UHPLC-HRMS seems thus highly suitable for the analysis of the TEX_{86}, $U^{K'}_{37}$ and LDI together, we find small but significant differences between LDI and $U^{K'}_{37\,7}$ values obtained with this method in comparison with traditional methods. Even though Becker et al. (2015) showed that the $U^{K'}_{37}$ and LDI indices over temperature ranges gave similar values on LC-MS as compared to the traditional methods (i.e., GC-FID and GC-MS, respectively), absolute responses, and relative responses between compounds can differ substantially per MS. For example, the round-robin study of Schouten et al. (2013a), in which the GDGT indices were compared between 35 laboratories, showed differences in the TEX_{86}, and especially in the BIT index, a proxy for soil organic matter input based on a ratio of branched GDGTs and crenarchaeol. These offsets are likely due to differences in instrumental characteristics. Therefore, it is highly recommended to use standard mixtures to obtain consistent proxy values. The differences in LDI and $U^{K'}_{37}$ values between LC and GC obtained for our culture fractions are ± 1.87 °C and ± 0.84 °C, respectively, when translated to temperature. Although these differences are within the calibration errors of the proxies (2 °C and 1.5 °C for LDI and $U^{K'}_{37}$, respectively), for consistency with studies of e.g. proxy calibrations from different laboratories using different methods, it would be desirable that standard mixtures would be available.

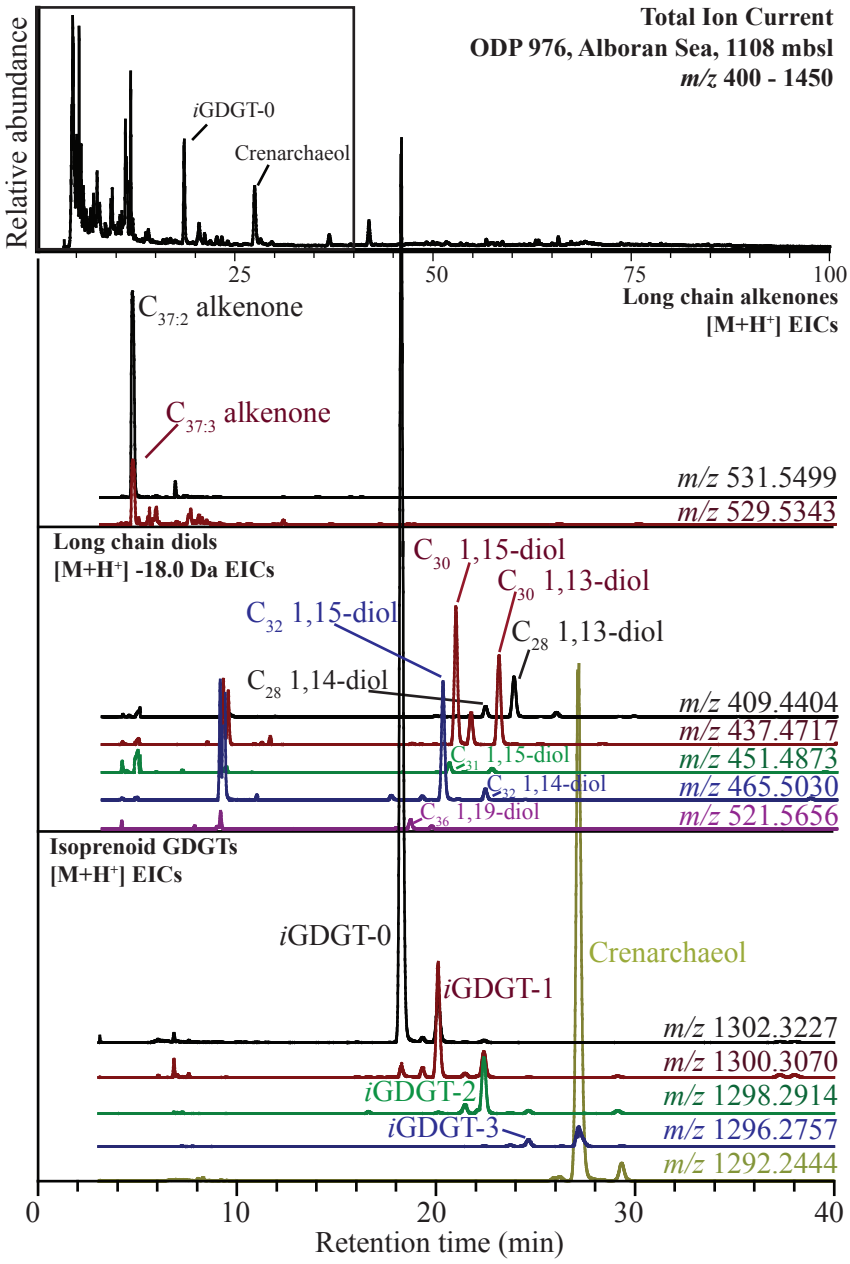

Fig. 9 The upper panel shows the total ion current (TIC) of a sediment sample deriving from the Alboran Sea (Rodrigo-Gámiz et al., 2014) analyzed on the Orbitrap UHPLC-HRMS. The lower three panels show partial extracted ion chromatograms (0 - 40 min) of long-chain alkenones, long-chain diols and isoprenoid GDGTs (from top to bottom).

4. Conclusions

We have developed and compared different methods to analyze LCDs and LCAs. Firstly, we developed a method for automated silylation using a robot autosampler which substantially reduced sample preparation time. We also developed a triple quadrupole GC-MS/MS method for the detection of LCDs, using MRM transitions, resulting in substantial lowering of background levels, and thus increased reliability of identification. Due to this improved selectivity, this method is potentially convenient for detection of LCDs in environmental matrix-rich samples. The LOQ (ca. 0.3 pg C_{28} 1,13-diol injected on-column) is slightly lower than the original GC-MS SIM method (ca. 0.5 pg). The reproducibility was also slightly better. However, for quantification purposes, authentic standards are needed to quantify the LCDs, posing a limitation. Additionally, we have evaluated the multi-proxy approach, i.e. analysis of multiple proxies with a single method as introduced by Becker et al. (2015), using the NP-UHPLC method of Hopmans et al. (2016) combined with Orbitrap HRMS and single quadrupole UHPLC-MS. The HRMS revealed for LCDs a similar sensitivity as GC-MS (LOQ ca. 1.5 pg), and the best reproducibility. In contrast, the LOQ of the low (nominal mass) resolution MS was more than one order of magnitude higher (ca. 15 pg) as compared to the traditional GC-MS method, and therefore less suitable for the analysis of LCDs. The LOQ of the LCAs used for determination of the $U_{37}^{K'}$ index was also in the pg range for both UHPLC-HRMS and UHPLC-MS, which is a substantial improvement as compared to the detection limit of 5–10 ng on GC-FID. Although UHPLC-HRMS is an excellent method for multi-proxy analysis, standard mixtures are recommended to enable quantification and monitor the absolute response of the LCAs and LCDs.

Acknowledgments

This research has been funded by the European Research Council (ERC) under the European Union's Seventh Framework Program (FP7/2007-2013) ERC grant agreement [339206] to S.S. S.S. and J.S.S.D. receive financial support from the Netherlands Earth System Science Centre (NESSC). We thank Dr. David Chivall for growing the *Emiliani huxleyi* culture used in the experiments.

Chapter 3

Impact of culturing conditions on the abundance and composition of long-chain alkyl diols in species of the genus *Nannochloropsis*

Sergio Balzano, Laura Villanueva, Marijke W. de Bar, Jaap S. Sinninghe Damsté and Stefan Schouten

Organic Geochemistry 108 (2017)

DOI: 10.1016/j.orggeochem.2017.02.006

Abstract

Long-chain alkyl diols (LCDs) are widespread in sediments and are synthesized, among others, by microalgae of the genus *Nannochloropsis*. The factors regulating the synthesis of LCDs and their biological function are, however, unclear. We investigated the changes in abundance of free + ester-bound LCDs, extracted by saponification and acid hydrolysis, during the growth of three *Nannochloropsis* species and incubated the species with the highest LCD abundance (*Nannochloropsis oceanica*) under different conditions known to affect the fatty acid content (i.e. light irradiance, salinity, nitrogen depletion, desiccation, cold shock) in order to evaluate their impact on LCDs production. LCD abundances were relatively stable suggesting that they are not used as storage lipids, and support the assumption that LCDs derive primarily from an aliphatic biopolymer located in the outer cell wall (algaenan). Oxidative stress caused by hydrogen peroxide led to a decrease in $C_{32:1}$ diol, as well as other algaenan-derived compounds such as 15-OH-$C_{32:0}$ fatty acid and $C_{32:2}$ alkenol suggesting that algaenans can play a role in the protection of *Nannochloropsis* cells. The relatively constant amount of LCDs per cell suggests that the abundance of LCDs in aquatic environments may be used as an indicator for the abundance of diol-producing algae. Interestingly, the abundance of $C_{30:0}$ 13-hydroxy and $C_{32:0}$ 15-hydroxy fatty acids, potential precursors for LCDs, correlate with those of the major $C_{14:0}$ and $C_{16:0}$ fatty acids. This supports the idea that the biosynthesis of LCHFAs might proceed by hydroxylation and elongation of shorter C_{14}-C_{16} fatty acids.

1. Introduction

Long-chain alkyl diols (LCDs) are lipids that contain an *n*-alkyl chain with 28 to 32 carbons, hydroxyl groups at C-1 and a mid-chain position (predominantly at C-13, C-14, or C- 15), and can be saturated or monounsaturated. LCDs have been identified in several *Nannochloropsis* species (Volkman et al., 1992; Gelin et al., 1997a; 1997b; Rampen et al., 2014b), as well as other Eustigmatophyceae (Volkman et al., 1999a; Rampen et al., 2014b), the Dichtyochophycea *Apedinella radians* (Rampen et al., 2011), and diatoms from the genus *Proboscia* (Sinninghe Damsté et al., 2003; Rampen et al., 2009). In spite of their presence in only a few algal taxa, which account for minor proportions of the phytoplankton biomass in seawater (de Vargas et al., 2015), LCDs are widespread in both sediment and suspended particulate matter from freshwater (Xu et al., 2007; Zhang et al., 2011; Atwood et al., 2014; Villanueva et al., 2014) and marine environments (Versteegh et al., 1997; Rampen et al., 2007; Rampen et al., 2008; Volkman et al., 2008; Rampen et al., 2014b). The distribution of LCDs has also been explored as potential proxy for ancient water temperatures (Rampen et al., 2008; Rampen et al., 2012; Rampen et al., 2014b; de Bar et al., 2016; Rodrigo-Gámiz et al., 2016) and nutrient conditions (Rampen et al., 2014a).

Despite their potential as biomarker lipid and proxy, relatively little is known about LCDs, in terms of both biological function and biosynthetic pathways. LCDs are thought to be the precursors of algaenans, aliphatic biopolymers occurring in the cell wall of algae and consisting of long-chain *n*-alkyl units linked by ether and ester bonds (de Leeuw et al., 1981; Tegelaar et al., 1989; Gelin et al., 1997a; Volkman et al., 1998; Scholz et al., 2014; Zhang and Volkman, 2017). Algaenans in *Nannochloropsis* cell wall are likely to contain also several compounds with similar carbon number and often functionalized at the same positions as the LCDs, such as long-chain alkenols (LCAs, Volkman et al., 1992; Volkman et al., 1999a), keto-ols (Mejanelle et al., 2003), long-chain hydroxy fatty acids (LCHFAs, Volkman et al. 1999b), and long-chain dihydroxy fatty acids (Gelin et al., 1997b). Because of the high similarities in their chemical structures, LCAs and LCDs in *Nannochloropsis* species have been suggested to originate from the reduction of the carboxylic groups of the LCHFAs (Gelin et al., 1997b).

Factors controlling the composition and abundance of LCDs in algae have rarely been studied in detail. Rampen et al. (2014a) showed that LCDs increase in chain length and in the proportion of saturated diols with increasing temperatures. However, it is not clear whether other environmental conditions can affect LCD abundance and composition. Since Eustigmatophyceae comprise both freshwater and marine species (Hibberd, 1981) and occur in estuarine and hypersaline environments (Vinogradova and Darienko, 2008; Samanta and Bhadury, 2014; Balzano et al., 2015), they possess the metabolic plasticity to adapt to different salinities. Estuarine phytoplankton can also experience rapid shifts in nutrients because of the interactions between nutrient-rich freshwater and nutrient-poor seawater as

well as shifts in light irradiance caused by water turbidity. The reliability of proxies based on LCDs might be compromised if the cellular levels and composition of LCDs change with these varying conditions of light, salinity, and nutrients, which typically occur in the environment where LCD-producers occur. Indeed, culture experiments with *Nannochloropsis* spp. show that their fatty acid composition may vary strongly during algal growth (Dunstan et al., 1993) or under different salinity, light irradiance, and nitrate regimes (Pal et al., 2011; Martinez-Roldan et al., 2014).

In the present study, we analyzed the concentrations of LCDs in three species (*Nannochloropsis gaditana*, *Nannochloropsis oceanica*, and *Nannochloropsis oculata*) during different stages of their growth. We incubated the species yielding the highest levels of LCDs, LCHFAs, and LCAs (*N. oceanica*) under different culturing (light irradiance, salinity) or stress (nitrogen depletion, desiccation, cold shock, oxidative stress) conditions, which are known to enhance the fatty acid content or in general to affect the lipid composition, in order to evaluate the impact of such conditions on the production of LCDs and on LCD-related compounds.

2. Material and methods

2.1 General culturing conditions

For the growth experiments, three marine strains from the genus *Nannochloropsis* were used in this study: *Nannochloropsis gaditana* strain CCMP526, *N. oceanica* strain CCMP1779, and *N. oculata* strain CCMP2195. For all subsequent experiments only *N. oceanica* was used. The strains were cultured in f/2 medium (Guillard, 1975) and maintained in sterile conditions under a 16:8 light: dark. *Nannochloropsis oculata* was cultured at 15 °C, whereas *N. oceanica* and *N. gaditana* were grown at 20 °C, as recommended by the supplier (ncma.bigelow.org). The strains were grown in 0.8 L volumes within 1.5 L glass Erlenmeyer flasks. Except for the growth rate experiments, where cells were harvested at different stages of their growth, cells were sampled for lipid analyses from exponentially growing cultures. For all the experiments, except those related to the impact of different light regimes on LCDs, the flasks were exposed to an irradiance of 100 $\mu E\ m^{-2}\ s^{-1}$, which was measured using a Universal Light Meter-500 (Walz, Germany). The strains were cultured in batch for all the experiments, except those related to the impact of different salinities, where they were cultured in semi-continuous mode.
Algal growth was regularly monitored by flow cytometry (Marie et al., 2001) and, at the end of each experiment, cells were harvested by filtration through 0.7 μm GF/F filters (Whatman, Maidstone, UK).

2.2 Growth rate experiments

An aliquot of 50 mL containing about 1.5×10^7 cells was inoculated in 9 replicate 2.5 L Erlenmeyer flasks containing 1.45 L f/2 medium. Cells were enumerated daily and the growth rate subsequently calculated as described previously (Balzano et al., 2011). The cells were harvested for the first time (early exponential phase) from triplicate flasks, when their abundance reached 10^6 cells mL^{-1} (Supplementary Fig. S1). When a decline in the growth rate was observed (late exponential phase) three further flasks from each strain were filtered, and cells were harvested from the last three flasks when no further growth was observed for two consecutive days (stationary phase, Supplementary Figure S1).

2.3 Light irradiance

Six replicate volumes of 10 mL, containing about 2×10^7 cells each from *N. oceanica*, were transferred into six 1.5 L flasks containing 740 mL f/2 medium and were incubated at 20 °C. Three replicate flasks were exposed to an irradiance of about 300 μE m^{-2} s^{-1} and used as high light (HL) treatment, whereas the other three flasks were covered by several shading nets (irradiance 25 μE m^{-2} s^{-1}) and were considered to reflect low light (LL) conditions. Cells grew faster in the HL treatment and were harvested from the cultures when their concentration exceeded 5×10^6 cells mL^{-1}, on Day 6 for the HL treatment and Day 7 for the LL treatment (Supplementary Figure S2).

2.4 Osmotic stress

To assess the impact of salinity on LCD abundance and composition, cells from *N. oceanica* were pre-adapted to grow at both brackish (below seawater salinity) and hypersaline (above seawater salinity) conditions until reaching the highest and the lowest salinities allowing growth (i.e. 10 and 50 psu, respectively). Brackish conditions were achieved by mixing 0.2 μm filtered seawater with deionized water, whereas sodium chloride was added to seawater to reach hypersaline conditions. The media were then autoclaved and 0.2 μm filtered nutrient solutions were added to reach typical f/2 concentrations. Cells were then inoculated in triplicate in 1.5 L flasks containing 800 mL medium at the appropriate salinity under semicontinuous growth conditions. The growth rates achieved were lower at 50 psu (0.56 doublings per day) compared to 10 and 35 psu (0.73 and 0.80 doublings per day, respectively) and cells were harvested after 5 days of constant growth rate ($\leq$ 0.1 doublings per day).

2.5 Nitrogen depletion

Cells from *N. oceanica* were added to a medium containing all the nutrients except sodium nitrate at typical f/2 concentrations (N–); f/2 medium (N+) was used as control. Cells were initially harvested by centrifugation at 3500 g for 5 min and two mL of pellet containing 1.6×10^8 cells were added in each N+ treatment whereas 20 mL from the same pellet were added

to the N– treatment. All the flasks were incubated at 20 °C and harvested after 6 days (Supplementary Fig. S2).

2.6 Desiccation

Cells were harvested by centrifugation as described above and a volume of 20 mL containing about 2×10^8 cells was poured in six Petri plates which were incubated at 20 °C under laminar flow. The lids were removed from three replicate Petri plates to allow water evaporation, whereas the other three Petri plates served as control and the lids were kept closed to prevent evaporation. After 48 h of incubation about 90 % water was evaporated from the desiccation treatments and cells were harvested from all the Petri plates.

2.7 Cold shock

We evaluated the impact of immediate exposure to a lower temperature on LCDs, i.e. a so-called cold shock. Cells of *N. oceanica* were incubated in eight × 1.5 L flasks at 20 °C under a dark/light regime. After three days, four flasks were transferred at 10 °C under the same conditions of light irradiance whereas the others were kept at 20 °C as control treatment. Cells were then harvested from two replicate flasks of each treatment after 6 and 12 h.

2.8 Oxidative stress (hydrogen peroxide treatment)

We assessed the impact of radical stress on LCDs by exposing *N. oceanica* to hydrogen peroxide. Hydrogen peroxide reacts with dissolved iron and copper, which are present in the f/2 medium, forming hydroxyl radicals that can cause several damages to cells (Gutteridge and Wilkins, 1983). We hypothesized that such damage mostly affects the algaenan-rich outer cell wall of *N. oceanica* with potential consequences on the abundance of LCDs. Cells from *N. oceanica* were incubated in eight replicate 1.5 L flasks at the same culturing conditions used above and an initial density of 1.3×10^6 cells mL^{-1}. Four flasks were then amended with 100 μM hydrogen peroxide every morning at the same time, whereas the other flasks were used as control and cells were harvested after three days. Algal growth in the control treatment was slightly faster than those of the amended treatment (Supplementary Fig. S2).

2.9 Lipid extraction and analysis

Frozen filters were dried using a LyoQuest (Telstart, Life Sciences) freeze-drier. The freeze-dried filters were then saponified and subsequently acid hydrolyzed according to Rodrigo-Gámiz et al. (2015). A $C_{22:0}$ 7,16-diol was added as internal standard to the total lipid extract (TLE). The total lipid extracts were methylated by the addition of diazomethane and subsequently cleaned over a small silicagel 60 column, by eluting with ethyl acetate. The TLEs were then silylated, and dissolved in ethyl acetate as described before (de Bar et al.,

2016) and analyzed by gas chromatography (GC) and GC-mass spectrometry. GC analysis was done on a HP 6890 Series GC System, mounted with a 25 m fused silica column with 0.32 mm diameter, coated with CB Sil-5 (thickness = 0.12 µm) and flame ionization detection. The carrier gas was helium at a constant pressure of 70 kPa. The oven temperature was 70 °C at injection, and was then increased by 20 °C per min to 130 °C and subsequently by 4 °C per min until 320 °C, at which it was held for 10 min. A selection of the samples was analyzed on an Agilent 7890B GC interfaced to a 7000 C GC/MS Triple Quad, for identification. The applied temperature program and column were identical to those described for the GC system. Helium was used as carrier gas at a constant flow of 2 mL min^{-1}. The mass spectrometer operated with an ionization energy of 70 eV. The LCAs, LCDs, and LCHFAs were identified by means of the characteristic mass spectra obtained in full scan mode, using a *m*/*z* range of 50–800 (Versteegh et al., 1997). The abundance of the compounds were quantified by integration of the peak areas of the compounds and the internal standard in the GC-FID using Atlas 8.2 software (Thermo Electron). For the co-eluting diols we determined the relative contributions of each diol to the total peak area in the GC-FID by integration of the characteristic fragment ions of each compound (Versteegh et al., 1997) using MassHunter software (Agilent Technologies).

2.10 Statistical analysis

In order to evaluate whether the lipid changes observed were statistically significant, a 2-sample T testing using Welch's test (Welch, 1947) was carried out using R software (https://www.r-project.org). We also performed a principal component analyses (PCA). The PCA on the distribution of the most abundant short chain fatty acids ($C_{14:0}$, $C_{16:0}$, $C_{16:1}$, $C_{20:5}$), LCDs, LCHFAs and LCAs was computed using R software for a total of 11 compounds across 70 data points (24 samples in 2, 3, or 4 replicates). The cellular concentrations of these lipids were square-transformed and PCA was performed using the function prcomp and displayed using the function biplot.

3. Results and discussion

3.1 Impact of growth phase on lipid abundance and composition of *Nannochloropsis* species

Analysis of lipids of the three *Nannochloropsis* species investigated here revealed that the saturated fatty acids were dominated by $C_{14:0}$ and $C_{16:0}$, whereas $C_{16:1}$ and $C_{20:5}$ were the most abundant unsaturated fatty acids, consistent with previous studies on *Nannochloropsis* spp. (Volkman et al., 1993; Olofsson et al., 2012; Xiao et al., 2013; Mitra et al., 2015) as well as other Eustigmatophyceae (Volkman et al., 1999b). *N. oceanica* exhibited higher concentrations of total lipids (p-value < 0.05), saturated (p-value < 0.01), and unsaturated (p-value < 0.01) fatty acids than the other two species (Figs. 1d-f). The concentrations of LCAs,

LCDs, and LCHFAs were an order of magnitude lower than that of the fatty acids (i.e. ca. 30 fg cell^{-1} vs. ca. 500 fg cell^{-1} for the fatty acids, Figs. 1a-c). Greater concentrations of LCAs, LCDs, and LCHFAs were also found in *N. oceanica* (Fig. 1a) compared to *N. gaditana* (p-value < 0.01, Fig. 1b) and *N. oculata* (p-value < 0.05, Fig. 1c). The composition of LCDs, LCAs and LCHFAs is consistent with that reported in literature for these three species (Volkman et al., 1992; Mejanelle et al., 2003; Rampen et al., 2014b), and other Eustigmatophyceae (Volkman et al., 1992; Gelin et al., 1997b; Volkman et al., 1999a; Rampen et al., 2014b), i.e.. $C_{30:0}$ 1,13 and 1,15 diols, $C_{32:1}$ 1,15 diol, $C_{32:0}$ 1,15 diol, $C_{30:0}$ 13-hydroxy and $C_{32:0}$ 15-hydroxy fatty acids and $C_{32:1}$ and $C_{32:2}$ alkenols.

We examined the lipid composition of *N. gaditana*, *N. oceanica*, and *N. oculata*, harvested during the early exponential phase, the late exponential phase, and the stationary phase (Table 1). *Nannochloropsis oceanica* differed from *N. gaditana* and *N. oculata* in both the abundance and changes with growth phase of LCAs, LCDs, and LCHFAs. The total LCD abundance ranged from 14 ± 2.5 to 20 ± 4.2 fg cell^{-1} in *N. gaditana*, 16 ± 5.2 to 34 ± 5.8 fg cell^{-1} in *N. oceanica* and 11 ± 2.1 to 12 ± 3.8 in *N. oculata* (Table 1). *N. oceanica* showed also the highest concentrations of LCAs (9.4 ± 2.9 to 27 ± 11 fg cell^{-1}) and LCHFAs (2.3 ± 0.5 to 7.3 ± 2.9 fg cell^{-1}) compared to the other two species (Table 1). During the growth of *N. oceanica*, $C_{32:0}$ and $C_{32:1}$ diols as well as LCAs increased towards the stationary phase, whereas the $C_{30:0}$ 13-hydroxy fatty acid decreased, while no significant changes were observed for the $C_{30:0}$ diol and the $C_{32:0}$ 15-hydroxy fatty acid (Fig. 1a). In contrast, LCHFA concentration decreased during the growth of *N. gaditana*, while concentrations of LCDs and LCAs did not change significantly (Fig. 1b) whereas for *N. oculata* LCA, LCD, and LCHFA concentrations were fairly constant (Fig. 1c). Overall we did not find a consistent trend with growth phase for LCAs, LCDs, and LCHFAs across the three species, and thus the distribution and abundance of these compounds does not seem to be affected by growth stage. Because of the higher concentrations of LCAs, LCDs, and LCHFAs in *N. oceanica* (Table 1), we used this species for the subsequent experiments.

3.2 Impact of cultivation conditions on lipid abundance and composition

3.2.1 Effect of light intensity

Higher abundance of saturated fatty acids occurred in cells incubated under HL conditions (Fig. 2d), which agrees with previous studies where *Nannochloropsis* sp. stored higher amounts of triacylglycerols (TAGs), mostly consisting of $C_{16:0}$ and $C_{18:0}$ fatty acids, under HL conditions (Sukenik and Carmeli, 1990; Fabregas et al., 2004; Pal et al., 2011). As for LCDs and LCD-related compounds, cells of *N. oceanica* cultured at HL conditions exhibited significantly higher concentrations of LCHFAs (3.4 ± 0.7 vs. 0.3 ± 0.05 fg cell^{-1} at LL conditions), $C_{32:2}$ alkenol (6.3 ± 1.1 vs. 2.7 ± 0.7 fg cell^{-1}), and $C_{32:1}$ diol (8.0 ± 0.9 vs. 3.9 ± 0.7), whereas the concentration of $C_{32:1}$ alkenol and that of other LCDs did not change significantly (Fig. 2a). Thus, there is no consistent pattern in changes of LCDs and only the

LCHFAs seemed to substantially increase in abundance although the cause for this is not clear as LCHFAs are unlikely to be part of TAGs.

3.2.2 Effect of salinity

N. oceanica was cultured at salinities of 10, 35, and 50 psu. Cells at 50 psu exhibited the highest contents in lipids (p-value < 0.05) and saturated fatty acids (Table 1, Fig. 2e), which is 2–3 fold higher than at lower salinities, confirming previous findings (Pal et al., 2011). The concentration of $C_{30:0}$ 13-hydroxy fatty acid at 10 psu was only ca. 25 % of that measured at both 35 and 50 psu, whereas the cellular content in $C_{32:0}$ 15-hydroxy fatty acid, LCAs, and LCDs did not change significantly with salinity (Fig. 2b). Since the fractional and absolute abundance of most compounds analyzed here did not change significantly at changing salinities (Fig. 2b) the osmotic pressure does not seem to affect the composition and abundance of LCAs and LCDs. The algaenan layer present in the outer cell wall of *Nannochloropsis* spp. is therefore unlikely to undergo compositional changes as a consequence of increased or decreased salinity. This suggests that algaenans do not play a role in protecting the cell from osmotic pressure.

3.2.3 Nitrogen limitation

N. oceanica was incubated into N+ and N– medium to evaluate the impact of nitrogen starvation on LCAs, LCDs, and LCHFAs. The cells grew under N+ conditions much faster than in the N– treatment (Supplementary Fig. S2). Cells incubated at N– conditions exhibited lower concentrations of total lipids (Table 1), unsaturated and saturated fatty acids (Fig. 2f). Under nitrogen-deficient conditions phytoplankton cells typically accumulate storage lipids (Dunstan et al., 1993; Li et al., 2014; Jia et al., 2015), and we observed indeed, in the N– treatment, a substantial increase in C_{14}-C_{20} saturated and unsaturated fatty acids (Fig. 2f). The cellular concentration of LCHFAs also increased by almost eight fold (Fig. 2c). However, the $C_{32:0}$ diols only doubled in concentration at N– conditions while the concentrations of the other LCDs and of LCAs did not change significantly (Fig. 2c). It has been suggested that the lack of nitrogen in the medium promotes a preferential synthesis of lipids over proteins leading to an increase in the fatty acid content (Vieler et al., 2012). Under nitrogen deprivation, *Nannochloropsis* spp. typically accumulates TAGs and to a lesser extent other glycerolipids (Tonon et al., 2002; Jia et al., 2015), in agreement with our observation that C_{14}-C_{20} saturated and unsaturated fatty acids in the N– treatments increased substantially (Fig. 2f). This accumulation seems also to enhance the production of LCHFAs but not that of LCAs and LCDs (Fig. 2c). Since under conditions which typically stimulate lipid accumulation, i.e. increased light intensity, salinity and nutrient deficiency, LCDs and LCAs did not systematically increase like the fatty acids, these compounds are unlikely to serve as storage lipids within *Nannochloropsis* cells. Since they do not accumulate under culturing conditions which promote energy storage, LCDs might thus serve as structural lipids present

in the outer cell wall as building blocks of algaenans, as has been previously hypothesized (de Leeuw et al., 1981; Tegelaar et al., 1989; Gelin et al., 1997a; Volkman et al., 1998; Scholz et al., 2014; Zhang and Volkman, 2017).

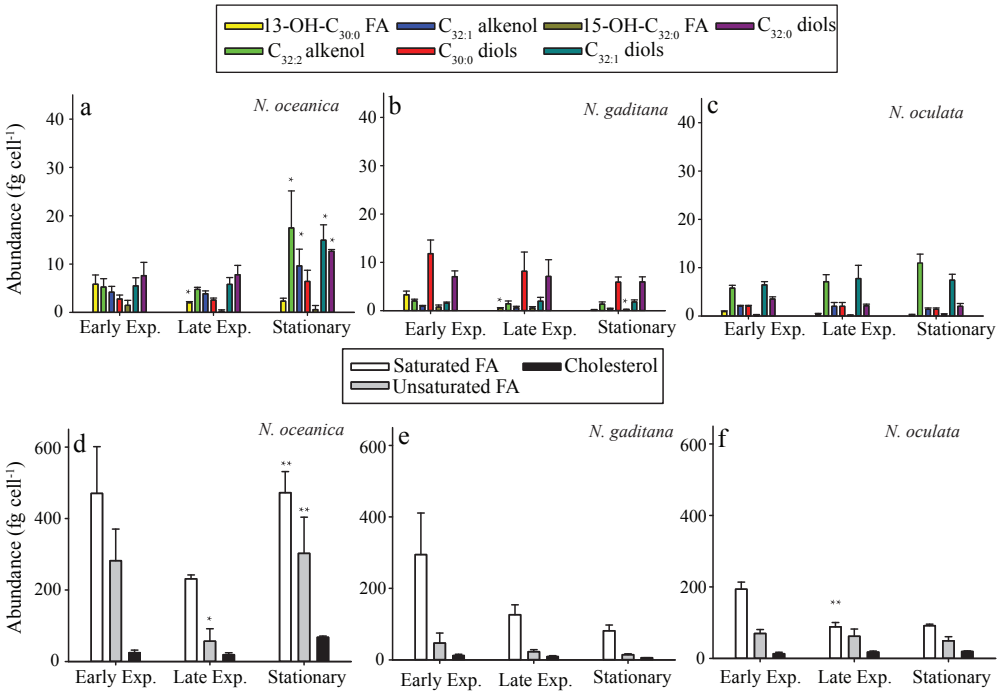

Fig. 1 Compositional changes in the cellular abundances of **(a-c)** LCDs, LCAs and LCHFAs, and **(d-f)** sum of saturated and unsaturated fatty acids and cholesterol during different stages of the growth of the strains investigated in the present study. Error bars represent standard deviation of triplicate cultures. Experiments were performed with **(a,d)** *Nannochloropsis oceanica* CCMP1779, **(b,e)** *Nannochloropsis gaditana* CCMP526, and **(c,f)** *Nannochloropsis oculata* CCMP2195. Early exp., early exponential phase; late exp., late exponential phase. The level of significance of the differences between the concentration at a growth stage and the previous one is indicated (*, p-value < 0.05; **, p-value < 0.01).

3.2.4 Desiccation

We evaluated the impact of desiccation on LCAs, LCDs, and LCHFAs in *N. oceanica* by incubating our cultures in open Petri plates for two days. We hypothesized that desiccation stress may create an unfavorable environment inducing *Nannochloropsis* cells to elapse into resting stages, potentially leading to major changes in its lipid composition, in particular in

the outer cell wall. For example *Chlorella kessleri* and *Chlamydomonas reinhardtii* substantially increased their fatty acid content upon desiccation (Shiratake et al., 2013). Resting cells often have a thicker cell wall to better resist degradation and spores with a thicker cell wall have been observed in *Nannochloropsis limnetica* (Fietz et al., 2005), as well as in other Eustigmatophyceae (Pribyl et al., 2012). Two days after the experiment started, about 90 % of the medium volume evaporated in the desiccation treatment while no evaporation occurred in the control. No visible difference was noted between cells from desiccation and the control treatment under light microscopy and no significant changes in lipids, fatty acids, LCDs, and LCD-derivatives were observed between the desiccated culture and the positive control (Table 1, Fig. 3a). LCAs, LCDs, and LCHFAs are thus not affected by desiccation stress.

3.2.5 Cold shock

Another factor, which can potentially affect outer cell walls and lipid composition, is cold shock. Rapid exposure of phytoplankton to a temperature lower than that of their standard culturing conditions has been observed to promote desaturation of fatty acids in diatoms (Jiang and Gao, 2004) and dinoflagellates (Jiang and Chen, 2000). Therefore, cultures of *N. oceanica* were rapidly transferred from their standard temperature for growth (20 °C) to 10 °C and lipids were analyzed after 6 h and 12 h. The abundance of fatty acids, LCAs, LCDs, and LCHFAs did not change as a response to cold shock over the relatively short incubation times used here (Fig. 3b, 3e). Compositional changes in LCDs with growth temperature have been previously reported by Rampen et al. (2014b) for *N. gaditana*. However, in that study the cultures were actively growing at different temperatures. Apparently, such changes do not occur when a strain is exposed to a different culturing temperature over the short incubation times applied here.

3.2.6 Oxidative stress

Stress from radicals can induce defense mechanisms in phytoplankton affecting the abundance and composition of lipids and potentially also their outer cell wall. Hydrogen peroxide is a known source of radicals and *Nannochloropsis oculata* has been previously found to grow in the presence of up to 50 µM hydrogen peroxide (Taylor et al., 2012).
In the present study, *N. oceanica* was able to grow with hydrogen peroxide daily added to the cultures at concentrations up to 100 µM (Supplementary Fig. S2). We evaluated the composition of lipids in cultures amended with 100 µM H_2O_2: the hydrogen peroxide-amended cultures were significantly depleted in unsaturated fatty acids (38 % decrease), LCHFAs (37 %), $C_{32:2}$ alkenol (36 %), and $C_{32:1}$ diol (48 %) compared to the unamended control (Fig. 3c) suggesting that some of these compounds were either partially degraded by hydrogen peroxide or synthesized at a lower rate. Interestingly, most of the compounds that

Experiment	Species/strain	Treatment	Replicates	Duration (days)	Abundance (cells/mL)	Lipid content		LCAs (fg/cell)	LCDs (fg/cell)	LCHFAs (fg/cell)
						(pg/cell)	(% w/w)			
Growth rate	*N. oceanica* CCMP1779	Early[a]	3	7	$1.8 \pm 0.2 \times 10^6$	2.5 ± 0.2	12 ± 1	9.4 ± 2.9	16 ± 5.2	7.3 ± 2.9
		Late[b]	3	10	$3.1 \pm 0.5 \times 10^6$	4.7 ± 1.9	n.a.	8.6 ± 1.0	16 ± 4	2.3 ± 0.5
		Stationary[c]	3	11	$5.6 \pm 1.1 \times 10^6$	2.2 ± 0.4	11 ± 2	27 ± 11	34 ± 5.8	2.9 ± 1.4
	N. gaditana CCMP526	Early	3	9	$1.5 \pm 0.1 \times 10^6$	2.2 ± 0.4	14 ± 3	2.9 ± 0.6	20 ± 4.2	4.1 ± 1.2
		Late	3	12	$7.4 \pm 0.5 \times 10^6$	1.0 ± 0.1	11 ± 3	2.1 ± 0.9	17 ± 8.2	1.0 ± 0.4
		Stationary	3	19	$1.3 \pm 0.2 \times 10^7$	1.0 ± 0.2	11 ± 2	1.8 ± 0.5	14 ± 2.5	0.5 ± 0.1
	N. oculata CCMP2195	Early	3	7	$1.4 \pm 0.2 \times 10^6$	2.5 ± 0.9	13 ± 6	7.8 ± 0.8	12 ± 1.3	1.1 ± 0.3
		Late	3	10	$6.5 \pm 0.6 \times 10^6$	1.4 ± 0.5	16 ± 9	9.1 ± 2.2	12 ± 3.8	0.5 ± 0.2
		Stationary	3	15	$1.4 \pm 0.1 \times 10^7$	1.4 ± 0.4	21 ± 9	12 ± 2.1	11 ± 2.1	0.5 ± 0.2
Light	*N. oceanica* CCMP1779	HL[d]	3	7	$5.6 \pm 0.1 \times 10^6$	2.3 ± 0.5	17 ± 4	9.4 ± 2.9	20 ± 3.6	3.4 ± 0.7
		LL[e]	3	9	$4.3 \pm 0.3 \times 10^5$	5.5 ± 0.4	3.5 ± 0.3	8.6 ± 1.0	20 ± 2.8	0.3 ± 0.05
Salinity	*N. oceanica* CCMP1779	10 ppt	3	7	$2.6 \pm 0.1 \times 10^6$	3.9 ± 0.6	15 ± 3	16 ± 4.2	47 ± 14	4.1 ± 0.8
		35 ppt	3	7	$2.9 \pm 0.1 \times 10^6$	3.7 ± 1.3	11 ± 4	18 ± 7.7	55 ± 18	14 ± 6.4
		50 ppt	3	7	$9.8 \pm 0.4 \times 10^5$	8.5 ± 2.7	8 ± 2	22 ± 10	43 ± 19	25 ± 11
Nitrogen depletion	*N. oceanica* CCMP1779	N−[f]	3	6	$2.7 \pm 0.4 \times 10^6$	5.7 ± 1.2	18 ± 5	16 ± 7	33 ± 14	26 ± 12
		Control	3	6	$5.2 \pm 0.8 \times 10^6$	2.3 ± 0.1	16 ± 4	6.8 ± 0.5	17 ± 5.5	3.4 ± 0.7
Desiccation	*N. oceanica* CCMP1779	Desiccated	3	2	$1.3 \pm 0.2 \times 10^7$	3.6 ± 0.9	6 ± 4	7.5 ± 2.8	21 ± 5.6	0.3 ± 0.2
		Control	3	2	$1.3 \pm 0.2 \times 10^7$	2.6 ± 0.5	6 ± 1	8.6 ± 0.5	22 ± 5.4	0.2 ± 0.1
Cold shock	*N. oceanica* CCMP1779	Cold 6 h	2	0.25	$3.4 \pm 0.2 \times 10^6$	2.5 ± 0.5	15 ± 5	12 ± 0.3	23 ± 0.3	3.5 ± 0.1
		Control 6 h	2	0.25	$4.0 \pm 0.1 \times 10^6$	2.5 ± 0.1	13 ± 1	11 ± 1.0	19 ± 3.0	4.6 ± 0.4
		Cold 12 h	2	0.5	$3.4 \pm 0.2 \times 10^6$	2.5 ± 0.6	11 ± 3	14 ± 5.6	26 ± 7.4	5.6 ± 1.6
		Control 12 h	2	0.5	$4.0 \pm 0.2 \times 10^6$	2.3 ± 0.2	12 ± 1	12 ± 1.3	23 ± 5.7	8.3 ± 1.3
Oxidative stress	*N. oceanica* CCMP1779	H_2O_2[g]	4	3	$5.5 \pm 0.8 \times 10^6$	2.3 ± 0.1	11 ± 1	10 ± 1.0	17 ± 1.5	8.3 ± 0.7
		Control	4	3	$2.9 \pm 0.7 \times 10^6$	2.2 ± 0.8	17 ± 5	14 ± 2.1	24 ± 5.4	13 ± 2.7

Table 1 Cell abundance, and concentrations of total lipids and the sum of long-chain alkenols (LCAs), long-chain alkyl diols (LCDs), and long chain hydroxy fatty acids (LCHFAs) for the different experiments carried out during this study.
[a] Early exponential phase; [b] Late exponential phase; [c] Stationary phase; [d] 25 μE/(m^2s); [e] 300 μE/(m^2s); [f] Culture incubated in f/2 medium without sodium nitrate. No addition nitrogen sources were present in the medium; [g] Treatment amended daily with 100 μM hydrogen peroxide.

decreased in the presence of hydrogen peroxide, are unsaturated, and their double bonds are likely to be highly reactive towards hydrogen peroxide. Similarly, in the presence of radicals, the degradation rates of alkenones increases with increasing number of double bonds (Rontani et al., 2006a). The decrease in unsaturated fatty acids, LCHFAs, $C_{32:2}$ alkenol, and $C_{32:1}$ diol is thus unlikely the result of changes in their biosynthetic pathways but these compounds may have been directly chemically oxidized by hydrogen peroxide. In any case, our results suggest that radicals do not affect LCD synthesis rates.

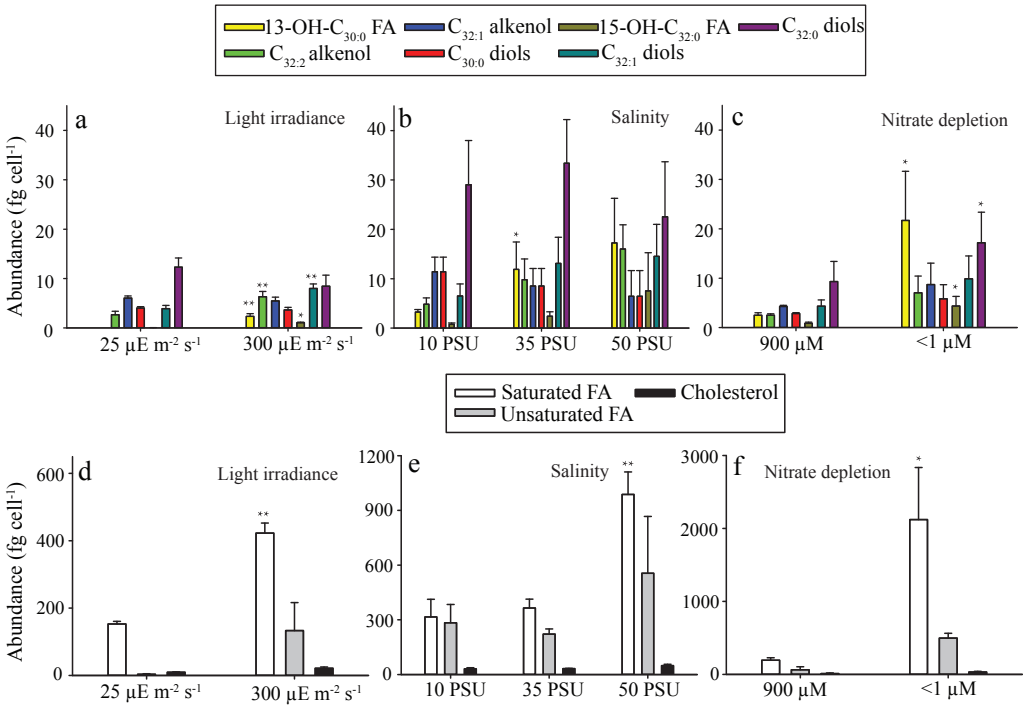

Fig. 2 Impact of different culturing conditions on the cellular levels of **(a-c)** LCAs, LCDs, and LCHFAs, and **(d-f)** sum of saturated and unsaturated fatty acids and cholesterol on *Nannochloropsis oceanica* CCMP1779. Error bars represent standard deviation of triplicate cultures. Effect of **(a,d)** different levels of light irradiance, **(b,e)** different salinities of the culturing medium, and **(c,f)** depletion of nitrogen from the medium. Please note that the culturing medium used here, f/2, typically contains 900 µM nitrate. Refer to Fig. 1 for abbreviations. The level of significance of the differences between the concentration at a growth stage and the previous one is indicated (*, *p*-value < 0.05; **, *p*-value < 0.01).

3.3 Role of LCAs, LCDs, and LCHFAs in *Nannochloropsis*

Principal Component Analysis (PCA) of the fractional abundances of the major compounds in the differently grown cultures reveals that $C_{30:0}$ 13-hydroxy and the $C_{32:0}$ 15-hydroxy fatty acids cluster with $C_{16:0}$ and $C_{14:0}$ fatty acids (Fig. 4). This suggests that LCHFAs may originate from $C_{14:0}$ and $C_{16:0}$ fatty acids via hydroxylation and chain elongation. It is not clear at which point of the elongation process the hydroxylation occurs. LCHFAs were previously suggested to share the same biosynthetic pathways as the LCAs and the LCDs in *Nannochloropsis* spp., because compounds from these three classes exhibiting the same carbon number are functionalised at the same position (Volkman et al., 1992; Gelin et al., 1997b). However, LCHFAs, $C_{14:0}$, and $C_{16:0}$ fatty acids do not cluster with LCDs as well as LCAs abundance in our PCA, suggesting that not all the LCHFAs biosynthesised by *Nannochloropsis* spp. were converted to LCDs and LCAs.

In *Nannochloropsis* species, LCAs, LCDs, and LCHFAs are thought to be bound together via ether or ester bonds to form algaenans (Gelin et al., 1996; Gelin et al., 1997a; Volkman et al., 1998; Gelin et al., 1999; Zhang and Volkman, 2017). Algaenans have also been described in several genera of Chlorophyta (Derenne et al., 1988; Gelin et al., 1997a; Blokker et al., 1998; Blokker et al., 1999; Allard and Templier, 2001) and the dinoflagellate *Gymnodinium catenatum* (Gelin et al., 1999). Algaenans are thought to be highly resistant to degradation (Tegelaar et al., 1989; Volkman et al., 1998) and are likely present in the outer layers of the cell walls, forming a trilaminar structure (Gelin et al., 1999). Fourier transform infrared spectroscopy on the cell wall of *N. gaditana* confirmed the ether linked aliphatic structures of algaenans and revealed also the presence of C=O bonds (Scholz et al., 2014), which likely correspond to ketone or carboxylic functional groups of long-chain keto-ols, LCHFAs and dihydroxy fatty acids, respectively, which were previously reported to occur in *Nannochloropsis* spp. (Volkman et al., 1992; Gelin et al., 1997b; Versteegh et al., 1997). Making up the outer cell wall of *Nannochloropsis* spp. algaenans might play a role in the protection of cells from chemical attack. This is evidenced in our study in which we report that *N. oceanica* was able to grow in the presence of high (100 μM) concentrations of hydrogen peroxide. In fact, phytoplankton can usually tolerate hydrogen peroxide concentrations higher than cyanobacteria (Drabkova et al., 2007; Barrington and Ghadouani, 2008) and heterotrophic bacteria (Xenopoulos and Bird, 1997). However, to the best of our knowledge, no phytoplankton species has been shown to grow, for three consecutive days, under a daily amendment of 100 μM hydrogen peroxide. We hypothesize that algaenans in *Nannochloropsis* spp. might then play a key role against oxidative stress making *Nannochloropsis* species highly resistant to radicals.

A protective role of some algaenan-associated compounds is also suggested by the higher proportions of LCHFAs, $C_{32:2}$ alkenol and $C_{32:1}$ diol found at HL conditions and by the increase in $C_{30:0}$ 13-hydroxy fatty acid and $C_{32:0}$ diol in nitrogen depleted medium (Fig. 2a). Both the exposure to excessive light (i.e. HL treatment), and the nutrient deficiency (i.e. N–) can stimulate the production of reactive oxygen species, although to a much lesser extent

than hydrogen peroxide (McKersie and Leshem, 1995). While the hydrogen peroxide amendment likely implied the degradation of part of the outer cell wall, leading to the lower proportions of LCAs, LCDs, and LCHFAs measured, the exposure to radicals under HL or N– conditions was likely to be less aggressive and might have stimulated a cellular response to biosynthesize higher amounts of algaenan-associated compounds in order to protect the cell.

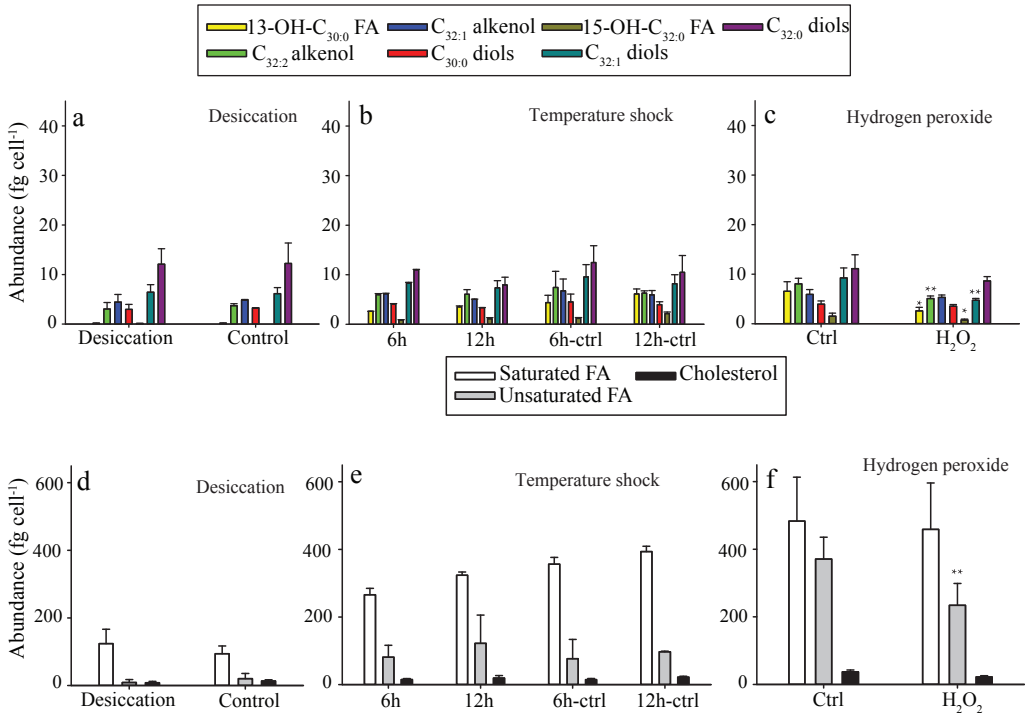

Fig. 3 Impact of different stress conditions on the concentration of **(a-c)** LCAs, LCDs, and LCHFAs, and **(d-f)** sum of saturated and unsaturated fatty acids and cholesterol on *Nannochloropsis oceanica* CCMP1779. Error bars represent standard deviation of triplicate cultures. **(a,d)** Effect of desiccation, the cultures were poured into Petri plates and exposed to the air for 48 h without the lid to promote the evaporation of the medium, the positive control consist in Petri plates with the lid. **(b,e)** Effect of cold shock: the cultures were rapidly transferred to a colder (10 °C) temperature and incubated for 6 or 12 hours. **(c,f)** Effect of daily amendment of hydrogen peroxide (radical stress). The level of significance of the differences between the concentration at a growth stage and the previous one is indicated (*, p-value < 0.05; **, p-value < 0.01).

3.4 LCDs as tracers for biomass of Eustigmatophyceae

Overall, the cellular levels of LCAs and LCDs found here in three different *Nannochloropsis* species, as well as those measured for *N. oceanica* under different culturing conditions and manipulation did not vary greatly, i.e. over all experiments and species, the concentrations were 12 ± 8.0 fg cell^{-1} for LCAs and 23 ± 15 fg cell^{-1} for LCDs. In contrast a greater variability was found for LCHFAs (8.2 ± 10 f fg cell^{-1}) and fatty acids (541 ± 570 fg cell^{-1}). This suggests that the cellular levels of LCAs and LCDs are fairly constant within Eustigmatophyceae investigated here. These consistent levels may be due to the fact that they are not storage lipids but are associated with the outer cell wall. In turn, it suggests that if cell size and cell wall thickness are fairly constant across the Eustigmatophyceae, the concentration of LCDs may be a good proxy for the abundance of Eustigmatophyceae in aquatic environments. Furthermore, sedimentary records of LCDs may be used to constrain relative changes in abundance, at least in regions not affected by variable past oxygen levels in the water column as diols are known to degrade at different rates between oxic and anoxic sediments (Rodrigo-Gámiz et al., 2016).

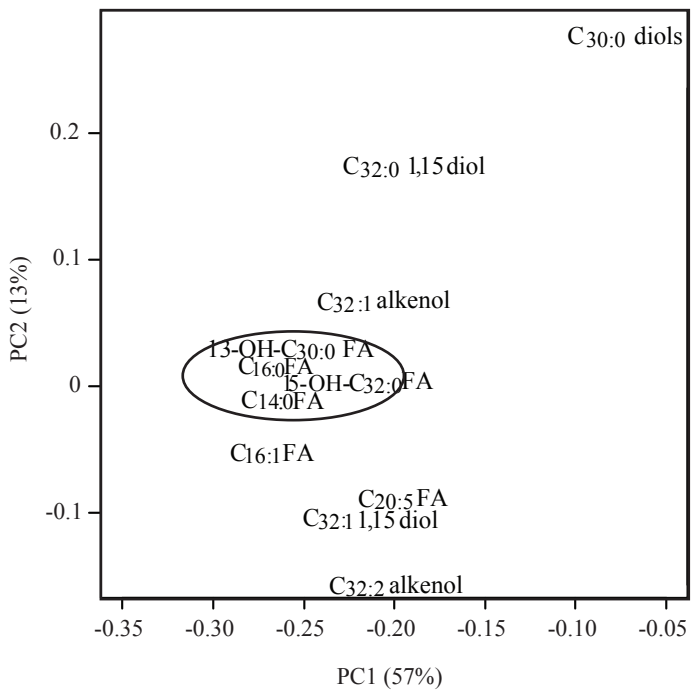

Fig. 4 Ordination of the different LCDs and LCD-derivatives as well as the major fatty acids in the space defined by principal component analyses: PCA1 on the *x*-axis and PCA2 on the *y*-axis. The values in brackets indicate the percentage of variance explained by each axis.

4. Conclusions

Culturing conditions that typically promote TAG accumulation in *Nannochloropsis* reveal a slight increase in LCHFAs but do not enhance the concentration of LCAs and LCDs. LCHFAs are likely to derive from $C_{14:0}$ and $C_{16:0}$ fatty acids, whereby $C_{14:0}$ and $C_{16:0}$ fatty acids might undergo one hydroxylation and several elongation steps to form LCHFAs which in turn can be precursors of LCAs and LCDs.

Our study indicates that LCAs, LCDs, and LCHFAs do not serve as storage lipids but likely function as structural lipids present in the outer cell wall playing a protective function from oxidative stress. The nearly constant concentrations of LCAs and LCDs, along with their specific chain length and position of functionalization for *Nannochloropsis* spp., suggest that these compounds might be considered as proxies for Eustigmatophyceae biomass in recent settings. A deeper understanding of the genetic mechanisms controlling the biosynthetic pathways of LCAs, LCDs, and LCHFAs can contribute, in the future, to a better understanding of the controls on LCD synthesis.

Acknowledgements

We thank K. Kooijman and J. Snoek for support in algal culturing and flow cytometry and S. Rampen for helpful discussions. This research was funded by the European Research Council (ERC) under the European Union's Seventh Framework Program (FP7/2007-2013) ERC grant agreement [339206]. S.S. and J.S.S.D. receive financial support from the Netherlands Earth System Science Centre (NESSC).

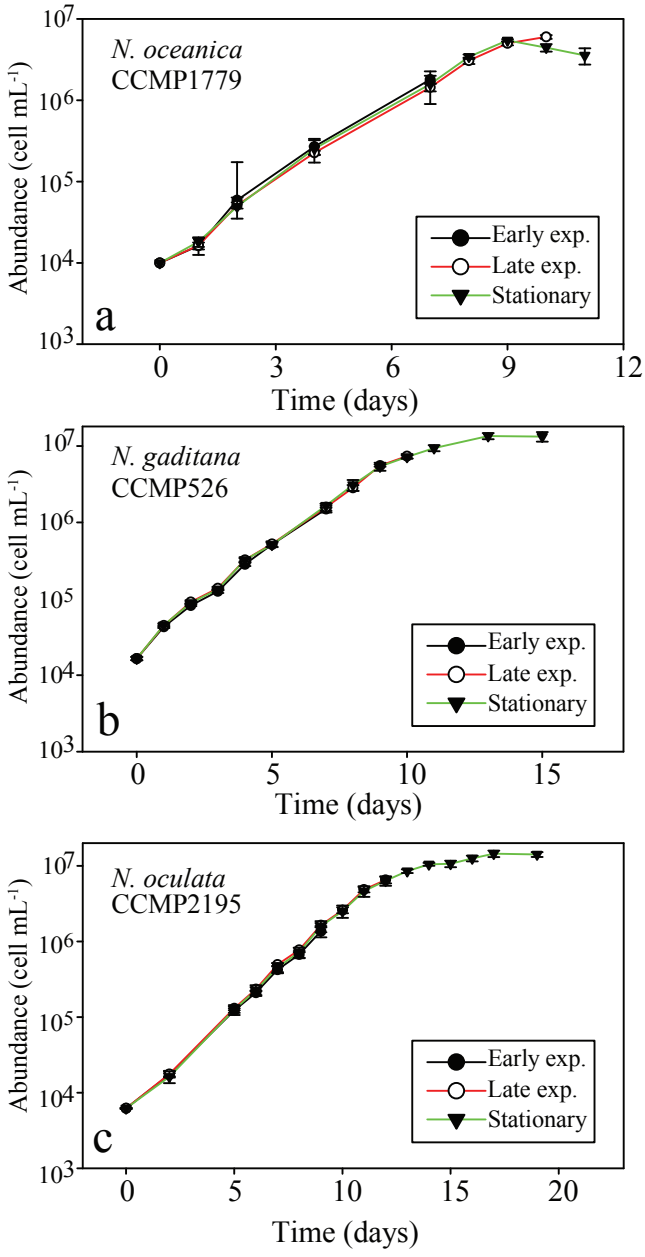

Fig. S1 Growth curves of **(a)** *Nannochloropsis oceanica* CCMP1779, **(b)** *Nannochloropsis gaditana* CCMP526, and **(c)** *Nannochloropsis oculata* CCMP2195. The different colours refer to the replicate samples harvested during the early exponential phase and the late exponential phase of their growth as well as the stationary phase.

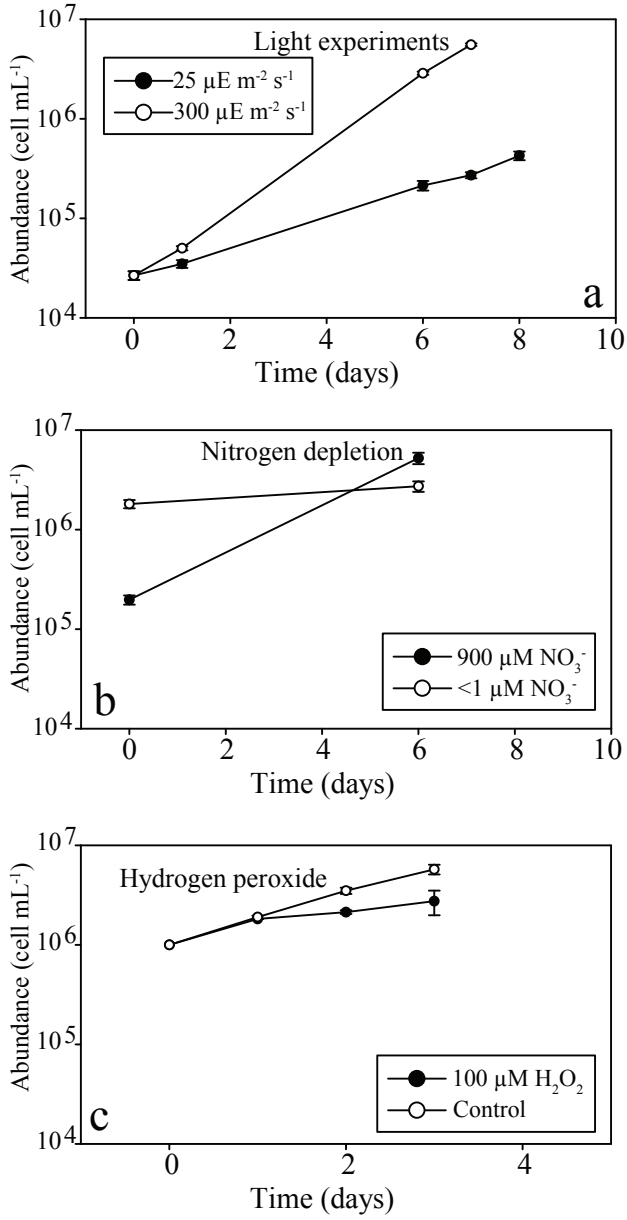

Fig. S2 Growth curve of *Nannochloropsis oceanica* CCMP1779 under different conditions of **(a)** light, **(b)** nitrate availability, and **(c)** when spiked with hydrogen peroxide.

Chapter 4

Long-chain diols in settling particles in tropical oceans: insights into sources, seasonality and proxies

Marijke W. de Bar, Jenny E. Ullgren, Robert C. Thunnell, Stuart G. Wakeham, Geert-Jan A. Brummer, Jan-Berend W. Stuut, Jaap S. Sinninghe Damsté and Stefan Schouten

Submitted to Biogeosciences

Abstract

In this study we have analyzed sediment trap time series from five tropical sites to assess seasonal variations in concentrations and fluxes of long-chain diols (LCDs) and associated proxies with emphasis on the Long chain Diol Index (LDI). For the tropical Atlantic, we observe that generally less than 2 % of LCDs settling from the water column are preserved in the sediment. The Atlantic and Mozambique Channel traps reveal minimal seasonal variations in the LDI, similar to the TEX_{86} and $U^{K'}_{37}$. However, annual mean LDI-derived temperatures are in good agreement with the annual mean satellite-derived sea surface temperatures (SSTs). In the Cariaco Basin the LDI shows larger seasonal variation, as do the TEX_{86} and $U^{K'}_{37}$. Here, the LDI underestimates SST during the warmest months, which is likely due to summer stratification and the habitat depth of the diol producers deepening to around 20 to 30 m. Surface sediment LDI temperatures in the Atlantic and Mozambique Channel compare well with the average LDI-derived temperatures from the overlying sediment traps, as well as with decadal annual mean SST. Lastly, we observed large seasonal variations in the Diol Index, as indicator of upwelling conditions, at three sites, potentially linked to Guinea Dome upwelling (Eastern Atlantic), seasonal upwelling (Cariaco Basin) and seasonal upwelling and/or eddy migration (Mozambique Channel).

1. Introduction

Several proxies exist for the reconstruction of past sea surface temperature (SST) based on lipids. The $U^{K'}_{37}$ is one of the most applied proxies and is based on the unsaturation of long-chain alkenones (LCAs), which are produced by phototrophic haptophyte algae, mainly the cosmopolitan *Emiliania huxleyi* (Volkman et al., 1980a; Brassell et al., 1986; Prahl and Wakeham, 1987; Conte et al., 1994). This index exhibits a strong positive correlation with SST (Müller et al., 1998; Conte, 2006). Another widely used organic paleotemperature proxy is the TEX_{86}, as originally proposed by Schouten et al. (2002), based on the relative distribution of archaeal membrane lipids, i.e. glycerol dialkyl glycerol tetraethers (GDGTs), and in the marine realm are mainly thought to be derived from the phylum Thaumarchaeota. Schouten et al. (2002) showed that the TEX_{86} index measured in marine surface sediments is correlated with SST, and since then its application in paleoenvironmental studies has increased. However, research showed that despite the highest abundance of Thaumarchaeota in the upper 100 m of the water column, they can be present down to 5000 m depth (Karner et al., 2001; Herndl et al., 2005). Accordingly, GDGTs may be found in high concentrations below 100 m depth (e.g., Sinninghe Damsté et al., 2002; Wuchter et al., 2005) and several studies have indicated that TEX_{86} might be more reflective of subsurface temperatures in some regions (e.g., Huguet et al., 2007; Lopes dos Santos et al., 2010; Kim et al., 2012a; 2012b; 2015; Schouten et al., 2013b; Chen et al., 2014; Tierney et al., 2017; see Zhang and Liu, 2018 for review).

Most recently a SST proxy based on the distribution of long-chain diols (LCDs), called the Long-chain Diol Index, or LDI was proposed (Rampen et al., 2012). This index is a ratio of 1,13- and 1,15-diols (i.e., alcohol groups at position C-1 and C-13 or C-15), and the analysis of globally distributed surface sediments revealed that this index strongly correlates with SST. Since then, the index has been applied in several paleoenvironmental studies (e.g., Naafs et al., 2012; Lopes dos Santos et al., 2013; Jonas et al., 2017; Warnock et al., 2017). However, large gaps still remain in the understanding of this proxy. The largest uncertainty is that the main marine producer of LCDs is unknown. Although these diols have been observed in cultures of certain marine eustigmatophyte algae (e.g. Volkman et al., 1992; 1999; Méjanelle et al., 2003; Rampen et al., 2014b), the LCD distributions in cultures are different from those observed in marine sediments. Furthermore, Balzano et al. (2018) combined lipid analyses with 18S rRNA gene amplicon sequencing on suspended particulate matter (SPM) and did not find a significant direct correlation between LCD concentrations and sequences of known LCD-producers. Rampen et al. (2012) observed the strongest empirical relation between surface sediment derived LDI values and SSTs for autumn to summer, suggesting that these are the main growth seasons of the source organisms. Moreover, the strongest correlation was also observed for the upper 20 m of the water column, suggesting that the LCDs are likely produced by phototrophic algae which thrive in the euphotic zone. Nevertheless, LDI-temperatures based on surface sediments reflect an

integrated signal of many years, which complicates the interpretation of the LDI in terms of seasonal production and depth of export production.

One way of resolving seasonality in LCD flux and LDI is to analyze time series samples from sediment traps that continuously collect sinking particles in successive time intervals over periods of a year or more. Such studies have been carried out for the $U^{K'}_{37}$ as well as for the TEX_{86} and associated lipids (e.g., Müller and Fischer, 2001; Wuchter et al., 2006b; Huguet et al., 2007; Fallet et al., 2011; Yamamoto et al., 2012; Rosell-Melé and Prahl, 2013; Türich et al., 2013). However, very few studies have been done for LCDs. Villanueva et al. (2014) carried out a sediment trap study in Lake Challa (East Africa) and Rampen et al. (2008) in the upwelling region off Somalia. The latter study showed that 1,14-diols, produced by *Proboscia* diatoms strongly increased early in the upwelling season in contrast to 1,13- and 1,15-diols and thus can be used to trace upwelling. However, none of these sediment trap studies have evaluated the LDI.

In this study, we assess seasonal patterns of the LDI for sediment trap series at five sites, i.e., in the Cariaco Basin, the Mozambique Channel and three sites in the tropical North Atlantic and compared the LDI values to satellite-derived SST, as well as results obtained for other temperature proxies, i.e. the TEX^{H}_{86} and $U^{K'}_{37}$. Moreover, for the Atlantic and Mozambique Channel, we compare the sediment trap proxy signals with those preserved in the underlying sediments, after settling and burial. Finally, we assess the applicability of the Diol Index, based on 1,14-diols produced by *Proboscia* diatoms (Sinninghe Damsté et al., 2003), as tracer of upwelling and/or productivity in these regions.

2. Materials and methods

2.1 Study sites and sample collection

2.1.1 Tropical North Atlantic

The ocean current and wind patterns of the tropical Atlantic are mostly determined by the seasonal latitudinal shift of the intertropical convergence zone (ITCZ; Figure 1). The ITCZ migrates southward during boreal winter, and northward during boreal summer. During summer, the south-east trade winds prevail, whereas during winter the north-east trade winds intensify. The north-east trade winds drive the North Equatorial Current (NEC) which flows westward. South of this current flows the North Equatorial Countercurrent (NECC) towards the east (Stramma and Schott, 1999). The South Equatorial Current flows westward and branches off in the north Brazil Current (NBC; Stramma and Schott, 1999). When the ITCZ is in the north, the NBC retroflects off the South American coast, and is carried eastward into the NECC, and thus into the western tropical Atlantic (e.g., Richardson and Reverdin, 1987). North of the NBC, the Guiana Current (GC) disperses the outflow from the Amazon River towards the Caribbean Sea (Muller-Karger et al., 1988; 1995).

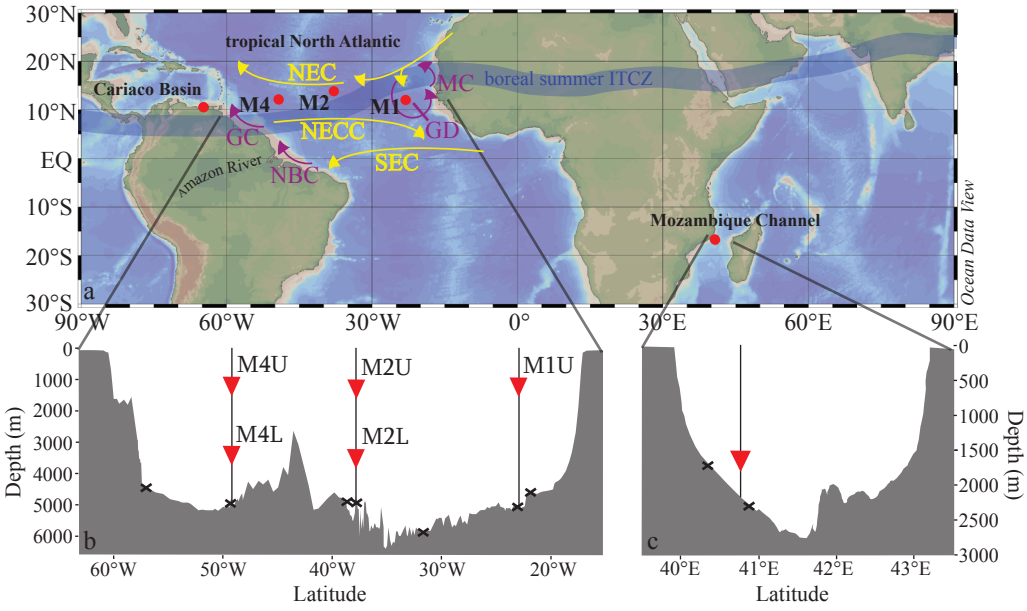

Fig. 1 **(a)** Location map showing the five sediment trap mooring sites in the Cariaco Basin, the tropical North Atlantic (M1, M2 and M4) and the Mozambique Channel. Two of the moorings in the tropical North Atlantic (M2 and M4) contain an upper ('U') and a lower ('L') trap, shown in the bathymetric section below **(b)** with traps depicted as red triangles and surface sediments shown as black crosses. A similar section profile is shown for the Mozambique Channel **(c)**, where also the sediment trap and the surface sediments are indicated. All maps/sections are generated in Ocean Data View (Schlitzer, 2015).

However, during boreal summer the NBC may retroflect, carrying the Amazon River plume far into the western Atlantic (e.g., Lefèvre et al., 1998; Muller-Karger et al., 1998; Coles et al., 2013). In fact, every late summer/autumn, the Amazon River outflow covers around 2×10^6 km^2 of the western North Atlantic, and the river delivers approximately half of all freshwater input into the tropical Atlantic (see Araujo et al., 2017 and references therein).

The eastern tropical North Atlantic is characterized by upwelling caused by the interaction between the trade winds and the movement of the ITCZ. Cropper et al. (2014) measured upwelling intensity along the NW African coastline between 1981 and 2012, in terms of wind speed, SST and other meteorological data. They recognized three latitudinal zones: weak permanent annual upwelling north of 26°N, strong permanent upwelling between 21° and 26°N and seasonal upwelling between 12° and 19°N related to the seasonal migration of the trade winds. Southeast of Cape Verde, large-scale cyclonic circulation forms the Guinea Dome (GD; Fig. 1), which centers around 10°N/22°W (Mazeika, 1967), i.e., close to mooring site M1. It is a thermal upwelling dome, formed by near-surface flow fields associated with the westward NEC, eastward NECC and the westward North Equatorial Undercurrent

(NEUC) (Siedler et al., 1992). It forms a cyclonic circulation as result of the eastward flowing NECC and the westward flowing NEC (Rossignol and Meyrueis, 1964; Mazeika, 1967). The GD develops from late spring to late fall due to the northward ITCZ position and the resulting Ekman upwelling, but shows significant interannual variability (Siedler et al., 1992; Yamagata and Iizuka, 1995; Doi et al., 2009) judging from general ocean circulation models. According to Siedler et al. (1992), upwelling is most intense between July and October when the ITCZ is in the GD region and the NECC is strongest.

At three sites, we analyzed five sediment trap series along a latitudinal transect in the North Atlantic (~12°N) to determine seasonal variations in the LDI. This transect has been studied previously for Saharan dust deposition in terms of grain sizes (van der Does et al., 2016), as the tropical North Atlantic receives approximately one third of the wind-blown Saharan dust (e.g., Duce et al., 1991; Stuut et al., 2005), which might potentially act as fertilizer because of the high iron levels (e.g., Martin and Fitzwater, 1988; Korte et al., 2017; Guirreiro et al., 2017; Goudie and Middleton, 2001 and references therein). Furthermore, Korte et al. (2017) assessed mass fluxes and mineralogical composition, Guerreiro et al. (2017) measured coccolith fluxes for two of the time series, while Schreuder et al. (2018a; 2018b) measured long-chain *n*-alkanes, long-chain *n*-alkanols and fatty acids, and levoglucosan for the same sediment trap samples and surface sediments as analyzed in this study.

At site M1 (12.00°N, 23.00°W), the sediment trap, referred to as M1U, was moored at a water depth of 1150 m (Fig. 1). This mooring is located in the proximity of the Guinea Dome, and might therefore potentially be influenced by seasonal upwelling. At station M2 (13.81°N, 37.82°W), two sediment traps were recovered, i.e., an ‘upper’ (M2U) trap at a water depth of 1235 m, and a ‘lower’ (M2L) trap at a depth of 3490 m. Lastly, at mooring station M4 (12.06°N, 49.19°W), also an upper and lower trap series were recovered and analyzed (M4U and M4L), at 1130 and 3370 m depth, respectively. This mooring site may seasonally be affected by Amazon River discharge (van der Does et al., 2016; Korte et al., 2017; Guirreiro et al., 2017; Schreuder et al., 2018a). All sediment traps were equipped with 24 sampling cups, which sampled synchronously over 16-day intervals from October 2012 to November 2013, using $HgCl_2$ as a biocide and borax as a pH buffer to prevent in situ decomposition of the collected material.

2.1.2 Mozambique Channel

The Mozambique Channel is located between Madagascar and Mozambique and is part of the Agulhas Current system hugging the coast of South Africa (Lutjeharms, 2006). The Agulhas Current system is an important conveyor in the transport of warm and salty waters from the Indian to the Atlantic Ocean (Gordon, 1986; Weijer et al., 1999; Peeters et al., 2004). The northern part of the channel is also influenced by the East African monsoon winds (Biastoch and Krauss, 1999; Sætre and da Silva, 1982; Malauene et al., 2014). Between

September and March, these winds blow from the northeast, parallel to the Mozambique coastline, favoring coastal upwelling. Additionally, the Mozambique Channel is largely influenced by fast-rotating, mesoscale eddies which migrate southward towards the Agulhas region. Using satellite altimetry, Schouten et al. (2003) observed on average 4 to 6 eddies, ca. 300 km in diameter, propagating yearly from the central Mozambique Channel (15°S) toward the Agulhas area (35°S) between 1995 and 2000. Seasonal upwelling occurs off Northern Mozambique (between ca. 15 and 18°S) (Nehring et al., 1987; Malauene et al., 2014), from August to March with a dominant period of about two months although periods of one to four weeks have also been observed (Malauene et al., 2014).

The sediment trap was moored at 16.8°S and 40.8°E, at a water depth of 2250 m (Fig. 1; Fallet et al., 2010, 2011) and of the same type as used for the North Atlantic transect. We analyzed the LCD proxies for two respective time intervals: the first interval covers ca. 3.5 years, from November 2003 to September 2007, with a sampling interval of 21 days. The second interval covers another year, between February 2008 and February 2009, with a sampling interval of 17 days. Previously, Fallet et al. (2011) published foraminiferal, $U_{37}^{K'}$ and TEX_{86} records for the first time interval, and the organic carbon content for the follow-up time series. For further details on the deployments and sample treatments, we refer to Fallet et al. (2011, 2012). The two surface sediments are located across the narrowest transect between Mozambique and Madagascar, and were analyzed for $U_{37}^{K'}$ and TEX_{86} by Fallet et al. (2012) and for LCDs by Lattaud et al. (2017b).

2.1.3 Cariaco Basin

The Cariaco Basin is one of the largest marine anoxic basins (Richards, 1975), located on the continental shelf of Venezuela. The basin is characterized by permanent stratification and strongly influenced by the migration of the intertropical convergence zone (ITCZ). During late autumn and winter, the ITCZ migrates to the south which results in decreased precipitation and trade wind intensification which in turn induces upwelling and surface water cooling. This seasonal upwelling is a major source of nutrients that leads to strong phytoplankton growth along the Venezuelan coast (e.g., Muller-Karger et al., 2001; Thunell et al., 2007). Between August and October, the ITCZ moves northward again, resulting in a rainy season and diminishing of the trade winds inhibiting upwelling. During this wet season the contribution of terrestrially derived nutrients is higher. Due to the prevalent anoxic conditions in the basin, there is no bioturbation which has resulted in the accumulation of varved sediments which provide excellent annually to decadally resolved climate records (e.g., Peterson et al., 1991; Hughen et al., 1996; 1998). Moreover, in November 1995, a time series experiment started to facilitate research on the link between biogeochemistry and the downward flux of particulate material under anoxic and upwelling conditions (Thunell et al., 2000). This project (CARIACO; http://imars.marine.usf.edu/cariaco) involved hydrographic cruises (monthly), water column chemistry measurements and sediment trap sampling (every

14 days). One mooring containing four automated sediment traps (Honjo and Doherty, 1988) was deployed at 10.50°N and 64.67°W, at a bottom depth of around 1400 m. These traps were moored at 275 m depth, just above the oxic/anoxic interface (Trap A), 455 m (Trap B), 930 m (Trap C) and 1255 m (Trap D). All traps contain a 13-cup carousel which collected sinking particles over 2 weeks, and were serviced every half year. For further details on trap deployment and recovery, and sample collection, storage and processing we refer to Thunell et al. (2000) and Goñi et al. (2004). In addition to the sediment trap sampling, the primary productivity of the surface waters was measured every month using ^{14}C incubations (Muller-Karger et al., 2001; 2004). For this study, we investigated two periods, i.e., May 1999–May 2000 and July 2002–July 2003 for Traps A and B. These years include upwelling and non-upwelling periods, as well as a disastrous flooding event in December 1999 (Turich et al., 2013). Turich et al. (2013) identified the upwelling periods, linked to the migration of the ITCZ, as indicated by decreasing SST in the CTD and satellite-based measurements (indicated by grey boxes in figures 9 and 10), and shoaling of the average depths of primary production and increased primary production. Moreover, Turich et al. (2013) evaluated the $U_{37}^{K'}$ and TEX_{86} proxies for the same two time series for which we analyzed the LCD proxies.

2.2 Instrumental data

Satellite SST, precipitation and wind speed time series of the M1, M2 and M4 moorings in the Atlantic derive from Guerreiro et al. (2017 and in revision) who retrieved these data from the Ocean Biology Processing Group (OBPG, 2014) (Frouin et al., 2003), the Goddard Earth Sciences Data and Information Services Center (2016) (Huffman et al., 2007; Xie and Arkin, 1997) and NASA Aquarius project (2015a; 2015b) (Lee et al., 2012) (see supplement of Guerreiro et al., 2017 for detailed references). The SST and Chlorophyll *a* time series data for the Mozambique Channel were adapted from Fallet et al. (2011), who retrieved these data from the Giovanni database (for details see Fallet et al., 2011). Surface sediment proxy temperatures were compared to annual mean SST estimates derived from the World Ocean Atlas (2013) (decadal averages from 1955 to 2012; Locarnini et al., 2013). Sea surface temperature data for the Cariaco Basin were adopted from Turich et al. (2013) and combined with additional CTD temperatures from the CARIACO time series data base for the depths of 2, 5, 10, 15 and 20 m (http://www.imars.usf.edu/CAR/index.html.; CARIACO time series composite CTD profiles; lead principal investigator: Frank Muller-Karger).

2.3 Lipid extraction

2.3.1 Tropical North Atlantic

The 120 sediment trap samples were sieved through a 1 mm mesh wet-split into five aliquots (van der Does et al., 2016), of which one was washed with Milli-Q water, freeze-dried and homogenized for chemical analysis (Korte et al., 2017). For organic geochemistry, weight

sub-aliquots were extracted as described by Schreuder et al. (2018a). Shortly, ca. 100 mg dry weight of sediment trap residue, and between 1.5 and 10 g of dry weight of surface sediment were extracted by ultrasonication using a mixture of dichloromethane:methanol (DCM:MeOH) (2:1; vol./vol.), and dried over a Na_2SO_4 column. For quantification of LCDs, LCAs and GDGTs, we added the following internal standards to the total lipid extracts (TLEs): 2.04 µg C_{22} 7,16-diol (Rodrigo-Gámiz et al., 2015), 1.50 µg 10-nonadecanone ($C_{19:0}$ ketone) and 0.1 µg C_{46} GDGT (Huguet et al., 2006), respectively. Subsequently, the TLEs were separated into apolar (containing *n*-alkanes), ketone (containing LCAs) and polar (containing LCDs and GDGTs) fractions over an activated (2h at 150 °C) Al_2O_3 column by eluting with hexane/DCM (9:1; vol./vol.), hexane/DCM (1:1; vol./vol.) and DCM/MeOH (1:1; vol./vol.), respectively. The apolar fractions were analyzed by Schreuder et al. (2018a) for *n*-alkanes. Polar fractions were split for GDGT (25 %) and LCD (75 %) analysis. The LCD fraction was silylated by the addition of BSTFA (N,O-bis(trimethylsilyl)trifluoroacetamide) and pyridine, and heating at 60 °C for 20 min, after which ethyl acetate was added prior to analysis. The ketone fraction was also dissolved in ethyl acetate, and the GDGT fraction was dissolved in hexane:isopropanol (99:1, vol./vol.) and analyzed by GC and GC/MS. Next, the GDGT fractions were filtered through a 0.45 µm polytetrafluoroethylene (PTFE) filter and analyzed by HPLC-MS.

2.3.2 Mozambique Channel

Aliquots of the sediment trap samples from the Mozambique Channel were previously extracted and analyzed by Fallet et al. (2011) and Fallet et al. (2012), respectively. The sediment trap material was extracted by ultrasonication using a mixture of DCM/MeOH (2:1; vol./vol.), dried over Na_2SO_4, and separated into apolar, ketone and polar fractions via alumina pipette column chromatography, by eluting with hexane/DCM (9:1; vol./vol.), hexane/DCM (1:1; vol./vol.) and DCM/MeOH (1:1; vol./vol.), respectively. These existing polar fractions of the sediment trap material were silylated (as described above), dissolved in ethyl acetate and re-analyzed for LCDs by GC-MS. Since no record was kept of the aliquoting of extracts and polar fractions, we report the results in relative abundance rather than concentrations and fluxes of diols.

2.3.3 Cariaco Basin

Sediment trap material was extracted as described by Turich et al. (2013). Briefly, 1/16 aliquots of the trap samples were extracted by means of Bligh-Dyer extraction with sonication using a phosphate buffer and a trichloroacetic acid (TCA) buffer, after which the extracts were separated by adding 5 % NaCl in solvent-extracted distilled deionized water, and the organic phase was collected and the aqueous phase was extracted two more times. The extracts were pooled and dried over Na_2SO_4 and separated by means of Al_2O_3 column

chromatography, eluting with hexane:DCM (9:1; vol./vol.), DCM:MeOH (1:1; vol./vol.) and MeOH. For this study, the DCM:MeOH (1:1; vol./vol.) fraction was silylated (as described above), dissolved in ethyl acetate, and analyzed for LCDs using GC-MS. Similar to the Mozambique Channel samples, no record was kept of the aliquoting of extracts and polar fractions, and thus we report the results in relative abundance.

2.4 Instrumental analysis

2.4.1 GDGTs

The GDGT fractions of the surface sediments and sediment traps SPM samples of the tropical North Atlantic were analyzed for GDGTs by means of Ultra High Performance Liquid Chromatography Mass Spectrometry (UHPLC-MS). We used an Agilent 1260 HPLC, which is equipped with an automatic injector, interfaced with a 6130 Agilent MSD, and HP Chemstation software according to Hopmans et al. (2016). Compound separation was achieved by 2 silica BEH HILIC columns in tandem (150 mm × 2.1 mm; 1.7 µm; Waters Acquity) in normal phase, at 25 °C. GDGTs were eluted isocratically for 25 min with 18 % B, followed by a linear gradient to 35 % B in 25 minutes and finally a linear gradient to 100 % B in the last 30 min. A = hexane; B = hexane:isopropanol (9:1; vol./vol.). The flow rate was constant at 0.2 mL min^{-1}, and the injection volume was 10 µL. The APCI-MS conditions are described by Hopmans et al. (2016). Detection and quantification of GDGTs was achieved in single ion monitoring (SIM) mode of the protonated molecules ($[M+H]^+$) of the GDGTs. We used a mixture of crenarchaeol and the C_{46} GDGT (internal standard) to assess the relative response factor, which was used for quantification of the GDGTs in the samples (c.f. Huguet et al., 2006).

Sea surface temperatures were calculated by means of the TEX_{86}^{H} as defined by Kim et al. (2010), which is a logarithmic function of the original TEX_{86} index (Schouten et al., 2002):

$$TEX_{86}^{H} = \log([GDGT\text{-}2+GDGT\text{-}3+cren']/[GDGT\text{-}1+GDGT\text{-}2+GDGT\text{-}3+cren']) \quad (1)$$

where the numbers indicate the number of cyclopentane moieties of the isoprenoid GDGTs, and Cren´ reflects an isomer of crenarchaeol, i.e. containing a cyclopentane moiety with a cis stereochemistry (Sinninghe Damsté et al., 2018). The TEX_{86}^{H} values were translated to SSTs using the core-top calibration of Kim et al. (2010):

$$SST = 68.4 \times TEX_{86}^{H} + 38.6 \quad (2)$$

The Branched Isoprenoid Tetraether (BIT) index is a proxy for the relative contribution of terrestrial derived organic carbon (de Jonge et al., 2014a; 2015). This ratio is based on the original index as proposed by Hopmans et al. (2004), but includes the 6-methyl brGDGTs:

BIT = [brGDGT Ia+brGDGT IIa+IIa´+brGDGT IIIa+IIIa´]/[brGDGT Ia+brGDGT IIa+IIa´+brGDGT IIIa+IIIa´+Cren] (3)

where the numbers reflect different branched GDGTs (see Hopmans et al., 2004) and Cren reflects crenarchaeol. The branched GDGTs were always around the detection limit in the Atlantic samples, implying a BIT index of around zero and thus minimal influence of soil organic carbon (Hopmans et al., 2004), and thus the BIT index is not discussed any further.

2.4.2 LCAs

The ketone fractions of the surface sediments and sediment traps samples of the tropical North Atlantic were analyzed for LCAs on an Agilent 6890N gas chromatograph (GC) with flame ionization detection (FID) after dissolving in ethyl acetate. The GC was equipped with a fused silica column with a length of 50 m, a diameter of 0.32 mm, and a coating of CP Sil-5 (film thickness = 0.12 µm). Helium was used as carrier gas, and the flow mode was a constant pressure of 100 kPa. The ketone fractions were injected on-column at a starting temperature of 70 °C, which increased by 20 °C min^{-1} to 200 °C followed by 3 °C min^{-1} until the final temperature of 320 °C was reached. This end temperature was held for 25 min.

The $U_{37}^{K'}$ index was calculated according to Prahl and Wakeham (1987):

$$U_{37}^{K'} = [C_{37:2} \text{ alkenone}]/[C_{37:2}+C_{37:3} \text{ alkenones}] \quad (4)$$

The $U_{37}^{K'}$ values were translated to SST after the calibration of Müller et al. (1998):

$$SST = (U_{37}^{K'}-0.044)/0.033 \quad (5)$$

We have also applied the recently proposed BAYSPLINE Bayesian calibration of Tierney and Tingley (2018). The authors showed that the $U_{37}^{K'}$ estimates substantially attenuate above temperatures of 24 °C, moving the upper limit of the $U_{37}^{K'}$ calibration from approximately 28 to 29.6 °C at unity. Since our traps are located in tropical regions with SSTs > 24 °C, we have applied this calibration as well.

2.4.3 LCDs

The silylated polar fractions were injected on-column on an Agilent 7890B gas chromatograph (GC) coupled to an Agilent 5977A mass spectrometer (MS). The starting temperature was 70 °C, and increased to 130 °C by 20 °C min^{-1}, followed by a linear gradient of 4 °C min^{-1} to an end temperature of 320 °C, which was held for 25 min. 1µL was injected, and separation was achieved on a fused silica column (25 × 0.32 mm) coated with CP Sil-5 (film thickness 0.12 µm). Helium was used as carrier gas with a constant flow of 2 mL min^{-1}. The MS operated with an ionization energy of 70 eV. Identification of LCDs was done

in full scan mode, scanning between *m*/*z* 50–850, based on characteristic fragmentation patterns (Volkman et al., 1992; Versteegh et al., 1997). Proxy calculations and LCD quantifications were performed by analysis in SIM mode of the characteristic fragments (*m*/*z* 299, 313, 327 and 341; Rampen et al., 2012; *m*/*z* 187 for internal diol standard). For quantification of LCDs in the sediment traps and seafloor sediments of the tropical Atlantic, the peak areas of the LCDs were corrected for the average relative contribution of the selected SIM fragments to the total ion counts, i.e., 16 % for the saturated LCDs, 9 % for unsaturated LCDs and 25 % for the C_{22} 7,16-diol internal standard.

Sea surface temperatures were calculated using the LDI index, according to Rampen et al. (2012):

$$\text{LDI} = [C_{30}\ 1,15\text{-diol}]/[C_{28}\ 1,13\text{-diol}+C_{30}\ 1,13\text{-diol}+C_{30}\ 1,15\text{-diol}] \quad (6)$$

These LDI values were converted into SSTs using the following equation (Rampen et al., 2012):

$$\text{SST} = (\text{LDI}–0.095)/0.033 \quad (7)$$

Upwelling conditions were reconstructed using the Diol Index as proposed by Rampen et al. (2008):

$$\text{Diol Index} = [C_{28}+C_{30}\ 1,14\text{-diol}]/[C_{28}+C_{30}\ 1,14\text{-diol}+C_{30}\ 1,15\text{-diol}] \quad (8)$$

In 2010, Willmott et al. introduced an alternative Diol Index, which is defined as the ratio of 1,14-diols over 1,13-diols. Since the index of Rampen et al. (2008) includes the C_{30} 1,15-diol, it can be affected by temperature variation, and therefore we would normally prefer to use the index of Willmott et al. (2010). However, we often did not detect the C_{28} 1,13-diol, or it co-eluted with cholest-5-en-7-one-3β-ol, compromising the calculation of the Diol Index of Willmott et al. (2010). Moreover, the temperature variations in all three sediment traps are minimal as recorded by the LDI. Accordingly, we chose to apply the Diol Index according to Rampen et al. (2008).

Potential fluvial input of organic carbon was determined by the fractional abundance of the C_{32} 1,15-diol (de Bar et al., 2016; Lattaud et al., 2017a):

$$F C_{32}\ 1,15\text{-diol} = [C_{32}\ 1,15\text{-diol}]/[C_{28}\ 1,13\text{-diol}+C_{30}\ 1,13\text{-diol}+C_{30}\ 1,15\text{-diol}+C_{32}\ 1,15\text{-diol}] \quad (9)$$

The fractional abundance of the C_{32} 1,15-diol was always lower than 0.23, suggesting low input of river derived organic carbon (Lattaud et al., 2017a).

2.5 Time-series analysis

We performed time-series spectral analysis on the Diol Index data from the Mozambique Channel to assess the influence of meso-scale eddies. Analyses were performed in MATLAB®. The two parts of the Diol Index time series, i.e. the 2003–2007 and the 2008–2009 periods, were analyzed both separately and together. The data were linearly interpolated in time (to 21-day intervals for the 2003–2007 period, and 17-day intervals for the 2008–2009 period) to adjust for disjunct sampling intervals or short gaps, and detrended. A runs test for randomness (Gibbons & Chakraborty, 2003) showed that for the second, shorter time series (2008–2009) the null hypothesis – that the values in the series are in random order – could not be rejected at the 5 % significance level. The second series also lacked statistically significant autocorrelation according to the Ljung-Box test (Ljung & Box, 1978). Therefore, there was little point in analysing the shorter 2008–2009 time series for periodicity. We performed a wavelet analysis to detect transient features in the Mozambique Channel Diol Index 2003–2007 time series following the methods of Torrence and Compo (1998; http://paos.colorado.edu/research/wavelets/) and using the Morlet wavelet as mother wavelet.

3. Results

3.1 Tropical North Atlantic

We have analyzed sediment trap samples from a latitudinal transect (~ 12°N) in the tropical North Atlantic (two upper traps at ca. 1200 m water depth, and three lower traps at ca. 3500 m; Fig. 1), covering November 2012–November 2013, as well as seven underlying surface sediments, for LCDs, LCAs and GDGTs. Below we present the results for these lipid biomarkers and associated proxies.

3.1.1 LCDs

The LCDs detected in the sediment trap samples and surface sediments from the tropical North Atlantic are the C_{28} and (mono-unsaturated and saturated) C_{30} 1,14- (between 1 and 49 % of all LCDs), C_{28} and C_{30} 1,13- (0–3 %) and the C_{30} 1,15- (44–99 %) and C_{32} 1,15-diols (0–7 %). In the M2 and M4 traps, the C_{30} 1,15-diol constitutes between 87 and 95 % of total LCDs. We detected the C_{29}-OH fatty acid in the traps from M1 and M4, in a few samples of the M2 traps and in all surface sediments. Similarly, the C_{28} 1,14-diol was detected in all samples from M1 and M4, in only a few M2 samples and in all surface sediments. For most samples from M2U and M2L, the C_{28} 1,14-diol was often part of a high background signal, making identification and quantification problematic. In these cases, 1,14-diol fluxes and Diol Index were solely based on the (saturated and mono-unsaturated) C_{30} 1,14-diol. In contrast, the saturated C_{30} 1,14-diol was detected in all samples.

The average [1,13+1,15]-diol flux is 2.6 (± 1.0) µg m^{-2} d^{-1} at M1U, 1.4 (± 1.2) and 1. 2 (± 1.1) µg m^{-2} d^{-1} for M2U and M2L, respectively, and 7.0 (± 7.8) and 2.2 (± 3.3) µg m^{-2} d^{-1} for M4U and M4L, respectively (Fig. 3). The [1,13+1,15]-diol and 1,14-diol concentrations in the underlying sediments vary between 0.05 µg g^{-1} and 0.50 µg g^{-1}, and between 3 ng g^{-1} and 0.06 µg g^{-1}, respectively. The [1,13+1,15]-LCD flux is more than three times higher in the upper trap of M4 than in the lower trap, whereas at M2, where the average LCD fluxes are much lower, the difference is not appreciable. The 1,14-diol flux for M1U averages 0.5 (± 0.8) µg m^{-2} d^{-1} with a pronounced maximum of 3.5 µg m^{-2} d^{-1} in late April (Fig. 5a), irrespective of the total mass flux. The average 1,14-diol flux at M2 is much lower and similar for the upper and lower traps, being around 0.01–0.02 (± 0.01) µg m^{-2} d^{-1}. At M4, the average 1,14-diol fluxes are 0.3 (± 0.5) and 0.1 (± 0.2) µg m^{-2} d^{-1} for the upper and lower trap, respectively. There are two evident maxima in the [1,13+1,15]-diols and 1,14-diol fluxes in late April and during October/November, concomitant with maxima in the total mass flux (Fig. 3d and 3e). However, in the lower trap this flux maximum is distributed over two successive trap cups, corresponding to late April/early May (Fig. 3e and 3j).

The LDI ranged between 0.95 and 0.99 in all traps, corresponding to temperatures of 26.0 to 27.3 °C with no particular trends (Fig. 4). For most M2 and M4 samples the C_{28} 1,13-diol was below quantification limit and, hence, LDI was always around unity, corresponding to 26.9 to 27.3 °C (Fig. 4), whereas in others samples the C_{28} 1,13-diol co-eluted with cholest-5-en-7-one-3β-ol, prohibiting the calculation of the LDI and Diol Index (Fig. 4 and 5). The flux-weighted annual average LDI-derived SSTs are 26.6 °C for M1U, and 27.1 °C for M2U, M2L, M4U and M4L. The underlying sediment is very similar, with LDI values between of 0.95 and 0.98 corresponding to 26.0 and 26.9 °C. The Diol Index varied from 0.03 to 0.30 in M1U, showing a pronounced maximum during spring (Fig. 5a). The Diol Index at M2 ranges between 0.01 and 0.05 without an evident pattern, while the Diol Index at M4 ranges from 0.01 to 0.10 and shows the same pattern in the lower and upper trap, with highest values during spring (ca. 0.1), followed by a gradual decrease during summer (Fig. 5d; 5e).

3.1.2 LCAs

We detected C_{37}, C_{38} and C_{39} long-chain alkenones in the sediment trap and surface sediments. The $C_{37:3}$ alkenone was generally around the limit of quantification for the M2L and M4L traps, and below the limit of quantification for 4 out of the 7 surface sediment samples, while the $C_{37:2}$ alkenone was always sufficiently abundant. The annual mean fluxes of the C_{37} LCAs are 4.3 (± 3.5) µg m^{-2} d^{-1} for M1U, 1.2 (± 0.9) µg m^{-2} d^{-1} and 0.4 (± 0.2) µg m^{-2} d^{-1} for M2U and M2L, respectively, and 2.8 (± 5.0) µg m^{-2} d^{-1} and 1.2 (± 2.0) µg m^{-2} d^{-1} for M4U and M4L, respectively. The concentrations of the C_{37} LCAs in the underlying surface sediments range between 0.02 and 0.41 µg g^{-1}. At M4, the two total mass flux peaks at the end of April and during October/November are also clearly pronounced in the C_{37} alkenone fluxes (Fig. 3d, 3e and 5g), as well as the increased signal in the cup reflecting the

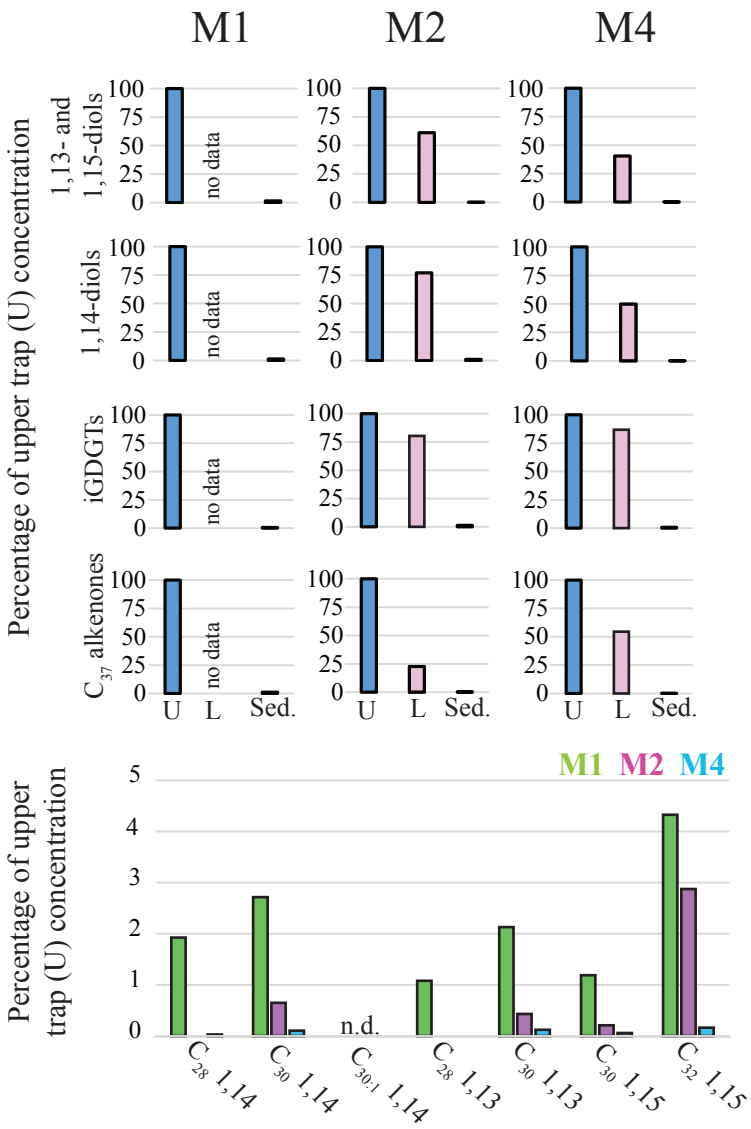

Fig. 2 Relative concentrations of biomarker lipids for the mooring sites M1, M2 and M4 in the tropical North Atlantic. Upper panel: percentages of lipid biomarkers in the lower traps ('L'; 3500 m) and the surface sediments ('Sed.') relative to the annual flux-weighted concentrations in the upper traps ('U'; 1200 m; set at 100 %). The lower panel shows the preservation of the individual LCDs (sediments versus upper trap flux-weighted concentration) for the three sediment trap sites. For M1 and M2 the sedimentary LCD concentration were based on the average of the two nearby underlying surface sediments (Fig. 1). When no bar is shown than the LCD was not detected.

beginning of May, which follows the cup which recorded the peak in total mass flux at the end of April. The $U^{K'}_{37}$ varied from 0.87 to 0.93, corresponding to 25.1 to 27.0 °C (Fig. 6c) for 3 out of 7 surface sediments in which the $C_{37:3}$ was above quantification limit. The flux-weighted average SSTs are 26.1 °C for M1U, 25.7 and 26.4 °C for M2U and M2L, respectively, and 28.2 and 27.5 °C for M4U and M4L, respectively (Fig. 6). SST variations per sediment trap are generally within a 2–3 °C range (Fig. 4) with no apparent trends.

3.1.3 GDGTs

The main GDGTs detected were the isoprenoidal GDGT-0, -1, -2, -3, crenarchaeol and the isomer of crenarchaeol. Branched GDGTs were typically around or below quantification limit. Additionally, we detected three hydroxyl GDGTs (OH-GDGTs), i.e. OH-GDGT-0, -1 and -2. These OH-GDGTs contributed ca. 0.1–0.2 % to the total GDGT pool (i.e., hydroxyl and isoprenoidal) in the sediment traps, but in the surface sediments their fractional abundance was higher, around 1 %. The average iGDGT flux in M1U is 15.5 (± 4.6) μg m^{-2} d^{-1}, 2.4 (± 1.1) and 2.6 (± 0.3) μg m^{-2} d^{-1} in M2U and M2L, respectively, and 4.3 (± 1.5) and 2.9 (± 1.2) μg m^{-2} d^{-1} in M4U and M4L, respectively (Fig. 3). The surface sediments exhibit iGDGT concentrations between 0.4 and 1.7 μg g^{-1}. Sediment TEX^{H}_{86} values vary between 0.62 and 0.69, corresponding to 24.3 to 27.4 °C. The TEX^{H}_{86} flux-weighted average SSTs are 25.2 °C for M1U, 27.3 and 26.6 °C for M2U and M2L, respectively, and 27.8 and 26.7 °C for M4U and M4L, respectively. SSTs vary typically within a range of 1 and 2 °C. At M2U and M4U, the TEX^{H}_{86} temperatures decrease slightly (ca. 1–2 °C) during January and July (Fig. 4b and 4d).

3.2 Mozambique Channel

For two time series (November 2003–September 2007 and February 2008–February 2009), we have analyzed LCDs collected in the sediment trap at 2250 m water depth as well as nearby underlying surface sediments (Fig. 1). The main LCDs observed in the sediment traps and surface sediments are the C_{28} 1,12-, 1,13- and 1,14-diols, the C_{30} 1,13-, 1,14- and 1,15-diols and the C_{32} 1,15-diol. We also observed the $C_{30:1}$ 1 1,14 diol in some trap samples, and the C_{29} 12-OH fatty acid in all trap and sediment samples. The C_{30} 1,15 is generally highest in abundance, varying between 28 and 85 % of the total LCD assemblage. The C_{28} and C_{30} 1,14-diols contribute between 11 and 67 % of total LCDs. In 24 samples, the C_{28} 1,13-diol co-eluted with cholest-5-en-7-one-3β-ol, and henceforth we did not calculate the LDI for these samples. The LDI varied between 0.94 and 0.99, i.e., close to unity, corresponding to 25.5 to 27.2 °C, without an evident trend (Fig. 8a). The Diol Index ranges between 0.11 and 0.69, showing substantial variation, although not with an evident trend (Fig. 8b). The average LDI-derived temperature of two underlying surface sediments is 26.0 °C.

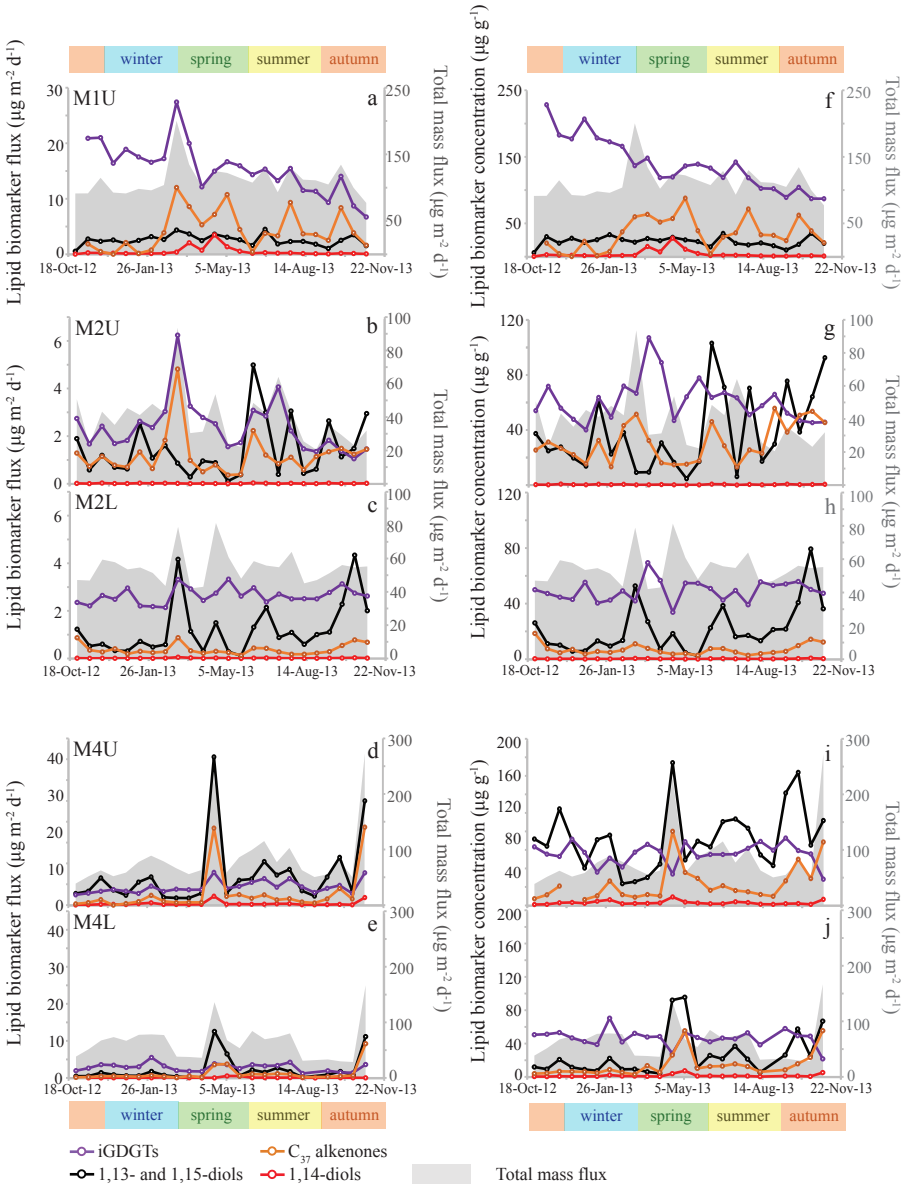

Fig. 3 Lipid biomarker fluxes for the tropical North Atlantic sediment traps, i.e., M1, upper and lower M2, and upper and lower M4 in panels **(a)** to **(e)**. Lipid biomarker fluxes (iGDGTs in purple; C_{37} alkenones in orange; 1,13- and 1,15-diols in black; 1,14-diols in red) are indicated on the left *y*-axis, and the total mass flux (grey stack; Korte et al., 2017) on the right *y*-axis. Lipid biomarker concentrations are plotted in panels **(f)** to **(j)**, with biomarker concentrations on the left *y*-axis, and the total mass flux on the right *y*-axis. Note that the *y*-axes are different per sediment trap site, but identical for upper (U) and lower (L) traps.

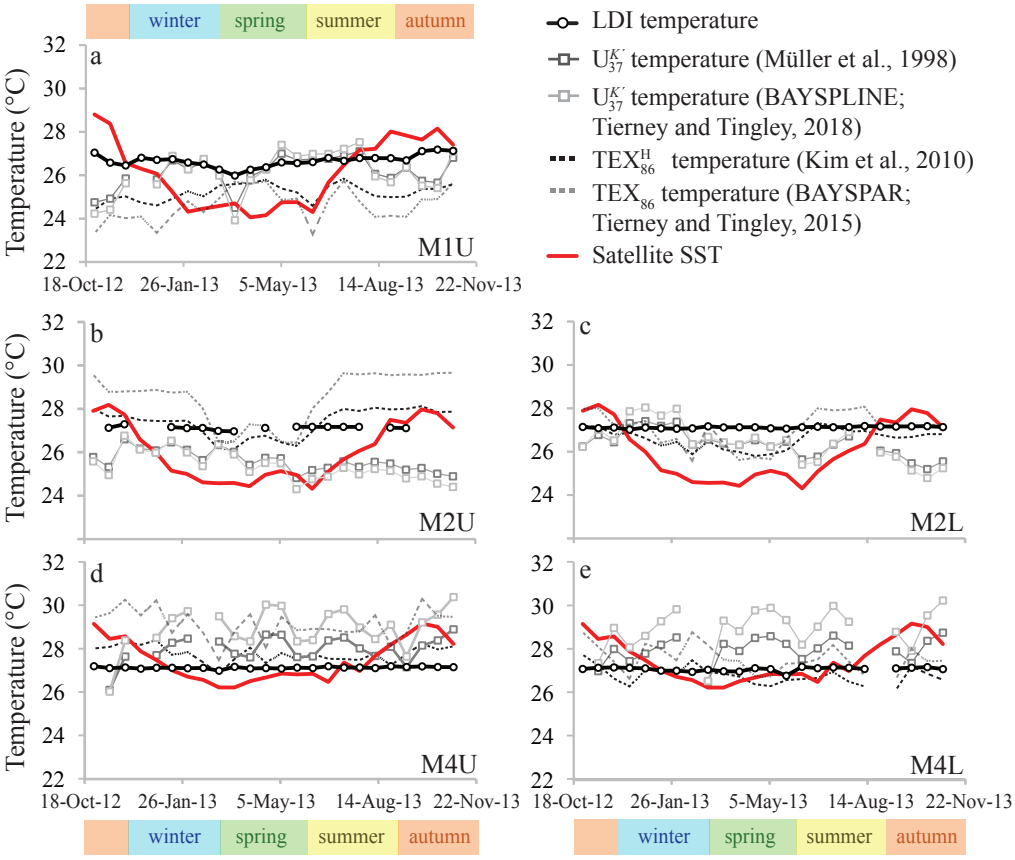

Fig. 4 Temperature proxy records for the tropical North Atlantic. Panel **(a)** shows upper trap station M1, **(b)** upper trap station M2 and **(c)** lower trap M2, respectively, **(d)** upper trap station M4 and **(e)** lower trap station M4, respectively

3.3 Cariaco Basin

We analyzed LCDs for two time series (May 1999–May 2000 and July 2002–July 2003) from the upper (Trap A; 275 m) and the lower trap (Trap B; 455 m) in the Cariaco Basin. The main LCDs detected for both time series are the C_{28} 1,14-, C_{30} 1,14-, $C_{30:1}$ 1,14-, C_{28} 1,13-, C_{30} 1,15- and C_{32} 1,15-diols, as well as the C_{29} 12-OH fatty acid. The C_{30} 1,15-diol contribution varies between 3 and 92 % of all LCDs, the C_{28} and C_{30} 1,14-diol contribution between 3 and 96 %, and the C_{28} and C_{30} 1,13-diols constitute between 0 and 8 %. For some samples we did not compute the LDI, as the C_{28} 1,13-diol co-eluted with cholest-5-en-7-one-3β-ol. The calculated LDI values range between 24.3 and 25.3 °C and 22.0 and 27.2 °C for Trap A and B of the 1999–2000 time series, respectively, with the lowest temperature during winter, and

the highest during summer. For the 2002–2003 time series, LDI temperatures for Trap A range between 23.3 and 26.2 °C, and for Trap B between 22.5 °C and 26.5 °C.

For the May 1999–May 2000 time series, the Diol Index varies between 0.05 and 0.97 for Trap A, and between 0.05 and 0.91 for Trap B (Fig. 9) with similar trends, i.e. the lowest values of around 0.1–0.2 just before the upwelling period during November, rapidly increasing towards values between ca. 0.8 and 1 during the upwelling season (January and February). For the time series of July 2002–July 2003, the Diol Index shows similar trends, i.e. Diol Index values around 0.8–0.9 during July, which rapidly decrease towards summer values of around 0.2–0.3. Similar to the 1999-2000 time series, the lowest index values (ca. 0.2) are observed just before the upwelling period (during September), after which they increase towards values of around 0.8–0.9 between December and March at the start of the upwelling season. At the end of the upwelling season the Diol Index increases, followed by another maximum of around 0.6 during May.

4. Discussion

4.1 LCD sources and seasonality

The 1,14 diols can potentially be derived from two sources, i.e. *Proboscia* diatoms (Sinninghe Damsté et al., 2003; Rampen et al., 2007) or the dictyochophyte *Apedinella radians* (Rampen et al., 2011). The non-detection of the C_{32} 1,14-diol, which is a biomarker for *Apedinella radians* (Rampen et al., 2011), and the detection of the $C_{30:1}$ 1,14 diol and C_{29} 12-OH fatty acid, which are characteristic of *Proboscia* diatoms (Sinninghe Damsté et al., 2003), suggests that *Proboscia* diatoms are most likely the source of 1,14-diols in the tropical North Atlantic, the Mozambique Channel and the Cariaco Basin.

In the Cariaco Basin, the Diol Index shows a strong correlation with primary production rates, suggesting that *Proboscia* productivity was synchronous with total productivity (Fig. 9). Primary productivity in the Cariaco Basin is largely related to seasonal upwelling which occurs between November and May when the ITCZ is at its southern position. Hence, the Diol Index seems to be an excellent indicator of upwelling intensity in the Cariaco Basin.

The index also shows considerable variation over time in the Mozambique Channel (Fig. 8b). Previous studies have shown that upwelling occurs in the Mozambique Channel between ca. 15 and 18°S (Nehring et al., 1987; Malauene et al., 2014), i.e. at the location of our sediment trap. Upwelling is reflected by cool water events and slightly enhanced Chlorophyll *a* levels, and Malauene et al. (2014) observed cool water events at ca. two month intervals although periods of 8 to 30 days were also observed. The two main potential forcing mechanisms for upwelling in the Mozambique Channel are the East African monsoon winds and the meso-scale eddies migrating through the channel. Fallet et al. (2011) showed that subsurface temperature, current velocity and the depth of surface-mixed layer all revealed a dominant

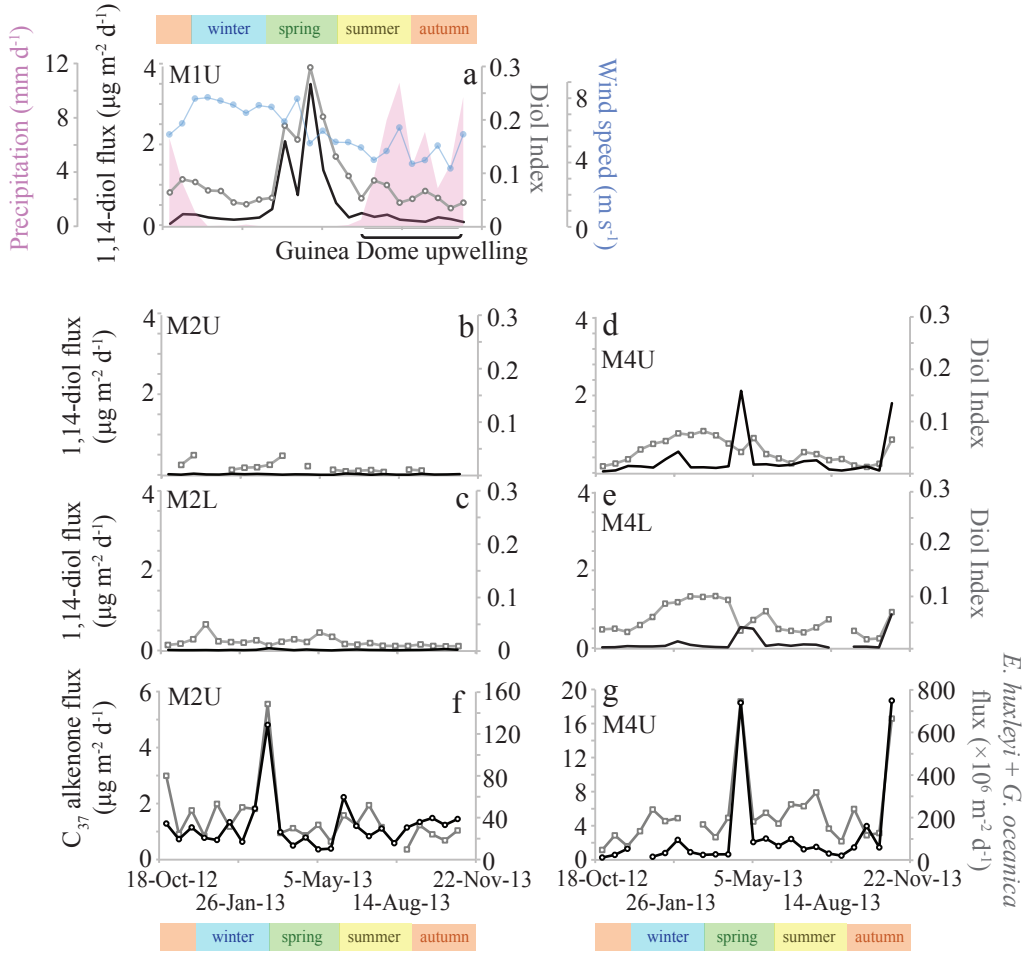

Fig. 5 Phytoplankton productivity records for the tropical North Atlantic. Panels **(a)** – **(e)** show the 1,14-diol fluxes (left *y*-axis; black) and the Diol Index (right *y*-axis; grey) for sediment traps. The *y*-axes are the same for these panels. Wind speed and precipitation data were adapted from Guerreiro et al. (in revision); for references regarding remote sensing parameters, see Guerreiro et al. (2017). Panels **(f)** and **(g)** show the C_{37} alkenone fluxes (left *y*-axis; black) and combined fluxes of *E. huxleyi* and *G. oceanica* (from Guerreiro et al., 2017; right *y*-axis; grey) for the upper traps of M2 and M4.

periodicity of meso-scale eddies in the channel (Harlander et al., 2009; Ridderinkhof et al., 2010), implying that eddy passage strongly influences the water mass properties. Wavelet analysis of the Diol Index for the period 2003–2007 (not shown) revealed short periods, occurring around January of 2004, 2005, and 2006, of significant (above the 95 % confidence level) variability at about bimonthly frequencies (60-day period). Both the frequency and the

timing of the observed time periods of enhanced Diol Index variability are similar to those of the cool water events as observed by Malauene et al. (2014), associated with upwelling (Fig. 8b). The strongest variability of the Diol Index at frequencies of four cycles per year and higher occurred in the first half of 2006. During the same period, salinity time series showed the passage of several eddies that had a particularly strong effect on the upper layer hydrography (Ullgren et al., 2012). Malauene et al. (2014) showed that neither upwelling-favorable winds, nor passing eddies, can by themselves explain the observed upwelling along the northern Mozambique coast. The two processes may act together, and both strongly influence the upper water layer and the organisms living there, potentially including the LCD producers.

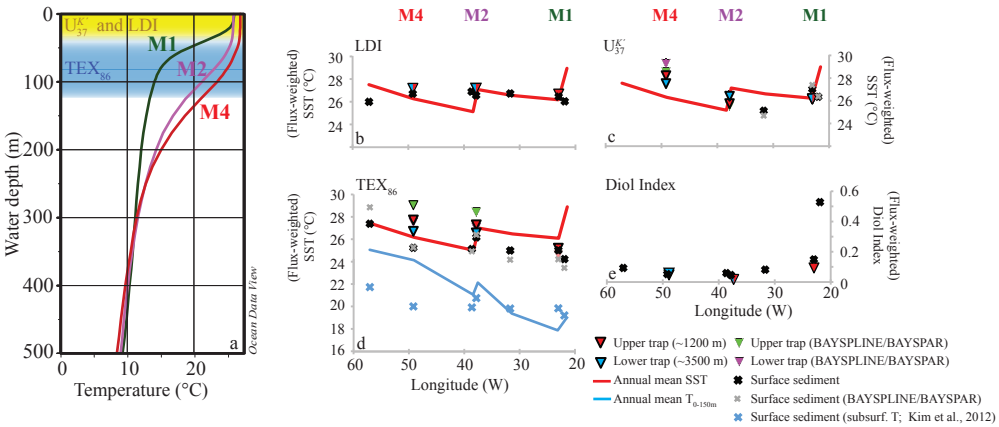

Fig. 6 **(a)** Annual mean temperature profiles at the sediment trap locations (World Ocean Atlas 2013) with approximate proxy-lipid production depths indicated, as deduced from Balzano et al. (unpublished results). **(b)** Flux-weighted average (annual) proxy results for the sediment traps compared with the underlying sediments (crosses) and annual mean SST (red line; World Ocean Atlas 2013). Panel **(b)**, **(c)** and **(d)** show the LDI, $U^{K'}_{37}$ and TEX_{86} temperature results, respectively. Triangles reflect sediment trap results (red = upper/~1200 m; blue = lower/~3500 m), and crosses represent surface sediments. In case of the $U^{K'}_{37}$ and TEX_{86}, the green and purple triangles and grey crosses reflect the temperatures calculated using the BAYSPLINE and BAYSPAR models (Tierney and Tingley, 2014; 2015; 2018), whereas the other temperatures were calculated by means of the Müller et al. (1998) and Kim et al. (2010; TEX^{H}_{86}) calibrations, respectively. The blue line and crosses in panel **(d)** reflect the depth-integrated temperature for the upper 0-150 m, and subsurface TEX^{H}_{86} temperatures (Kim et al., 2012b). Panel **(e)** shows the flux-weighted average Diol Index values for the sediment traps, and the Diol Index estimates for the surface sediments.

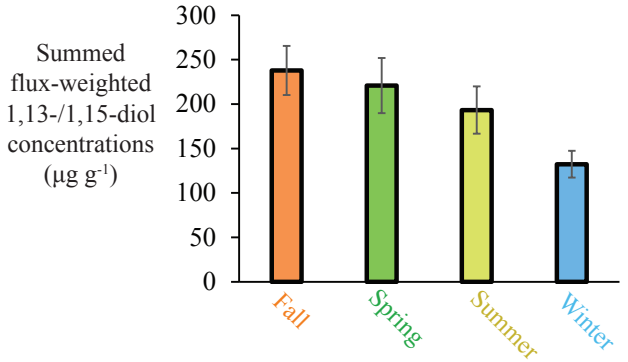

Fig. 7 Seasonal summed flux-weighted average of 1,13-/1,15-diol concentrations in all sediment traps (station M1 upper trap, station M2 upper and lower trap and station M4 upper and lower trap) of the tropical North Atlantic.

The least (seasonal) variation in the Diol Index is observed at M2 in the tropical North Atlantic (Fig. 5b and 5c), which is likely due to its central open ocean position, associated with relatively stable, oligotrophic conditions (Guerreiro et al., 2017). In contrast, M4 and M1 are closer to the south American and west African coast, respectively, and thus are potentially under the influence of Amazon river runoff and upwelling, respectively, and specific wind and ocean circulation regimes (see Sect. 2.1.1). However, at M4, the Diol Index is also low (max. 0.1), suggesting low *Proboscia* productivity (Fig. 5d and 5e). At M1, by contrast, we observe enhanced values for the Diol Index of up to ~0.3 during spring (Fig. 5a). Most likely, an upwelling signal at this location is associated with the seasonal upwelling of the Guinea Dome. This upwelling is generally most intense between July and October (Siedler et al., 1992), due to the northward movement of the ITCZ and the resulting intensified Ekman upwelling. Specifically, during this period, the trade winds are weaker, atmospheric pressure is lower, and the regional wind stress is favorable to upwelling of the North Equatorial Undercurrent (Voituriez, 1981). Indeed, a decrease in wind speed and increased precipitation during summer to autumn was observed (Fig. 5a) which confirms that during these seasons the ITCZ was indeed at a northern position, and that during 2013 the upwelling associated with the Guinea Dome was most favored between July and October. The timing of the Diol Index peak, i.e., between March and June is consistent with previous sediment trap studies elsewhere which have shown that *Proboscia* diatoms and 1,14-diols are typically found during pre-upwelling or early upwelling periods (Koning et al., 2001; Smith, 2001; Sinninghe Damsté et al., 2003; Rampen et al., 2007). The surface sediment at 22°W just east of M1 also reveals the highest Diol Index (0.53), likely due its closer vicinity to the Guinea Dome center. Several studies have reported *P. alata* diatoms offshore NW Africa (Lange et al., 1998; Treppke et al., 1995; Crosta et al., 2012; Romero et al., 1999), pointing to *P. alata* as a plausible source organism. The sedimentary annual diol indices compare well with the sediment trap indices (Fig. 7e), which is consistent with the results of Rampen et al. (2008).

To assess variations in seasonal production of 1,13- and 1,15-diols in the tropical Atlantic, for which we have the most complete dataset, we calculated the flux-weighted 1,13- and 1,15-diol concentrations for the different traps, and summed these per season (Fig. 7). Highest production is observed in autumn, followed by spring and summer, with the lowest production during winter (~60 % compared to autumn). This is in agreement with Rampen et al. (2012) who observed, for an extensive set of surface sediments, the strongest correlation between LDI and SST for autumn, suggesting that production of the source organisms of the LDI mainly occurs during autumn. At M4, there are two evident peaks in the 1,13- and 1,15-diol fluxes at the end of April and October 2013. These maxima correlate with peaks in other lipid biomarker fluxes (i.e., 1,14-diols, C_{37} alkenones and iGDGTs), total mass flux, calcium carbonate ($CaCO_3$), OM and the residual mass flux which includes the deposition flux of Saharan dust (Korte et al., 2017). According to Guerreiro et al. (2017), the maximum in total mass flux at the end of April 2013 is likely caused by enhanced export production due to nutrient enrichment as a result of wind-forced vertical mixing. The peak at the end of October 2013, is likely associated with discharge from the Amazon River. Moreover, both peaks are concomitant with prominent dust flux maxima, suggesting that Saharan dust also acted as nutrient fertilizer (Korte et al., 2017; Guerreiro et al., 2017). Guirreirro et al. (2017) suggested that during the October-November event the Amazon River may not only have acted as nutrient supplier, but also as buoyant surface density retainer of dust-derived nutrients in the surface waters, resulting in the development of algal blooms within just a few days, potentially explaining the peak 1,13- and 1,15-diol fluxes, as well as the peak fluxes of the other lipid biomarkers. However, they might also partially result from enhanced particle settling, caused by e.g. dust ballasting or faecal pellets of zooplankton (see Guerreiro et al. 2017 and references therein). This agrees with the results of Schreuder et al. (2018a) who show that the *n*-alkane flux also peaks concomitant with the peaks in total mass flux and biomarkers, whereas *n*-alkanes are terrestrial derived (predominantly transported by dust) and increased deposition can therefore not result from increased primary productivity in the surface waters.

The C_{37} alkenone flux at M4U also reveals these two distinct maxima at the end of April and October during 2013 (Fig. 5g). Interestingly, this flux, as well as the alkenone flux at M2U, is consistent with coccolith export fluxes of the species *Emiliania huxleyi* and *Gephyrocapsa oceanica* (Guerreiro et al., 2017). In fact, when we combine the coccolith fluxes of both species, we observe strong correlations with the C_{37} alkenone fluxes for both M2U and M4U (Fig. 5f and 5g, respectively; R^2 = 0.60 and 0.84 for M2U and M4U, respectively). This implies that these two species are the main LCA producers in the tropical North Atlantic, which agrees with previous findings (e.g., Marlowe et al., 1984a; 1984b; Brassell, 2014; Conte et al., 1994; Volkman et al., 1995).

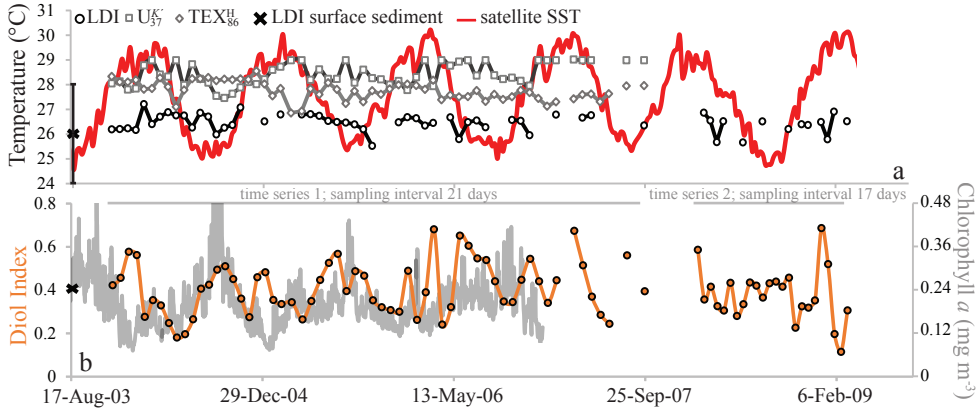

Fig. 8 The LDI-derived temperatures, together with the TEX^{H}_{86} and $U^{K'}_{37}$-derived temperatures and satellite SST (Fallet et al., 2011) **(a)** and the Diol Index **(b)** for the Mozambique Channel sediment trap. The black cross in panel **(a)** reflects the average LDI temperature of two underlying surface sediments, with the LDI calibration error. The chlorophyll *a* data is from Fallet et al. (2011).

4.2 Preservation of LCDs

The sediment trap data from the North Atlantic can be used to assess the relative preservation of LCDs, as well as other proxy lipid biomarkers, by comparing the flux-weighted concentration in the traps with the concentrations in the surface sediments. For all four biomarker groups, i.e., C_{37} alkenones, iGDGTs, 1,14-diols and 1,13- and 1,15-diols, we observe that in general the flux-weighted concentrations are higher in the upper traps (ca. 1200 m) as compared to the lower traps (ca. 3500 m; Fig. 2) by a factor of between 1.2 and 4.4, implying degradation during settling down the water column. The concentrations in the surface sediments are 2 to 3 orders of magnitude lower in concentration (i.e., between 0.1–1.5 % of upper trap signal), implying that degradation of lipids is mainly taking place at the water-sediment surface rather than the water column. A similar observation was made for levoglucosan in these sediment traps (Schreuder et al., 2018b). This is likely linked to the extent of the oxygen exposure time (Hartnett et al., 1998; Hedges et al., 1999) at the seafloor (Hartnett et al., 1998; Sinninghe Damsté et al., 2002), since during settling the lipids are exposed to oxygen for weeks, whereas for surface sediments this is typically decades to centuries. Our results compare well with several other sediment trap studies which showed that LCDs, LCAs and iGDGTs generally have a preservation factor of around 1 % (surface sediment vs. trap) (e.g., Prahl et al., 2000; Wakeham et al., 2002; Rampen et al., 2007; Yamamoto et al., 2012).

We have also identified the C_{30} and C_{32} 1,15-keto-ol for in the Atlantic as well as the Mozambique and Cariaco sediment traps and surface sediments. These lipids are structurally related to LCDs and occur ubiquitously in marine sediments (e.g., Versteegh et al., 1997; 2000; Bogus et al., 2012; Rampen et al., 2007; Sinninghe Damsté et al., 2003; Wakeham et al., 2002; Jiang et al., 1994), and were inferred to be oxidation products of LCDs (Ferreira et al., 2001; Bogus et al., 2012; Sinninghe Damsté et al., 2003). We have not detected 1,14-keto-ols, which supports the hypothesis of Ferreira et al. (2001) and Sinninghe Damsté et al. (2003) that the silica frustules of *Proboscia* diatoms sink relatively fast and thus are exposed to oxygen for a shorter period than the 1,13- and 1,15-diols, and thus less affected by oxidation.

For both the tropical Atlantic and the Cariaco Basin, we observe highly similar LDI values for the upper and the lower traps. In the Atlantic there is no statistical difference between upper and lower trap that are 2200 m apart (two-tailed $p > 0.8$), but we have too little data for the Cariaco Basin for statistical comparison (Fig. 6b, 9c and 9f). This suggests that degradation in the water column does not affect the LDI proxy. This is in agreement with the study of Reiche et al. (2018) who performed a short-term degradation experiment (< 1 year) and found that the LDI index was not affected by oxic exposure on short time scales. However, the oxygen exposure time on the seafloor is much longer, and Rodrigo-Gámiz et al. (2016) showed for sediments in the Arabian Sea, deposited under a range of bottom water oxygen conditions, that different LCDs had different degradation rates, which compromised the LDI ratio. For the three sites in the tropical North Atlantic, we have calculated the flux-weighted average proxy values for every sediment trap and compare these with the underlying surface sediments (Fig. 6b–6e). For all indices, i.e., Diol Index, LDI, $U^{K'}_{37}$ and TEX_{86}, we observe very good correspondence between the sediment trap and surface sediment values, implying minimal alteration of the proxies after settling and during burial. Similarly, for the Mozambique Channel, the mean Diol Index and LDI from the sediment trap (i.e., 0.41 and 0.97, respectively) are very similar to the surface sediment values (i.e., 0.42 and 0.95, respectively). In agreement with the consistent diol indices, we observe that all individual LCDs are also preserved relatively equally in the tropical Atlantic (1.2–4.3 % at station M1, 0.1–2.9 % at station M2 and 0.03–0.16 % at station M4). This contrasts with the findings of Rodrigo-Gámiz et al. (2016) who found that the 1,15-diols have the highest degradation rate, followed by the 1,14- and 1,13-diols. Only the C_{32} 1,15-diol seems relatively better preserved than the other LCDs at all three North Atlantic mooring sites (Fig. 2), suggesting that the C_{32} 1,15-diol is less impacted by degradation. The C_{32} 1,15-diol likely partially derives from the same source as the other 1,13- and 1,15-diols, but is also produced in fresh water systems (e.g., Versteegh et al., 1997; 2000; Rampen et al., 2014b; de Bar et al., 2016; Lattaud et al., 2017a; 2017b). Hence, the different preservation characteristics might be the result of a different source for this LCD.

4.3 Relationship between LDI and SST

In the tropical Atlantic and Mozambique Channel, the LDI-derived SSTs show minimal differences (<2 °C), while in the Cariaco Basin we observe much larger changes that range from 22.0 °C to 27.2 °C (Fig. 9). Both time series in the Cariaco Basin show low temperatures between November and May associated with the seasonal upwelling and surface water cooling, and significantly higher temperatures during the rainy summer. However, during the warmest periods, the LDI temperatures are generally lower than measured at the surface by CTD, whereas during the colder phases, the LDI agrees well with the measurements. The LDI calibration reaches unity at 27.4 °C, and therefore it is not possible to resolve the highest temperatures which are between ca. 28 and 30 °C. However, the LDI-derived temperatures are sometimes well below 27.4 °C where the CTD data suggest SSTs > 28 °C. Consequently, the LDI-based temperatures agree with CTD-based SSTs within calibration error for most of the record, but during summer when SST is highest, are offset outside the calibration error ($\Delta T \sim 2.5$ °C). Interestingly, the $U^{K'}_{37}$- and TEX^{H}_{86}-derived temperature trends show the same phenomenon (Turich et al., 2013; Fig. 9), where the proxy temperatures are cooler than the measured temperatures during the warmer months. For $U^{K'}_{37}$, Turich et al. (2013) pointed out that a time lag between synthesis, export and deposition could potentially explain the difference between the proxy and CTD temperatures. However, previous analysis of plankton biomass, primary productivity, bio-optical properties and particulate organic carbon fluxes for the same time period (Muller-Karger et al., 2004), as well as the total mass and terrigenous fluxes assessed by Turich et al. (2013) showed best correlation at zero-time lag on the basis of their 14-day sample interval. We compared our LDI temperature estimates with monthly CTD measurements between 0 and 50 m depth, the temperature at depth of maximum primary productivity and the temperature at the chlorophyll maximum (Turich et al., 2013; http://www.imars.usf.edu/cariaco) (Fig. 10). During the upwelling season, temperatures are significantly lower due to the upward migration of isotherms, whereas during the non-upwelling period, temperatures are higher, particularly in the upper 20 m, and the water column is more stratified (Fig. 10). LDI underestimates SST during stratification, which suggests that the LCD producers may thrive at depths of ca. 20–30 m. During upwelling, LDI-temperatures agree better with SST, implying that the habitat of the LCD producers potentially was closer to the surface, coincident with the shoaling of the nutricline and thermocline (Fig. 10). Turich et al. (2003) found that the $U^{K'}_{37}$-derived temperatures agreed reasonably well with the measured temperatures at the chlorophyll maximum, which is generally found below 20 m depth (average 30–34 m depth; ranging between 1 and 55 m) in the Cariaco Basin. The LDI temperatures are almost always higher than the temperatures at the chlorophyll maximum (Fig. 10), and higher than the temperatures at 30 m depth, implying that the LDI producers may reside in the upper 30 m of the water column, which is consistent with the results of Rampen et al. (2012), who showed that LDI-derived temperatures have the strongest correlation with temperatures of the upper 20 m of the water column. This also agrees with Balzano et al. (2018) who observed highest LCD abundances within the upper 20 m of the water column in the Tropical Atlantic.

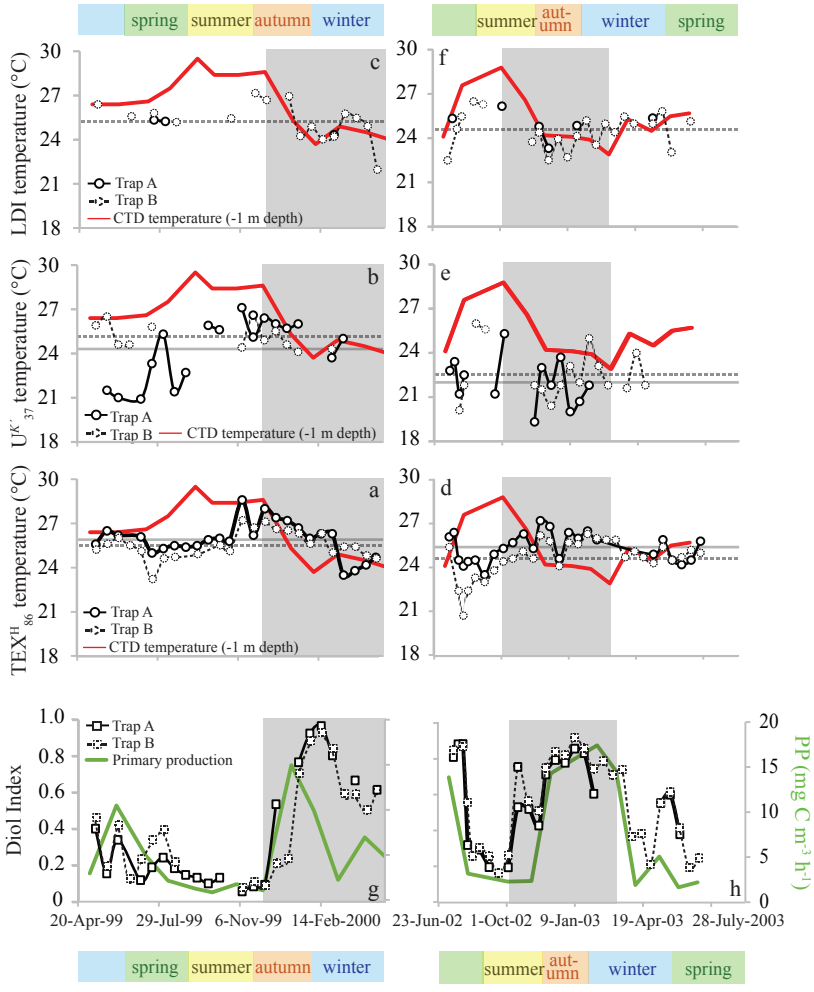

Fig. 9 Seasonal proxy derived temperature and upwelling/productivity records for the sediment traps in the Cariaco Basin. Panels **(a)**, **(b)** and **(c)** show the May 1999 – May 2000 time series TEX^{H}_{86}-, $U^{K'}_{37}$- and LDI-derived temperature reconstructions for Trap A (275 m depth; solid symbols) and Trap B (455 m depth; dashed symbols), respectively. Panels **(d)**, **(e)** and **(f)** show the proxy data for the July 2002 – July 2003 time series, with CTD-temperatures (1 m depth) in red. The $U^{K'}_{37}$, TEX^{H}_{86} and CTD temperatures are adopted from Turich et al. (2013). The horizontal lines reflect the average proxy-derived temperatures (Trap A = solid; Trap B = dashed). Panel **(g)** and **(h)** show the 1,14-diol based Diol Index (Rampen et al., 2008) for the 1999–2000 and 2002–2003 time series, respectively, for Trap A (275 m depth; solid symbols) and Trap B (455 m depth; dashed symbols). Primary productivity in mg C m^{-3} h^{-1} is plotted in green (data adopted from Turich et al., 2013). The shaded area reflects the period of upwelling.

In the Mozambique Channel, the LDI temperature variations are much smaller (< 2 °C; Fig. 8a) than the seasonal SST variation ranging between ca. 24.5 and 30.5 °C. Accordingly, during the warmest months of the year, the difference between LDI-derived and satellite-derived SST is outside of the calibration error (i.e., > 2 °C). However, this is similar to the $U^{K'}_{37}$ and TEX^{H}_{86} which also did not reveal seasonal variations. This lack of seasonality was explained by lateral advection and re-suspension of fine sediment material by migrating meso-scale eddies and thus ending up in the deeply moored sediment trap (Fallet et al., 2011; 2012). Most likely, this also explains the lack of seasonal variation in our LDI record (Fig. 8a). Nevertheless, the average LDI temperature for the sediment trap of 26.4 °C agrees reasonably well with the annual mean satellite-derived SST of 27.6 °C for the sampled years. Additionally, there is a good agreement with the average LDI temperature of 26.0 °C for two underlying surface sediments, as well as with the decadal average SST of 26.7 °C for 1955-2012 (Locarnini et al., 2013) given by the World Ocean Atlas (2013). For the North Atlantic, we also observe rather constant LDI temperatures during the year (Fig. 4) which contrasts with seasonal variations in satellite SSTs of ca. 3 to 5 °C. Nevertheless, differences are mostly within the calibration error, except at M1 and M2 where during winter and spring LDI-derived temperatures are between 0.5 and 2.8 °C higher than satellite SSTs. Similar to the LDI, also the TEX^{H}_{86} and $U^{K'}_{37}$-derived SSTs for the tropical Atlantic sediment traps do not reveal clear seasonal variation. As all three proxies show minimal seasonal variability, this might indicate that the lipids are potentially allochtonous and partially derive from distant regions, resulting in an integrated average temperature signal, similar to the Mozambique Channel. Nevertheless, the flux-weighted annual LDI temperatures of the tropical Atlantic sediment traps (26.6 for M1 and 27.1 °C for M2 and M4) agree well with the annual mean satellite-derived SSTs of 26.1, 26.0 and 27.5 °C for M1, M2 and M4, respectively. Moreover, the LDI-derived temperatures in the underlying sediments (26.5, 26.6 and 26.7 °C, respectively) do not only agree well with those found in a single year in the sediment traps but also with the decadal average SSTs for 1955 to 2012 (26.2, 27.1 and 26.3 °C, respectively; Locarnini et al., 2013; Fig. 6b).

Interestingly, TEX^{H}_{86} temperature estimates are relatively similar for traps M2 and M4 but at M1 they are lower than satellite SST in both the sediment trap and surface sediments (Fig. 6d). This underestimation of SST at M1 might suggest GDGT addition from colder subsurface waters. Indeed Balzano et al. (unpublished results) show that crenarchaeol is typically abundant between ca. 40 and 100 m water depth, agreeing with previous findings which have shown that the TEX_{86} can reflect subsurface temperatures rather than surface temperature in some regions (e.g., Huguet et al., 2007; Kim et al., 2012a; 201b; 2015; Schouten et al., 2013b; Chen et al., 2014; Wuchter et al., 2006b). Consequently, for the surface sediments, we also calculated subsurface temperatures, using the calibration of Kim et al. (2012b) (Fig. 6d), and compared these with the depth-integrated annual mean temperatures of the upper 150 m (Locarnini et al., 2013), calculated following Kim et al. (2008), which indeed shows a better correspondence for the eastern Atlantic surface

sediment, i.e., the sediments close to M1. This is likely caused by the steepening of the thermocline towards the east, as shown in Fig. 6a,d, in which we have indicated the approximate production depths of the temperature proxies. The thermocline at M1 is much steeper and shallower, which implies that GDGTs produced at ~ 100 m depth will record a lower temperature than at M2 and M4.

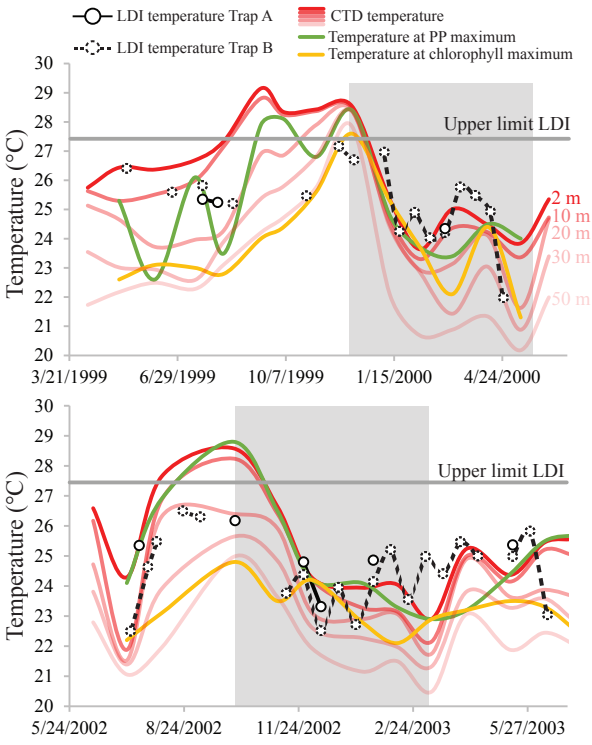

Fig. 10 LDI temperature records for the Cariaco Basin time series May 1991 – May 2000 and July 2002 – July 2003 for Trap A (275 m depth; solid symbols) and Trap B (455 m depth; dashed symbols), with CTD-derived temperatures at 2, 10, 20, 30 and 50 m depth (in red; http://www.imars.usf.edu-/CAR/index.html; CARIACO time series composite CTD profiles), the temperature at the depth of maximum primary production (green) and the temperature at the depth of the chlorophyll maximum (yellow; data adapted from Turich et al., 2013). The shaded area represents the upwelling season.

5. Conclusions

In this study we have evaluated LCD-based proxies, particularly the LDI, in sediment trap time series from five sites in the tropical North Atlantic, the Cariaco Basin and the Mozambique Channel. For the North Atlantic we found that in the water column ca. 25–85 % of the export of these lipid biomarkers is preserved during settling from 1200m to 3500m, and that generally less than 2 % was preserved in the surface sediments. Despite substantial degradation at the seafloor, likely linked to the prolonged oxygen exposure time, LCD-derived temperatures from the sediments are generally very similar to the annual mean LCD-derived temperatures in both the deep and shallow traps as well as to annual mean SST for the specific sampling year and on decadal time scales for the specific sites. In the Cariaco Basin we observe a strong seasonality in the LDI which is linked to the upwelling season at temperatures associated with a water depth of up to ca. 30 m during summer stratification, and at SST during winter upwelling accompanied by shoaling of both the nutricline and isotherms. The LDI temperatures in the Mozambique Channel and the tropical Atlantic reveal minimal seasonal change although seasonal SST contrasts amount to 3–5 °C. For the Mozambique Channel this is likely caused by lateral advection of re-suspended sediment by meso-scale eddy migration, a signal not substantially altered by diagenesis. Seasonal variations in the Diol Index are minimal in the central and western North Atlantic and 1,14-diol concentrations are rather low, implying little *Proboscia* diatom productivity. However, in the eastern Atlantic closest to the African continent, the Diol Index attains a clear spring maximum that is likely associated with upwelling in the Guinea Dome during summer to autumn, suggesting the Diol Index reflects a pre-upwelling signal, consistent with the current knowledge on *Proboscia* ecology. In the Cariaco Basin, controlled by seasonal upwelling, the Diol Index reveals the same clear seasonal trend observed in primary productivity, arguing that for this location the Diol Index is an excellent indicator of upwelling intensity.

Acknowledgements

We are grateful to Laura Schreuder and Denise Dorhout for analytical support, Wim Boer for help with MatLab calculations (BAYSPLINE), Laura Korte and Catarina Guerreiro for constructive discussions, and Isla Castañeda, Ulrike Fallet and Courtney Turich for providing and working up samples. This research has been funded by the European Research Council (ERC) under the European Union's Seventh Framework Program (FP7/2007-2013) ERC grant agreement [339206] to S.S. and ERC grant agreement [311152] as well as NWO project [822.01.008] to J-B.S.. S.S. and J.S.S.D. receive financial support from the Netherlands Earth System Science Centre (NESSC) through a gravitation grant from the Dutch ministry for Education, Culture and Science (grant number 024.002.001).

Chapter 5

Global temperature calibration of the Long chain Diol Index in marine surface sediments

Marijke W. de Bar, Gabriella M. Weiss, Caglar Yildiz, Sebastiaan W. Rampen, Julie Lattaud, Nicole J. Bale, Furu Mienis, Geert-Jan A. Brummer, Hartmut Schulz, Darci Rush, Yung-Hyun Kim, Barbara Donner, Jochen Knies, Andreas Lückge, Jan-Berend W. Stuut, Jaap S. Sinninghe Damsté and Stefan Schouten

In preparation

Abstract

The Long chain Diol Index (LDI) is a relatively novel organic geochemical proxy for sea surface temperature (SST), based on the abundance of the C_{30} 1,15-diol relative to the summed abundance of the C_{28} 1,13- and C_{30} 1,13- and 1,15-diols. Here we substantially extend and re-evaluate the initial core top calibration by combining the original dataset with 233 data-points derived from previously published studies, and 291 newly generated surface sediment LDI data points. In total, we considered 597 globally distributed surface sediments with a substantially enhanced geographical coverage compared to the original calibration. The relation with SST is similar to that of the original calibration but with substantially increased scatter. We evaluate the effects of fresh water input (e.g. river runoff) and long-chain diol contribution from *Proboscia* diatoms on the LDI. Exclusion of non-marine core-tops (deposited at salinity < 32), as well as core-tops with high *Proboscia*-derived C_{28} 1,12-diol abundance, resulted in a substantial improvement of the relation between LDI and annual mean SST. The final LDI calibration (LDI=0.0325×SST+0.1073; $R^2 = 0.88$; n = 516) is not statistically different from the original calibration of Rampen et al. (2012), though with a larger calibration error of 3 °C, confirming the robustness of the LDI index as an SST proxy.

1. Introduction

The present-day release of anthropogenic greenhouse gases into the atmosphere has resulted in warming of the Earth's atmosphere and surface oceans, which is expected to continue in the coming decades (IPCC, 2014). However, the actual extent of this temperature rise and its implications on global climate is difficult to accurately predict due to the complexity of the Earth's climate system. For the prediction of future climate conditions, we typically rely on computer simulations of ocean-atmosphere circulation models, which in turn rely on time-series of observational data of various climate parameters. However, instrumental records only extend back to the last century after the onset of anthropogenic global warming. Therefore, to accurately predict climate, it is essential to study natural climate evolution on geological timescales. For instance, during the Late Cretaceous to Early Eocene, greenhouse gas concentrations in the atmosphere and Earth's temperature were much higher compared to today (e.g., Zachos et al., 2001; Bijl et al., 2009; Anagnostou et al., 2016; Foster et al., 2017; O'Brien et al., 2017), and certain periods can serve as potential analogs for the current climate change. For the reconstruction of past climate conditions on geological timescales, proxies are used, which are characteristics of fossil remains holding information on the environment in which they were formed.

One of the most important climate parameters is past sea surface temperature (SST), since oceans make up more than two thirds of the world's surface, and therefore profoundly influence global climate. Commonly, proxies are based on measurements of either inorganic or organic remnants of (extinct) organisms preserved in sediment. One of the most robust inorganic paleotemperature proxies uses the stable oxygen isotopic composition ($\delta^{18}O$) of the carbonate shells of foraminifera (e.g., Emiliani, 1955; Shackleton et al., 1967). Also, the Mg/Ca ratio measured in a foraminiferal shell is correlated with temperature (e.g., Nürnberg et al., 1996). Organic temperature proxies, on the other hand, are generally based on lipid biomarkers, which are specific for a certain organism or a group of organisms. In paleoclimatic studies there are two biomarker proxies for SST which are frequently applied. The first is the $U^{K'}_{37}$ index, based on long-chain unsaturated alkenones, detected in marine sediments world-wide, uses the ratio of the di-unsaturated C_{37} methyl alkenone over the tri-unsaturated C_{37} methyl alkenone (Prahl and Wakeham, 1987). This ratio is positively correlated with temperature, since the modern-day alkenone producers (mainly E*miliani huxleyi* and *Gephyrocapsa oceanica*; e.g., Volkman et al., 1980a, 1995; Marlowe et al., 1984a; Conte et al., 1995) synthesize C_{37} alkenones, of which the degree of saturation varies with growth temperature (Brassell et al., 1986; Prahl and Wakeham, 1987). The temperature range of the proxy is between -1 and 29 °C (Müller et al., 1998; Conte et al., 2006), and a recently published Bayesian calibration has extended the upper limit of the calibration to 29.6 °C (Tierney and Tingley, 2018). The TEX_{86} proxy is based on the distribution of isoprenoid glycerol dialkyl glycerol tetraethers (GDGTs), produced by the archaeal phylum

Thaumarchaeota (see Schouten et al., 2013b for a review). These archaea biosynthesize GDGTs containing 0 to 3 cyclopentane moieties (GDGT-0 to -3) and crenarchaeol which contains 4 cyclopentane rings and a cyclohexane moiety (Schouten et al., 2002; Sinninghe Damsté et al., 2002). The proxy is based on the relative abundance of GDGT-1, -2 and 3 and an isomer of crenarchaeol (Schouten et al., 2002). The index is positively correlated with annual mean SST, showing an increase in the number of cyclopentane moieties with increasing temperature, and can be applied, with caution, at temperatures > 30 °C.

In 2012, Rampen et al. proposed the Long chain Diol Index (LDI), based on the fractional abundances of long-chain alkyl diols (LCDs), specifically the C_{28} and C_{30} 1,13- and C_{30} 1,15-diols, which contain a hydroxy group at C1 and a hydroxy group at the C13 or C15 position, respectively:

$$LDI = [C_{30}\ 1,15\text{-diol}]/[C_{28}\ 1,13\text{-diol}+C_{30}\ 1,13\text{-diol}+C_{30}\ 1,15\text{-diol}] \quad (1)$$

The LDI, based on 161 globally distributed core-top sediments, shows a strong correlation with SST described by the following transfer function:

$$LDI = 0.033 \times SST + 0.095 \quad (n = 161;\ R^2 = 0.97;\ RE = 2.0\ °C) \quad (2)$$

The main limitation of the LDI is the fact that the producers of the 1,13- and 1,15-diols in the ocean are still unknown. Cultivated freshwater and marine Eustigmatophyte algae produce 1,13- and 1,15-diols (Volkman et al., 1992; 1999; Gelin et al., 1997a; 1997b; Méjanelle et al., 2003; Shimokawara et al., 2010; Rampen et al., 2014b). However, the LCD distributions observed in marine cultures are dissimilar from the distributions observed in the marine environment. Moreover, these Eustigmatophyte algae rarely occur in the ocean (e.g., Balzano et al., 2018). In contrast, Shimokawara et al. (2010) observed that the LCD distributions in the Eustigmatophyte *Nannochloropsis* sp. (containing a dominant C_{32} 1,15-diol) were similar to that observed in sediments of Lake Baikal, suggesting that Eustigmatophytes might produce LCDs in lakes. Additionally, Villanueva et al (2014) observed similar trends for 18S rRNA gene copy numbers of (yet unknown) Eustigmatophytes with LCD concentrations in an African lake, confirming Eustigmatophytes as potential LCD producers in fresh water. However, Rampen et al. (2014b) tested the LDI in 62 lakes and found that the correlation with temperature was weak (R^2 = 0.33), which is likely because of the various Eustigmatophyte groups, each possessing different LCD distributions, implying that the applicability of the LDI is limited to the marine environment.

Besides unknown producers, other issues have been recognised with the LDI. De Bar et al. (2016) and Lattaud et al. (2017a) observed that the LDI-derived temperatures in surface sediments near river mouths significantly deviated from satellite-derived SSTs. The diol distributions are characterized by elevated C_{32} 1,15-diol abundance, due to the freshwater input where the C_{32} 1,15 diol is in high abundance (Rampen et al., 2014b). Consequently, applying the LDI in marine regions with riverine input should be done with caution. Rodrigo-

Gámiz et al. (2015) showed that for surface sediments and suspended particulate matter (SPM) in the subpolar region around Iceland, the LDI considerably underestimated satellite SST. Relatively high C_{28} and C_{30} 1,14-diol abundances were observed in this area, which are characteristic for *Proboscia* diatoms (Sinninghe Damsté et al., 2003; Rampen et al., 2007), although they were also identified in the estuarine *Apedinella radians* (Rampen et al., 2011). Accordingly, the authors hypothesized that *Proboscia* diatoms (at least partially) contributed to the 1,13- and 1,15-diol production, and thereby compromised the LDI. For surface sediments in the Okhotsk Sea, also a subpolar region, the LDI showed a strong correlation with SST, but this relation was statistically different from the global calibration (Lattaud et al., 2018b). Lastly, down-core applications of the LDI have shown that the index is highly promising as a SST proxy but often reveals a slightly larger glacial-interglacial temperature amplitude than found in $U^{K'}_{37}$ and TEX_{86} records (Rampen et al., 2012; Lopes dos Santos et al., 2013; Rodrigo-Gámiz et al., 2014; Jonas et al., 2017; de Bar et al., 2018).

Thus, despite the relatively robust core top calibration and successful down core applications, questions remain on the calibration and environments in which this proxy can be applied. Therefore, in this study we substantially extended the initial global LDI core-top calibration of Rampen et al. (2012) with literature data and newly generated data, adding 431 data points and substantially increasing global coverage. Comparison with SST and salinity allowed us to determine the main controls on the LDI and identify potential constraints on the applicability of the LDI.

2. Materials and methods

2.1 Surface sediments

We have combined the global core-top LCD data of Rampen et al. (2012) with other previously published LCD data and newly acquired core-top data. We partially re-evaluated the original LDI core-top dataset of Rampen et al. (2012), existing of 209 measurements (black dots in Fig. 1), since we also quantified other diols, in particular the C_{28} 1,12-diol. Re-integration has led to minor changes in LDI values of <0.06. For eleven samples we could not retrieve the original data and therefore we were not able to reintegrate the LCD peak areas (indicated in the Supplemental Table). Differences in contributions of the selected ions to the total ion counts (*m*/*z* 50–800) of saturated versus unsaturated LCDs were considered by applying correction factors, as described by Rampen et al. (2009). For the dataset of Rampen et al. (2012), we applied two different correction factors to the two mass spectrometer (MS) systems on which the LCDs were analyzed (Supplemental Table). Additionally, we re-integrated previously published LCD data (pink dots in Fig. 1), i.e., the core-top sediment data from around Iceland of Rodrigo-Gámiz et al. (2015), the Iberian margin surface sediment data of de Bar et al. (2016), the Gulf of Lion, Amazon Basin, Berau delta and Kara Sea data of Lattaud et al. (2017a), the Mozambique Channel data of Lattaud et al. (2017b),

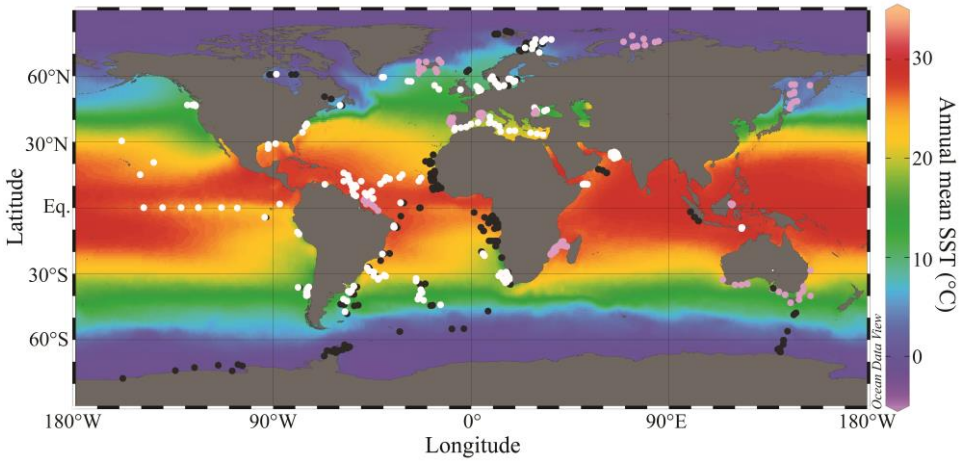

Fig. 1 Core-top sediment locations investigated in this study. Black circles indicate the surface sediments of Rampen et al. (2012), pink circles indicate surface sediments analyzed for long-chain alkyl diols in previous studies (de Bar et al., 2016; Lattaud et al., 2017a; 2017b; 2018; Smith et al., 2013; Rodrigo-Gámiz et al., 2015), and the white circles represent new surface sediment data obtained in this study. Map of sea surface temperatures (SST) is based on data of the World Ocean Atlas (2013) (Locarnini et al., 2013) and made in Ocean Data View (Schlitzer, 2015).

the Okhotsk Sea data of Lattaud et al. (2018b) and partially the Black Sea data of Lattaud et al. (2018a). We also adopted the LDI data of the region around Australia of Smith et al. (2013) but did not have the original MS data and thus were not able to re-evaluate the LCD distributions. Re-evaluation of data of de Bar et al. (2016) showed that the fractional abundance of the unsaturated LCDs was not corrected for the differences in contributions of the selected ions to the total mass spectrum, which is corrected here. In total, the previously published data comprise 233 sediment locations. Additionally, we have analyzed 105 polar fractions for long-chain diols which were analyzed previously by Kim et al. (2008; 2010) for the global TEX_{86} core-top calibration. Furthermore, we analyzed 186 new core-tops from several regions for a better spatial coverage (white dots in Fig. 1). In total, 733 surface sediment samples were considered in this study.

2.2 Lipid extraction and instrumental analysis

The 186 new surface sediments (mostly 0–1 cm) were freeze-dried and extracted with an Accelerated Solvent Extractor (ASE 200; DIONEX) using a dichloromethane:methanol (DCM:MeOH) mixture (9/1; vol./vol.) at a temperature of 100 °C and a pressure of 7–8 × 10^6 Pa. Lipid extracts were dried under nitrogen and separated into three fractions (apolar, ketone, polar) using activated (2h at 150 °C) Al_2O_3. Separation was achieved using the eluents hexane/DCM (9/1; vol./vol.), hexane/DCM (1/1; vol./vol.) and DCM/MeOH (1/1; vol./vol.), respectively (Method 2 in Supplementary Table). The polar fractions were silylated by the addition of pyridine and N,O-bis(trimethylsilyl)trifluoroacetamide (BSTFA) and heating at 60 °C for 20 min. Prior to injection, ethyl acetate was added. GC-MS analyses were done on an Agilent 7890B gas chromatograph interfaced with an Agilent 5977A mass spectrometer. Samples were injected on-column at a starting temperature of 70 °C, which was programmed to 130 °C by 20 °C min^{-1}, and a subsequent gradient of 4 °C min^{-1} to the end temperature of 320 °C, which was kept for 25 min. The GC was equipped with a fused silica column (25 m × 0.32 mm) with a CP Sil-5 coating (film thickness 0.12 µm). Helium was used as carrier gas with a constant flow of 2 ml min^{-1}, and the MS operated with an ionization energy of 70 eV. We identified the LCDs in full scan, scanning between *m*/*z* 50 to 850, based on their characteristic fragmentation patterns (de Leeuw et al., 1981; Versteegh et al., 1997). Quantification of the LCDs was achieved in selected ion monitoring (SIM) mode of the characteristic fragmentation ions (i.e., *m*/*z* 299, 313, 327 and 341; Rampen et al., 2012). The LDI was calculated according to Rampen et al. (2012) integrating the relevant peak areas in SIM mode (Eq. 1). For the calculation of fractional abundances, we applied a correction factor for the relative contribution of the selected fragments during SIM to the total ion counts for the saturated (16.1 %) versus unsaturated (9.1 %) LCDs.

Lipid extraction methods for re-analyzed polar fractions (from Kim et al., 2010) and the LCD data which we re-evaluated or adopted, are described in the original literature. We have classified these methods into five groups, indicated in the Supplementary Table (Methods 1-5). Generally, these methods differ in extraction protocol, i.e. ASE, ultrasonic extraction, ASE followed by saponification of the extract or Bligh and Dyer, or in fractionation protocol, i.e. two (apolar-polar) or three fraction (apolar-ketone-polar) separation using Al_2O_3, three fraction separation using silica gel or separation of core lipids and intact polar lipids over silica gel.

2.3 Oceanographic data

The LCD data were compared with temperature, salinity and nutrient data from the World Ocean Atlas 2013 (WOA13). Annual mean, seasonal sea surface temperatures (°C; 0 m depth), temperatures for different depths, and salinity were obtained from the 0.25° grid databases (Locarnini et al., 2013; Zweng et al., 2013). Annual mean phosphate and nitrate concentrations (µmol L^{-1}) were obtained from the 1° grid WOA13 databases (Garcia et al.,

2014). In case there was no temperature data for the 0.25° grid corresponding to the core-top location, we adopted the SST value for the 0.25° grid closest by. For SST, we used data within 1° distance; if not available, we did not include the data. Exceptions are two Arctic and eight Antarctic sediments for which we used SST data 1 to 2° degrees away, as in these regions SST data was generally scarcer. For salinity, we used values within 1.5° distance of the core-top location, and for phosphate and nitrate we stayed within a 2.5° radius.

2.4 Statistical analysis

We performed Principal Component Analysis (PCA) on the fractional abundances of the various LCDs, annual mean SST and phosphate and nitrate concentrations, using the XLSTAT software (Addinsoft, 2018). When a LCD was not detected, its fractional abundance was considered zero. Comparison of different regression slopes was done by means of analysis of covariance (ANCOVA) using R software.

3. Results and discussion

We have combined several data sets to extend the core-top calibration of the LDI, as originally published by Rampen et al. (2012), to re-assess the calibration of the index, and identify potential constraints on the proxy. We have (partially) re-evaluated the core-top data of Rampen et al. (2012), re-evaluated and adopted previously published LCD data (Smith et al., 2013; Rodrigo-Gámiz et al., 2015; de Bar et al., 2016; Lattaud et al., 2017a; 2017b; 2018a; 2018b) and added new core-tops, which in total resulted in LCD distributions from 733 core-tops. Of these 733 sediments, the LDI could not be calculated for 136 sediments due to quantification limit issues, related to high backgrounds obscuring the signals of the LDI-diols or low abundances of all LCDs. Hence, in total we obtained 597 LDI data points and cover an annual mean temperature range of -1.8 to 30.3 °C (Fig. 2; Supplementary Table). Although we have improved global coverage compared to Rampen et al. (2012), it must be noted that almost 40 % of our surface sediments originates from the tropical temperature regime, i.e. > 25 °C.

We have linearly cross-correlated our LDI core-top data with annual mean SST (WOA13; Locarnini et al., 2013), resulting in a significant positive regression and a correlation coefficient (R^2) of 0.82 (Fig. 2). The relation (LDI=0.032×SST+0.111) is statistically identical in slope and intercept (ANCOVA p-value ~ 0.3) to the original LDI-relation as proposed by Rampen et al. (2012; Eq. 2), confirming that the LDI contains a strong temperature signal. Additionally, we performed a Principle Component Analysis to confirm the environmental behavior of the different LCDs (Fig. 3a). The first two principal components only explained 54 % of the total variance, which is likely due to the large number of variables considered. The mono-unsaturated and saturated C_{28} 1,14-diol closely aggregate together with nitrate and phosphate concentrations confirming a relation between nutrient

concentrations and the relative abundance of the C_{28} 1,14-diol as previous reported by Gal et al. (2018). The C_{28} and C_{30} 1,13-diols load opposite of the C_{30} 1,15-diol, the LDI and annual mean SST on Factor 1, which is consistent with a higher C_{30} 1,15-diol abundance, and thus a higher LDI, with higher SST, and higher 1,13-diol abundances with lower SST (cf. Rampen et al., 2012). Accordingly, the variance explained by Factor 1 (38 %) is likely primarily temperature, confirmed by the strong correlation ($R^2 = 0.78$) between the scores of Factor 1 with annual mean SST (Fig. 3b). The C_{32} 1,15-diol has almost no factor loading on the Factor 1 axis, suggesting that temperature has minimal influence on the abundance of the C_{32} 1,15-diol, consistent with the results of Rampen et al. (2012). Nevertheless, a number of data points do not fall closely on the calibration line and the decrease in correlation coefficient from 0.97 of the original calibration of Rampen et al. (2012) to 0.82 in this study as well as visual inspection shows increased scatter. In the following sections we will discuss factors potentially responsible for this increased scatter in the LDI calibration, and evaluate potential constraints on the proxy.

3.1 Non-marine LCD contributions

Previous studies have shown that river outflow can compromise the LDI (de Bar et al., 2016; Lattaud et al., 2017a), although the effect of riverine input on the LDI is likely specific for each region. For instance, de Bar et al. (2016) observed lower LDI-derived SSTs than satellite-derived SSTs in surface sediments close to the river mouths on the Portuguese margin, whereas Lattaud et al. (2017a) obtained LDI SSTs which were significantly higher than satellite SSTs for Kara Sea sediments closest to the Yenisei River. Surface sediments deposited in low salinity environments (<32) are mainly derived from the Hudson Bay (salinity 26–31), Baltic Sea (7–30), Black Sea (11–18) and the Kara Sea (10–32), all of which are impacted by river inflow. The LDI values from the Baltic and Black Sea are clearly positioned above the regression line (Fig. 2a) with temperature differences up to ca. +12 °C. This might suggest that the LDI is unlikely to work in low salinity environments, consistent with Rampen et al. (2014b) who observed that the LDI does not work in lakes. Indeed, when we exclude surface sediments deposited at salinities < 32 (57 samples originating from the Baltic Sea, Black Sea, Hudson Bay, Gulf of St. Lawrence and the Kara Sea), the correlation improves substantially ($R^2 = 0.86$; Fig. 2b). The core-tops from the Hudson Bay and Gulf of St. Lawrence originate from the dataset of Rampen et al. (2012) but were also excluded in the original core-top calibration.

One way to screen for sediments impacted by freshwater inflow would be to use the abundance of the C_{32} 1,15-diol, which is often elevated near rivers (Versteegh et al., 1997; 2000; Rampen et al., 2014b; de Bar et al., 2016; Lattaud et al., 2017a; 2017b). Although there is no strong correlation, many of these low salinity sediments are also associated with a

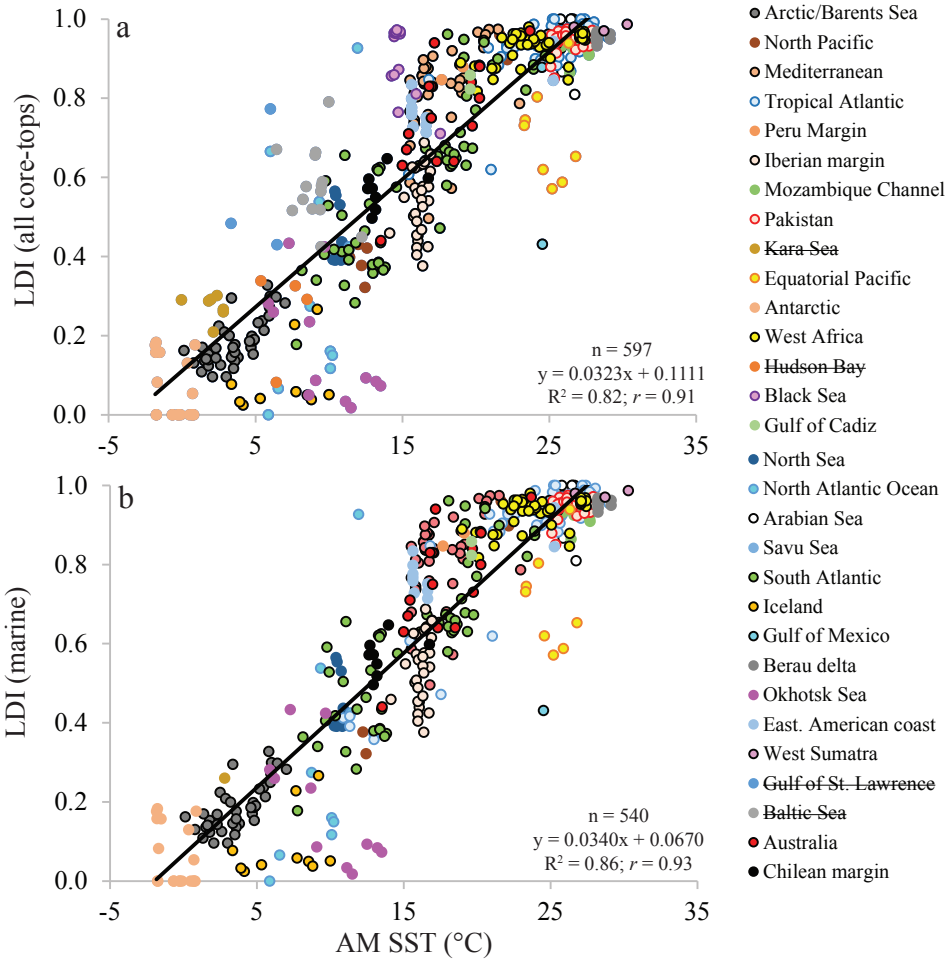

Fig. 2 (a) LDI values of all surface sediments vs. annual mean SST (0 m depth; WOA13), and **(b)** LDI values of marine surface sediments vs. annual mean SST when excluding all stations where surface salinity < 32. The associated excluded sediments belong to the Hudson Bay, Black Sea, Gulf of St. Lawrence, Kara Sea (7 of 8 sediments excluded) and the Baltic Sea (indicated in the legend by strike-through).

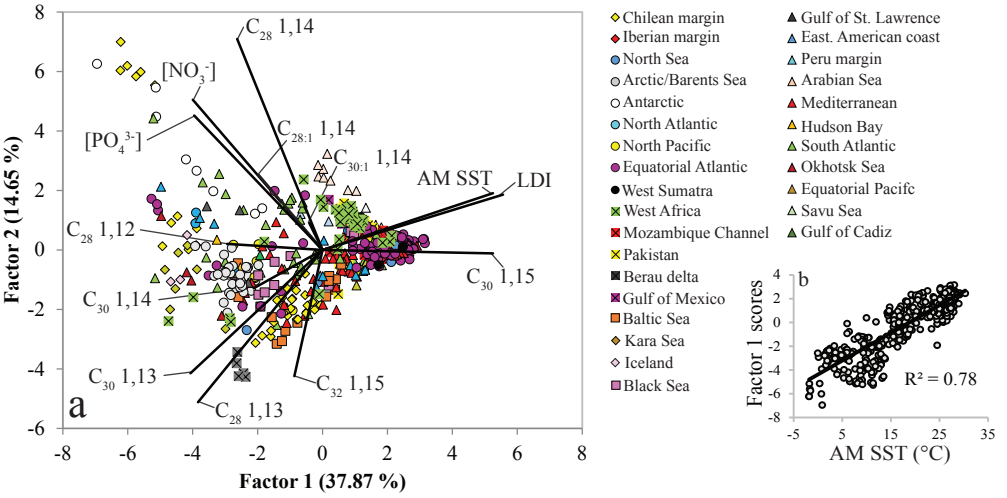

Fig. 3 (a) PCA biplot of the fractional abundances of the different long-chain diols, the LDI, annual mean sea surface temperature (AM SST; °C) and annual mean phosphate and nitrate concentrations (µmol L^{-1}). **(b)** Factor 1 scores for all observations correlated against annual mean SST (°C).

relatively high fractional abundance of the C_{32} 1,15-diol (C_{32} 1,15-diol with respect to the C_{28} 1,13, C_{30} 1,13- and 1,15- and C_{32} 1,15-diol; Fig. S1). Thus, a high abundance of the C_{32} 1,15 diol can serve as an indicator for a potential bias although an exact threshold cannot be given. In any case, this study as well as other studies (e.g. Rampen et al., 2012; de Bar et al., 2016; Lattaud et al., 2017a) show that the application of the LDI in low salinity environments or very close near river mouths may be problematic.

3.2 *Proboscia* influence on the LDI

Our dataset includes the core-top data of Rodrigo-Gámiz et al. (2015) of the subpolar region around Iceland. However, as mentioned in the introduction, the LDI substantially underestimates satellite SST in this region likely because *Proboscia* seem to be at least a partial source of the 1,13-diols. Since this may also occur in other regions, we screened for the biasing influence of *Proboscia* diatoms using two Diol Indices based on 1,14-diols versus the 1,15- and 1-1,3 diols, respectively (Rampen et al., 2008; Willmott et al., 2010, respectively). Cross correlating the temperature difference between annual mean SST and the LDI-regression based SST (Fig. 2b) with these indices (Fig. S2), does not reveal strong correlations, although several sediments have a high Diol Index 1 (Rampen et al., 2008) as well as a cold bias in the LDI-derived SST. However, most core-tops with such a high Diol

Index do not reveal this cold bias. Thus, the Diol Index does not provide an unambiguous indication for a potential bias on the LDI caused by *Proboscia* LCD contribution.

We closely examined the data points which fall well below the LDI regression line, i.e., many of the Iceland data-points (yellow dots with black outline), the Okhotsk Sea (purple dots) and northwestern North Atlantic Ocean (blue dots; transect Ireland-Greenland) (Fig. 2b). Examination of the chromatograms showed often an atypical LCD distribution compared to other marine sediments (Fig. 4). One sediment from the Gulf of Mexico also shows this unusual distribution, and interestingly this is the only data-point of this region which also substantially underestimates SST when compared to the LDI regression (LDI 0.43, SST 24.5 °C; Fig. 2b). These sediments are characterized by high mono-unsaturated and saturated 1,14-diol abundances, but also relatively high C_{26} and C_{28} 1,12-diols. The C_{28} 1,12-diol has been observed in low amounts in lake sediments (Shimokawara et al., 2010; Rampen et al., 2014b), freshwater eustigmatophyte algae (Volkman et al., 1999a; Rampen et al., 2014b) and in *Proboscia* diatoms (Rampen et al., 2007) as well as in marine sediments with high 1,14-diol concentrations (Willmott et al., 2010; Rampen et al., 2007; ten Haven and Rullkötter, 1991; de Bar et al., 2018). The C_{26} 1,12-diol has been observed in cultures of *P. inermis* and

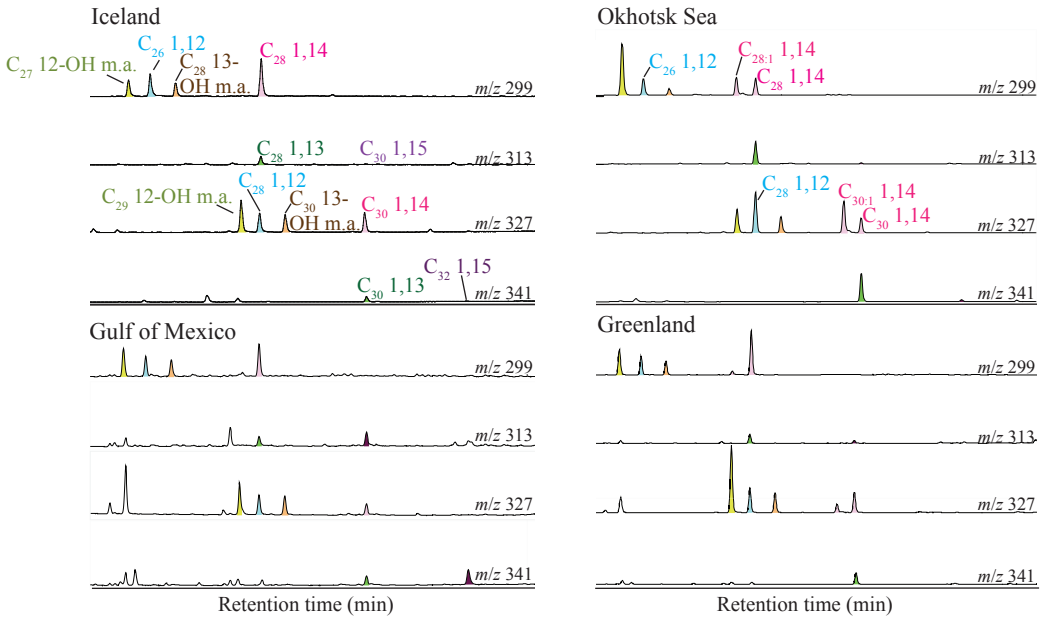

Fig. 4 Selected Ion Monitoring chromatograms of four sediments with LDI values which deviated substantially from the LDI calibration versus annual mean SST (see Fig 3). The SIM traces show diol distributions revealing relatively high C_{26} and C_{28} 1,12-diols (blue), as well as the C_{27} and C_{29} 12-OH (green) and C_{28} and C_{30} 13-OH methyl alkanoates (brown). The 'Greenland' sediment is classified as 'North Atlantic Ocean' in Figures 2, 3, 5 and 6.

P. indica (Rampen et al., 2007), but to our knowledge was not yet reported for environmental samples. In the same sediments we detected relatively high abundances of the C_{27} and C_{29} 12-hydroxy and C_{28} and C_{30} 13-hydroxy methyl alkanoates (Fig. 4). Sinninghe Damsté et al. (2003) and Rampen et al. (2007) observed C_{27} and C_{29} 12- hydroxy methyl alkanoates in cultures of *P. indica*, *P. alata* and *P. inermis*. Small amounts of the C_{28} and C_{30} 13-hydroxy methyl alkanoates were detected solely in *P. indica*. Since, to date, *Proboscia* is the only group of organisms known to produce these hydroxyl methyl alkanoates and 1,14- and 1,12-diols, this is a very strong indication that the LCDs and mid-chain hydroxy methyl alkanoates in these sediments are produced by *Proboscia* species. However, the unusual distributions with the high C_{26} and C_{28} 1,12-diols and C_{28} and C_{30} 12-hydroxy methyl alkanoates detected in several sediments compared to those of cultures also strongly suggest that they are sourced by *Proboscia* species which have not yet been cultured and evaluated for LCDs.

The fact that the sediments with unusual distributions of 1,12-diols all reveal very low LDI values compared to the LDI regression, indicates that particular *Proboscia* species likely contribute 1,13-diols, and possibly also 1,15-diols, thereby compromising the LDI. Accordingly, we plotted the fractional abundance of the C_{28} 1,12-diol (with respect to the C_{28} 1,13-, 1,14-, C_{30} 1,13-, 1,14- and 1,15-diols) against the residual temperature errors of the LDI calibration (i.e., LDI SST – AM SST; Fig. 5). The fractional abundance of the C_{28} 1,12-diol is below 0.1 for the large majority of the sediments (95 % of total), but when the fractional abundance increases, the LDI is biased towards colder temperatures (up to ca. -14 °C difference). Accordingly, the relative abundance of the C_{28} 1,12-diol might serve as a

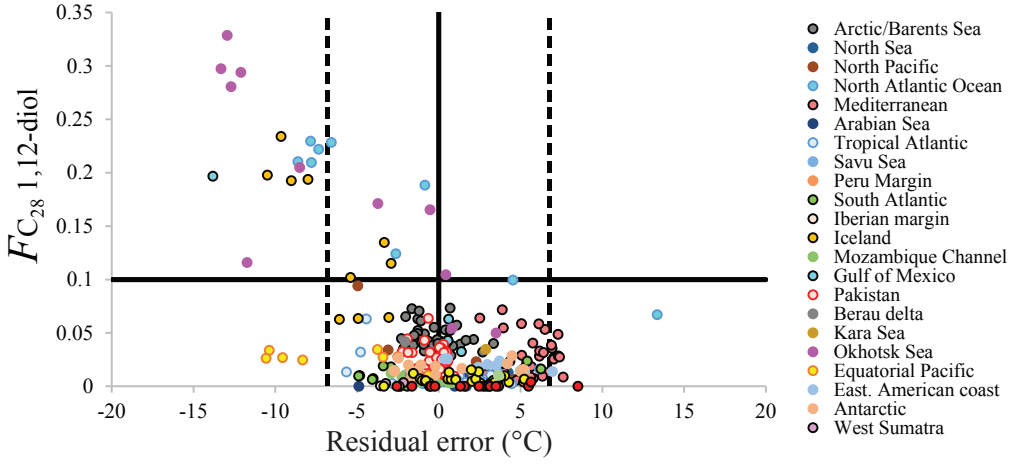

Fig. 5 The fractional abundance of the C_{28} 1,12-diol vs. the residual error in SST estimation based on the regression plotted in Fig. 3. The black solid lines indicate a fractional abundance of 0.1, and a residual error of 0. The dotted lines reflects the negative and positive 2×SD value of 6.8 °C.

better indication for the influence of *Proboscia* on the LDI than the abundance of 1,14-diols. When we exclude core-top data with a fractional abundance of the C_{28} 1,12-diol > 0.1 (24 core-tops), this improves the correlation to $R^2 = 0.88$ (Fig. 6).

The resulting LDI calibration with annual mean SST is as follows (Fig. 6):

$$LDI = 0.0325 \times SST + 0.1073 \qquad (n = 516;\ R^2 = 0.88;\ RE = 3.0\ °C) \qquad (3)$$

This regression equation is statistically (ANCOVA *p*-value > 0.2; although the data is not normally distributed) not different from the one originally reported by Rampen et al. (2012; Eq. 2).

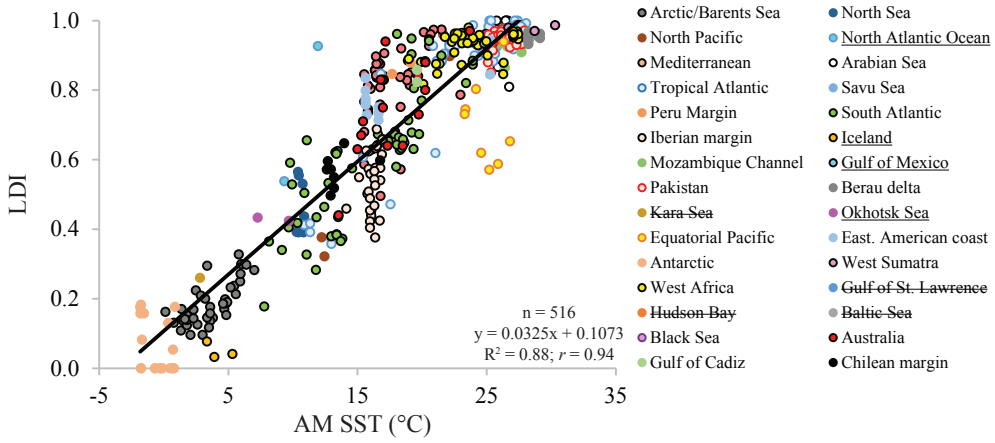

Fig. 6 LDI calibration when estuarine sediments (salinity < 32) are excluded, as well as surface sediments in which the fractional abundance of the C_{28} 1,12-diol is higher than 0.1. Regions of which surface sediments were excluded based on the C_{28} 1,12-diol abundance and salinity are indicated by underline and strike-through in the legend, respectively.

3.3 Residual errors in estimation

The residual errors of the LDI-derived SSTs (LDI SST – annual mean SST) are between –11.1 and +13.3 °C (Fig. 7), without a relation between the residuals and annual mean SST. The resulting calibration error, i.e. the standard deviation on the residual errors, is 3.0 °C, which is higher than the 2.0 °C of the original calibration of Rampen et al. (2012). The cross-correlation of the LDI with mean seasonal SSTs reveals that the LDI correlates best with summer temperatures (R^2 = 0.90; Fig. S4) and correlation with depth showed the best correlation with the upper 30 m of the water column (R^2 = around 0.88), similar to Rampen et al. (2012). Residual errors are plotted in Fig. 8 on a global map. The regions where the

LDI temperatures differ more than ±2SD from the regression line are mainly derived from the Mediterranean, the Equatorial Pacific and the Iberian margin. The LDI of the surface sediments in the Mediterranean overestimate annual mean SST (up 7.8 °C) while the core-tops of the equatorial Pacific show severe underestimation (up to –11 °C). In these Pacific sediments, the 1,14-diols are also relatively high in abundance (between 30 and 90 %), but the samples do not reveal unusual LCD distributions, i.e. a high abundance of 1,12-diols. Moreover, the PCA biplot does not show that the Equatorial Pacific or the Mediterranean data cluster as distinct groups separated from the other data. Accordingly, the reasons for the cold and warm bias in these regions stay elusive but may be due to regional conditions. For instance, in the Equatorial Pacific, the LDI temperature signal might potentially be brought to the surface by equatorial upwelling of cold waters. Finally, four data-points from the Iberian margin are outside the ±2SD range and underestimate SST (up 8.1 °C) which is potentially due to local river outflow influence despite that salinity is > 32 (de Bar et al., 2016).

The LDI data at the upper end of the calibration (> 18 °C) shows a reduction in slope. This could indicate nonlinearity in the relation between LDI and temperature, which has also been inferred for the $U^{K'}_{37}$ (Conte et al., 2001; 2006). Indeed, the residual errors are not normally distributed, and the regression over- and underestimates temperature in the low and high temperature regions, respectively, with respect to the LDI-temperature data-points (Fig. 6). However, application of a third order polynomial relation results only in a moderate increase in correlation coefficient to 0.90 (data not shown).

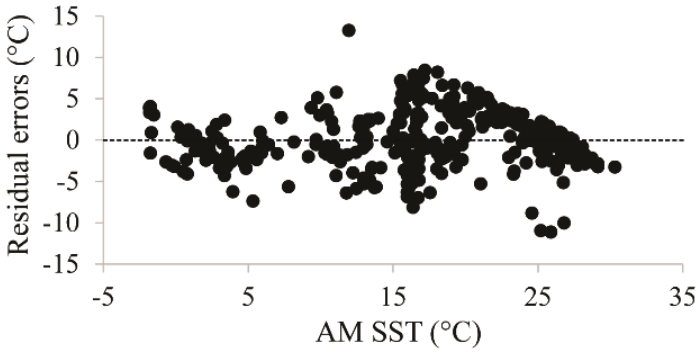

Fig. 7 Residual SST errors (LDI SST – annual mean SST) against annual mean SST.

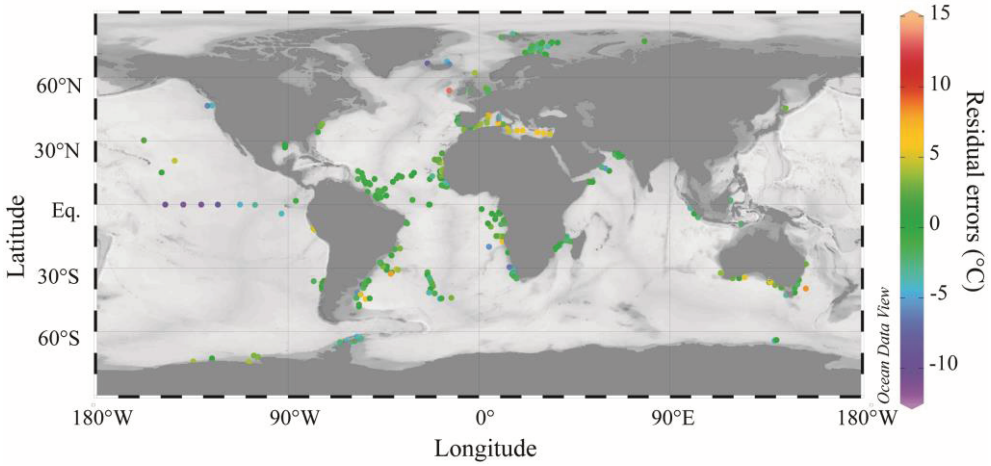

Fig. 8 Residual SST errors (LDI SST – measured annual mean SST) plotted on the global map (created in Ocean Data View; Schlitzer, 2015).

3.4 Implications for LDI temperature reconstructions

Our new extended LDI calibration is statistically equal to the original proposed by Rampen et al. (2012), suggesting that previous temperature reconstructions based on the LDI (e.g. Lopes dos Santos et al., 2013; Warnock et al., 2017; Jonas et al., 2017) likely do not require major adjustments. The maximal temperature difference between the previous SST calibration and the present calibration is +0.43 °C at the lower end of the calibration (LDI=0) and –0.04 °C at the upper end (LDI=1). However, due to the substantial increase in data-points included in the calibration, the residual error increased from 2 to 3 °C, which is larger than that of the $U^{K'}_{37}$ (1.5 °C) and the TEX^{H}_{86} (2.5 °C) and thus differences between proxy values observed in sediment records may now fall within proxy errors.

Importantly, our results provide new constraints on the application of the LDI. Firstly, the LDI should not be applied in low-salinity environments, e.g., environments substantially influenced by river runoff. Enhanced C_{32} 1,15 diol abundances do provide an indication for river runoff, although an exact threshold cannot be given. Importantly, high abundances of the C_{26} and C_{28} 1,12-diols and C_{27} and C_{29} 12-hydroxy and C_{28} and C_{30} 13-hydroxy methyl alkanoates hint at LCD contributions from *Proboscia*, and we advise to reject LDI data in case the fractional abundance of the C_{28} 1,12-diol (vs. C_{28} 1,13-, 1,14-, C_{30} 1,13-, 1,14- and 1,15-diols) is > 0.1. This LCD may often not be included in the quantification of diols, but our data show it is useful to include it in future studies to assess the potential influence of *Proboscia* LCD contribution on the LDI. In any case, caution is advised when applying the LDI in case of high and/or variable 1,14-diol abundances. Since previous LDI records have

not reported the abundance of C_{28} 1,12 diols we cannot evaluate whether these were compromised by *Proboscia*-derived LCDs.

4. Conclusions

We have extended the global core-top temperature calibration of the Long chain Diol Index and confirmed that LDI values are strongly correlated with annual mean SST, but with an increase in scatter and a decrease in the correlation coefficient (0.97 to 0.82). We observed that most surface sediments with low salinities (particularly from the Baltic and Black Sea) were substantially different from the LDI regression and exclusion of low-saline core-tops (salinity < 32) improved the quality of correlation (R^2 = 0.86). Examination of diol distributions with high input of 1,14-diols from *Proboscia* diatoms show that the Diol Index is not a good indicator to identify biases in the LDI but that high abundances of the C_{26} and C_{28} 1,12-diols, as well as the C_{27} and C_{29} 12-hyrdroxy and C_{28} and C_{30} 13-hydroxy methyl alkanoates are associated with a cold bias in the LDI-based temperatures. Therefore, we have defined a cut-off of 0.1 in the C_{28} 1,12-diol fractional abundance which again improved the correlation between the LDI and annual mean SST. The new relation between the LDI and SST (LDI = 0.0325×SST+0.1073; n = 516; R^2 = 0.88) covers a temperature range between –3.3 and 27.5 °C with a calibration error of 3 °C. The relationship is statistically equal to the Rampen et al. (2012) calibration, and thus validates previous down-core LDI applications to yield similar absolute LDI-derived temperatures. However, re-evaluation of the reliability of the LDI records in terms of fresh water influence (salinity, C_{32} 1,15-diol abundance) and *Proboscia* contribution (high/variable 1,14-diol abundances, C_{28} 1,12-diol abundance) is recommended. Our results confirm that the LDI can be a robust proxy for the reconstruction of annual mean SST in marine sediment cores.

Acknowledgements

We are grateful to various people who have worked-up or provided core-top sediments: Tjerk Veenstra, and Steven D'Hondt for Pacific core-tops recovered during the R/V Knorr expedition 195-3 (US National Science Foundation grant OCE-0752336), Isla Castañeda (Mozambique Channel), Ivan Tomberg and Roselyne Buscail (Gulf of Lion), Claudia Zell and David Hollander (Amazon Basin), Kees Booij (Berau Delta), Cindy de Jonge, Alina Stadnitskaia and Georgy Cherkashov (Kara Sea), Li Lo (Okhotsk Sea), Marcel van der Meer (Mediterranean), Laura Villanueva (Black Sea) and Zeynep Erdem (Chilean margin). We thank Allert Bijleveld for statistical advice. This research has been funded by the European Research Council (ERC) under the European 555 Union's Seventh Framework Program (FP7/2007-2013) ERC grant agreement [339206] to S.S. S.S. and J.S.S.D. receive funding from the Netherlands Earth System Science Center (NESSC) through a Gravitation grant from the Dutch ministry for Education, Culture and Science (grant number 024.002.001).

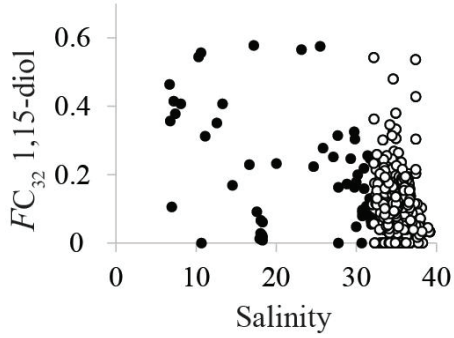

Fig. S1 Fractional abundance of the C_{32} 1,15-diol with respect to the 1,13- and 1,15-diols (cf. de Bar et al., 2016) versus salinity. The black dots reflect surface sediments with salinity <32, and the white dots reflect the 'marine' surface sediments with a salinity > 32.

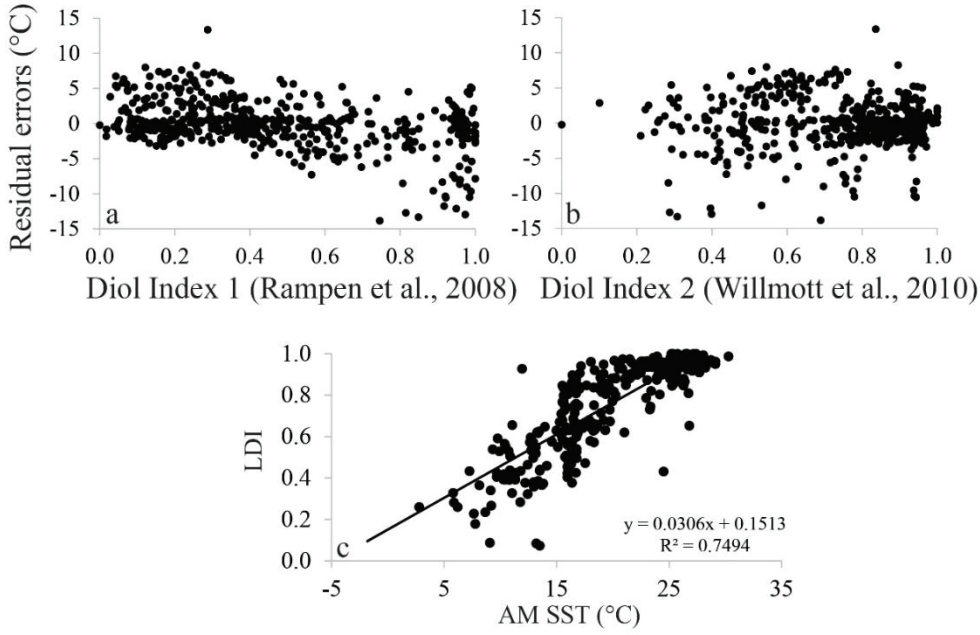

Fig. S2 Residual temperature errors based on the regression including all marine core-tops (plotted in Fig. 2) versus the two Diol Indices (1: Rampen et al., 2008 **(a)**; 2: Willmott et al., 2010 **(b)**). These cross-correlations do not reveal strong correlations although there are evidently a number of sediments with high Diol Index 1 values revealing a cold bias in the LDI temperature estimate. Panel **(c)** shows the LDI values of all marine surface sediments when excluding all core-tops where Diol Index 1 is larger than 0.90.

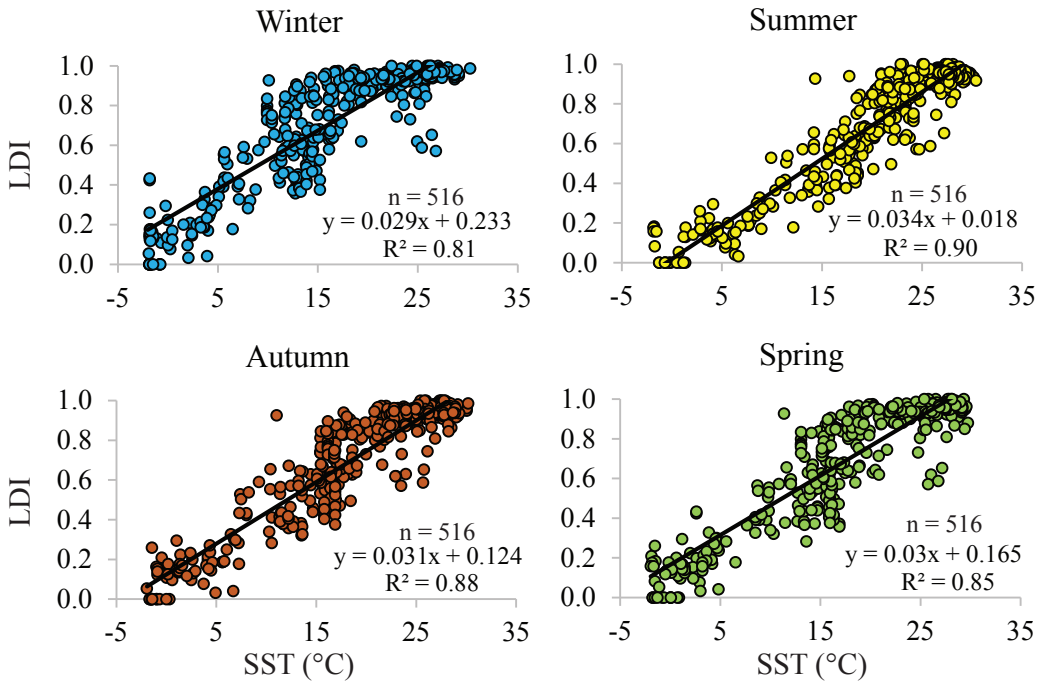

Fig. S3 The LDI versus seasonal mean SSTs (WOA13). Differences in seasonality between Northern and Southern hemisphere were taken into account.

Supplemental Table 1

Name	Region	Lat	Long	Work-up method [a]	Correction unsat vs. sat [b]	LDI	DI1 [c]	DI2 [d]	FC_{28} 1,12 [e]	Salinity [f]	AM SST [g]	Final LDI [h]
BS679	Barents Sea	76.62	34.45	2	16.1/9.1	0.16	0.94	0.75	0.03	34.05	0.13	**0.16**
BS643	Barents Sea	76.49	29.90	2	16.1/9.1	0.22	0.95	0.84	0.04	34.05	2.49	**0.22**
BS681	Barents Sea	76.43	37.17	2	16.1/9.1	0.21	0.95	0.83	0.04	33.17	2.86	**0.21**
BS677	Barents Sea	75.97	33.73	2	16.1/9.1	0.20	0.93	0.78	0.07	34.73	3.21	**0.20**
BS675	Barents Sea	75.32	33.07	2	16.1/9.1			0.81		34.74	2.45	
BS649	Barents Sea	74.53	28.57	2	16.1/9.1	0.20	0.96	0.86	0.05	34.98	4.74	**0.20**
BS671	Barents Sea	74.15	29.55	2	16.1/9.1	0.21	0.96	0.87	0.05	35.02	5.58	**0.21**
BS657	Barents Sea	72.63	25.27	2	16.1/9.1					34.84	5.53	
BS665	Barents Sea	72.17	28.40	2	16.1/9.1	0.24	0.96	0.87	0.04	34.85	5.45	**0.24**
BS692	Barents Sea	70.62	31.71	2	16.1/9.1	0.33	0.89	0.80		34.42	5.81	**0.33**
HB-4	Hudson Bay	60.62	-87.71	2	16.1/9.1					29.29	6.95	
Drammensfjord D0-5	Drammensfjord	59.63	10.42	2	16.1/9.1	0.45	0.58	0.53		14.55	12.23	
BY310 Landsort deep oxic	Baltic Sea	58.62	17.71	2	16.1/9.1	0.67	0.00	0.00		6.78	6.42	
BY31 Landsort deep	Baltic Sea	58.62	18.71	2	16.1/9.1	0.52	0.03	0.03		6.68	7.5	
BS5 Gotland deep	Baltic Sea	57.62	20.71	2	16.1/9.1	0.79	0.01	0.05		6.97	9.98	
BY5 Bornholm	Baltic Sea	55.62	15.71	2	16.1/9.1	0.58	0.07	0.09	0.00	7.41	8.44	
Mokbaai	Mokbaai	53.00	4.08	2	16.1/9.1	0.39	0.34	0.25		34.62	10.81	**0.39**
WM4 MC21	North Pacific	46.82	-125.00	2	16.1/9.1	0.43	0.78	0.72	0.02	31.89	11.98	
CB2 MC19	North Pacific	46.77	-125.83	2	16.1/9.1	0.38	0.81	0.73	0.03	32.22	12.22	**0.38**
WM5 MC20	North Pacific	46.75	-125.20	2	16.1/9.1	0.42	0.79	0.73	0.02	31.84	12.58	
CB1 MC15	North Pacific	46.75	-128.00	2	16.1/9.1	0.32	0.90	0.80	0.09	32.35	12.44	**0.32**
WM3 MC28	North Pacific	46.67	-124.63	2	16.1/9.1					31.28	11.95	
CL03-35 BC	North Atlantic	46.62	-58.71	2	16.1/9.1	0.67	0.04	0.07	0.00	31.25	6	
WM2 MC30	North Pacific	46.50	-124.38	2	16.1/9.1	0.40	0.85	0.79		27.78	11.39	
WM1 MC33	North Pacific	46.33	-124.30	2	16.1/9.1		0.88	0.79		27.78	11.39	
BS 01E-27	Black Sea	45.50	29.50	2	16.1/9.1	0.71	0.09	0.19		10.67	17.58	
BS 06E-335	Black Sea	44.50	35.00	2	16.1/9.1	0.87	0.04	0.20		18.05	14.74	
BS 04E-114	Black Sea	44.50	30.00	2	16.1/9.1	0.86	0.04	0.21	0.00	17.58	14.24	
BS 07E-1288	Black Sea	44.00	34.00	2	16.1/9.1	0.76	0.03	0.09	0.00	18.08	14.71	
BS 05E-564	Black Sea	44.00	30.50	2	16.1/9.1	0.81	0.03	0.11	0.00	17.95	15.92	
OMEX 98-5	Mediterranean	41.38	9.29	2	16.1/9.1	0.57	0.43	0.50		38.15	18.33	**0.57**
OMEX 99-15	Mediterranean	39.35	9.37	2	16.1/9.1	0.50	0.48	0.47			16.78	**0.50**
NIOP 905	Arabian Sea	10.92	51.94	2	16.1/9.1	0.96	0.67	0.98	0.01	35.76	25.76	**0.96**
NIOP 906	Arabian Sea	10.81	52.13	2	16.1/9.1	0.95	0.68	0.98	0.01	35.67	24.54	**0.95**
NIOP 907	Arabian Sea	10.80	52.25	2	16.1/9.1	0.95	0.68	0.97	0.01	35.67	24.54	**0.95**
NIOP 904	Arabian Sea	10.79	51.77	2	16.1/9.1	0.94	0.63	0.96	0.01	35.76	25.76	**0.94**
NIOP 903	Arabian Sea	10.78	51.66	2	16.1/9.1	0.97	0.61	0.98	0.01	35.65	25.85	**0.97**
NIOP 902	Arabian Sea	10.78	51.58	2	16.1/9.1					35.65	25.85	
NIOP 908	Arabian Sea	10.78	52.91	2	16.1/9.1	1.00	0.67	1.00			26.49	**1.00**
NIOP 915	Arabian Sea	10.69	53.52	2	16.1/9.1	1.00	0.66	1.00		35.81	26.62	**1.00**
NIOP 325	Arabian Sea	10.68	53.55	2	16.1/9.1	0.97	0.72	0.99		35.81	26.62	**0.97**
Cariaco Basin	Cariaco Basin	10.67	-65.60	2	16.1/9.1					35.48	26.63	
GeoB1515-2	Equatorial Atlantic	4.24	-43.67	2	16.1/9.1	1.00	0.05	1.00		35.75	27.4	**1.00**

GeoB1504-1	Equatorial Atlantic	2.29	-31.29	2	16.1/9.1	0.99	0.02	0.71		35.53	28.04	**0.99**
GeoB2202-5	Equatorial Atlantic	-8.20	-34.26	2	16.1/9.1	0.94	0.02	0.21		36.77	27.43	**0.94**
GeoB2206-1	Equatorial Atlantic	-8.56	-34.48	2	16.1/9.1	1.00				36.44	27.16	**1.00**
GeoB2207-2	Equatorial Atlantic	-8.74	-34.14	2	16.1/9.1	0.98	0.04	0.64		36.7	27.25	**0.98**
G2-85 pist 0-1	Savu Sea	-8.99	123.64	2	16.1/9.1	0.95	0.37	0.92	0.01	34.39	27.92	**0.95**
G2-85 7 0-1	Savu Sea	-9.00	123.60	2	16.1/9.1	0.95	0.54	0.96	0.01	34.33	27.82	**0.95**
G2-9 trp 0-1	Savu Sea	-9.34	123.59	2	16.1/9.1	0.97	0.19	0.89	0.00	34.44	28	**0.97**
G2-9 box 0-1	Savu Sea	-9.34	123.59	2	16.1/9.1	0.95	0.43	0.93	0.01	34.44	28	**0.95**
Peru Margin PM7	Peru Margin	-11.05	-78.07	2	16.1/9.1	0.88	0.13	0.52	0.01	35.13	19.12	**0.88**
Peru Margin PM1	Peru Margin	-11.98	-77.32	2	16.1/9.1	0.85	0.18	0.55	0.01	34.98	17.67	**0.85**
T89-41	South Atlantic	-20.80	6.00	2	16.1/9.1					35.57	21.4	
GeoB2124-1	South Atlantic	-20.96	-39.56	2	16.1/9.1	0.93	0.08	0.52		37.15	25.79	**0.93**
T89-40	South Atlantic	-21.62	6.78	2	16.1/9.1		0.65	0.91		35.8	20.1	
GeoB2107-5	South Atlantic	-27.18	-46.46	2	16.1/9.1	0.93	0.08	0.53		36.76	25.32	**0.93**
GeoB2110-1	South Atlantic	-28.65	-45.52	2	16.1/9.1	0.94	0.11	0.64		36.2	23.71	**0.94**
GeoB2830-1	South Atlantic	-29.02	-44.00	2	16.1/9.1	0.88	0.16	0.59		36.69	21.13	**0.88**
GeoB8333-1	South Atlantic	-29.12	16.61	2	16.1/9.1	0.37	0.55	0.42		34.83	12.98	**0.37**
GeoB8332-3	South Atlantic	-29.13	16.66	2	16.1/9.1	0.36	0.50	0.36	0.06	34.83	12.98	**0.36**
GeoB2112-1	South Atlantic	-29.14	-43.38	2	16.1/9.1	0.91	0.14	0.61	0.01	35.91	24.72	**0.91**
GeoB8338-1	South Atlantic	-29.50	14.32	2	16.1/9.1	0.47	0.74	0.72	0.01	35.2	17.54	**0.47**
GeoB8327-1	South Atlantic	-29.70	17.01	2	16.1/9.1	0.41	0.44	0.36		34.82	10.87	**0.41**
GeoB8329-1	South Atlantic	-29.93	17.03	2	16.1/9.1	0.39	0.52	0.41		34.87	11.33	**0.39**
GeoB8328-1	South Atlantic	-29.94	17.06	2	16.1/9.1	0.42	0.47	0.39		34.87	11.33	**0.42**
GeoB2821-2	South Atlantic	-30.45	-38.82	2	16.1/9.1	0.94	0.09	0.62		35.96	20.54	**0.94**
GeoB8325-1	South Atlantic	-30.60	17.28	2	16.1/9.1	0.38	0.54	0.42		34.87	12.96	**0.38**
GeoB2820-1	South Atlantic	-30.82	-38.44	2	16.1/9.1	0.90	0.04	0.29	0.02	35.83	19.18	**0.90**
GeoB2819-2	South Atlantic	-30.85	-38.34	2	16.1/9.1	0.95	0.04	0.45		35.83	19.18	**0.95**
GeoB8343-1	South Atlantic	-30.85	13.33	2	16.1/9.1		0.69	0.88		35.51	17.84	
GeoB2829-3	South Atlantic	-30.87	-43.43	2	16.1/9.1	0.87	0.13	0.51		35.85	23.92	**0.87**
GeoB2817-3	South Atlantic	-30.92	-38.07	2	16.1/9.1	0.96	0.03	0.43		35.88	22.53	**0.96**
GeoB8324-1	South Atlantic	-31.75	18.09	2	16.1/9.1	0.37	0.55	0.42	0.01	34.82	13.82	**0.37**
GeoB8321-1	South Atlantic	-31.86	18.12	2	16.1/9.1	0.39	0.59	0.47	0.01	34.73	13.37	**0.39**
GeoB2826-1	South Atlantic	-31.90	-40.97	2	16.1/9.1	0.82	0.22	0.57		35.99	23.4	**0.82**
GeoB6429-1	South Atlantic	-31.95	-24.25	2	16.1/9.1	0.81	0.22	0.54		35.83	19.36	**0.81**
GeoB8322-1	South Atlantic	-31.95	18.12	2	16.1/9.1	0.38	0.59	0.48	0.01	34.73	13.37	**0.38**
GeoB8313-1	South Atlantic	-32.12	15.94	2	16.1/9.1	0.63	0.77	0.85		35.5	18.27	**0.63**
GeoB8317-1	South Atlantic	-32.33	15.16	2	16.1/9.1		0.78	0.89		35.45	17.5	
GeoB8311-1	South Atlantic	-32.37	16.31	2	16.1/9.1	0.65	0.82	0.89		35.41	17.39	**0.65**
GeoB8319-1	South Atlantic	-32.50	18.08	2	16.1/9.1	0.37	0.64	0.50	0.01	34.76	13.7	**0.37**
GeoB2825-3	South Atlantic	-32.50	-41.43	2	16.1/9.1	0.96	0.26	0.90		35.86	18.06	**0.96**
GeoB6428-3	South Atlantic	-32.51	-24.25	2	16.1/9.1	0.90	0.16	0.64		35.77	21.49	**0.90**
GeoB8316-1	South Atlantic	-32.74	15.73	2	16.1/9.1	0.65	0.81	0.89		35.45	18.63	**0.65**
GeoB8315-5	South Atlantic	-32.89	15.70	2	16.1/9.1	0.67	0.82	0.90		35.47	17.86	**0.67**
GeoB8310-1	South Atlantic	-32.91	16.38	2	16.1/9.1	0.58	0.83	0.87	0.02	35.43	18	**0.58**
GeoB6427-1	South Atlantic	-33.18	-24.25	2	16.1/9.1	0.77	0.32	0.61		35.98	19.97	**0.77**

GeoB8306-1	South Atlantic	-33.74	16.84	2	16.1/9.1	0.63	0.79	0.87	0.01	35.4	18.39	**0.63**
GeoB8307-5	South Atlantic	-33.83	16.50	2	16.1/9.1	0.66	0.81	0.90		35.41	18.19	**0.66**
GeoB8308-2	South Atlantic	-33.92	16.27	2	16.1/9.1		0.68	0.88		35.41	18.19	
GeoB2813-1	South Atlantic	-35.53	-52.56	2	16.1/9.1	0.63	0.27	0.38		33.6	16.12	**0.63**
GeoB2812-3	South Atlantic	-35.60	-52.39	2	16.1/9.1	0.63	0.30	0.42		34.96	19.33	**0.63**
GeoB6420-2	South Atlantic	-37.16	-22.15	2	16.1/9.1	0.62	0.66	0.76		35.38	13.46	**0.62**
GeoB2805-1	South Atlantic	-37.61	-53.44	2	16.1/9.1	0.64	0.32	0.45		33.9	18.04	**0.64**
GeoB2701-4	South Atlantic	-37.81	-55.02	2	16.1/9.1	0.28	0.63	0.41		33.85	11.77	**0.28**
GeoB6418-3	South Atlantic	-38.43	-21.54	2	16.1/9.1	0.62	0.66	0.76		35.3	13.28	**0.62**
GeoB2703-7	South Atlantic	-38.51	-54.20	2	16.1/9.1	0.53	0.35	0.38		34.25	12.75	**0.53**
GeoB6402-9	South Atlantic	-39.74	-22.76	2	16.1/9.1	0.64	0.64	0.76		35.23	16.57	**0.64**
GeoB2708-5	South Atlantic	-41.42	-57.30	2	16.1/9.1	0.18	0.69	0.32		33.92	7.77	**0.18**
GeoB6404-3	South Atlantic	-41.51	-23.46	2	16.1/9.1	0.43	0.83	0.79		34.85	13.5	**0.43**
GeoB6406-1	South Atlantic	-42.00	-20.78	2	16.1/9.1	0.46	0.85	0.83	0.02	35.04	12.43	**0.46**
GeoB2706-6	South Atlantic	-42.37	-55.54	2	16.1/9.1	0.59	0.52	0.61		34.14	9.77	**0.59**
GeoB6414-1	South Atlantic	-44.00	-13.07	2	16.1/9.1	0.53	0.74	0.76		34.08	9.93	**0.53**
GeoB2717-8	South Atlantic	-47.16	-56.49	2	16.1/9.1	0.50	0.67	0.68		34	10.88	**0.50**
I Dougo 1	Iberian margin	41.13	-8.69	1	16.1/9.1	0.46	0.84	0.82		34.6	14.1	**0.46**
I Dougo 2	Iberian margin	41.15	-8.87	1	16.1/9.1	0.55	0.80	0.83		35.27	15.1	**0.55**
I Dougo 3	Iberian margin	41.24	-9.07	1	16.1/9.1	0.45	0.62	0.58		35.63	16.1	**0.45**
I Dougo 4	Iberian margin	41.13	-9.08	1	16.1/9.1	0.44	0.63	0.57		35.63	16.1	**0.44**
I Dougo 5	Iberian margin	41.14	-9.34	1	16.1/9.1	0.62	0.34	0.45		35.73	15.9	**0.62**
I Dougo 6	Iberian margin	41.13	-9.37	1	16.1/9.1	0.57	0.38	0.45		35.73	15.9	**0.57**
I Dougo 7	Iberian margin	41.14	-9.61	1	16.1/9.1	0.63	0.36	0.48		35.78	15.7	**0.63**
II Mondego 1	Iberian margin	40.13	-8.97	1	16.1/9.1		0.87			35.53	15.4	
II Mondego 2	Iberian margin	40.13	-9.25	1	16.1/9.1	0.50	0.61	0.61		35.7	15.8	**0.50**
II Mondego 3	Iberian margin	40.13	-9.7	1	16.1/9.1	0.69	0.25	0.42		35.84	16.5	**0.69**
II Mondego 4	Iberian margin	40.13	-9.83	1	16.1/9.1	0.63	0.36	0.49		35.84	16.4	**0.63**
II Mondego 5	Iberian margin	40.13	-9.97	1	16.1/9.1	0.58	0.39	0.47		35.84	16.4	**0.58**
III Estremadura 1	Iberian margin	38.95	-9.47	1	16.1/9.1	0.58	0.72	0.78		35.59	16.8	**0.58**
III Estremadura 2	Iberian margin	38.93	-9.48	1	16.1/9.1	0.54	0.71	0.74		35.59	16.8	**0.54**
III Estremadura 3	Iberian margin	39.03	-9.67	1	16.1/9.1	0.56	0.56	0.62		35.84	16.0	**0.56**
III Estremadura 4	Iberian margin	38.97	-9.64	1	16.1/9.1	0.51	0.56	0.57		35.82	15.9	**0.51**
III Estremadura 5	Iberian margin	39.01	-10	1	16.1/9.1	0.61	0.31	0.42		35.93	16.9	**0.61**
III Estremadura 6	Iberian margin	39.26	-10	1	16.1/9.1	0.66	0.25	0.39		36.01	16.9	**0.66**
III Estremadura 7	Iberian margin	39.34	-10.1	1	16.1/9.1	0.66	0.32	0.48		36.01	16.9	**0.66**
III Estremadura 8	Iberian margin	39.42	-10.2	1	16.1/9.1	0.66	0.36	0.52		36.01	16.9	**0.66**
IV Tagus 1	Iberian margin	38.61	-9.36	1	16.1/9.1	0.42	0.52	0.44		34.96	16.0	**0.42**
IV Tagus 2	Iberian margin	38.58	-9.36	1	16.1/9.1	0.49	0.63	0.62		34.96	16.0	**0.49**
IV Tagus 3	Iberian margin	38.65	-9.47	1	16.1/9.1	0.45	0.58	0.54		34.96	16.0	**0.45**
IV Tagus 4	Iberian margin	38.56	-9.37	1	16.1/9.1	0.40	0.54	0.44		34.96	16.0	**0.40**
IV Tagus 5	Iberian margin	38.42	-9.42	1	16.1/9.1	0.47	0.41	0.38		35.77	16.3	**0.47**
IV Tagus 6	Iberian margin	38.39	-9.43	1	16.1/9.1	0.54	0.45	0.49		35.77	16.3	**0.54**
IV Tagus 7	Iberian margin	38.23	-9.48	1	16.1/9.1	0.64	0.43	0.57		36.06	16.5	**0.64**
V Sado 1	Iberian margin	38.45	-8.99	1	16.1/9.1	0.42	0.70	0.63	0.00	35.82	16.7	**0.42**

V Sado 2	Iberian margin	38.42	-9.06	1	16.1/9.1	0.38	0.56	0.44		35.84	16.4	**0.38**
V Sado 3	Iberian margin	38.34	-9.24	1	16.1/9.1	0.53	0.46	0.49		35.84	16.4	**0.53**
V Sado 4	Iberian margin	38.33	-9.26	1	16.1/9.1	0.57	0.41	0.48		35.77	16.3	**0.57**
LCD01-3	Iceland	62.00	-16.00	2	9.7/6.5	0.05	0.99	0.78	0.20	35.22	10	
LCD03-3	Iceland	63.37	-16.63	2	9.7/6.5	0.27	0.77	0.54	0.13	34.98	9.2	
LCD05-3	Iceland	63.58	-22.14	2	9.7/6.5	0.06	0.96	0.60	0.19	34.75	7.74	
LCD06-3	Iceland	63.24	-22.56	2	9.7/6.5	0.05	0.98	0.70	0.19	35.16	8.52	
LCD07-3	Iceland	61.50	-24.17	2	9.7/6.5	0.04	0.99	0.78	0.23	35.17	8.79	
LCD08-3	Iceland	64.29	-24.15	2	9.7/6.5	0.23	0.90	0.72	0.12	35.04	7.65	
LCD10-3	Iceland	66.68	-24.18	2	9.7/6.5	0.04	0.96	0.50	0.06	34.79	5.32	**0.04**
LCD11-3	Iceland	66.63	-20.83	2	9.7/6.5	0.02	0.99	0.73	0.10	34.30	4.15	
LCD13-3	Iceland	67.50	-15.07	2	9.7/6.5	0.08	0.97	0.71	0.06	34.46	3.35	**0.08**
LCD14-3	Iceland	66.30	-13.97	2	9.7/6.5	0.03	0.97	0.56	0.06	34.61	3.92	**0.03**
S2	Australia	-41.41	148.8	2	?	0.6			?	35.4	14.99	**0.63**
S3	Australia	-39.28	148.9	2	?	0.6			?	35.57	17.32	**0.64**
S4	Australia	-37.69	150.3	2	?	0.6			?	35.54	18.5	**0.64**
S5	Australia	-35.45	150.9	2	?	0.7			?	35.54	19.74	**0.73**
S8	Australia	-28.09	154	2	?	1			?	35.43	23.68	**0.97**
S10	Australia	-39.66	154	2	?	0.9			?	35.69	17.17	**0.94**
S11	Australia	-32.29	114.1	2	?	0.9			?	35.79	20.26	**0.88**
S15	Australia	-34.77	119.6	2	?	0.8			?	35.59	19.68	**0.84**
S17	Australia	-34.68	122.7	2	?	0.8			?	35.42	20.24	**0.80**
S18	Australia	-34.25	125.3	2	?	0.8			?	35.72	16.96	**0.83**
MUC03	Australia	-36.72	136.8	2	?	0.8			?	35.53	16.96	**0.75**
S19	Australia	-37.88	139.6	2	?	0.7			?	35.33	15.42	**0.71**
S20	Australia	-39.19	142.5	2	?	0.7			?	35.39	15.28	**0.67**
S21	Australia	-42.76	144.8	2	?	0.44			?	35.21	13.53	**0.44**
64PE304-56	Mozambique Channel	-16.85	41.32	2	16.1/9.1	0.95	0.42	0.93	0.01	34.95	27.7	**0.95**
64PE304-63	Mozambique Channel	-16.59	40.36	2	16.1/9.1	0.96	0.42	0.94	0.00	34.99	27.4	**0.96**
64PE304-66	Mozambique Channel	-16.53	40.05	2	16.1/9.1	0.96	0.39	0.93		35.07	27.51	**0.96**
64PE304-68	Mozambique Channel	-16.50	40.03	2	16.1/9.1	0.95	0.39	0.93		34.77	26.17	**0.95**
LOCO 2008 1-1	Mozambique Channel	-17.25	43.10	2	16.1/9.1	0.96	0.42	0.95	0.00	34.98	25.74	**0.96**
LOCO 2008 1-2	Mozambique Channel	-17.25	43.10	2	16.1/9.1	0.97	0.44	0.96	0.00	34.98	25.74	**0.97**
LOCO 2008 2-1	Mozambique Channel	-17.27	43.16	2	16.1/9.1	0.96	0.41	0.95		35.03	26.93	**0.96**
LOCO 2008 2-2	Mozambique Channel	-17.27	43.16	2	16.1/9.1	0.96	0.40	0.94		35.03	26.93	**0.96**
LOCO 2008 3-1	Mozambique Channel	-16.92	41.60	2	16.1/9.1	0.95	0.38	0.92		35.31	27.63	**0.95**
LOCO 2008 3-2	Mozambique Channel	-16.92	41.60	2	16.1/9.1	0.92	0.45	0.91		35.31	27.63	**0.92**
LOCO 2008 4-1	Mozambique Channel	-16.56	40.13	2	16.1/9.1	0.97	0.39	0.95		35.07	27.51	**0.97**
LOCO 2008 5-1	Mozambique Channel	-16.73	40.87	2	16.1/9.1					34.99	27.14	
LOCO 2008 5-2	Mozambique Channel	-16.73	40.87	2	16.1/9.1	0.94	0.40	0.92		34.99	27.14	**0.94**
LOCO 2008 6-1	Mozambique Channel	-17.10	42.48	2	16.1/9.1					35.08	27.93	
LOCO 2008 6-2	Mozambique Channel	-17.10	42.48	2	16.1/9.1	0.97	0.40	0.95	0.01	35.08	27.93	**0.97**
VA06-399VL	Mozambique Channel	-20.97	35.75	2	16.1/9.1	0.93	0.36	0.89		34.91	25.84	**0.93**
VA02-340GR	Mozambique Channel	-19.33	36.93	2	16.1/9.1	0.94	0.45	0.92	0.01	35.01	26.93	**0.94**
VA02-408VL	Mozambique Channel	-19.19	38.17	2	16.1/9.1	0.86	0.46	0.84		34.96	26.39	**0.86**

VA02-460KL	Mozambique Channel	-17.71	38.14	2	16.1/9.1					34.91	25.52	
VA02-556GR	Mozambique Channel	-15.12	40.76	2	16.1/9.1					35.02	27.24	
VA02-404VL	Mozambique Channel	-19.26	37.41	2	16.1/9.1	0.94	0.39	0.90	0.01	35.06	26.43	**0.94**
VA02-474VL	Mozambique Channel	-17.10	39.20	2	16.1/9.1	0.94	0.42	0.92	0.01	34.86	25.87	**0.94**
VA02-65VL	Mozambique Channel	-19.77	36.67	2	16.1/9.1	0.95	0.36	0.91	0.01	35.12	25.68	**0.95**
VA02-439RKL	Mozambique Channel	-18.13	37.85	2	16.1/9.1	0.95	0.40	0.92	0.01	35.23	26.69	**0.95**
VA02-561RKL	Mozambique Channel	-16.00	41.31	2	16.1/9.1	0.92	0.44	0.89	0.01	34.99	27.66	**0.92**
VA02-373GR	Mozambique Channel	-18.60	37.23	2	16.1/9.1	0.94	0.34	0.89	0.01	34.9	26.03	**0.94**
VA06-403VL	Mozambique Channel	-20.98	35.96	2	16.1/9.1	0.95	0.46	0.94	0.01	35	26.16	**0.95**
VA02-432GR	Mozambique Channel	-18.17	37.53	2	16.1/9.1	0.96	0.19	0.84	0.01	35.08	25.7	**0.96**
VA02-41VL	Mozambique Channel	-19.62	36.93	2	16.1/9.1	0.94	0.35	0.90		34.95	26.61	**0.94**
VA02-515BGR	Mozambique Channel	-16.12	40.28	2	16.1/9.1					35.33	27.67	
VA02-545GR	Mozambique Channel	-15.59	40.63	2	16.1/9.1					34.98	26.17	
VA02-551RKL	Mozambique Channel	-15.00	41.42	2	16.1/9.1	0.91	0.41	0.87	0.01	35.21	27.69	**0.91**
VA02-555FGR	Mozambique Channel	-15.15	40.70	2	16.1/9.1	0.94	0.21	0.81	0.01	35.02	27.24	**0.94**
VA02-546	Mozambique Channel	-15.60	40.61	2	16.1/9.1					34.98	26.17	
VA02-039	Mozambique Channel	-20.00	36.72	2	16.1/9.1	0.94	0.35	0.90	0.01	35.38	26.34	**0.94**
VA02-040	Mozambique Channel	-20.00	37.07	2	16.1/9.1	0.94	0.42	0.92	0.01	35.16	26.47	**0.94**
VA02-547	Mozambique Channel	-15.60	40.59	2	16.1/9.1	0.96	0.21	0.86	0.00	34.98	26.17	**0.96**
VA02-038	Mozambique Channel	-19.89	36.58	2	16.1/9.1	0.95	0.38	0.92	0.01	35.12	25.68	**0.95**
VA02-473	Mozambique Channel	-17.15	39.14	2	16.1/9.1	0.94	0.43	0.92	0.00	34.86	25.87	**0.94**
VA02-105	Mozambique Channel	-18.95	37.13	2	16.1/9.1	0.96	0.26	0.90	0.00	35.12	26.63	**0.96**
VA02-501	Mozambique Channel	-16.61	39.78	2	16.1/9.1	0.92	0.45	0.91	0.01	34.75	26.6	**0.92**
VA02-441	Mozambique Channel	-17.90	37.77	2	16.1/9.1	0.96	0.37	0.93	0.00	34.55	25.31	**0.96**
VA02-464	Mozambique Channel	-17.38	38.64	2	16.1/9.1	0.95	0.36	0.92	0.00	34.64	26.29	**0.95**
VA02-515GR	Mozambique Channel	-16.11	40.31	2	16.1/9.1	0.93	0.32	0.87	0.01	35.33	27.67	**0.93**
VA02-515AGR	Mozambique Channel	-16.11	40.29	2	16.1/9.1	0.94	0.43	0.92	0.01	35.33	27.67	**0.94**
64PE434-2a	Gulf of Mexico	28.80	-91.33	2	16.1/9.1	0.88	0.41	0.83	0.08	29.84	24.49	
64PE434-2a	Gulf of Mexico	28.44	-91.34	2	16.1/9.1	0.93	0.31	0.86	0.06	33.76	24.9	**0.93**
64PE434-2a	Gulf of Mexico	27.74	-91.23	2	16.1/9.1	0.96	0.22	0.86	0.04	35.50	25.6	**0.96**
64PE434-2a	Gulf of Mexico	28.01	-91.28	2	16.1/9.1	0.96	0.21	0.87	0.03	34.76	24.92	**0.96**
64PE434-2a	Gulf of Mexico	27.91	-91.27	2	16.1/9.1	0.94	0.22	0.80	0.03	34.78	25.48	**0.94**
64PE434-2a	Gulf of Mexico	26.97	-91.35	2	16.1/9.1	0.96	0.19	0.84	0.03	34.86	25.75	**0.96**
10	Pakistan	24.86	64.3	2	16.1/9.1	0.95	0.61	0.97	0.01	36.53	25.59	**0.95**
12	Pakistan	24.86	64.3	2	16.1/9.1	0.94	0.50	0.94	0.02	36.53	25.59	**0.94**
18	Pakistan	24.96	64.3	2	16.1/9.1	0.95	0.55	0.96	0.04	36.53	25.59	**0.95**
20	Pakistan	24.85	64.3	2	16.1/9.1	0.95	0.51	0.95	0.01	36.53	25.59	**0.95**
23	Pakistan	24.88	64.29	2	16.1/9.1	0.96	0.61	0.97	0.01	36.53	25.59	**0.96**
24	Pakistan	24.78	64.31	2	16.1/9.1	0.94	0.59	0.96	0.04	36.53	25.59	**0.94**
28	Pakistan	24.69	64.25	2	16.1/9.1	0.95	0.50	0.95	0.02	36.64	26.91	**0.95**
29	Pakistan	24.81	64.33	2	16.1/9.1	0.95	0.62	0.97	0.01	36.53	25.59	**0.95**
34	Pakistan	24.9	64.29	2	16.1/9.1	0.96	0.62	0.97	0.01	36.53	25.59	**0.96**
39KG	Pakistan	24.83	65.92	2	16.1/9.1	0.97	0.39	0.95	0.01	36.53	25.61	**0.97**
87	Pakistan	23.59	64.22	2	16.1/9.1	0.92	0.63	0.95	0.03	36.4	26.79	**0.92**
95	Pakistan	22.49	65.65	2	16.1/9.1	0.93	0.58	0.95	0.03	36.42	27.69	**0.93**

99	Pakistan	22.93	66.35	2	16.1/9.1	0.93	0.61	0.95	0.04	36.78	27.3	**0.93**
107	Pakistan	23.06	66.51	2	16.1/9.1	0.95	0.49	0.95	0.03	36.68	27.91	**0.95**
112	Pakistan	23.12	66.5	2	16.1/9.1	0.96	0.38	0.94	0.01	36.61	26.35	**0.96**
113	Pakistan	23.19	66.61	2	16.1/9.1	0.97	0.37	0.95	0.02	36.68	27.91	**0.97**
115	Pakistan	22.73	66.19	2	16.1/9.1	0.96	0.31	0.93	0.02	36.58	27.18	**0.96**
120	Pakistan	23.47	66.89	2	16.1/9.1	0.97	0.37	0.95	0.02	36.39	26.72	**0.97**
124	Pakistan	23.28	66.71	2	16.1/9.1	0.97	0.39	0.96	0.02	36.56	26.2	**0.97**
129	Pakistan	23.24	66.67	2	16.1/9.1	0.97	0.33	0.94	0.02	36.68	27.91	**0.97**
135	Pakistan	23.18	66.49	2	16.1/9.1	0.96	0.43	0.95	0.04	36.61	26.35	**0.96**
142	Pakistan	24.78	65.83	2	16.1/9.1	0.95	0.54	0.96	0.01	36.53	25.61	**0.95**
143	Pakistan	24.75	65.74	2	16.1/9.1	0.95	0.55	0.96	0.02	36.51	26.39	**0.95**
144	Pakistan	24.61	65.59	2	16.1/9.1	0.95	0.48	0.95	0.02	36.51	26.39	**0.95**
153	Pakistan	24.83	65.91	2	16.1/9.1	0.95	0.49	0.95	0.03	36.53	25.61	**0.95**
1	Pakistan	25.41	65.61	2	16.1/9.1	0.96	0.48	0.96		36.47	25.14	**0.96**
2	Pakistan	25.23	66	2	16.1/9.1	0.91	0.53	0.92	0.02	36.55	25.48	**0.91**
3	Pakistan	25.1	66	2	16.1/9.1	0.95	0.44	0.94	0.02	36.55	25.48	**0.95**
8	Pakistan	24.17	66	2	16.1/9.1	0.96	0.48	0.96	0.03	36.46	26.06	**0.96**
12	Pakistan	24.76	66.68	2	16.1/9.1	0.95	0.53	0.95	0.02	36.48	23.48	**0.95**
16	Pakistan	24.57	67	2	16.1/9.1	0.88	0.60	0.92		36.58	25.09	**0.88**
20	Pakistan	24.21	67.02	2	16.1/9.1	0.85	0.39	0.78		36.5	25.34	**0.85**
28	Pakistan	23.26	66.92	2	16.1/9.1	0.97	0.41	0.96	0.03	36.39	26.72	**0.97**
29	Pakistan	22.92	66.9	2	16.1/9.1	0.95	0.59	0.96	0.06	36.72	26.53	**0.95**
30	Pakistan	22.92	67.01	2	16.1/9.1	0.96	0.49	0.96	0.04	36.32	27.21	**0.96**
33	Pakistan	23.23	67.63	2	16.1/9.1	0.96	0.27	0.90	0.01	36.32	25.9	**0.96**
MC1	Pakistan	24.75	65.77	2	16.1/9.1	0.95	0.53	0.95	0.03	36.43	26.49	**0.95**
MC2	Pakistan	24.63	66.08	2	16.1/9.1	0.96	0.44	0.95	0.03	36.58	26.12	**0.96**
MC3	Pakistan	24.63	66.08	2	16.1/9.1	0.96	0.40	0.95	0.02	36.58	26.12	**0.96**
MC4	Pakistan	24.64	66.07	2	16.1/9.1	0.97	0.39	0.95	0.01	36.58	26.12	**0.97**
MC5	Pakistan	24.64	66.05	2	16.1/9.1	0.95	0.40	0.93	0.02	36.58	26.12	**0.95**
MC6	Pakistan	24.65	66.02	2	16.1/9.1	0.96	0.39	0.93	0.02	36.58	26.12	**0.96**
HI-A	Gulf of Lion	42.57	3.65	2	16.1/9.1	0.87	0.28	0.72	0.03	37.93	16.60	**0.87**
HI-B	Gulf of Lion	42.44	3.85	2	16.1/9.1	0.84	0.25	0.62	0.03	37.97	16.48	**0.84**
HI-E	Gulf of Lion	42.44	3.53	2	16.1/9.1					37.87	16.55	
HI-F	Gulf of Lion	42.37	3.82	2	16.1/9.1	0.84	0.25	0.63	0.03	37.97	16.48	**0.84**
HI-L	Gulf of Lion	42.08	4.67	2	16.1/9.1	0.76	0.13	0.31		38.29	16.74	**0.76**
HI-M	Gulf of Lion	42.15	3.58	2	16.1/9.1	0.84	0.29	0.69	0.04	37.72	17.01	**0.84**
HII-C'	Gulf of Lion	42.36	4.20	2	16.1/9.1	0.80	0.25	0.58	0.02	38.08	16.01	**0.80**
HII-G'	Gulf of Lion	42.31	3.61	2	16.1/9.1	0.85	0.34	0.74	0.05	37.87	16.55	**0.85**
HII-H'	Gulf of Lion	42.22	3.82	2	16.1/9.1	0.86	0.29	0.71	0.04	38	16.34	**0.86**
HII-I'	Gulf of Lion	42.22	4.27	2	16.1/9.1	0.83	0.18	0.52	0.02	38.19	17.04	**0.83**
HII-L'	Gulf of Lion	42.08	4.67	2	16.1/9.1	0.81	0.20	0.52	0.03	38.29	16.74	**0.81**
HII-N'	Gulf of Lion	42.13	3.78	2	16.1/9.1	0.86	0.32	0.74	0.04	38	16.34	**0.86**
HII-O'	Gulf of Lion	42.12	4.04	2	16.1/9.1	0.91	0.22	0.73	0.01	38.1	17.07	**0.91**
HII-PLA	Gulf of Lion	43.02	5.20	2	16.1/9.1	0.88	0.17	0.59	0.03	37.87	16.74	**0.88**
HII-MIN	Gulf of Lion	40.49	4.03	2	16.1/9.1	0.84	0.21	0.58	0.02	37.86	18.30	**0.84**

MT34bis	Gulf of Lion	42.69	3.33	2	16.1/9.1	0.88	0.30	0.76	0.05	37.77	16.61	**0.88**
MT37bis	Gulf of Lion	42.58	3.21	2	16.1/9.1	0.81	0.35	0.70	0.06	37.43	15.81	**0.81**
MT353	Gulf of Lion	42.71	3.15	2	16.1/9.1	0.74	0.33	0.58	0.05	37.43	15.81	**0.74**
MT10	Gulf of Lion	43.35	4.42	2	16.1/9.1					36.97	16.48	
MT11	Gulf of Lion	43.16	4.33	2	16.1/9.1					37.17	17.00	
MT14	Gulf of Lion	43.38	4.20	2	16.1/9.1	0.84	0.20	0.58	0.03	37.2	16.42	**0.84**
MT17	Gulf of Lion	43.03	4.21	2	16.1/9.1					37.67	16.64	
MT20	Gulf of Lion	43.27	3.41	2	16.1/9.1	0.79	0.20	0.48		37.4	22.96	**0.79**
MT24	Gulf of Lion	43.17	3.67	2	16.1/9.1					37.49	16.57	
MT25	Gulf of Lion	43.05	3.85	2	16.1/9.1	0.88	0.18	0.61	0.03	37.61	16.47	**0.88**
MT31	Gulf of Lion	42.82	3.73	2	16.1/9.1					37.74	16.75	
MT33	Gulf of Lion	43.03	3.15	2	16.1/9.1					37.07	16.43	
T2	Gulf of Lion	42.72	3.11	2	16.1/9.1	0.74	0.36	0.62		37.43	15.81	**0.74**
T4	Gulf of Lion	42.69	3.13	2	16.1/9.1					37.43	15.81	
T5	Gulf of Lion	42.69	3.18	2	16.1/9.1					37.43	15.81	
T6	Gulf of Lion	42.66	3.13	2	16.1/9.1	0.74	0.38	0.64	0.07	37.43	15.81	**0.74**
BT-B	Gulf of Lion	42.66	4.93	2	16.1/9.1					38.12	16.13	
BT-C	Gulf of Lion	42.72	4.78	2	16.1/9.1					38.12	16.13	
BT-D	Gulf of Lion	42.79	4.74	2	16.1/9.1					37.41	17.36	
BT-F	Gulf of Lion	42.88	4.73	2	16.1/9.1					37.41	17.36	
BT-G	Gulf of Lion	42.90	4.71	2	16.1/9.1					37.41	17.36	
Riomar B	Gulf of Lion	43.30	4.84	2	16.1/9.1	0.77	0.16	0.39	0.06	34.94	15.51	**0.77**
Riomar C	Gulf of Lion	43.27	4.78	2	16.1/9.1					34.94	15.51	
Riomar E	Gulf of Lion	43.22	4.70	2	16.1/9.1					36.87	17.04	
Riomar F	Gulf of Lion	43.17	4.65	2	16.1/9.1					36.87	17.04	
Riomar G	Gulf of Lion	43.31	4.79	2	16.1/9.1					34.94	15.51	
Riomar H	Gulf of Lion	43.27	4.82	2	16.1/9.1	0.85	0.16	0.51	0.03	34.94	15.51	**0.85**
Riomar I	Gulf of Lion	43.27	4.88	2	16.1/9.1					34.94	15.51	
Riomar J	Gulf of Lion	43.27	4.89	2	16.1/9.1					34.94	15.51	
Riomar K	Gulf of Lion	43.30	4.85	2	16.1/9.1	0.68	0.12	0.23	0.06	34.94	15.51	**0.68**
Riomar L	Gulf of Lion	43.30	4.88	2	16.1/9.1					34.94	15.51	
Riomar M	Gulf of Lion	43.17	4.73	2	16.1/9.1					36.87	17.04	
Riomar N	Gulf of Lion	43.30	4.80	2	16.1/9.1					34.94	15.51	
Riomar T	Gulf of Lion	43.32	4.87	2	16.1/9.1	0.59	0.00	0.00		34.94	15.51	**0.59**
Riomar Pbis	Gulf of Lion	43.41	4.42	2	16.1/9.1					36.97	16.48	
Riomar R2	Gulf of Lion	43.24	4.88	2	16.1/9.1	0.90	0.12	0.55		36.51	16.42	**0.90**
KNR BC 3	Amazon Basin	4.46	-48.61	5	16.1/9.1	0.99			0.00	36.12	27.27	**0.99**
KNR BC 14	Amazon Basin	4.04	-48.35	5	16.1/9.1	0.98			0.00	35.81	27.06	**0.98**
KNR BC17	Amazon Basin	3.96	-48.54	5	16.1/9.1	0.98				35.92	26.88	**0.98**
KNR BC 24	Amazon Basin	3.95	-48.61	5	16.1/9.1	0.98				35.92	26.88	**0.98**
KNR MC 28	Amazon Basin	3.68	-49.06	5	16.1/9.1					35.92		
KNR BC 44	Amazon Basin	3.78	-48.17	5	16.1/9.1	0.97			0.00	35.85	27.11	**0.97**
KNR BC 50	Amazon Basin	3.07	-47.64	5	16.1/9.1	0.98			0.00	35.71	27.18	**0.98**
KNR BC 55	Amazon Basin	3.07	-47.64	5	16.1/9.1	0.98				35.71	27.18	**0.98**
KNR BC 61	Amazon Basin	2.85	-47.74	5	16.1/9.1					35.99	27.35	

KNR BC 66	Amazon Basin	2.57	-47.85	5	16.1/9.1					35.96	27.25	
KNR BC 69	Amazon Basin	2.09	-48.05	5	16.1/9.1					36.4	27.82	
KNR BC 71	Amazon Basin	3.39	-46.25	5	16.1/9.1	0.98				36.1	27.64	**0.98**
KNR BC 75	Amazon Basin	1.64	-45.36	5	16.1/9.1					35.85	27.32	
KNR BC 80	Amazon Basin	0.66	-44.35	5	16.1/9.1					35.82	27.48	
KNR BC 90	Amazon Basin	-1.03	-42.74	5	16.1/9.1					36.33	26.89	
1C	Berau delta	2.18	117.68	2	16.1/9.1						27.70	
2A	Berau delta	2.15	117.91	2	16.1/9.1						29.12	
2B	Berau delta	2.20	117.86	2	16.1/9.1						29.12	
3A	Berau delta	2.08	117.90	2	16.1/9.1						29.12	
4B	Berau delta	2.20	118.04	2	16.1/9.1						29.12	
8A	Berau delta	2.17	117.97	2	16.1/9.1						29.12	
8B	Berau delta	2.12	117.81	2	16.1/9.1						29.12	
10A	Berau delta	2.10	118.05	2	16.1/9.1						29.12	
11A	Berau delta	2.03	118.03	2	16.1/9.1						29.12	
11B	Berau delta	1.97	118.13	2	16.1/9.1					33.97	28.23	
12A	Berau delta	1.94	118.04	2	16.1/9.1					33.97	28.23	
12B	Berau delta	1.84	118.12	2	16.1/9.1					33.97	28.23	
13B	Berau delta	1.89	118.00	2	16.1/9.1					33.97	28.23	
15B	Berau delta	2.02	117.84	2	16.1/9.1						29.12	
18A	Berau delta	1.94	118.05	2	16.1/9.1					33.97	28.23	
20A	Berau delta	1.97	118.17	2	16.1/9.1	0.93	0.22	0.79		33.97	28.23	**0.93**
21A	Berau delta	1.98	118.22	2	16.1/9.1	0.95	0.17	0.81		33.97	28.23	**0.95**
21B	Berau delta	1.98	118.22	2	16.1/9.1	0.94	0.17	0.78		33.97	28.23	**0.94**
22A	Berau delta	2.00	118.27	2	16.1/9.1	0.95	0.15	0.77		33.04	29.12	**0.95**
23B	Berau delta	2.01	118.31	2	16.1/9.1	0.96	0.13	0.79		33.04	29.12	**0.96**
23C	Berau delta	2.01	118.32	2	16.1/9.1					33.04	29.12	
24A	Berau delta	2.03	118.38	2	16.1/9.1					33.04	29.12	
25B	Berau delta	2.05	118.44	2	16.1/9.1					33.04	29.12	
26B	Berau delta	2.07	118.49	2	16.1/9.1					33.04	29.12	
27A	Berau delta	2.06	118.47	2	16.1/9.1					33.04	29.12	
28A	Berau delta	2.05	118.45	2	16.1/9.1					33.04	29.12	
29C	Berau delta	2.05	118.45	2	16.1/9.1					33.04	29.12	
32A	Berau delta	1.63	118.20	2	16.1/9.1	0.95	0.18	0.82		33.97	28.23	**0.95**
33A	Berau delta	1.66	118.23	2	16.1/9.1	0.96	0.16	0.82		33.97	28.23	**0.96**
34A	Berau delta	1.68	118.26	2	16.1/9.1	0.94	0.16	0.76		33.97	28.23	**0.94**
36B	Berau delta	1.73	118.35	2	16.1/9.1	0.96	0.12	0.74		33.97	28.23	**0.96**
37C	Berau delta	1.75	118.37	2	16.1/9.1	0.96	0.12	0.76		33.97	28.23	**0.96**
38A	Berau delta	1.77	118.40	2	16.1/9.1	0.96	0.09	0.71		33.97	28.23	**0.96**
39B	Berau delta	1.79	118.43	2	16.1/9.1	0.95	0.09	0.68		33.97	28.23	**0.95**
40A	Berau delta	1.81	118.46	2	16.1/9.1					33.97	28.23	
41A	Berau delta	1.83	118.49	2	16.1/9.1	0.96	0.10	0.75	0.00	33.97	28.23	**0.96**
42A	Berau delta	1.85	118.52	2	16.1/9.1					33.97	28.23	
43C	Berau delta	1.86	118.54	2	16.1/9.1	0.97	0.11	0.79	0.01	33.97	28.23	**0.97**
44A	Berau delta	1.87	118.55	2	16.1/9.1	0.96	0.08	0.66	0.04	33.97	28.23	**0.96**

KS SS1	Kara Sea	77.22	78.09	5	16.1/9.1	0.26	0.24	0.10	0.03	32.20	2.8	**0.26**
KS SS2	Kara Sea	75.84	68.91	5	16.1/9.1	0.29	0.29	0.14		17.21	1.8	
KS SS4	Kara Sea	78.48	72.80	5	16.1/9.1					20.23	-0.7	
KS SS5	Kara Sea	74.29	78.62	5	16.1/9.1	0.27	0.34	0.16	0.02	10.62	2.81	
KS SS6	Kara Sea	75.68	83.20	5	16.1/9.1	0.29	0.19	0.09		25.48	1.95	
KS SS7	Kara Sea	76.09	84.86	5	16.1/9.1	0.29	0.17	0.08		23.17	-0.05	
KS SS8	Kara Sea	73.56	73.30	5	16.1/9.1	0.30	0.47	0.28		10.32	2.37	
KS SS9	Kara Sea	73.84	75.09	5	16.1/9.1	0.21	0.86	0.61	0.03	13.31	2.13	
55-14-2	Okhotsk Sea	56.07	153.68	2	16.1/9.1	0.09	0.92	0.53	0.12	32.66	12.5	
55-17-2	Okhotsk Sea	56.31	146.84	2	16.1/9.1	0.03	0.95	0.40	0.29	32.92	11.12	
55-18-2	Okhotsk Sea	56.34	145.31	2	16.1/9.1	0.02	0.97	0.40	0.33	32.91	11.49	
55-23-2	Okhotsk Sea	53.01	146.51	2	16.1/9.1	0.08	0.82	0.29	0.28	32.03	13.2	
55-25-2	Okhotsk Sea	52.56	146.51	2	16.1/9.1	0.07	0.85	0.31	0.30	32.91	13.5	
55-27-2	Okhotsk Sea	52.00	144.56	2	16.1/9.1	0.09	0.81	0.28	0.20	32.18	9.08	
55-30-2	Okhotsk Sea	52.00	144.94	2	16.1/9.1	0.05	0.92	0.37	0.30	31.68	8.62	
55-34-2	Okhotsk Sea	48.81	147.87	2	16.1/9.1	0.26	0.56	0.31	0.17	32.3	6.2	
55-36-2	Okhotsk Sea	48.58	146.36	2	16.1/9.1	0.23	0.57	0.29	0.17	32.31	8.67	
55-44-2	Okhotsk Sea	47.52	145.16	2	16.1/9.1	0.28	0.47	0.26	0.10	32.21	5.87	
55-46-2	Okhotsk Sea	45.51	144.54	2	16.1/9.1	0.42	0.41	0.34	0.05	32.47	9.68	**0.42**
55-47-2	Okhotsk Sea	45.52	144.47	2	16.1/9.1	0.43	0.35	0.29	0.05	32.19	7.27	**0.43**
HCC_1_0-1A	Tropical Atlantic	15.02	-30.56	2	16.1/9.1	0.97	0.10	0.76	0.01	35.90	25.79	**0.97**
HCC_1_0-1B	Tropical Atlantic	15.02	-30.56	2	16.1/9.1	0.97	0.08	0.75	0.01	35.90	25.79	**0.97**
HCC_1_0-1C	Tropical Atlantic	15.02	-30.56	2	16.1/9.1	0.97	0.10	0.76	0.01	35.90	25.79	**0.97**
HCC_3_0-1A	Tropical Atlantic	13.16	-36.21	2	16.1/9.1	0.98	0.08	0.79	0.00	35.90	25.21	**0.98**
HCC_3_0-1B	Tropical Atlantic	13.16	-36.21	2	16.1/9.1	1.00	0.07			35.90	25.21	**1.00**
HCC_3_0-1C	Tropical Atlantic	13.16	-36.21	2	16.1/9.1	0.98	0.07	0.79	0.00	35.90	25.21	**0.98**
HCC_5_0-1A	Tropical Atlantic	10.83	-40.47	2	16.1/9.1	0.98	0.12	0.85	0.00	36.37	26.6	**0.98**
HCC_5_0-1B	Tropical Atlantic	10.83	-40.47	2	16.1/9.1	0.98	0.12	0.86	0.00	36.37	26.6	**0.98**
HCC_5_0-1C	Tropical Atlantic	10.83	-40.47	2	16.1/9.1	0.97	0.11	0.82	0.00	36.37	26.6	**0.97**
HCC_7_0-1A	Tropical Atlantic	7.52	-44.28	2	16.1/9.1	0.98	0.12	0.88	0.00	36.13	27.54	**0.98**
HCC_7_0-1B	Tropical Atlantic	7.52	-44.28	2	16.1/9.1	0.98	0.13	0.87	0.00	36.13	27.54	**0.98**
HCC_7_0-1C	Tropical Atlantic	7.52	-44.28	2	16.1/9.1	0.98	0.12	0.87	0.00	36.13	27.54	**0.98**
HCC_8_0-1A	Tropical Atlantic	6.49	-45.45	2	16.1/9.1	0.98	0.11	0.83		35.99	27.68	**0.98**
HCC_8_0-1B	Tropical Atlantic	6.49	-45.45	2	16.1/9.1	0.98	0.13	0.87	0.00	35.99	27.68	**0.98**
HCC_8_0-1C	Tropical Atlantic	6.49	-45.45	2	16.1/9.1	0.98	0.13	0.88	0.00	35.99	27.68	**0.98**
HCC_9_0-1A	Tropical Atlantic	5.60	-46.40	2	16.1/9.1	0.98	0.15	0.87	0.00	36.00	27.52	**0.98**
HCC_9_0-1B	Tropical Atlantic	5.60	-46.40	2	16.1/9.1	0.98	0.13	0.87	0.00	36.00	27.52	**0.98**
HCC_9_0-1C	Tropical Atlantic	5.60	-46.40	2	16.1/9.1	0.98	0.14	0.87	0.00	36.00	27.52	**0.98**
HCC_10_0-1A	Tropical Atlantic	6.68	-47.49	2	16.1/9.1	0.98	0.15	0.88	0.00	35.94	27.75	**0.98**
HCC_10_0-1B	Tropical Atlantic	6.68	-47.49	2	16.1/9.1	0.98	0.14	0.89	0.00	35.94	27.75	**0.98**
HCC_10_0-1C	Tropical Atlantic	6.68	-47.49	2	16.1/9.1	0.97	0.17	0.88	0.00	35.94	27.75	**0.97**
HCC_11_0-1C	Tropical Atlantic	5.53	-51.49	2	16.1/9.1					33.06	27.61	
HCC_12_0-1A	Tropical Atlantic	6.07	-52.46	2	16.1/9.1	0.98	0.11	0.84		34.84	27.38	**0.98**
HCC_12_0-1B	Tropical Atlantic	6.07	-52.46	2	16.1/9.1	0.98	0.10	0.84		34.84	27.38	**0.98**
HCC_12_0-1C	Tropical Atlantic	6.07	-52.46	2	16.1/9.1	0.98	0.10	0.83		34.84	27.38	**0.98**

HCC_13_0-1A	Tropical Atlantic	7.60	-53.02	2	16.1/9.1	0.97	0.16	0.87		30.77	28.02	
HCC_13_0-1B	Tropical Atlantic	7.60	-53.02	2	16.1/9.1	0.97	0.16	0.88	0.00	30.77	28.02	
HCC_13_0-1C	Tropical Atlantic	7.60	-53.02	2	16.1/9.1	0.98	0.15	0.88	0.00	30.77	28.02	
HCC_14_0-1A	Tropical Atlantic	9.53	-51.32	2	16.1/9.1	0.97	0.20	0.90	0.01	36.26	27.34	**0.97**
HCC_14_0-1B	Tropical Atlantic	9.53	-51.32	2	16.1/9.1	0.97	0.20	0.89	0.01	36.26	27.34	**0.97**
HCC_14_0-1C	Tropical Atlantic	9.53	-51.32	2	16.1/9.1	0.98	0.17	0.89	0.00	36.26	27.34	**0.98**
HCC_16_0-1A	Tropical Atlantic	10.22	-51.88	2	16.1/9.1	0.97	0.18	0.89	0.00	34.51	27.36	**0.97**
HCC_16_0-1B	Tropical Atlantic	10.22	-51.88	2	16.1/9.1	0.97	0.18	0.90	0.00	34.51	27.36	**0.97**
HCC_16_0-1C	Tropical Atlantic	10.22	-51.88	2	16.1/9.1	0.97	0.16	0.87	0.00	34.51	27.36	**0.97**
HCC_17_0-1A	Tropical Atlantic	9.90	-53.27	2	16.1/9.1	0.97	0.18	0.87	0.00	35.62	26.96	**0.97**
HCC_17_0-1B	Tropical Atlantic	9.90	-53.27	2	16.1/9.1	0.97	0.16	0.87	0.00	35.62	26.96	**0.97**
HCC_20_0-1A	Tropical Atlantic	11.27	-54.15	2	16.1/9.1	0.97	0.14	0.86	0.00	34.59	26.92	**0.97**
HCC_20_0-1B	Tropical Atlantic	11.27	-54.15	2	16.1/9.1	0.97	0.14	0.85	0.00	34.59	26.92	**0.97**
HCC_20_0-1C	Tropical Atlantic	11.27	-54.15	2	16.1/9.1	0.97	0.16	0.87	0.00	34.59	26.92	**0.97**
HCC_21_0-1A	Tropical Atlantic	13.02	-54.67	2	16.1/9.1	0.97	0.13	0.81	0.00	34.10	27.4	**0.97**
HCC_21_0-1B	Tropical Atlantic	13.02	-54.67	2	16.1/9.1	0.97	0.11	0.81		34.10	27.4	**0.97**
HCC_21_0-1C	Tropical Atlantic	13.02	-54.67	2	16.1/9.1	0.97	0.08	0.73	0.01	34.10	27.4	**0.97**
HCC_22_0-1A	Tropical Atlantic	14.80	-55.18	2	16.1/9.1					34.94	27.35	
HCC_22_0-1B	Tropical Atlantic	14.80	-55.18	2	16.1/9.1	0.97	0.08	0.76	0.00	34.94	27.35	**0.97**
HCC_22_0-1C	Tropical Atlantic	14.80	-55.18	2	16.1/9.1					34.94	27.35	
HCC_23_0-1A	Tropical Atlantic	15.79	-57.05	2	16.1/9.1	0.97	0.11	0.81	0.00	35.66	27.37	**0.97**
HCC_23_0-1B	Tropical Atlantic	15.79	-57.05	2	16.1/9.1	0.97	0.10	0.79	0.00	35.66	27.37	**0.97**
HCC_23_0-1C	Tropical Atlantic	15.79	-57.05	2	16.1/9.1	0.97	0.13	0.84	0.01	35.66	27.37	**0.97**
MUC@M1 surface	Tropical Atlantic	12.00	-23.00	2	16.1/9.1	0.97	0.15	0.84	0.00	35.89	26.19	**0.97**
MUC@M2 surface	Tropical Atlantic	13.81	-37.82	2	16.1/9.1	0.97	0.05	0.63		36.51	27.09	**0.97**
MUC@M3 surface	Tropical Atlantic	12.39	-38.63	2	16.1/9.1	0.98	0.06	0.78		35.7	25.13	**0.98**
MUC@M4 surface	Tropical Atlantic	12.06	-49.19	2	16.1/9.1	0.98	0.05	0.70		36.27	26.27	**0.98**
MUC@M5 surface	Tropical Atlantic	12.02	-57.04	2	16.1/9.1	0.95	0.09	0.68		34.76	27.52	**0.95**
13M0-1 surface	Tropical Atlantic	13.53	-21.92	2	16.1/9.1	0.95	0.53	0.96	0.00	36.31	28.96	**0.95**
13M1a-2 surface	Tropical Atlantic	13.73	-31.71	2	16.1/9.1	0.98	0.08	0.79		36.03	26.57	**0.98**
NiCycle III S.1 slice 1	North Sea	55.17	3.15	2	16.1/9.1	0.55	0.51	0.56		34.84	10.46	**0.55**
NiCycle III S.2 slice 1	North Sea	54.72	3.68	2	16.1/9.1	0.53	0.48	0.51		34.7	10.74	**0.53**
NiCycle III S.3 slice 1	North Sea	54.40	4.35	2	16.1/9.1	0.56	0.54	0.61	0.01	34.57	10.39	**0.56**
NiCycle III S.4 slice 1	North Sea	54.13	4.33	2	16.1/9.1	0.44	0.63	0.57	0.02	34.55	10.87	**0.44**
NiCycle III S.5 slice 1	North Sea	53.92	4.60	2	16.1/9.1	0.39	0.64	0.53		34.41	10.43	**0.39**
NiCycle III S.6 slice 1	North Sea	53.77	4.77	2	16.1/9.1					34.41	11.11	
NiCycle III S.7 slice 1	North Sea	53.40	5.15	2	16.1/9.1					31.53	11.12	
1 MC4 0-5	Equatorial Pacific	1.80	-86.18	2	16.1/9.1	0.94	0.32	0.88	0.01	33.75	26.31	**0.94**
2 MC7 0-5	Equatorial Pacific	-4.23	-92.95	2	16.1/9.1	0.74	0.69	0.86	0.03	34.8	23.35	**0.74**
3A MC1 0-5	Equatorial Pacific	-0.04	-105.42	2	16.1/9.1	0.80	0.73	0.92	0.03	34.69	24.17	**0.80**
4 MC6 0-5	Equatorial Pacific	0.12	-112.60	2	16.1/9.1	0.73	0.83	0.93	0.03	34.51	23.29	**0.73**
5 MC3 0-5	Equatorial Pacific	0.07	-123.02	2	16.1/9.1	0.62	0.91	0.94	0.02	34.86	24.57	**0.62**
6 MC2 0-5	Equatorial Pacific	0.04	-130.88	2	16.1/9.1	0.57	0.92	0.94	0.03	35.24	25.19	**0.57**
7 MC7 0-5	Equatorial Pacific	0.00	-139.32	2	16.1/9.1	0.59	0.92	0.94	0.03	35.21	25.87	**0.59**
8 MC1 0-5	Equatorial Pacific	0.01	-147.78	2	16.1/9.1	0.65	0.89	0.94	0.03	35.17	26.79	**0.65**

9 G3 S1 0-5	North Pacific	15.12	-149	2	16.1/9.1	0.95	0.14	0.76	0.01	34.95	25.90	**0.95**
10 G2 S1 0-5	North Pacific	20.68	-143	2	16.1/9.1	0.96	0.07	0.66	0.01	35.00	21.63	**0.96**
11 MC4 0-5	North Pacific	30.35	-158	2	16.1/9.1	0.90	0.12	0.54	0.02	35.12	22.14	**0.90**
407_1_0-0.5A	Western Medit.	34.75	14.18	2	16.1/9.1	0.93	0.07	0.51	0.01	37.63	20.53	**0.93**
407_2_0-0.5A	Western Medit.	36.99	13.47	2	16.1/9.1	0.88	0.16	0.59	0.02	37.64	18.90	**0.88**
407_3_0-0.5A	Western Medit.	37.98	11.50	2	16.1/9.1	0.81	0.09	0.30	0.01	37.30	19.04	**0.81**
407_4_0-0.5A	Western Medit.	38.49	8.99	2	16.1/9.1	0.92	0.13	0.64	0.01	37.91	18.38	**0.92**
407_6_0-0.5A	Western Medit.	38.75	3.75	2	16.1/9.1	0.85	0.15	0.49	0.01	37.30	19.15	**0.85**
407_7_0-0.5A	Western Medit.	37.99	0.74	2	16.1/9.1	0.85	0.17	0.53	0.01	37.43	18.91	**0.85**
407_8_0-0.5A	Western Medit.	36.74	-1.47	2	16.1/9.1	0.83	0.25	0.62	0.02	36.99	18.83	**0.83**
407_9_0-0.5A	Western Medit.	36.32	-3.97	2	16.1/9.1	0.68	0.36	0.55	0.01	36.69	17.90	**0.68**
407_10_0-0.5A	Western Medit.	36.25	-6.49	2	16.1/9.1	0.75	0.18	0.40	0.01	36.17	18.33	**0.75**
406_1_0-1B	Eastern Medit.	33.30	33.39	2	16.1/9.1	0.97	0.05	0.64	0.00	39.18	21.50	**0.97**
406_2_0-1B	Eastern Medit.	33.73	30.60	2	16.1/9.1	0.97	0.06	0.70	0.01	39.18	20.88	**0.97**
406_3_0-1B	Eastern Medit.	34.10	27.60	2	16.1/9.1	0.97	0.06	0.66	0.01	39.10	20.13	**0.97**
406_5_0-1B	Eastern Medit.	35.04	20.64	2	16.1/9.1	0.96	0.07	0.65	0.01	38.95	20.65	**0.96**
406_6_0-1B	Eastern Medit.	34.97	18.10	2	16.1/9.1	0.95	0.13	0.73	0.02	38.21	20.53	**0.95**
Baltic_1_0-0.5B	Baltic	58.50	9.60	2	16.1/9.1	0.6	0.58	0.66	0.02	30.00	9.55	
Baltic_2_0-0.5A	Baltic	57.77	11.12	2	16.1/9.1	0.5	0.62	0.64	0.02	27.69	9.39	
Baltic_3_0-0.5A	Baltic	56.60	11.78	2	16.1/9.1	0.7	0.61	0.75	0.01	20.03	9.08	
Baltic_4_0-0.5A	Baltic	56.28	12.28	2	16.1/9.1	0.7	0.61	0.75	0.01	16.65	9.06	
Baltic_5_0-0.5A	Baltic	55.93	12.71	2	16.1/9.1	0.6	0.52	0.60	0.01	12.58	9.48	
Baltic_6_0-0.5A	Baltic	55.82	12.76	2	16.1/9.1	0.4	0.52	0.44	0.00	11.15	9.45	
Baltic_7_0-0.5A	Baltic	54.89	13.41	2	16.1/9.1	0.5	0.25	0.26	0.00	8.10	8.85	
Baltic_9_0-0.5A	Baltic	55.47	15.48	2	16.1/9.1					7.50	8.79	
Baltic_10_0-0.5A	Baltic	57.21	19.95	2	16.1/9.1	0.5	0.05	0.06		7.21	8.22	
64PE409-53 BC	North Sea	53.60	-4.08	2	16.1/9.1					33.75	10	
64PE409-41 BC	North Sea	53.60	-4.08	2	16.1/9.1	0.39	0.59	0.49		33.75	10.28	**0.39**
NF2012-30 BC	Baltimore canyon	38.17	-73.85	2	16.1/9.1	0.80	0.23	0.54		33.33	15.62	**0.80**
NF2012-30 BC	Baltimore canyon	38.17	-73.85	2	16.1/9.1	0.83	0.24	0.61	0.01	33.33	15.62	**0.83**
NF2012-046 BC	Baltimore canyon	38.12	-73.84	2	16.1/9.1	0.78	0.26	0.55	0.02	33.33	15.62	**0.78**
NF2012-65 BC	Baltimore canyon	38.06	-73.87	2	16.1/9.1	0.77	0.22	0.48	0.01	33.33	15.62	**0.77**
NF2012-69 BC	Baltimore canyon	38.04	-73.80	2	16.1/9.1	0.76	0.24	0.50	0.00	33.33	15.62	**0.76**
NF2012-84 BC	Baltimore canyon	38.01	-73.75	2	16.1/9.1	0.73	0.29	0.52	0.02	33.88	15.72	**0.73**
NF2012-182 BC	Norfolk Canyon	37.02	-74.65	2	16.1/9.1	0.71	0.27	0.48	0.02	33.80	16.62	**0.71**
NF2012-182 BC	Norfolk Canyon	37.02	-74.65	2	16.1/9.1					33.80	16.62	
NF2012-191 BC	Norfolk Canyon	37.04	-74.63	2	16.1/9.1	0.73	0.30	0.54	0.02	33.80	16.62	**0.73**
NF2012-193 BC	Norfolk Canyon	37.04	-74.58	2	16.1/9.1	0.75	0.31	0.57	0.02	33.80	16.62	**0.75**
M2005-14 BC	Gulf of Cadiz	35.31	-6.80	2	16.1/9.1	0.82	0.14	0.43	0.00	36.43	19.61	**0.82**
M2004-11 BC	Gulf of Cadiz	35.28	-6.76	2	16.1/9.1	0.86	0.10	0.40	0.01	36.43	19.61	**0.86**
M2003-18 BC	Rockal Bank	55.62	-15.82	2	16.1/9.1	0.42	0.76	0.70	0.19	35.38	11.38	
M2001-15 BC	Porcupine Bank	53.77	-13.92	2	16.1/9.1	0.93	0.29	0.84	0.07	35.42	11.93	**0.93**
TRACOS2010-36 BC	Cape Lookout	34.21	-75.86	2	16.1/9.1	0.85	0.27	0.67		36.13	25.26	**0.85**
TRACOS2010-36 BC	Cape Lookout	34.21	-75.86	2	16.1/9.1	0.94	0.29	0.87	0.03	36.13	25.26	**0.94**
TRACOS2010-75 BC	Cape Lookout	34.21	-75.87	2	16.1/9.1	0.94	0.31	0.87	0.03	36.13	25.26	**0.94**

SJ62 BC	Gulf of Mexico	29.17	-88.01	2	16.1/9.1	0.43	0.75	0.69	0.20	34.21	24.52	
64PE275-30-2	North Atlantic Ocean	57.37	-26.55	2	16.1/9.1	0.16	0.94	0.75	0.22	34.89	10.09	
64PE275-3-10	North Atlantic Ocean	57.45	-27.91	2	16.1/9.1	0.15	0.95	0.76	0.21	34.99	10.23	
64PE275-6-1	North Atlantic Ocean	59.35	-38.86	2	16.1/9.1	0.07	0.98	0.79	0.23	34.82	6.55	
64PE275-9-1	North Atlantic Ocean	59.25	-39.66	2	16.1/9.1					34.88	5.87	
64PE275-9	North Atlantic Ocean	59.25	-39.66	2	16.1/9.1	0	1.00	0.79	0.23	34.88	5.87	
64PE275-30-2	North Atlantic Ocean	57.37	-26.55	2	16.1/9.1	0.12	0.96	0.76	0.21	34.89	10.09	
418-2 ufs	Black Sea	43.16	29.96	2	16.1/9.1	0.86	0.06	0.28		18.29	14.43	
418-2 0-1L	Black Sea	43.16	29.96	2	16.1/9.1	0.96	0.23	0.87		18.29	14.43	
418-2 0-1K	Black Sea	43.16	29.96	2	16.1/9.1	0.96	0.19	0.86	0.04	18.29	14.43	
418 12/3 0-1G	Black Sea	42.94	30.03	2	16.1/9.1	0.96	0.21	0.87	0.07	18.22	14.83	
418-12/3 0-1F	Black Sea	42.94	30.03	2	16.1/9.1	0.97	0.21	0.89	0.06	18.22	14.83	
418-4 0-1H	Black Sea	42.78	29.35	2	16.1/9.1	0.96	0.17	0.85	0.06	18.14	14.54	
418-4 0-1I	Black Sea	42.78	29.35	2	16.1/9.1	0.97	0.16	0.85	0.05	18.14	14.54	
408-2.2 0-1	Black Sea	42.90	30.52	2	16.1/9.1	0.97	0.20	0.90	0.04	18.22	14.62	
SO161-5 106	Chilean margin	-38.28	-74.08	6	16.1/9.1					33.67	13.96	
SO161-5 107	Chilean margin	-38.33	-74.08	6	16.1/9.1					33.67	13.96	
SO161-5 109	Chilean margin	-38.35	-74.04	6	16.1/9.1	0.65	0.31	0.46		33.67	13.96	**0.65**
SO161-5 110	Chilean margin	-38.33	-73.80	6	16.1/9.1					33.79	13.05	
SO161-5 120	Chilean margin	-36.00	-73.03	6	16.1/9.1					33.98	12.93	
SO161-5 122	Chilean margin	-36.00	-72.98	6	16.1/9.1	0.60	0.22	0.30		33.65	12.7	**0.60**
SO161-5 77	Chilean margin	-39.85	-74.03	6	16.1/9.1					33.22	12.92	
SO161-5 78	Chilean margin	-39.85	-74.00	6	16.1/9.1	0.50	0.30	0.29		33.22	12.92	**0.50**
SO161-5 83	Chilean margin	-39.85	-73.90	6	16.1/9.1					33.32	11.77	
SO161-5 84	Chilean margin	-39.66	-73.82	6	16.1/9.1					33.36	11.84	
SO161-5 86	Chilean margin	-39.66	-73.62	6	16.1/9.1					34.17	12.04	
SO161-5 42	Chilean margin	-38.74	-73.94	6	16.1/9.1	0.52	0.24	0.26		33	13.17	**0.52**
SO161-5 43	Chilean margin	-38.75	-73.90	6	16.1/9.1	0.55	0.24	0.27		33	13.17	**0.55**
SO161-5 1	Chilean margin	-36.95	-73.73	6	16.1/9.1	0.57	0.25	0.31		33.82	12.63	**0.57**
SO161-5 14	Chilean margin	-36.21	-73.22	6	16.1/9.1	0.57	0.18	0.22		33.98	12.93	**0.57**
SO161-5 8	Chilean margin	-36.12	-77.84	6	16.1/9.1	0.60	0.24	0.32		34.04	16.75	**0.60**
NBP0702 SMG#3	Antarctic	-77.47	-158.27	1	12.9/7.6		1.00	0.95	0.01		-0.90	
NBP0702 SMG#10	Antarctic	-74.10	-108.61	1	12.9/7.6	0.18	0.99	0.95	0.02	33.72	-1.77	**0.18**
NBP0702 SMG#13	Antarctic	-73.94	-134.52	1	12.9/7.6	0.18	0.99	0.96	0.01	33.63	-1.83	**0.18**
NBP0702 SMG#15	Antarctic	-72.56	-125.81	1	12.9/7.6	0.08	1.00	0.95	0.01	33.22	-1.69	**0.08**
NBP0702 SMG#22	Antarctic	-71.75	-104.01	1	12.9/7.6	0.16	0.98	0.90	0.03	33.14	-1.81	**0.16**
NBP0702 SMG#17	Antarctic	-71.54	-114.99	1	12.9/7.6		0.99	0.92	0.04	32.70	-1.56	
NBP0702 SMG#20	Antarctic	-71.13	-106.01	1	12.9/7.6	0.16	0.98	0.92	0.02	33.02	-1.53	**0.16**
LMG 98 02 KC-6	Antarctic	-67.22	-66.88	1	12.9/7.6	0.00	1.00	0.94	0.02	32.96	-0.11	**0.00**
NBP 06 03 KC-3	Antarctic	-65.77	-61.57	1	12.9/7.6	0.00	1.00	0.90			0.67	**0.00**
ST 45 MC	Antarctic	-65.47	140.50	1	12.9/7.6		0.92	0.76		33.37	-1.31	
PD 90-7 SMG-9	Antarctic	-65.17	-63.23	1	12.9/7.6							
PD 90-7 SMG-8	Antarctic	-65.16	-63.22	1	12.9/7.6							
PD 90-7 SMG-6	Antarctic	-65.12	-63.19	1	12.9/7.6		1.00	0.92	0.02			
PD 90-7 SMG-21	Antarctic	-64.91	-62.60	1	12.9/7.6		1.00	0.77			0.13	

NBP 01 07 KC-17	Antarctic	-64.85	-65.40	1	12.9/7.6	0.05	1.00	0.93	0.02	33.41	0.71	**0.05**
NBP 99 03 KC-21	Antarctic	-64.84	-62.98	1	12.9/7.6					33.70	0.35	
NBP 99 03 KC-20	Antarctic	-64.84	-62.92	1	12.9/7.6	0.13	0.99	0.95	0.02	33.70	0.35	**0.13**
LMG 05 02 KC-25	Antarctic	-64.80	-60.38	1	12.9/7.6	0.00	1.00	0.96	0.01	34.14	-0.27	**0.00**
AMR-2	Antarctic	-64.66	139.98	1	12.9/7.6		0.86	0.79		33.73	-0.04	
NBP 00 03 KC-28	Antarctic	-64.37	-58.52	1	12.9/7.6	0.00	1.00	0.93	0.02	34.49	-1.76	**0.00**
NBP 00 03 KC-29	Antarctic	-64.36	-58.44	1	12.9/7.6		1.00	0.94	0.01			
NBP 01 07 KC-28 0	Antarctic	-64.32	-62.05	1	12.9/7.6	0.00	1.00	0.94	0.01	34.03	0.79	**0.00**
NBP 00 03 KC-1	Antarctic	-64.29	-58.58	1	12.9/7.6		1.00	0.98				
MD03-2603 0-1	Antarctic	-64.29	139.38	1	12.9/7.6	0.00	1.00	0.80	0.03	33.55	0.50	**0.00**
MD03-2604 0-1	Antarctic	-64.29	139.38	1	12.9/7.6		1.00	0.70	0.03		0.50	
NBP 00 03 KC-30	Antarctic	-64.28	-58.45	1	12.9/7.6	0.00	1.00	0.95	0.01	34.49	-1.76	**0.00**
AMR 1MC	Antarctic	-63.86	140.24	1	12.9/7.6	0.18	0.95	0.79		33.80	0.87	**0.18**
NBP 01 07 KC-49	Antarctic	-63.67	-56.38	1	12.9/7.6	0.00	1.00	0.95	0.01	33.99	-0.65	**0.00**
LMG 04 04 KC-3	Antarctic	-63.14	-55.31	1	12.9/7.6	0.00	1.00	0.96	0.01	34.35	-0.28	**0.00**
LMG 04 04 KC-16	Antarctic	-63.07	-55.82	1	12.9/7.6	0.00	1.00	0.95	0.01	34.36	-0.68	**0.00**
NBP 95 07 KC-2 1	Antarctic	-62.21	-57.49	1	12.9/7.6	0.00	1.00	0.94	0.01	34.10	0.73	**0.00**
ST 35 MC	Antarctic	-62.01	141.68	1	12.9/7.6					33.75	1.14	
ST 34 MC	Antarctic	-60.05	142.00	1	12.9/7.6		0.75	0.84		33.86	2.38	
ST 32 MC	Antarctic	-56.00	143.68	1	12.9/7.6					33.78	3.53	
AII 107- GGC-9	Central South Atlantic	-56.20	-32.50	1	12.9/7.6		1.00	0.86		34.21	0.41	
AII-107-6 GGC-19 5-7	Central South Atlantic	-54.91	-8.72	1	12.9/7.6		0.82	0.68	0.02		1.51	
AII-107-GGC-22	Central South Atlantic	-54.79	-3.33	1	12.9/7.6						1.03	
TSP 3MC	Indian Ocean	-48.56	146.41	1	12.9/7.6					34.15	9.11	
TSP 2MC	Indian Ocean	-48.13	146.90	1	12.9/7.6					34.46	10.13	
GeoB2727-1	Western South Atlantic	-48.01	-56.54	1	12.9/7.6	0.36	0.81	0.71		34.05	8.14	**0.36**
TSP 1MC	Indian Ocean	-47.57	147.49	1	12.9/7.6							
AII-107-GGC 28	Central South Atlantic	-46.88	7.54	1	12.9/7.6					33.75	5.44	
GeoB2730-1	Western South Atlantic	-44.48	-53.25	1	12.9/7.6	0.66	0.48	0.64	0.02	34.59	11.07	**0.66**
GeoB6411-4	Central South Atlantic	-44.36	-18.35	1	12.9/7.6	0.33	0.81	0.68	0.02	34.52	11.05	**0.33**
GeoB6412-1	Central South Atlantic	-44.25	-17.65	1	12.9/7.6	0.41	0.79	0.73		34.40	9.67	**0.41**
GeoB2731-1	Western South Atlantic	-44.21	-51.42	1	12.9/7.6	0.58	0.60	0.67		34.21	14.58	**0.58**
GeoB2715-1	Western South Atlantic	-43.90	-57.66	1	12.9/7.6	0.42	0.72	0.64	0.02	34.08	10.34	**0.42**
GeoB2714-5	Western South Atlantic	-43.86	-58.00	1	12.9/7.6	0.34	0.82	0.70		34.08	9.14	**0.34**
GeoB2712-1	Western South Atlantic	-43.68	-59.33	1	12.9/7.6		0.77	0.69		33.80	11.48	
GeoB2734-2	Western South Atlantic	-39.29	-54.34	1	12.9/7.6	0.43	0.61	0.54		33.99	11.82	**0.43**
GeoB2705-7	Western South Atlantic	-39.24	-53.36	1	12.9/7.6					34.18	16.70	
GeoB2803-2	Western South Atlantic	-37.41	-53.70	1	12.9/7.6	0.67	0.29	0.46		32.67	16.58	**0.67**
GeoB2802-2	Western South Atlantic	-37.21	-53.98	1	12.9/7.6	0.62	0.32	0.43		33.97	13.36	**0.62**
MD2607	Australia	-36.58	137.24	1	12.9/7.6	0.83	0.49	0.82	0.00	35.69	16.80	**0.83**
GeoB2810-2	Western South Atlantic	-35.98	-51.98	1	12.9/7.6	0.71	0.27	0.48		35.33	18.93	**0.71**
GeoB6422-5	Central South Atlantic	-35.71	-22.73	1	12.9/7.6	0.68	0.38	0.57		35.27	19.19	**0.68**
GeoB8301-5	Central South Atlantic	-34.78	17.70	1	12.9/7.6	0.66	0.83	0.91	0.01	35.39	18.51	**0.66**
GeoB6424-1	Central South Atlantic	-34.61	-23.28	1	?	0.67	0.50	0.67	?	35.49	19.76	**0.67**
GeoB2022-3	Western South Atlantic	-34.44	-20.91	1	12.9/7.6						19.57	

GeoB8318	Eastern South Atlantic	-32.15	16.81	1	12.9/7.6					35.21	16.56	
GeoB2829-1	Western South Atlantic	-30.87	-43.43	1	12.9/7.6	0.88	0.12	0.51		36.33	23.92	**0.88**
GeoB8331	Tropical Atlantic	-29.14	16.71	1	12.9/7.6					34.83	12.98	
GeoB2111-2	Western South Atlantic	-29.11	-45.22	1	12.9/7.6	0.93	0.12	0.65		36.23	22.10	**0.93**
GeoB2108	Western South Atlantic	-27.49	-46.23	1	12.9/7.6	0.90	0.15	0.62		36.47	24.37	**0.90**
geoB2104-1	Western South Atlantic	-27.29	-46.38	1	12.9/7.6	0.90	0.11	0.53		36.69	24.05	**0.90**
GeoB2105-3	Western South Atlantic	-27.29	-46.74	1	12.9/7.6	0.88	0.10	0.46		36.11	25.50	**0.88**
GeoB2102-1	Western South Atlantic	-23.98	-41.20	1	12.9/7.6	0.93	0.16	0.72		36.81	25.42	**0.93**
T89-36	Eastern South Atlantic	-22.60	13.84	1	12.9/7.6	0.61	0.56	0.66	0.01	35.12	15.42	**0.61**
GeoB2125-2	Western South Atlantic	-20.82	-39.86	1	12.9/7.6	0.90	0.15	0.62		37.01	25.64	**0.90**
GeoB2130-1	Western South Atlantic	-20.62	-37.10	1	12.9/7.6	0.99	0.22	0.95		37.14	23.94	**0.99**
T89-42	Eastern South Atlantic	-19.88	4.79	1	13.8/8.4	0.62	0.65	0.75	0.03	35.92	21.03	**0.62**
T89-35	Eastern South Atlantic	-17.29	11.23	1	13.8/8.4	0.85	0.34	0.74	0.02	35.62	16.79	**0.85**
T89-34	Eastern South Atlantic	-15.01	11.97	1	13.8/8.4	0.93	0.27	0.83	0.00	35.65	20.84	**0.93**
T89-33	Eastern South Atlantic	-14.97	11.62	1	13.8/8.4	0.90	0.31	0.81	0.01	35.78	21.71	**0.90**
T89-32	Eastern South Atlantic	-14.96	10.67	1	13.8/8.4	0.93	0.27	0.83	0.00	35.76	22.62	**0.93**
T89-31	Eastern South Atlantic	-14.89	9.17	1	13.8/8.4	0.88	0.37	0.82	0.01	36.00	20.27	**0.88**
T89-30	Eastern South Atlantic	-14.88	8.22	1	13.8/8.4	0.88	0.36	0.81	0.01	36.02	21.54	**0.88**
T89-28	Eastern South Atlantic	-10.39	5.64	1	13.8/8.4	0.93	0.21	0.77	0.01	36.47	22.10	**0.93**
T89-25	Eastern South Atlantic	-9.37	10.61	1	13.8/8.4	0.96	0.20	0.85	0.00	35.19	28.05	**0.96**
GeoB2208-1	Western South Atlantic	-8.92	-33.70	1	12.9/7.6	0.95	0.05	0.48		36.69	26.92	**0.95**
T89-24	Eastern South Atlantic	-8.91	12.06	1	13.8/8.4	0.94	0.29	0.86		35.53	23.58	**0.94**
T89-47	Eastern South Atlantic	-8.79	4.43	1	13.8/8.4	0.93	0.25	0.82	0.01	36.17	24.16	**0.93**
T89-23	Eastern South Atlantic	-8.51	12.11	1	13.8/8.4	0.92	0.29	0.83	0.00	35.43	27.05	**0.92**
GeoB2205-4	Western South Atlantic	-8.20	-34.26	1	12.9/7.6		0.03	0.68		36.77	27.43	
T89-20	Eastern South Atlantic	-7.31	11.54	1	13.8/8.4	0.92	0.24	0.78	0.00	33.62	27.05	**0.92**
T89-21	Eastern South Atlantic	-7.28	11.99	1	13.8/8.4	0.92	0.21	0.75		35.07	25.33	**0.92**
T89-22	Eastern South Atlantic	-7.13	12.07	1	13.8/8.4	1.00	0.25	1.00		34.46	25.33	**1.00**
T89-17	Eastern South Atlantic	-6.82	7.81	1	13.8/8.4	0.94	0.24	0.82	0.01	35.79	24.43	**0.94**
T89-19	Eastern South Atlantic	-6.04	9.96	1	13.8/8.4	0.87	0.26	0.70	0.00	29.74	26.45	
GeoB10038-3	West Sumatra	-5.94	103.25	3	12.9/7.6	0.97	0.19	0.88	0.00	33.76	28.71	**0.97**
T89-16	Eastern South Atlantic	-5.71	11.23	1	13.8/8.4	0.90	0.17	0.65		29.31	24.40	
GeoB6518-1	Eastern South Atlantic	-5.35	11.13	1	?	0.90	0.13	0.59	?	30.19	26.46	
T89-12	Eastern South Atlantic	-5.20	7.97	1	13.8/8.4	0.92	0.22	0.77		34.27	25.72	**0.92**
T89-11	Eastern South Atlantic	-4.25	6.05	1	13.8/8.4	0.92	0.31	0.84	0.01	35.61	25.18	**0.92**
T89-15	Eastern South Atlantic	-4.21	10.02	1	13.8/8.4	0.93	0.17	0.72	0.01	33.80	24.91	**0.93**
GeoB10034-3	West Sumatra	-4.17	101.50	3	12.9/7.6	0.98	0.17	0.91		33.98	26.67	**0.98**
T89-13	Eastern South Atlantic	-4.11	9.24	1	13.8/8.4	0.93	0.23	0.80	0.01	33.42	26.86	**0.93**
GeoB1501-1	Central South Atlantic	-3.68	-32.01	1	12.9/7.6					35.90	27.29	
T89-14	Eastern South Atlantic	-3.51	9.69	1	13.8/8.4	0.93	0.17	0.74	0.01	33.91	25.50	**0.93**
T89-10	Eastern South Atlantic	-2.08	1.32	1	13.8/8.4	0.94	0.19	0.79	0.01	35.78	25.10	**0.94**
GeoB10032-1	West Sumatra	-1.67	99.68	3	12.9/7.6	0.99	0.17	0.94	0.00	33.42	30.29	**0.99**
GeoB2216-2	Central South Atlantic	0.00	-23.10	1	12.9/7.6	0.98	0.09	0.80	0.01	35.85	26.86	**0.98**
GeoB2215-8	Central South Atlantic	0.01	-23.49	1	12.9/7.6	0.97	0.08	0.74	0.01	35.95	26.15	**0.97**
GeoB1503-2	Central Atlantic	2.31	-30.65	1	12.9/7.6					35.87	26.90	

GeoB9529-1	West Africa	8.35	-17.37	1	12.9/7.6		0.33	0.90	0.01	35.42	27.33	
GeoB9537-4	West Africa	8.60	-15.22	4	12.9/7.6	0.95	0.24	0.85	0.01	34.81	27.43	**0.95**
GeoB9538-5	West Africa	8.71	-15.83	4	12.9/7.6	0.97	0.26	0.91	0.01	34.82	27.36	**0.97**
GeoB9536-4	West Africa	8.71	-15.13	4	12.9/7.6	0.96	0.26	0.90	0.01	34.81	27.43	**0.96**
GeoB9535-5	West Africa	8.88	-14.96	4	12.9/7.6	0.97	0.22	0.89	0.00	34.00	27.06	**0.97**
GeoB9534-4	West Africa	8.90	-14.94	4	12.9/7.6	0.95	0.21	0.84	0.01	34.00	27.06	**0.95**
GeoB9533-3	West Africa	8.93	-14.91	4	12.9/7.6	0.96	0.22	0.87	0.00	34.00	27.06	**0.96**
GeoB9531-2	West Africa	8.94	-16.90	4	12.9/7.6	0.97	0.23	0.90		35.24	27.06	**0.97**
GeoB9532-1	West Africa	8.95	-14.89	4	12.9/7.6	0.96	0.19	0.84		34.00	27.06	**0.96**
GeoB9539-1	West Africa	9.02	-13.73	4	12.9/7.6	0.95	0.33	0.90	0.01	28.83	27.32	
GeoB9528-1	West Africa	9.17	-17.66	1	12.9/7.6	0.96	0.30	0.91	0.01	34.99	27.08	**0.96**
GeoB9540-1	West Africa	9.29	-14.16	4	?	0.95	0.36	0.91	?	29.98	27.24	
GeoB9541-1	West Africa	9.66	-14.57	4	?	0.96	0.38	0.94	?	31.40	27.27	
GeoB9542-1	West Africa	10.14	-15.03	4	?	0.88	0.65	0.93	?	35.20	26.30	**0.88**
GeoB9543-1	West Africa	10.40	-15.52	4	?	0.85	0.86	0.97	?	33.98	26.28	**0.85**
TY93	Arabian Sea	10.76	51.94	1	?	1.00	0.72	1.00	?	35.76	25.76	**1.00**
GeoB9544-1	West Africa	12.38	-17.07	4	?	0.90	0.58	0.92	?	35.27	25.06	**0.90**
GeoB13601-3	West Africa	12.43	-18.01	4	12.9/7.6	0.93	0.46	0.92	0.01	34.94	24.89	**0.93**
GeoB9526-4	West Africa	12.44	-18.06	1	12.9/7.6	0.94	0.51	0.94	0.01	34.94	24.89	**0.94**
GeoB 9525-5	West Africa	12.64	-17.88	1	12.9/7.6	0.93	0.48	0.92	0.01	35.03	24.32	**0.93**
GeoB9524-3	West Africa	12.85	-17.63	4	12.9/7.6	0.96	0.38	0.93		35.04	24.42	**0.96**
GeoB9545-1	West Africa	12.85	-17.08	4	12.9/7.6	0.93	0.53	0.94		34.87	24.79	**0.93**
GeoB9516-4	West Africa	13.67	-18.42	4	12.9/7.6	0.94	0.47	0.93		35.65	23.84	**0.94**
GeoB9520-4	West Africa	13.83	-17.59	4	12.9/7.6	0.94	0.40	0.92		35.36	23.99	**0.94**
GeoB9521-3	West Africa	13.85	-17.49	1	12.9/7.6	0.96	0.33	0.92	0.00	35.33	23.60	**0.96**
GeoB9522-2	West Africa	13.86	-17.45	4	12.9/7.6	0.98	0.33	0.96		35.33	23.60	**0.98**
GeoB9547-2	West Africa	13.95	-17.17	4	12.9/7.6	0.96	0.42	0.95		35.34	23.17	**0.96**
GeoB9515-2	West Africa	15.27	-17.05	4	12.9/7.6	0.93	0.33	0.88		35.52	23.08	**0.93**
GeoB9513-5	West Africa	15.32	-17.30	4	12.9/7.6	0.96	0.34	0.93	0.00	35.69	23.06	**0.96**
GeoB9512-4	West Africa	15.34	-17.37	4	12.9/7.6	0.96	0.33	0.92	0.00	35.69	23.06	**0.96**
GeoB9510-3	West Africa	15.42	-17.65	4	12.9/7.6	0.95	0.38	0.92	0.00	35.76	23.92	**0.95**
GeoB9508-4	West Africa	15.50	-17.95	4	12.9/7.6	0.94	0.36	0.89		35.56	23.51	**0.94**
GeoB9506-3	West Africa	15.61	-18.35	4	12.9/7.6	0.94	0.34	0.89		35.61	24.97	**0.94**
GeoB13604-2	West Africa	15.67	-17.28	4	12.9/7.6	0.95	0.35	0.92	0.00	35.77	21.77	**0.95**
GeoB13606-2	West Africa	15.96	-16.76	4	12.9/7.6	0.96	0.38	0.94	0.00	35.59	22.73	**0.96**
MS-4	Arabian Sea	15.99	61.50	1	?	1.00	0.85	1.00	?	36.17	26.46	**1.00**
GeoB9503-3	West Africa	16.07	-16.65	4	12.9/7.6	0.94	0.45	0.92	0.01	35.61	22.30	**0.94**
GeoB13609-4	West Africa	16.84	-16.72	4	12.9/7.6	0.91	0.50	0.91	0.01	35.81	22.49	**0.91**
GeoB9501-4	West Africa	16.84	-16.73	1	12.9/7.6	0.95	0.36	0.91	0.00	35.81	22.49	**0.95**
MS-3	Arabian Sea	17.21	59.59	1	?	0.81	0.77	0.93	?	36.18	26.73	**0.81**
MS-1	Arabian Sea	17.69	57.85	1	?	0.87	0.82	0.97	?	36.22	25.86	**0.87**
GeoB13610-2	West Africa	20.08	-18.83	4	12.9/7.6	0.88	0.58	0.91	0.01	35.99	19.91	**0.88**
GeoB7926-2	West Africa	20.13	-18.27	1	12.9/7.6	0.85	0.38	0.78		36.04	21.16	**0.85**
GeoB13613-3	West Africa	20.58	-17.98	4	12.9/7.6	0.89	0.65	0.94	0.01	35.99	18.96	**0.89**
GeoB13612-3	West Africa	20.75	-18.70	4	12.9/7.6	0.88	0.58	0.91	0.01	36.14	20.22	**0.88**

GeoB13615-4	West Africa	21.00	-19.83	4	12.9/7.6	0.87	0.65	0.93	0.01	36.63	23.06	**0.87**
GeoB13616-6	West Africa	21.27	-20.81	4	12.9/7.6	0.88	0.53	0.89	0.01	36.69	21.35	**0.88**
GeoB13611-3	West Africa	21.33	-18.84	4	?	0.88	0.59	0.91	?	36.44	21.08	**0.88**
GeoB13618-1	West Africa	24.23	-17.29	4	12.9/7.6	0.82	0.40	0.75	0.02	36.58	20.09	**0.82**
DNT05-22	Gulf of St. Lawrence	46.62	-58.71	1	12.9/7.6	0.77				31.25	6.00	
HON02-15**	Gulf of St. Lawrence	49.62	-63.71	1	12.9/7.6	0.48	0.09	0.08	0.00	30.99	3.33	
sept01-07	Gulf of St. Lawrence	50.62	-66.71	1	12.9/7.6	0.43	0.27	0.22		29.77	6.46	
BS-3	Baltic	55.62	16.71	1	12.9/7.6					7.37	8.34	
Gullmarsfjord	Baltic	58.33	11.50	1	12.9/7.6	0.56	0.62	0.67	0.01	24.68	9.44	
bs-6 baltic proper	Baltic	58.62	20.71	1	12.9/7.6					6.81	8.84	
HB6 0-1e*	Estuarine	60.62	-91.71	1	12.9/7.6	0.34	0.41	0.26	0.07	31.41	5.36	
HB5 0-1e*	Estuarine	60.62	-90.71	1	12.9/7.6	0.08	0.85	0.33	0.14	30.95	6.40	
STATION B	Hudson Bay	60.62	-81.71	1	12.9/7.6	0.29	0.27	0.13		27.15	8.50	
station A	Hudson Bay	60.62	-79.71	1	12.9/7.6	0.33	0.30	0.17	0.02	25.86	7.70	
M 2003-1	Others	62.00	-1.97	1	12.9/7.6	0.54	0.82	0.84	0.10	35.21	9.33	**0.54**
M 2003-8	Others	62.77	-1.13	1	12.9/7.6	0.27	0.93	0.84	0.12	35.19	8.72	
BS690	Arctic	71.01	30.95	1	12.9/7.6	0.30	0.91	0.82	0.04	34.47	5.99	**0.30**
BS661	Arctic	71.37	22.76	1	12.9/7.6	0.28	0.94	0.87	0.04	34.81	7.01	**0.28**
BS625	Arctic	71.72	21.75	1	12.9/7.6	0.30	0.94	0.87	0.05	34.87	6.39	**0.30**
BS659	Arctic	71.97	25.05	1	12.9/7.6	0.25	0.94	0.85	0.04	34.60	5.91	**0.25**
BS627	Arctic	72.32	24.05	1	12.9/7.6	0.27	0.95	0.88	0.04	34.85	5.94	**0.27**
BS667	Arctic	72.83	28.75	1	12.9/7.6		0.94	0.85	0.07	34.91	6.15	
BS629	Arctic	73.00	24.25	1	12.9/7.6	0.17	0.97	0.88	0.07	35.03	4.68	**0.17**
BS655	Arctic	73.30	25.53	1	12.9/7.6	0.19	0.97	0.88	0.05	35.02	4.81	**0.19**
BS655	Arctic	73.30	25.53	1	12.9/7.6	0.19	0.97	0.88	0.04	35.02	4.81	**0.19**
BS669	Arctic	73.50	29.15	1	12.9/7.6	0.19	0.96	0.85	0.06	34.98	4.91	**0.19**
BS631	Arctic	73.66	24.46	1	12.9/7.6	0.23	0.96	0.87	0.06	35.02	5.17	**0.23**
BS653	Arctic	73.97	25.80	1	12.9/7.6	0.19	0.96	0.86	0.06	35.00	4.59	**0.19**
BS633	Arctic	74.33	24.68	1	12.9/7.6		0.94	0.84	0.05	34.88	3.42	
BS651	Arctic	74.63	26.07	1	12.9/7.6	0.15	0.97	0.85	0.05	34.94	3.80	**0.15**
BS673	Arctic	74.67	32.49	1	12.9/7.6	0.10	0.98	0.85	0.04	34.80	3.00	**0.10**
BS635	Arctic	75.00	24.94	1	12.9/7.6	0.11	0.98	0.86	0.04	34.28	1.33	**0.11**
BS647	Arctic	75.20	29.00	1	12.9/7.6	0.15	0.97	0.84	0.04	34.93	4.83	**0.15**
BS639	Arctic	75.56	27.89	1	12.9/7.6	0.10	0.98	0.83	0.07	34.72	2.07	**0.10**
BS645	Arctic	75.85	29.45	1	12.9/7.6	0.14	0.97	0.86	0.04	34.56	1.52	**0.14**
NP-07-13-60	Arctic	78.93	12.06	1	12.9/7.6		0.95	0.75	0.12	32.31	2.64	
NP-07-13-40	Arctic	78.96	11.95	1	12.9/7.6	0.12	0.96	0.76		32.44	1.79	**0.12**
NP-07-13-41	Arctic	78.97	11.81	1	12.9/7.6	0.15	0.96	0.83	0.03	32.44	1.79	**0.15**
np-07-13-42	Arctic	78.99	11.84	1	12.9/7.6	0.14	0.95	0.75	0.03	32.44	1.79	**0.14**
NP-07-13-49	Arctic	79.01	11.38	1	12.9/7.6	0.14	0.95	0.77	0.04	32.58	3.59	**0.14**
np-07-13-24	Arctic	79.01	10.86	1	12.9/7.6	0.17	0.97	0.86	0.05	33.57	2.30	**0.17**
NP-07-13-23	Arctic	79.02	11.03	1	12.9/7.6	0.13	0.98	0.87	0.03	33.40	2.61	**0.13**
NP-07-13-47	Arctic	79.02	11.60	1	12.9/7.6	0.15	0.95	0.77		31.81	3.46	
NP-07-13-08	Arctic	79.03	10.75	1	12.9/7.6	0.15	0.97	0.84	0.04	33.59	3.36	**0.15**
NP-07-13-50	Arctic	79.03	11.31	1	12.9/7.6	0.18	0.95	0.82	0.04	32.58	3.59	**0.18**

np-07-13-25	Arctic	79.04	10.87	1	12.9/7.6	0.14	0.97	0.86	0.04	33.57	2.30	**0.14**
NP-07-13-51	Arctic	79.04	11.37	1	12.9/7.6					32.58	3.59	
NP-07-13-9	Arctic	79.06	10.67	1	12.9/7.6	0.29	0.93	0.85	0.04	33.59	3.36	**0.29**
NP-07-13-64	Arctic	79.06	11.49	1	12.9/7.6	0.16	0.94	0.73	0.04	32.58	3.59	**0.16**
NP-07-13-52	Arctic	79.07	11.38	1	12.9/7.6					32.58	3.59	
NP-07-13-11	Arctic	79.12	11.66	1	12.9/7.6	0.17	0.94	0.76	0.03	31.81	3.46	
NP-07-13-16	Arctic	79.19	11.76	1	12.9/7.6					31.71	3.38	
NP-07-13-21	Arctic	79.23	11.92	1	12.9/7.6		0.93	0.80		31.71	3.38	
NP-07-13-14	Arctic	79.27	11.67	1	12.9/7.6		0.90	0.74		30.69	4.26	
NP-07-13-13	Arctic	79.30	11.62	1	12.9/7.6					30.69	4.26	
np-07-13-35	Arctic	79.80	18.13	1	12.9/7.6	0.13	0.96	0.80	0.06	33.47	0.78	**0.13**
NP-07-13-33	Arctic	80.10	17.17	1	12.9/7.6	0.14	0.96	0.81	0.04	33.56	1.63	**0.14**
NP-07-13-32	Arctic	80.21	16.96	1	12.9/7.6		0.93	0.82	0.04	32.96	1.89	
NP-07-13-31	Arctic	80.36	16.28	1	12.9/7.6	0.17	0.96	0.85	0.04	34.05	1.37	**0.17**
np-07-13-30	Arctic	80.50	15.90	1	12.9/7.6	0.12	0.97	0.84	0.07	33.60	3.50	**0.12**

a 1 = ASE; apolar-polar fractionation using Al_2O_3 chromatography.
2 = ASE; apolar-ketone-polar separation using Al_2O_3 chromatography.
3 = ultrasonic extraction; apolar-ketone-polar separation over silica.
4 = ASE; saponification of ASE extract; apolar-ketone-polar separation over silica.
5 = modified Bligh and Dyer; separation of core GDGT lipids (used for LCDs) and IPLs over silica.

b 16.1/9.1 determined for Agilent 5977A MSD at NIOZ.
9.7/6.5 determined for Thermo DSQ MS at NIOZ by Rodrigo-Gámiz et al. (2015).
12.9/7.6 determined for Thermo DSQ MS at NIOZ by Rodrigo-Gámiz et al. (2016).
13.8/8.4 determined for VG Autospec Ultima MS at NIOZ by Rampen et al. (2009).

c Diol Index according to Rampen et al. (2008)

d Diol Index according to Willmott et al. (2010)

e Relative abundance of the C_{28} 1,12-diol vs. the C_{28} 1,13- and 1,14-diol and the C_{30} 1,13-, 1,14- and 1,15-diols.

f Annual mean salinity (0 m depth) obtained from the 0.25° grid 2013 World Ocean Atlas (WOA) (Zweng et al., 2013).

g Annual mean sea surface temperature (°C; 0 m depth) obtained from the 0.25° grid 2013 World Ocean Atlas (WOA) (Locarnini et al., 2013).

h LDI values when excluding core-tops where surface salinity < 32, and $\boldsymbol{F}C_{28}$ 1,12 is > 0.1.

? Data unknown.

Chapter 6

Constraints on the application of long-chain diol proxies in the Iberian Atlantic margin

Marijke W. de Bar, Denise J.C. Dorhout, Ellen C. Hopmans, Sebastiaan W. Rampen, Jaap S. Sinninghe Damsté and Stefan Schouten

Organic Geochemistry 101 (2016)
DOI: 10.1016/j.orggeochem.2016.09.005

Corrigendum: *Organic Geochemistry 130* (2019)
DOI: 10.1016/j.orggeochem.2019.01.010

Abstract

Long-chain diols are lipids that have gained interest over the last years due to their high potential to serve as biomarkers and diol indices have been proposed to reconstruct upwelling conditions and sea surface temperature (SST). However, little is known about the sources of the diols and the mechanisms impacting their distribution. Here we studied the factors controlling diol distributions in the Iberian Atlantic margin, which is characterized by a dynamic continental shelf under the influence of upwelling of nutrient-rich cold deep waters, and fluvial input. We analyzed suspended particulate matter (SPM) of the Tagus river, marine SPM and marine surface sediments along five transects off the Iberian margin, as well as riverbank sediments and soil from the catchment area of the Tagus river. Relatively high fractional abundances of the C_{32} 1,15-diol (normalized with respect to the 1,13- and 1,15-diols) were observed in surface sediments in front of major river mouths and this abundance correlates strongly with the BIT index, a tracer for continental input of organic carbon. Together with an even higher fractional abundance of the C_{32} 1,15-diol in the Tagus river SPM, and the absence of long-chain diols in the watershed riverbank sediments and soils, we suggest that this long-chain diol is produced in-situ in the river. Further support for this hypothesis comes from the small but distinct stable carbon isotopic difference of 1.3 ‰ with the marine C_{28} 1,13-diol. The 1,14-diols are relatively abundant in surface sediments directly along the northern part of the coast, close to the upwelling zone, suggesting that Diol Indices based on 1,14-diols would work well as upwelling tracers in this region. Strikingly, we observed a significant difference in stable carbon isotopic composition between the mono-unsaturated $C_{30:1}$ 1,14- and the saturated C_{28} 1,14-diol (3.8±0.7 ‰), suggesting different sources, in accordance with their different distributions. In addition, the Long chain Diol Index (LDI), a proxy for sea surface temperature, was applied for the surface sediments. The results correlate well with satellite SSTs offshore but reveal a significant discrepancy with satellite-derived SSTs in front of the Tagus and Sado rivers. This suggests that river outflow might compromise the applicability of this proxy.

1. Introduction

One of the most important climate parameters that earth scientists try to reconstruct is sea surface temperature (SST). During the last decades, several organic proxies have been developed that have become important tools for climate reconstruction. Two organic proxies are commonly used for the reconstruction of past SSTs: the $U^{K'}_{37}$ index (Brassell et al., 1986; Prahl and Wakeham, 1987) based on the degree of unsaturation of long-chain alkenones produced by haptophyte algae, and the TEX_{86} index (Schouten et al., 2002; Kim et al., 2010), based on the distribution of isoprenoid glycerol dialkyl glycerol tetraethers (GDGTs), mainly produced by Thaumarchaeota. Many studies have used alkenones, as these compounds are often abundant in marine sediments, occur worldwide, and are relatively easy to analyze. Since their producers, haptophyte algae, are light dependent and live near the sea surface, the $U^{K'}_{37}$ index shows a good correlation with SST (Müller et al., 1998; Herbert, 2003). However, there are compromising factors such as interspecies variation (Conte et al., 1998), seasonality, habitat depth and oxic degradation (e.g. Hoefs et al., 1998). In contrast to haptophyte algae, Thaumarchaeota are not phototrophic but nitrifiers that depend on ammonium (Könneke et al., 2005; Wuchter et al., 2006a), often sourced by the decay of phytoplanktonic organic matter. This means that the TEX_{86} proxy often reflects subsurface water column temperatures rather than SST (Lopes dos Santos et al., 2010; Kim et al., 2012a; 2012b; Schouten et al., 2013b; Chen et al., 2014). In addition, it suffers from similar pitfalls as the $U^{K'}_{37}$ proxy, i.e., uncertainties in seasonality and degradation (e.g. Schouten et al., 2004; 2013; Kim et al., 2009c; Basse et al., 2014). Moreover, riverine continental organic matter input can bias the TEX_{86} signal, although this can be assessed by means of the Branched versus Isoprenoid Tetraether index (BIT), a tracer for fluvial input of soil-derived and riverine organic carbon (e.g. Hopmans et al., 2004; Zell et al., 2013; 2014; de Jonge et al., 2014a).

Long-chain diols form a group of lipids increasingly investigated over the last decades because of their potential to serve as biomarkers. They were first identified in Black Sea sediments (de Leeuw et al., 1981). This discovery was followed by many studies that reported long-chain diols in marine (e.g. Versteegh et al., 1997 and 2000; Hinrichs et al., 1999; Sinninghe Damsté et al., 2003; Rampen et al., 2007; 2008 and 2009) and lacustrine environments (e.g. Xu et al., 2007; Romero-Viana et al., 2012; Rampen et al., 2014b). From culture studies, it has become clear that marine and freshwater eustigmatophyte algae produce 1,13- and 1,15-diols, with chain lengths generally varying between C_{28} and C_{32}. However, their role as source organism of these diols in the marine environment is still uncertain, since the distribution found in marine sediments differs from that found in cultures (Volkman et al., 1992; Versteegh et al., 1997; Rampen et al., 2014b). Apart from 1,13- and 1,15-diols, 1,14 long-chain diols are also commonly found in marine sediments. These diols are usually assigned to *Proboscia* diatoms as Sinninghe Damsté et al. (2003) and Rampen et al. (2007) showed that this diatom genus produces saturated and mono-unsaturated C_{28} and C_{30} 1,14-diols. The saturated C_{28}, C_{30} and C_{32} 1,14-diols have also been reported in the marine

Dictyochophyte *Apedinella radians* (Rampen et al., 2011). However, the importance of this organism as source for 1,14-diols in the ocean is still unknown.

Recently, a new proxy for past sea surface temperature has been proposed based on the distribution of long-chain diols in marine sediments: the Long chain Diol Index (LDI; Rampen et al., 2012). Additionally, the Diol Index (Rampen et al., 2008; Willmott et al., 2010), a proxy for upwelling/high nutrient conditions, has been proposed. The LDI index is based on the fractional abundances of the C_{28} 1,13, C_{30} 1,13- and C_{30} 1,15-diols. Analysis of their distribution in a large set of marine surface sediments derived from all over the world shows that the abundance of these diols correlates strongly with annual mean SST: the C_{30} 1,15-diol has the strongest positive correlation ($R^2 = 0.95$), whereas the C_{28} and C_{30} 1,13-diols reveal slightly lesser negative correlations ($R^2 = 0.88$ and $R^2 = 0.80$, respectively). The C_{32} 1,15-diol does not correlate with SST ($R^2 = 0.01$). Based on this, the index is defined as the relative abundance of the C_{30} 1,15-diol versus the C_{28} and C_{30} 1,13-diols:

$$\text{LDI} = [C_{30}\ 1,15\text{-diol}]/[C_{28}\ 1,13\text{-diol}+C_{30}\ 1,13\text{-diol}+C_{30}\ 1,15\text{-diol}] \quad (1)$$

SST is calculated from the LDI index based on the following relation (Rampen et al., 2012):

$$\text{LDI} = 0.033\times\text{SST}+0.095 \qquad (R^2 = 0.969;\ n = 161;\ \text{SE} \pm 2\ °\text{C}) \quad (2)$$

Proboscia diatoms are often associated with high productivity and upwelling conditions (Hernández-Becerril, 1995; Lange et al., 1998; Koning et al., 2001). Their role as the most important 1,14-diol producers under upwelling conditions was confirmed by a sediment trap study in the Arabian Sea (Rampen et al., 2007), and based on this an index for upwelling intensity during the South Western Indian Monsoon was proposed (Rampen et al., 2008):

$$\text{Diol Index 1} = [C_{28}+C_{30}\ 1,14\text{-diol}]/[C_{28}+C_{30}\ 1,14\text{-diol}+C_{30}\ 1,15\text{-diol}] \quad (3)$$

A second upwelling index was proposed by (Willmott et al., 2010), for the Western Bransfield Basin (Antarctica) since the C_{28} and C_{30} 1,13-diols were more abundant than the C_{30} 1,15-diol:

$$\text{Diol Index 2} = [C_{28}+C_{30}\ 1,14\text{-diol}]/[C_{28}+C_{30}\ 1,14\text{-diol}+C_{28}+C_{30}\ 1,13\text{-diol}] \quad (4)$$

Preliminary application in sediment cores of the LDI and the two Diol Indices have shown their promise as proxies (Naafs et al., 2012; Rampen et al., 2012; 2014a; Seki et al., 2012; Lopes dos Santos et al., 2013; Smith et al., 2013; Rodrigo-Gámiz et al., 2014; Nieto-Moreno et al., 2015; Plancq et al., 2015). However, there are still uncertainties in the application of these biomarkers and it is crucial that additional studies are done to improve the reliability of these proxies. For example, studies have related increased abundances of *Proboscia* to stratified conditions rather than upwelling (e.g. Fernández and Bode, 1994). Indeed, Contreras et al. (2010) observed increased concentrations of the C_{28} 1,14-diol in the Peruvian upwelling system during times of stratification (interglacials) and low concentrations during times of upwelling.

Here we tested the long-chain diol proxies in surface sediments from the Atlantic Iberian margin. Previous organic geochemical work in this region has shown the presence of long-chain diols in surface sediments (Schmidt et al., 2010). This region experiences upwelling during summer and downwelling during winter due to the northerly and southerly trade winds and the Azores high pressure system driving the surface circulation. Additionally, the margin receives freshwater input from different rivers, of which the two largest are the Tagus and Douro. We analyzed long-chain diols in surface sediments of 5 transects along the Iberian margin (Fig. 1d). Transect I and IV are located in front of the Douro and Tagus, respectively, allowing the ability to assess the potential influence of fluvial input on the long-chain diol proxies. Transects II and V start in the estuaries of the smaller Mondego and Sado rivers, respectively, and transect III is not under the influence of riverine input. The results shed light on the applicability of long-chain diol proxies in a coastal environment under the influence of a seasonal upwelling system, and with terrestrial input via riverine transport.

2. Materials and methods

2.1 Site description

The Atlantic Iberian margin is characterized by a steep slope dissected by different submarine canyons, of which the most important are the Nazaré, Cascais and Setúbal-Lisbon canyons (e.g. Vanney and Mougenot, 1981). The shelf is relatively narrow, ranging between 20 and 50 km in width. The shelf break is located at a water depth of around 140 m (Mougenot, 1988). The surface ocean circulation off the Western Iberian Peninsula is driven by the Portugal Current (PC) System. The PC is a slow equatorward current (e.g. Martins et al., 2002). Between May and September (summer upwelling), the Portugal Coastal Current (PCC), along the coast dominates. This current is flowing southward induced by northerly Portugal trade winds and the Azores anticyclone moving towards the Iberian Peninsula (e.g. Fiúza et al., 1982; Martins et al., 2002). As a result, the cold, nutrient-rich subsurface water rises to the surface along the Iberian margin, leading to increased productivity (Fiúza, 1983). Fig. 1b shows the influence of upwelling waters during summer, lowering the SST, particularly in the northern part of the region (off the Douro river). Between September and October, the surface circulation is reversed by the dominance of the poleward Portugal Coastal Countercurrent (PCCC) driven by the southerly winds, which persist until April (winter downwelling season) (Álvarez-Salgado et al., 2003 and references therein). In January and February, another phytoplankton bloom occurs due to the large discharge of nutrients from the rivers (Dias et al., 2002), although less intense as compared to the plankton blooms associated with summer upwelling.

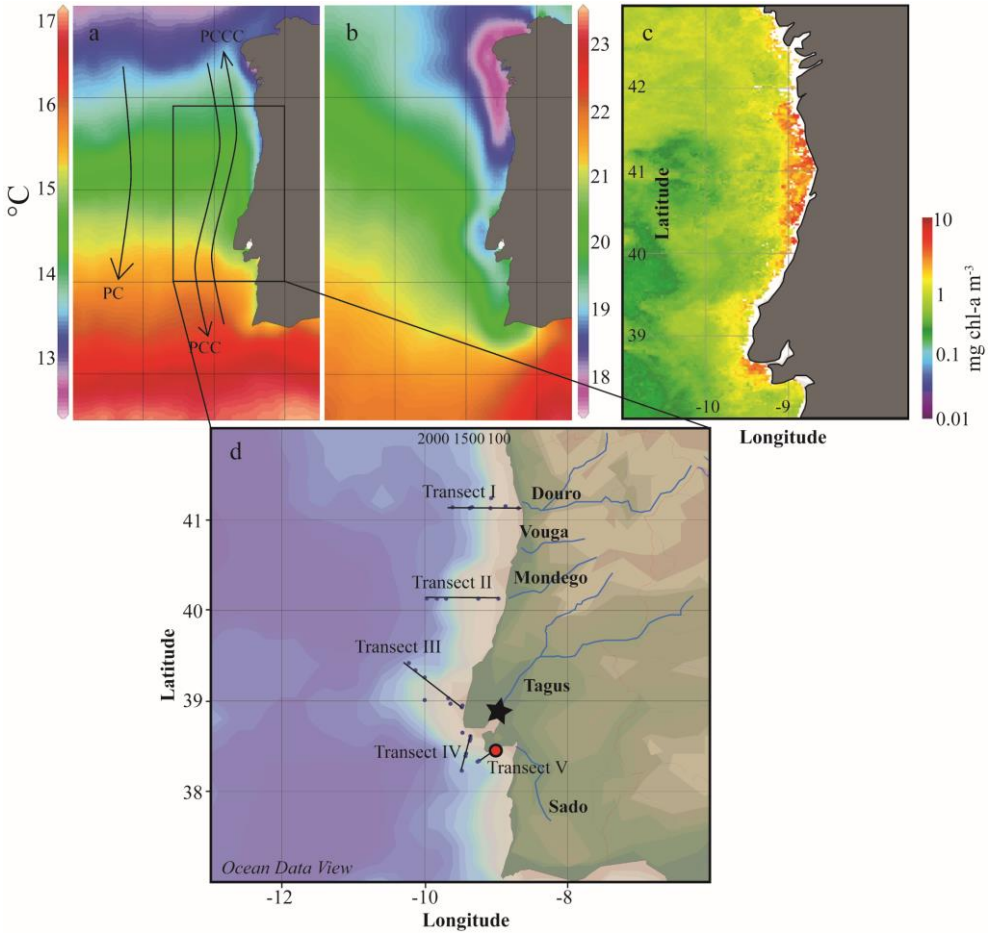

Fig. 1 Mean satellite-derived SST (°C) between 1985 and 2003 for the Portuguese margin during **(a)** winter and **(b)** summer, modified from Salgueiro et al. (2008) who integrated Pathfinder satellite measurements with a 9 km resolution (version 4.1; data from http://podaac-www.jpl.nasa.gov/sst/). Note the different axis scales. Major currents are indicated in panel **(a)**: the Portugal Current (PC), Portugal Coastal Current (PCC) and the Portugal Coastal Countercurrent (PCCC). The upper right panel **(c)** shows average chlorophyll *a* concentrations during April 2001. Visible are the high productivity zones along the Portuguese coast as result of upwelling and river discharge delivering nutrients into the ocean (SeaWiFS satellite data; http://emis.jrc.ec.europa.eu/; European Commision, Joint Research Centre, 2016). The lower panel **(d)** shows the study area with the sample locations of the surface sediments along the five transects. The star symbol indicates SPM sampling in the Tagus river mouth, and the red filled circle reflects the station used for stable carbon isotope analysis.

The two largest rivers delivering nutrients to shelf are the Douro and Tagus (Fig. 1d). The Tagus river has a length of ca. 1000 km, being the longest river of the Iberian Peninsula, with a watershed of about 80.600 km^2 (Jouanneau et al., 1998). The river forms an important source of freshwater input to the continental shelf and includes a large estuary with an area of around 300 to 340 km^2 (Vale and Sundby, 1985). Whereas the mean annual water discharge is around 360 $m^3 s^{-1}$, this discharge ranges between 80 and 720 $m^3 s^{-1}$ due to inter-annual variation, and between 1 and 2200 $m^3 s^{-1}$ on a seasonal scale, due to pronounced dry and wet seasons (Loureiro and Macedo, 1986; Jouanneau et al., 1998). There is a region of persistent high productivity in front of the Tagus river mouth, as evidenced by high chlorophyll concentrations (Fig. 1c; Moita et al., 2003). The Douro, located in the NW of the Iberian Peninsula, with a drainage basin of 95.700 km^2 has an annual mean water discharge of 500 $m^3 s^{-1}$ (Van der Leeden, 1975), and also shows a strong seasonality. Upwelling in front of the Douro shows a large offshore extent, as can be deduced from chlorophyll images (Alt-Epping et al., 2007; Fig. 1c). These dynamic conditions lead to the deposition of sandy sediments (Dias and Nitrouer, 1984). However, there are also deposits of fine-grained sediments, located offshore of the Douro and Tagus river inlets, mainly fed by the two rivers. Off the Douro, this so-called mud belt is around 500 km^2 large and 2 to 5 m thick, and it is located on the mid-shelf around a depth of 90 m (McCave, 1972; Araújo et al., 1994; Drago et al., 1998; 1999; Vitorino et al., 2002). The mud belt off the Tagus estuary covers the continental shelf from the estuary to the shelfbreak. This mud patch results from estuarine deposition, with an area of 560 km^2 and maximum thickness of 25 m (Rodrigues and Matos (1994) cited by Jouanneau et al., 1998). This deposit is confined by the incisions of the Lisbon and Setubal Canyons, delivering river sediment to the basin (Jouanneau et al., 1998). Other rivers entering the Iberian surface ocean, relevant for this study, are the Sado (mean annual discharge < 10 $m^3 s^{-1}$; Loureiro et al., 1986) and the Mondego (mean annual discharge of 82 $m^3 s^{-1}$; Van der Leeden, 1975; Fig. 1d).

2.2 Sample collection and lipid analysis

Marine suspended particulate matter (SPM) and sediment samples were collected during the PACEMAKER 64PE332 cruise with the R/V Pelagia, between 14th and 29th March 2011 (see Zell et al., 2014, 2015). Sediment cores from 31 stations were retrieved from five transects (Fig. 1d) going from inshore to offshore. The top 0.5 cm of the multi-cores were used in this study. Additional to the surface sediments, SPM was collected at three stations of transect I and at four stations of transect IV at different water depths. SPM from the Tagus river mouth was sampled over one year, every month (July 2011 until June 2012, with exception of August 2011; water depth 0 m; sample location indicated by the star symbol in Fig. 1d). Additionally, 16 surface soils and 10 riverbank sediments from the Tagus river watershed were sampled from the source to the mouth of the river in 2012 (for sample locations and description, see Zell et al., 2014). The complete sample set has been previously studied for glycerol dialkyl glycerol tetraethers (GDGTs) (Zell et al., 2014, 2015).

Extracts prepared and described by Zell et al. (2014, 2015) were reanalyzed for this study. Soil, riverbank sediments and marine surface sediments (~2 g dry weight) were extracted using Accelerated Solvent Extraction (ASE), and subsequently separated over an activated Al_2O_3 column into an apolar and polar fraction, using hexane:dichloromethane (DCM) (1:1, vol./vol.) and DCM:methanol (MeOH) (1:1, vol./vol.), respectively. Marine and river SPM samples were also previously extracted using a modified Bligh and Dyer (BD) technique following (Pitcher et al., 2009). These extracts were separated in core lipid (CL) and intact polar lipid (IPL) fractions over an activated silica gel column, using hexane:ethyl acetate (1:1, vol./vol.) and MeOH as eluents, respectively (Oba et al., 2006; Pitcher et al., 2009). Subsequently, the CL fractions were separated over Al_2O_3 into an apolar and polar fractions, using hexane:DCM (1:1, vol./vol.) and DCM:MeOH (1:1, vol./vol.), respectively. For diol analysis, these existing polar fractions were silylated by means of addition of BSTFA (N,O-bis(trimethylsilyl)trifluoroacetamide) and pyridine, and heating at 60 °C for 20 min. Subsequently, the samples were dissolved in ethyl acetate and injected on-column on an Agilent 7890B gas chromatograph (GC) coupled to an Agilent 5977A mass spectrometer (MS). The samples were injected at 70 °C. The oven temperature was programmed to 130 °C by 20 °C min^{-1}, and subsequently to 320 °C by 4 °C min^{-1}; this temperature was held for 25 min. The GC was equipped with an on-column injector and fused silica column (25 m × 0.32 mm) coated with CP Sil-5 (film thickness 0.12 μm). Helium was used as carrier gas at a constant flow of 2 mL min^{-1}. The mass spectrometer operated with an ionization energy of 70 eV and a cycle time of 1.9 s. The injection volume was 1 μL. The long-chain diols were quantified in selective ion monitoring (SIM) mode scanning of their characteristic fragments, i.e., *m*/*z* 299, 313, 327 and 341, with a gain factor of 3 and a dwell time of 100 ms per target ion. Identity confirmation was done in full scan mode by means of the characteristic fragmentation spectra (Versteegh et al., 1997). All samples were analyzed in duplicate, and some in triplicate with a mean SD of 0.01 for Diol Index 1 (Rampen et al., 2008), a mean SD of 0.02 for Diol Index 2 (Willmott et al., 2010), and a mean SD of 0.02 for the LDI, corresponding to 0.6 °C based on the calibration of Rampen et al. (2012). Distribution plots were created in Ocean Data View (ODV; Schlitzer, 2015) using the DIVA gridding algorithm.

2.3 Compound-specific stable carbon isotope analysis

Stable carbon isotopes were measured on isolated long-chain diols from the surface sediment of the first station of transect V, indicated by the red circle in Fig. 1d. For this purpose, the upper 1 cm core-top sediment (23.4 g dry weight) of this station was used. The sediment was homogenized and extracted by ASE with a DCM:MeOH (9:1, vol./vol.) mixture to obtain the total lipid extract (TLE). Solvent was removed under a stream of nitrogen. The TLE was subsequently redissolved in DCM and water was removed over anhydrous Na_2SO_4, after which the extracts were dried under a stream of nitrogen. The extract was separated by column chromatography. Activated (at 150 °C for 2 h) Al_2O_3 was used as stationary phase,

using DCM and DCM/MeOH (1:1, vol./vol.) as eluents to yield the apolar and polar fraction, respectively.

Since diols of the same chain length but different mid-chain positions of the alcohol groups coelute upon gas chromatographic separation, it was not possible to analyze the isotopic composition of individual isomers by GC-IRMS directly. Becker et al. (2015) previously demonstrated separation of diols with different mid-chain positions of the alcohol group using normal phase HPLC. We therefore applied semi-preparative normal phase HPLC to separate diols with differing mid-chain positions of the alcohol group prior to isotope analysis. The polar fraction was prepared for semi-preparative normal phase HPLC by dissolving in hexane/isopropanol (99:1, vol./vol.) and filtration over a polytetrafluoroethylene (PTFE) filter (0.45 µm pore size, Grace, USA). The polar fraction (8.9 mg) was then fractionated by high performance liquid chromatography (HPLC) using an Agilent 1100 series HPLC (Agilent Technologies, USA) equipped with a fraction collector (ISCO Foxy Jr, Teledyne ISCO, USA). Separation of the diol isomers was achieved over a semi-preparative silica column (250 mm × 10 mm; 10 µm; Alltech Econosphere, Grace, USA) at room temperature. Diols were eluted with 86 % A and 14 % B for the first 35 min, followed by a gradient to 100 % B in 1 min, kept for 30 min, after which B was brought back to 14 %. A = hexane and B = hexane/isopropanol (9:1, vol./vol.). The flow was kept constant at 3 mL min^{-1}. Thirty second fractions were collected, of which a small aliquot (~2 %) was analyzed for diols using GC-MS in SIM mode as described above. Diols eluted between 10 and 40 minutes. The fractions that were pooled together to isolate a certain diol isomer are highlighted by the rectangles surrounding the fractions (Fig. 3) and these pooled fractions were used to measure the individual $\delta^{13}C$ of the diol isomers. In this manner, the mono-unsaturated $C_{30:1}$ 1,14-diol, the saturated C_{32} 1,15-, C_{28} 1,13- and C_{28} 1,14-diol were isolated and analyzed by GC-IRMS. Purity of the isolated product was assessed by means of GC-MS in full scan mode (*m*/*z* 50–800).

Isotopic composition of the isolated diols was analyzed using gas chromatography – isotope ratio mass spectrometry (GC-IRMS). For this the diols were silylated, as described above, using BSTFA with a known $\delta^{13}C$ value of -32.2±0.5 ‰. The samples were analyzed on a Thermo Delta V isotope ratio monitoring mass spectrometer coupled to an Agilent 6890 GC. The GC conditions are the same as described for the GC-MS above. The samples were analyzed in triplicate; the reported data represent averaged values, and are reported in delta notation relative to the VPDB standard using CO_2 reference gas calibrated to the NBS-22 reference material. The instrument error was <0.3 ‰ based on repeated injection of external deuterated *n*-alkane standards (C_{20} and C_{24} perdeuterated *n*-alkanes) prior to and after sample analysis. Correction for the addition of the labelled trimethylsilyl groups was achieved via the following equation:

$$\delta^{13}C_{DC}\,(‰\ VPDB) = ((C_{DC}\times\delta^{13}C_{COM}) - (C_{BSTFA}\times\delta^{13}C_{BSTFA}))/C_{COM} \quad (5)$$

where $\delta^{13}C_{DC}$ is the $\delta^{13}C$ of the derivatised compound, C_{DC} the carbon number of the derivatised compound, $\delta^{13}C_{COM}$ the $\delta^{13}C$ of the underivatised compound, C_{BSTFA} the number of carbon atoms added by the BSTFA, $\delta^{13}C_{BSTFA}$ the $\delta^{13}C$ value of the BSTFA (-32.2 ‰), and C_{COM} the carbon number of the underivatised compound (Rieley, 1994). This correction leads to an additional uncertainty of ca. ±0.2‰.

3. Results

3.1 Long-chain diol distributions

3.1.1 Marine sediments and SPM

All 31 surface sediments contained detectable amounts of long-chain diols, although the abundances were generally low. Long-chain diols were not detected in the marine SPM. For the 1,13- and 1,15-diols, the dominant chain lengths were C_{28}, C_{30} and C_{32}, and for the 1,14-diols these were C_{28} and C_{30} (Table 1). The mono-unsaturated $C_{30:1}$ 1,14-diol and saturated C_{28} 1,14-diol were detected in only a few sediments. The $C_{30:1}$ 1,14-diol was mainly detected close to the coastline, whereas the C_{28} 1,14-diol was also observed offshore. Besides diols, the C_{30} and C_{32} keto-ols (Versteegh et al., 1997) and the C_{29} 12-hydroxy methyl alkanoate (Sinninghe Damsté et al., 2003) were detected in all sediments. The fractional abundance of the C_{32} 1,15-diol (normalized with respect to all diols) ranged between 0.05 and 0.23 with the highest values at the Tagus river mouth, and overall higher fractional abundances along the coast and lower abundances further offshore (Fig. 3). The C_{30} 1,14-diol had the highest fractional abundance (up to 0.91) directly along the coast (especially the northern part), while the C_{30} 1,15-diol and C_{28} 1,13-diol showed the opposite trend with higher abundances (up to 0.52 and 0.28, respectively) in open ocean surface sediments and lower abundances (0.10 and 0.05, respectively) along the Portuguese margin (Fig. 2). Accordingly, both upwelling indices based on diols (Eq. 3 and 4) were highest along the coastline (especially in the northern part) and decreased offshore (Figs. 5a-b). Diol Index 1 (Rampen et al., 2008) ranged between 0.87 and 0.25, and Diol Index 2 (Willmott et al., 2010) ranged between 0.83 and 0.38. LDI values varied between 0.38 and 0.69, corresponding with SSTs varying between 8.5 and 18 °C. The distribution plot of the LDI values (Fig. 5e) shows the lowest LDI values in front of the Tagus and Sado river, and higher LDI values offshore compared to onshore.

3.1.2. Riverine SPM and sediments

For the riverine SPM, the same long-chain diols were detected as in the marine surface sediments except for the C_{28} 1,13- and 1,14-diol and the $C_{30:1}$ 1,14-diol, which were not detected. Also, the C_{29} 12-hydroxy methyl alkanoate was not detected. However, we did identify the C_{32} 1,17-diol which was not detected in the marine surface sediments. Between

67 and 89 % of the long-chain diols was made up by the C_{30} and C_{32} 1,15-diol, while the C_{32} 1,17-diol contributed between 11 and 27 %. The C_{30} 1,13- and 1,14-diols had much lower fractional abundances compared to the marine surface sediments (Table 1). The relatively high fractional abundance of the C_{32} 1,15-diol, ranging between 0.25 and 0.50 is notable. LDI values could not be calculated due to the absence of the C_{28} 1,13-diol. Values for the diol upwelling indices were generally lower than in marine sediments, ranging between 0.03–0.10 for Diol Index 1 (Rampen et al., 2008) and between 0.20–0.49 for Diol Index 2 (Willmott et al., 2010). Long-chain diols were not detected in the riverbank sediments or in the soils of the river watershed.

3.2 Compound specific carbon isotopes

To determine the origin of long-chain diols in the Portuguese margin, we analyzed the stable carbon isotopic composition of several diol isomers in the core top sediment of the first station of transect V in front of the Sado (indicated by a red dot in Fig. 1d). Prior to stable isotope analysis the diol isomers were isolated by preparative HPLC since on GC-IRMS diols of the same chain length but different position of the alcohol position co-elute. Mass spectrometry analysis did not reveal co-eluting diol isomers in the pooled fractions of the C_{32} 1,15- and $C_{30:1}$ 1,14-diol. The pooled C_{28} 1,13-diol fraction contained a minor amount (3 %) of the co-eluting C_{28} 1,14-diol, and the C_{28} 1,14-diol fraction contained some (12 %) co-eluting C_{28} 1,13-diol. Isotopic analysis showed that the C_{32} 1,15-diol had the most ^{13}C-enriched value ($\delta^{13}C$ = -31.3±0.7 ‰), followed by the C_{28} 1,13-diol ($\delta^{13}C$ = -32.6±0.5‰), while the C_{28} 1,14- and $C_{30:1}$ 1,14-diols were more depleted in ^{13}C ($\delta^{13}C$ = -34.6±0.4 ‰ and -38.4±0.4 ‰, respectively).

									Indices		
	C_{28} 1,14	C_{28} 1,13	C_{30} 1,15	C_{30} 1,14	$C_{30:1}$ 1,14	C_{30} 1,13	C_{32} 1,15	C_{32} 1,17	**LDI**	**Diol Index 1**	**Diol Index 2**
Transect I											
1	n.d.	0.07	0.10	0.50	0.19	0.05	0.10	n.d.	0.46	0.84	0.82
2	n.d.	0.05	0.12	0.50	0.20	0.05	0.08	n.d.	0.55	0.80	0.83
3	n.d.	0.17	0.22	0.36	0.11	0.10	0.05	n.d.	0.45	0.62	0.58
4	n.d.	0.19	0.24	0.40	n.d.	0.12	0.06	n.d.	0.44	0.63	0.57
5	n.d.	0.15	0.48	0.25	n.d.	0.12	0.09	n.d.	0.62	0.34	0.45
6	n.d.	0.19	0.40	0.24	n.d.	0.11	0.06	n.d.	0.57	0.38	0.45
7	n.d.	0.17	0.43	0.24	n.d.	0.09	0.06	n.d.	0.63	0.36	0.48
Transect II											
1	n.d.	n.d.	0.13	0.91	n.d.	n.d.	n.d.	n.d.	-	0.87	-
2	n.d.	0.13	0.25	0.40	n.d.	0.12	0.09	n.d.	0.50	0.61	0.61
3	n.d.	0.15	0.52	0.17	n.d.	0.09	0.07	n.d.	0.69	0.25	0.42
4	0.03	0.16	0.44	0.23	n.d.	0.09	0.06	n.d.	0.63	0.36	0.49
5	n.d.	0.21	0.40	0.26	n.d.	0.08	0.05	n.d.	0.58	0.39	0.47
Transect III											
1	0.02	0.06	0.17	0.43	0.17	0.07	0.08	n.d.	0.58	0.72	0.78
2	n.d.	0.11	0.21	0.52	n.d.	0.07	0.08	n.d.	0.54	0.71	0.74
3	0.02	0.13	0.28	0.34	0.09	0.09	0.05	n.d.	0.56	0.56	0.62
4	0.03	0.18	0.28	0.33	0.03	0.09	0.06	n.d.	0.51	0.56	0.57
5	n.d.	0.17	0.45	0.20	n.d.	0.12	0.06	n.d.	0.61	0.31	0.42
6	n.d.	0.16	0.50	0.17	n.d.	0.10	0.07	n.d.	0.66	0.25	0.39
7	0.03	0.15	0.47	0.20	n.d.	0.10	0.07	n.d.	0.66	0.32	0.48
8	0.04	0.17	0.47	0.23	n.d.	0.07	0.06	n.d.	0.66	0.36	0.52
Transect IV											
1	n.d.	0.18	0.22	0.24	n.d.	0.13	0.23	n.d.	0.42	0.52	0.44
2	n.d.	0.10	0.18	0.31	0.13	0.09	0.19	n.d.	0.49	0.63	0.62
3	n.d.	0.18	0.25	0.35	n.d.	0.12	0.10	n.d.	0.45	0.58	0.54
4	n.d.	0.25	0.25	0.29	n.d.	0.12	0.10	n.d.	0.40	0.54	0.44
5	n.d.	0.24	0.33	0.23	n.d.	0.13	0.07	n.d.	0.47	0.41	0.38
6	0.03	0.18	0.35	0.25	n.d.	0.11	0.07	n.d.	0.54	0.45	0.49
7	0.04	0.13	0.40	0.26	n.d.	0.10	0.08	n.d.	0.64	0.43	0.57
Transect V											
1	0.03	0.13	0.17	0.36	0.11	0.10	0.10	n.d.	0.42	0.70	0.63
2	n.d.	0.28	0.23	0.30	n.d.	0.11	0.11	n.d.	0.38	0.56	0.44
3	0.03	0.19	0.34	0.26	n.d.	0.11	0.07	n.d.	0.53	0.46	0.49
4	0.03	0.19	0.38	0.23	n.d.	0.10	0.07	n.d.	0.57	0.41	0.48
SPM											
Tagus river											
12/07/2011	n.d.	n.d.	0.47	0.01	n.d.	0.02	0.25	0.24	-	0.03	0.39
16/09/2011	n.d.	n.d.	0.41	0.03	n.d.	0.05	0.34	0.17	-	0.06	0.36
18/10/2011	n.d.	n.d.	0.41	0.02	n.d.	0.05	0.30	0.21	-	0.05	0.34
22/11/2011	n.d.	n.d.	0.29	0.02	n.d.	0.08	0.48	0.13	-	0.07	0.20
16/12/2011	n.d.	n.d.	0.34	0.04	n.d.	0.07	0.41	0.14	-	0.10	0.35
16/01/2012	n.d.	n.d.	0.39	n.d.	n.d.	n.d.	0.50	0.11	-	-	-
17/02/2012	n.d.	n.d.	0.35	0.04	n.d.	0.06	0.36	0.20	-	0.09	0.38
16/03/2012	n.d.	n.d.	0.36	0.02	n.d.	0.04	0.35	0.23	-	0.06	0.36
12/04/2012	n.d.	n.d.	0.32	0.03	n.d.	0.03	0.34	0.27	-	0.08	0.45
24/05/2012	n.d.	n.d.	0.41	0.03	n.d.	0.04	0.28	0.24	-	0.08	0.49

Table 1 Relative abundances of the different long-chain diols and calculated indices for the different surface sediment transects. Transects are shown in Fig. 1; the numbers indicate the sample stations, with 1 representing the station closest to the coast, and increasing further offshore. The dates for the Tagus river SPM indicate the time of sampling. n.d. = not detected. The $C_{30:1}$ 1,14-diol abundances were not corrected for the differences in contributions of the selected ions to the total mass spectrum.

It is known that separation by HPLC can potentially cause isotopic fractionation and lead to erroneous $\delta^{13}C$ values if the compounds are not quantitatively recovered (Caimi and Brenna, 1997). To constrain this issue we isolated a pure C_{28} 1,13-diol standard using the identical approach as described above and its isotopic composition was compared to that determined directly by GC-IRMS. The 7 collection vials over which this standard became distributed contained 99.8 % of the starting material. The stable carbon isotopic variation across the chromatographic peak showed, as expected, relatively ^{13}C-depleted molecules eluting at the front of the peak and relatively ^{13}C-enriched molecules eluting in the tail (Fig. 4). Based on this experiment we estimate that when >80 % of a long-chain diol is isolated, isotopic fraction due to semi-preparative HPLC is < 0.5 ‰, i.e., within the analytical error of a typical GC-IRMS analysis. In our study, we isolated > 80 % for all diol isomers analyzed by GC-IRMS.

4. Discussion

4.1 Sources of 1,14-diols and the applicability of the Diol Indices

The 1,14-diols have been reported in *Proboscia* diatoms (Sinninghe Damsté et al., 2003; Rampen et al., 2007) and in the alga *Apedinella radians* of the Dictyochophyceae phylum (Rampen et al., 2011). *Proboscia* has been confirmed as a likely source of long-chain 1,14-diols (Rampen et al., 2008), but the importance of *Apedinella* as source of 1,14-diols in the ocean is still uncertain. Here, all the marine sediments contained the C_{29} 12-OH-methyl alkanoate, which is a typical biomarker for *Proboscia* diatoms (Sinninghe Damsté et al., 2003). Furthermore, we detected the mono-unsaturated $C_{30:1}$ 1,14-diol, present in *Proboscia* diatoms, but not the C_{32} 1,14-diol, which is present in *Apedinella radians* (Rampen et al., 2011). Additionally, two studies have reported *Proboscia alata* diatoms along the west coast of Portugal (Schott et al., 1997; Moita et al., 2003). Finally, the low fractional abundance of 1,14 diols in the Tagus river SPM (between 1 and 4 % of total long-chain diol assemblage; Table 1) is consistent with a predominant marine source for these diols, i.e., *Proboscia* diatoms.

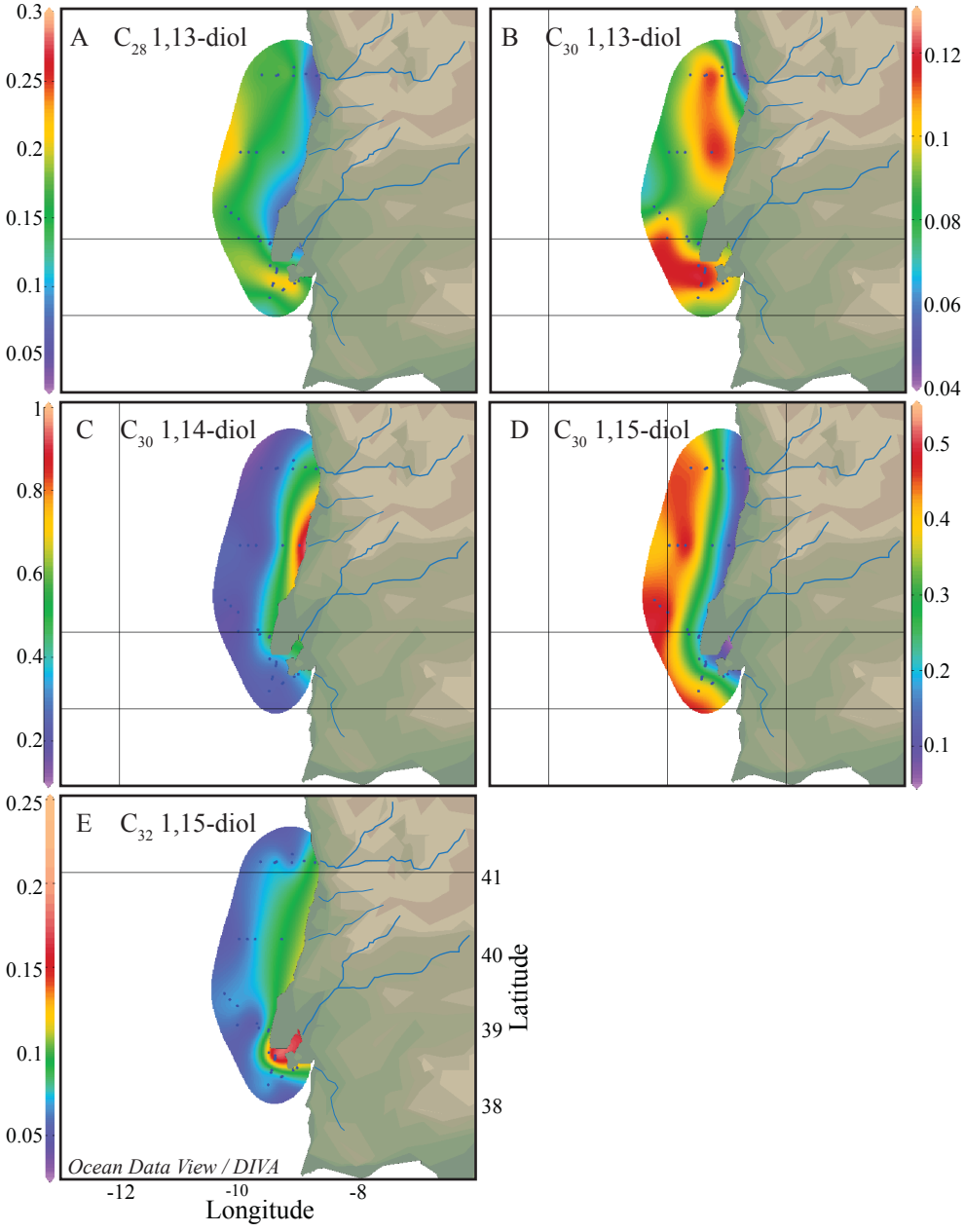

Fig. 2 Distribution plots for the five major long-chain diols normalized with respect to all diols (Table 1). Maps drawn in Ocean Data View, and modified manually.

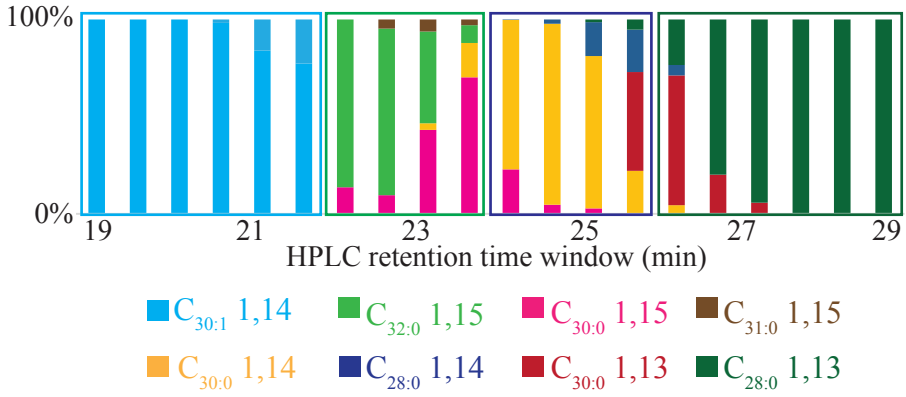

Fig. 3 A stacked column chart reflecting the distribution of long-chain diols in fractions prepped by HPLC of a surface sediment (transect V, indicated by red dot in the map of Fig. 1d). The long-chain diols were separated based on position of the mid-chain alcohol. Compound identification was achieved by analyzing every collection vial (every half minute) on GC-MS (the bars represent the different collection vials). The isolation of the diols after semi-preparative HPLC led to the additional detection of the C_{31} 1,15-diol. The long-chain diols selected for pooling and subsequent compound specific carbon analysis are highlighted by the 4 different colored boxes: $C_{30:1}$ 1,14-, $C_{32:0}$ 1,15-, $C_{28:0}$ 1,14- and $C_{28:0}$ 1,13-diol, from left to right.

To reinforce that the 1,14-diols derive from a different source than the 1,13- and 1,15-diols, the stable carbon isotope values for C_{28} 1,13-, C_{28} 1,14-, $C_{30:1}$ 1,14- and the C_{32} 1,15-diol were determined. The 1,14-diols were depleted in ^{13}C by 2.0 to 7.1 ‰ compared to the 1,13- and 1,15-diols in the sediments. Sinninghe Damsté et al. (2003) determined the $\delta^{13}C$ values of the C_{28} 1,14-diol (predominantly 1,14-isomer), $C_{30:1}$ 1,14-diol, C_{32}-diol (60 % 1,15-isomer, 40 % 1,17 isomer) and the C_{30} diol in an Arabian Sea sediment. Similar to our results, they observed that the 1,14-diols were depleted in ^{13}C relative to the 1,13- and 1,15-diols in the sediments (by 1.5 to 5.2 ‰), and that the C_{32}-diol was most enriched in ^{13}C relative to the other diols measured. The fact that the 1,14-diols are isotopically distinct from the 1,13- and 1,15-diols supports the hypothesis that they are derived from different sources. Interestingly, the $\delta^{13}C$ values of the C_{28} and $C_{30:1}$ 1,14-diols differed by ca. 4 ‰, suggesting that these compounds may be produced by different organisms. Alternatively, these compounds are produced by the same organism, but have biosynthetically induced different carbon isotope compositions. However, Sinninghe Damsté et al. (2003) found only a small (~1 ‰) isotopic offset between 1,14 diol isomers measured for a *P. indica* culture. This suggests that the large isotopic discrepancy which we observe between the C_{28} and $C_{30:1}$ 1,14-diols, is likely due to different source organisms (e.g. a different *Proboscia* source). This is in agreement with the different distributions of these diols in the surface sediments, as the $C_{30:1}$ 1,14-diol was only

detected close to the coastline (coinciding with high abundances of the saturated C_{30} 1,14-diol), whereas the C_{28} 1,14-diol was more abundant offshore.

Values of both Diol Index 1 (Rampen et al., 2008) and Diol Index 2 (Willmott et al., 2010) are relatively high along the northern part of the coastal studied area, and decrease further away from the coast (Figs. 5a-5b). This fits well with the coastal upwelling during summer (Figs. 1b-c), potentially with *Proboscia alata* blooms, suggesting the Diol Indices reflect summer upwelling in this region. Thus, both Diol Indices seem to be applicable here. It has been previously shown by Rampen et al. (2014a) that Diol Index 1 is also affected by temperature and therefore not suitable as a global upwelling index. However, since the SST gradient is relatively small (ca. 2 °C) in our study area, this has likely not affected the applicability of the index here in this region.

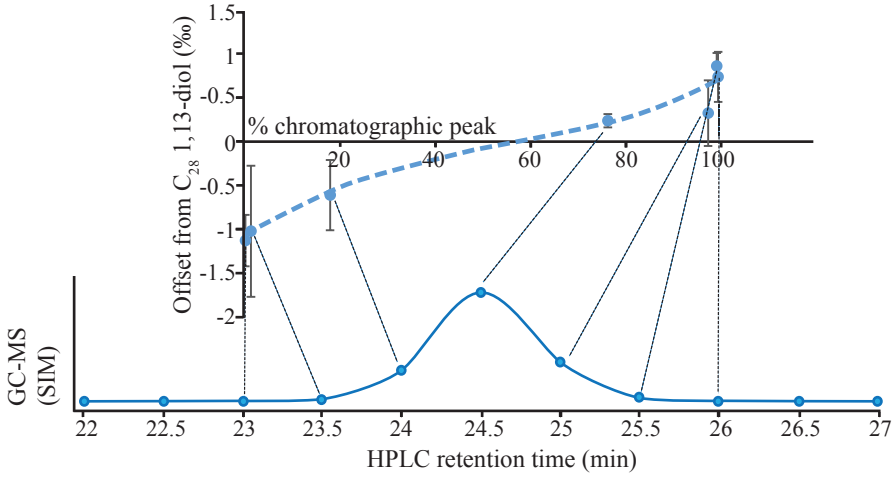

Fig. 4 The upper panel shows the variation in stable carbon isotopic composition across the chromatographic peak of the C_{28} 1,13-diol synthetic standard. The *x*-axis is the percentage of the total compound eluted, and the *y*-axis represents the offset from the $\delta^{13}C$ value of the prepped C_{28} 1,13-diol fractions versus the starting material. The dashed curve represents a third order polynomial fit. The lower panel shows the chromatographic peak (on LC) separated over 11 semi-preparative collection vials of which the C_{28} 1,13-diol of the central 7 collection vials was analyzed by GC-IRMS.

4.2 Sources of the C_{32} 1,15-diol

From our core top dataset, it is clear that the highest fractional abundance of the C_{32} 1,15-diol is near the river mouth of the Tagus (Table 1; Fig. 2e). However, when we consider the fractional abundance of this diol only with respect to the C_{28} 1,13- , C_{30} 1,13- and C_{30} 1,15-diol (i.e., normalize on the diol assemblage without the 1,14-diols so that we compare

compounds potentially all derived from the same source), it becomes evident that its fractional abundance is also high in front of the river mouth of the Douro (Fig. 5d). This distribution of the fractional abundance of the C_{32} 1,15-diol is remarkably similar to that reported for the BIT index (Zell et al., 2015) (Figs. 5c-d) and the two proxies correlate well ($R^2 = 0.67$; $p < 0.001$). Since the BIT index is a proxy for the input of soil and riverine organic matter transported from land into the marine realm (Hopmans et al., 2004; Huguet et al., 2006; Walsh et al., 2008; Kim et al., 2009a; Zell et al., 2013; 2014; de Jonge et al., 2014a), this could suggest that the C_{32} 1,15-diol is predominantly derived from land. Zell et al. (2015) showed for the Tagus river that the declining brGDGT concentrations with increasing distance from the river is the main factor in the declining BIT. Indeed, there is a strong correlation between the fractional abundance of the C_{32} 1,15-diol and the sum of non-cyclized brGDGTs (brGDGTs used in the BIT index; $R^2 = 0.80$, n = 30; $p < 0.001$; Fig. 6). A riverine source of the C_{32} 1,15-diol is confirmed by the high relative abundances of this long-chain diol in the Tagus river SPM: the average fractional abundance of the C_{32} 1,15-diol (with respect to the 1,13- and 1,15-diols) is 0.46, coinciding with an average BIT index of 0.71 (Zell et al., 2015). Collectively these data suggest that the C_{32} 1,15 diol is transported by rivers to the marine environment. Interestingly, we have not detected any long-chain diols in the soils in the watershed of the river, or in the riverbank sediments, suggesting that the C_{32} 1,15-diol is not produced in soils but in situ in the river itself. Fig. 7 shows the fractional abundances of the different diol isomers detected in the Tagus river SPM. Seemingly, the C_{32} 1,15-diol reveals an opposite pattern compared to the other diols, with highest fractional abundance during winter. This might suggest that the C_{32} 1,15-diol derives from a different source. Also the C_{32} 1,17-diol, solely detected in the river SPM, reveals an opposite trend as compared to the C_{32} 1,15-diol, with lowest fractional abundance during winter. Consequently, this also implies that the C_{32} 1,15-diol and C_{32} 1,17-diol are likely to be produced by different source organisms.

Results of previous studies support our hypothesis of a possible additional freshwater source for the C_{32} 1,15-diol in coastal marine environments. Versteegh et al. (1997) developed a Diol Index, defined as the ratio of the C_{30} 1,15-diol over the sum of the C_{30} 1,15- and C_{32} 1,15-diol and observed that the index was generally lower, implying relative high abundances of the C_{32} 1,15-diol, in freshwater sediments compared to the ocean sediments. Indeed, the C_{32} 1,15-diol is often the most abundant diol in lake sediments (Xu et al., 2007; Castañeda et al., 2009; Shimokawara et al., 2010; Romero-Viana et al., 2013; Rampen et al., 2014b). Furthermore, Versteegh et al. (2000) observed higher relative abundances of the C_{32} 1,15-diol and -keto-ol below the Congo River plume, while Rampen et al. (2014b) observed high fractional abundances of the C_{32} 1,15-diol in sediments of the Hudson Bay, which is a large inland sea in Canada, strongly influenced by riverine input. Collectively, this suggests that the C_{32} 1,15-diol might be a good tracer for the relative amount of fluvial input into coastal marine environments. However, to confirm this hypothesis, further studies of other coastal regions are needed.

Additional reinforcement of the hypothesis that the C_{32} 1,15-diol might derive from rivers comes from the stable carbon isotopic composition. The C_{32} 1,15-diol is, with a $\delta^{13}C$ value of -31.3‰, the most enriched in ^{13}C compared to other diols, and differs by 1.3‰ relative to the C_{28} 1,13-diol, generally assumed to be produced by the same organism. However, this difference is relatively small (on the edge of significance: two-tailed $p = 0.053$; measurement and instrument error 0.8 and 0.3‰) and it is not known yet how $\delta^{13}C$ values of different diol isomers vary within algal species. Therefore, culture studies are needed to assess if this truly signifies a different source or whether it reflects biosynthetic differences.

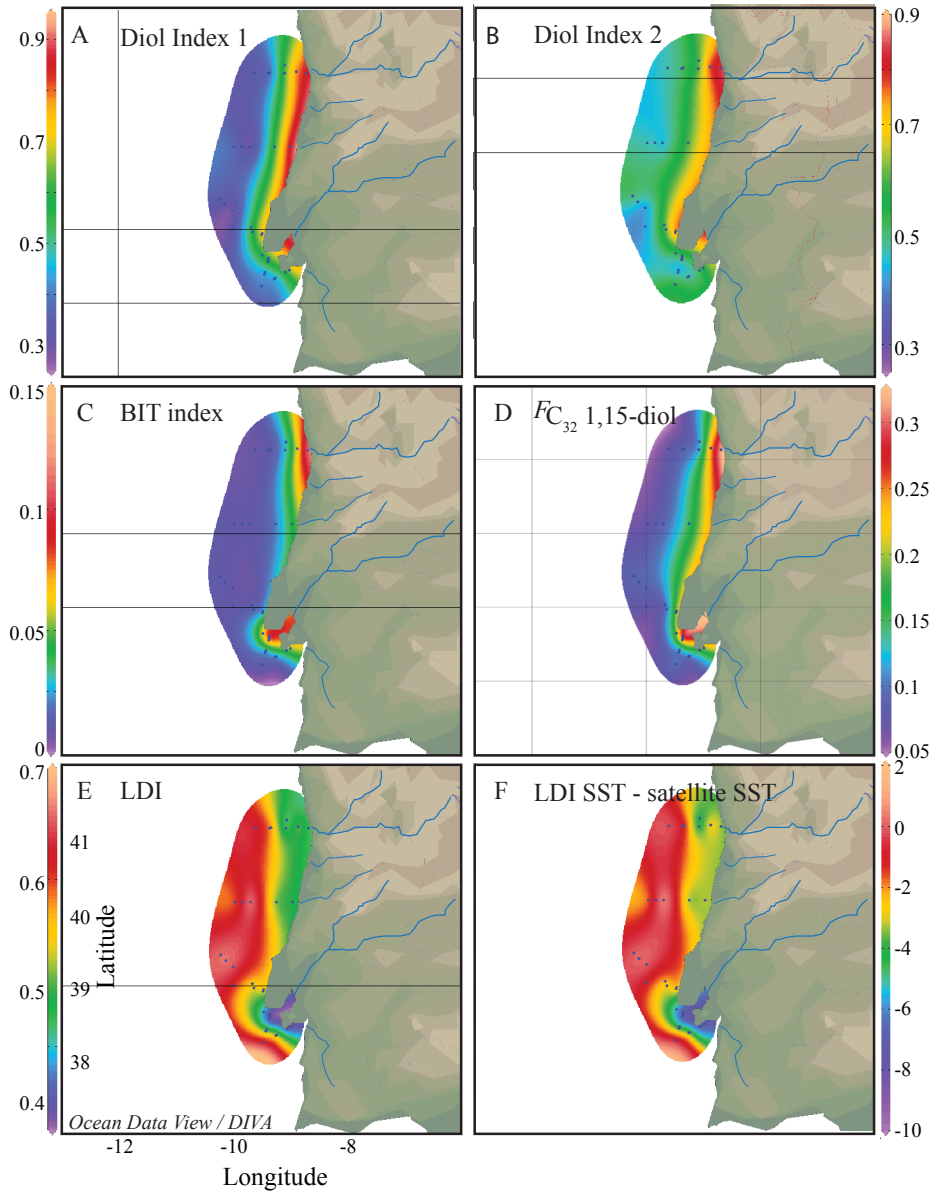

Fig. 5 Distribution plot of **(a)** Diol Index 1, **(b)** Diol Index 2, **(c)** the BIT index, **(d)** the fractional relative abundance ('*F*') of the C_{32} 1,15-diol relative to the fractional abundances of the C_{28} 1,13- and C_{30} 1,13- and 1,15-diols, **(e)** the Long chain Diol Index (LDI) and **(f)** the difference in absolute temperature (°C) between the LDI sea surface temperature estimates and the actual satellite mean annual SSTs. Maps drawn in Ocean Data View, and modified manually.

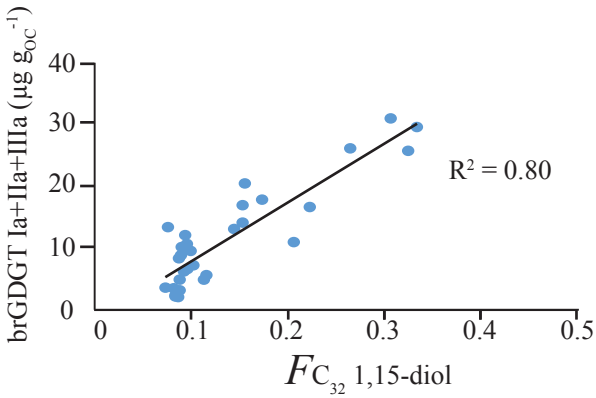

Fig. 6 Fractional abundance ('*F*') of the C_{32} 1,15-diol (relative to the fractional abundances of the C_{28} 1,13- and C_{30} 1,13- and 1,15-diols) in marine surface sediments versus the summed concentration of the main brGDGTs (Zell et al., 2015).

4.3 Long chain Diol Index (LDI)

We compared our LDI-derived SST data with satellite annual mean SSTs (from Kim et al., 2010). In this region, annual mean SST varies between ca. 15 and 17 °C, with a latitudinal temperature gradient, i.e., a decreasing SST from North to South. However, the LDI-derived SSTs revealed a much larger range of ca. 9 to 17 °C. Indeed, there is a poor correlation between the LDI-derived SST and satellite SST ($R^2 = 0.18$, n = 31; $p < 0.019$). Fig. 5F shows the spatial distribution of the mismatch between the calculated LDI temperatures and the mean annual SST. For most sediments, in particular offshore sediments, the offset was less than the 2 °C, the standard error of the estimate of the LDI (Rampen et al., 2012), suggesting that the LDI reflects mean annual SST. LDI temperature estimates offshore (~16–17 °C) agree best with annual mean SST (~16–17 °C), as winter SST offshore varies between ~14 and 15.5 °C and summer SST between ~18 and 20 °C. We observed mismatches of -3 to -4 °C between LDI SSTs and satellite annual mean SSTs along the coast line in front of the Douro and Mondego, and consequently LDI-derived SSTs agree better with winter SST. The LDI-derived temperatures in the Tagus prodelta and Sado estuary showed the largest offset of up to -9 °C compared to the annual mean SST, and up to -7 °C relative to winter SST. This large temperature difference is unlikely to result from cold deeper water rising to the surface during summer upwelling, since upwelling mainly occurs northward off the Douro, and upwelling conditions might lower SST by only ca. 2 °C (Fig. 1b). Moreover, the gradient in LDI SST estimates around the Tagus seems to trace the river outflow out of the Tagus and

Sado estuary. Since the Tagus has the highest discharge during winter it might be that the outflow of cold river water simply lowers the seawater temperature. However, this would also be evident from satellite SST, and we would expect the same effect for the Douro. Alternatively, it might be that the offset between LDI-derived temperatures and satellite SSTs is the result of an input of diols derived from the river. Based on our analysis of riverine SPM, it is likely that, apart from the C_{32} 1,15-diol, the river delivers other diols to the shelf region.

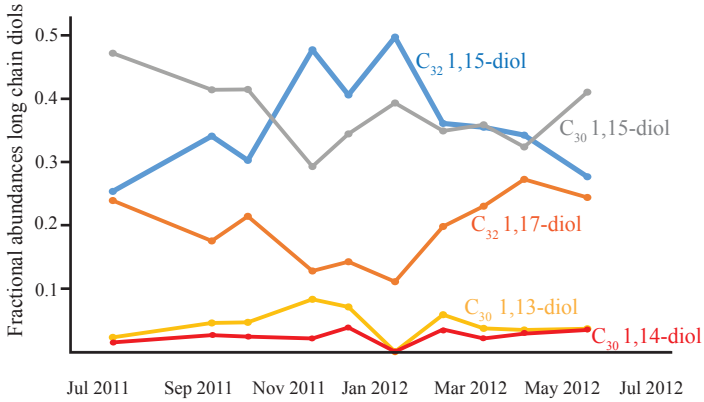

Fig. 7 The fractional abundances of the different diol isomers measured in the Tagus River suspended particulate matter over 2011 – 2012.

Averaged over the sampling year, the C_{30} 1,15-diol was slightly higher in abundance than the C_{32} 1,15-diol in the river SPM, so we would also expect to observe a riverine contribution of this diol into the marine realm. However, the relative abundance of the C_{30} 1,15-diol in the surface sediments is lowest in front of the rivers, and increases offshore. Moreover, a contribution of this diol would lead to a much higher LDI rather than lower. Furthermore, the C_{32} 1,17-diol (detected in Tagus river SPM) was not detected in the surface sediments in front of the Tagus river mouth. Therefore, it is unlikely that the input of riverine diols is an explanation for the offset in the values of the LDI in the areas affected by riverine input.

There is no substantial gradient in the annual mean salinity resulting from river outflow (Kim et al., 2016), and seasonal variations in salinity in the Tagus prodelta are relatively small (Bartels-Jónsdóttir et al., 2008), hence, it is unlikely that the proxy signal is affected by changes in salinity in this region. Possibly, the marine diol producers present in the region of the Tagus and Sado river outflows are different from those near the Douro and in the open ocean due to the input of (micro)nutrients. Indeed, chlorophyll *a* data reveal that there is persistently high productivity offshore of the mouth of the Tagus (e.g. Fig. 1c), as induced by summer, as well as the less intense winter upwelling, and the year-round discharge of the Tagus river (e.g. Alt-Epping et al., 2008). Off the Douro, coastal upwelling is likely the most important source for nutrients. Further research examining other coastal marine environments with large fluvial inputs is needed to investigate whether the LDI is compromised in these regions.

5. Conclusions

In this study, we have explored the long-chain diol distributions along the Iberian Atlantic margin. The two Diol Indices, based on the relative abundance of the 1,14-diols, were applied to test their applicability as upwelling indicators and both indices seemed to work well in this region. Carbon isotope analysis of different diol isomers implies that the 1,14-diols have different sources than the 1,13- and 1,15-diols. However, we observed a large isotopic discrepancy between the $C_{30:1}$ 1,14-diol and the C_{28} 1,14-diol (3.8±0.8 ‰), suggesting different sources.

Whereas offshore the LDI-based SST values are close to satellite mean annual SST, near-shore we observe large discrepancies in front of the Douro and Mondego rivers (-3 to -4 °C), but especially in the Tagus prodelta and Sado estuary with temperature offsets of up to -9 °C. This offset is likely not caused by the input of diols derived from the rivers, as the diol distribution in SPM of the Tagus river suggests that river contribution would lead to higher temperatures rather than lower. Possibly, freshwater and nutrient input from the Tagus and Sado rivers creates conditions in which different organisms proliferate as compared to the rest of the shelf and the open ocean, leading to these different diol distributions in the sediments. Further research is essential to assess whether fluvial input compromises the LDI proxy in other regions.

High fractional abundances of the C_{32} 1,15-diol in front of the Douro and Tagus rivers and in the Tagus river SPM as well as a strong correlation with the BIT suggest that it is partly derived from the continent. The absence of long-chain diols in riverbank sediments and watershed soils, leads to the hypothesis that the C_{32} 1,15-diol is predominantly produced in situ in rivers. Stable carbon isotope analysis of this diol supports this hypothesis, since we obtain an isotopic difference of 1.3 ‰ relative to the marine C_{28} 1,13-diol. However, culture studies are needed to assess whether this small isotopic offset is indeed the result of different sources.

Acknowledgements

We thank Anchelique Mets and Monique Verweij for analytical support, and Claudia Zell, Jung-Hyun Kim, Jérôme Bonnin and Marianne Baas for sampling. We thank an anonymous reviewer, Dr. Rodrigo-Gámiz and Dr, Elizabeth Canuel for useful comments which have improved the manuscript. The crew of the R/V Pelagia is thanked for their services. This research has been funded by the European Research Council (ERC) under the European Union's Seventh Framework Program (FP7/2007-2013) ERC grant agreement [339206] to S.S. S.S. and J.S.S.D. receive financial support from the Netherlands Earth System Science Centre (NESSC).

Chapter 7

A Late Quaternary climate record based on long-chain diol proxies from the Chilean margin

Marijke W. de Bar, Dave J. Stolwijk, Jerry F. McManus, Jaap S. Sinninghe Damsté and Stefan Schouten

Climate of the Past 14 (2018)

DOI: 10.5194/cp-14-1783-2018

Abstract

In this study we have applied different indices based on long-chain diols, i.e., the Long chain Diol Index (LDI) as proxy for past SST, the Diol Index as indicator of past upwelling conditions and the Nutrient Diol Index (NDI) as proxy for nitrate and phosphate concentrations in seawater. The proxies were analyzed in marine sediments recovered at ODP Site 1234, located within the Peru-Chile upwelling system, with a ~2 kyr resolution, covering the last 150 kyr. We also generated TEX_{86}^{H} and $U_{37}^{K'}$ temperature and planktonic $\delta^{18}O$ records, as well as total organic carbon (TOC) and accumulation rates (ARs) of TOC and lipid biomarkers (i.e., C_{37} alkenones, GDGTs, dinosterol and loliolide) to reconstruct past phytoplankton production. The LDI-derived SST record co-varies with TEX_{86}^{H}- and $U_{37}^{K'}$-derived SST records as well as with the planktonic $\delta^{18}O$ record, implying that the LDI reflects past SST variations at this site. TOC and phytoplankton AR records indicate increased export production during the Last Interglacial (MIS 5), simultaneous with a peak in the abundance of preserved *Chaetoceros* diatoms, suggesting intensified upwelling during this period. The Diol Index is relatively low during the upwelling period, but peaks before and after this period, suggesting that *Proboscia* diatoms were more abundant before and after the period of upwelling. The NDI reveals the same trends as the Diol Index suggesting that the input of nitrate and phosphate was minimal during upwelling, which is unrealistic. We suggest that the Diol Index and NDI should perhaps be considered as indicators for *Proboscia* productivity instead of upwelling conditions or nutrient concentrations.

1. Introduction

Paleoclimatic reconstructions typically rely on physical, biological, and geochemical proxies from sedimentary archives. Physical proxies include sediment composition, structure, grain size, density, and magnetic susceptibility, which may provide information on the paleodepositional environment. Biological proxies comprise preserved (micro-)organisms such as diatoms, foraminifera, dinoflagellates, corals, and mollusks, or remnants deriving from higher plants such as pollen and spores. Geochemical proxies are based on the chemical composition of either the sediment or fossilized organisms. Stable isotope and elemental concentrations are inorganic proxies typically measured in shells or skeletons of marine organisms (foraminifera, mollusks, corals) preserved in the sediment, providing insight into the chemistry of the seawater in which the organisms lived. Organic proxies are a relatively newer class of tools, based on fossilized molecules that are unique for a specific organism or group of organisms, referred to as biomarkers. The ratios of specific biomarker molecules are often related to physical parameters of the environment in which the source organism grew, such as temperature, salinity, oxygen availability or productivity, and therefore such organic proxies can also be applied to reconstruct past depositional environments (e.g., Brassell et al., 1986; Prahl and Wakeham, 1987; Schouten et al., 2002; Rampen et al., 2008, 2012; Willmott et al., 2010; Gal et al., 2018).

In the last decade long-chain diols (LCDs) have attracted attention as novel proxies to reconstruct past environmental conditions. The Long chain Diol Index (LDI) was proposed, based on the distribution of C_{28} and C_{30} 1,13- and 1,15-diols in marine surface sediments, which shows a good correlation with mean annual sea surface temperature (SST; Rampen et al., 2012). These compounds have been detected in cultures of Eustigmatophyte algae (e.g., Volkman et al., 1992; 1999; Méjanelle et al., 2003; Rampen et al., 2014b), but the LCD distributions observed are different to those observed in the marine realm (e.g., Versteegh et al., 1997; 2000; Rampen et al., 2012; 2014a), and hence, their role as LCD producers in the ocean remains uncertain. The Diol Index, which is an indicator for past upwelling/high nutrient conditions, is defined as the fractional abundance of 1,14-diols with respect to 1,13-diols (Willmott et al., 2010) or the C_{30} 1,15-diol (Rampen et al., 2008), where 1,14-diols are biomarkers for *Proboscia* diatoms (Sinninghe Damsté et al., 2003; Rampen et al., 2014a). *Proboscia* grows during the early stages of upwelling since they need relatively little silica and they are able to migrate to deeper waters to obtain nutrients (Koning et al., 2001) and, therefore, it was proposed that the relative abundance of 1,14-diols can trace past upwelling conditions. C_{28}, C_{30} and C_{32} 1,14-diols have also been observed in the marine Dictyochophyte *Apedinella radians* (Rampen et al., 2011) but its role as 1,14-diol producer in the marine realm is unknown. Recently, a new index based on the saturated and mono-unsaturated C_{28} 1,14-diol was proposed as a quantitative proxy for nitrate and phosphate concentrations (Gal

et al., 2018), called the Nutrient Diol Index (NDI). The authors found a strong positive correlation between the NDI and phosphate ($R^2 = 0.85$) and nitrate ($R^2 = 0.80$) concentrations for the marine sediment data sets of Rampen et al. (2014a) and de Bar et al. (2016). This suggests that the NDI might be a good indicator of past nutrient variations in surface waters.

Applications in sediment cores of these LCD proxies have shown that the LDI, as well as the Diol Index, are promising paleotemperature and paleo-upwelling indicators (e.g., Pancost et al., 2009; Lopes dos Santos et al., 2012; Rampen et al., 2012; Seki et al., 2012; Rodrigo-Gámiz et al., 2014; Plancq et al., 2015; Jonas et al., 2017). However, a number of uncertainties still exist in the application of these biomarkers. For example, recent studies of surface sediments from coastal regions reveal different 1,13- and 1,15-diol distributions compared to open ocean sediments (de Bar et al., 2016; Lattaud et al., 2017a; 2017b). Relatively high fractional abundances of the C_{32} 1,15-diol along the coast were observed, as a result of riverine input, significantly affecting the LDI signal, likely due to different 1,13- and/or 1,15-diol producers thriving in river outflow waters. Moreover, studies have related high *Proboscia* diatom abundances to stratified instead of upwelling conditions (e.g., Fernández and Bode, 1994). Similarly, Contreras et al. (2010) determined the relative abundance of the C_{28} 1,14-diol at ODP Site 1229 located in the Peruvian upwelling system, and observed increased concentrations during the Last Interglacial (LIG; MIS 5e) and related this to enhanced water column stratification. Furthermore, Rodrigo-Gámiz et al. (2015) showed that for sediment traps and surface sediments around Iceland, which were characterized by high concentrations of 1,14 diols (>75 % of all LCDs), the LDI did not correspond to SST. This makes application of the LDI at sites with high input of diols from Proboscia diatoms (e.g., upwelling sites) uncertain. Finally, due to its recent development no studies have been performed yet to test the applicability of the NDI as a paleo-nutrient proxy.

To constrain the uncertainties in applying the LCD proxies (LDI, Diol Index and NDI) at sites with upwelling and riverine input, we studied the Late Quaternary sedimentary record at ODP Site 1234. This site is located along the Chilean margin, within the Chile-Peruvian upwelling system, and near two major river mouths of the Andean river systems Río Bio-Bio and Río Itata, both draining large basins (Muratli et al., 2010a). We sampled the last ~150 kyr, including glacial and interglacial periods, and generated LDI, TEX_{86} and $U^{K'}_{37}$ based temperature records to constrain glacial-interglacial variations in SST throughout this entire interval. Additionally, we compared the Diol Index and the NDI record with other paleoproductivity indicators, including total organic carbon (TOC), organic matter stable carbon isotopes ($\delta^{13}C$), as well as phytoplanktonic lipid biomarkers that are characteristic for certain phytoplankton communities (C_{37} alkenones, loliolide and dinosterol).

2. Materials and methods

2.1 Study site

Marine sediments along the coast of Chile and Peru have been thoroughly studied, as it is a key region in the southern hemisphere for studying climate variability related to both atmospheric and oceanographic circulation (e.g., Lamy et al., 1998, 1999, 2002, 2004; Hebbeln et al., 2000, 2002; Mohtadi & Hebbeln, 2004; Stuut and Lamy, 2004; Heusser et al., 2006; Romero et al., 2006; Mohtadi et al., 2008; Muratli et al., 2010a, 2010b; Verleye & Louwye, 2010; Chase et al., 2014). The main circulation patterns include the Southern Westerly Winds (SWW) and the Antarctic Circumpolar Current (ACC; Fig 1). The ACC approaches the South American continent from the west, and initiates both the Humboldt Current (or Peru Chile Current) flowing northwards along the continental margin and the Cape Horn Current flowing southwards (e.g., Stuut et al., 2006; Fig. 1). The Humboldt Current flows along the Chilean coast and turns westwards as it approaches the equator, forming the South Equatorial Current (SEC). Variations in strength and location of the ACC and Southern Westerlies are thought to be the main climate controls in this region. Lamy et al. (2002) showed that long-term Holocene trends in temperature and productivity are linked to latitudinal shifts of the ACC and the Westerlies. On a millennial- to multidecennial-scale, paleotemperature variations are strongly connected to millennial-scale climate variations in Antarctica. When the ACC migrates northward, potentially associated with an expansion of Antarctic sea ice, cold, subantarctic waters are advected into the southern hemisphere mid-latitudes, including the Chilean margin (e.g., Lamy et al., 2004; Kaiser et al., 2005). The subtropical high-pressure system is an important climate control north of 33°S, which can enhance coastal upwelling (Mohtadi and Hebbeln, 2004).

ODP Site 1234 is located in the south east Pacific Ocean (36°13.153´S,73°40.902´W, 1015 m water depth), ca. 65 km offshore of Concepción, Chile. This site lies in the vicinity of two large Andean river systems: the Río BioBío and Río Itata, which drain basins of 24,000 km^2 and 11,200 km^2, respectively (Muratli et al., 2010a). The continental margin is under influence of terrestrial input due to rainfall and land erosion (Lamy et al., 2004), and terrestrial material deposited along the coastal margin derive mainly from two mountain ranges, i.e., the Coast Range and the Andes (Lopez-Escobar et al., 1977; Martin et al., 1999). Moreover, ODP Site 1234 is located within the Peru-Chile upwelling system, which is one of the most important upwelling regions on Earth (Berger et al., 1987), due to the combination of upwelling-favorable winds (Daneri et al., 2000; Carr and Kearns, 2003) and an eastern boundary current (Humboldt Current). The upwelling regime stretches from 5°S to 38°S, corresponding to ca. 5000 km of coastline. South of 38°S, onshore winds suppress upwelling (Strub et al., 1998), but high productivity is sustained by relatively high nutrient supply from the ACC (Hebbeln et al., 2000), which is typically rich in nitrate and limited in micronutrients such as iron (de Baar et al., 1995). Along the Chilean coast, iron availability (as well as other micronutrients) can increase due to fluvial supply as the precipitation of the Southern Westerlies onshore enhances river runoff (Mohtadi & Hebbeln, 2004).

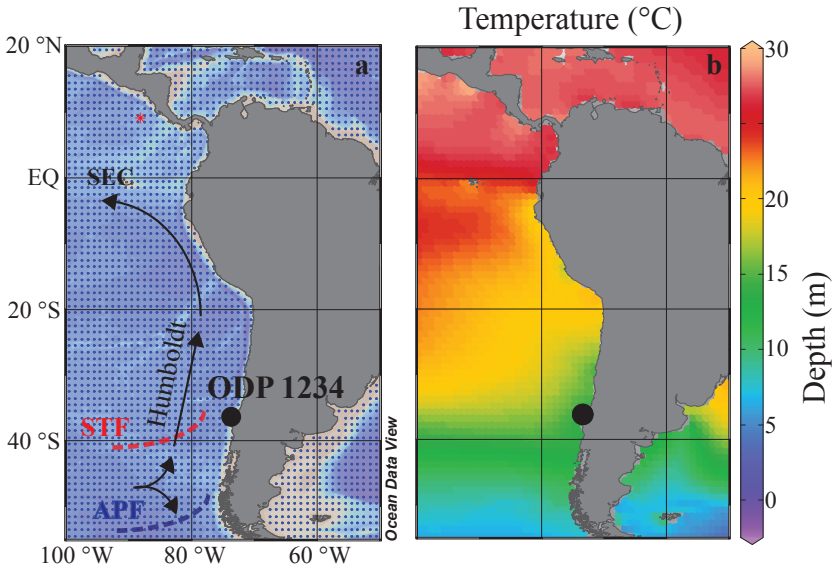

Fig. 1 Maps showing the location of ODP Site 1234. **(a)** A simplified illustration of the present-day atmospheric and oceanographic setting and the site location. SEC = South Equatorial Current; APF = Antarctic Polar Front; STF = Subtropical Front. **(b)** Present-day mean annual SST (°C) for the region. Data derived from the World Ocean Atlas 2013; maps were drawn in Ocean Data View (Schlitzer, 2015), and modified manually.

2.2 Age model and sample strategy

The core was drilled as part of Ocean Drilling Program (ODP) Leg 202. Sedimentation rates were relatively high (~80 cm kyr^{-1} on average Mix et al., 2003; Heusser et al., 2006). The age model used is from Heusser et al. (2006) and is based upon radiocarbon dates and correlation of benthic $\delta^{18}O$ to deep Atlantic core MD95204 (upper half) and the Vostok ice core chronology (lower half; see Heusser et al., 2006 and references therein). Heusser et al. (2006) switched between the two age models around 69 ka where they overlap, as indicated by the dashed line in Fig. 2a. However, this results in a substantial, and likely unrealistic, dip in the sedimentation rate between ca. 80 and 90 ka in the hiatus between the age models (Fig. 2b). Hence, we chose to use the upper age model (dark blue in Fig. 2) which extends up to ~83 ka, and linearly interpolate between this age and the age of ~90 ka constrained by the other age model for the lower half of the core. This depth-age range of linear interpolation between the two age models is highlighted in green in Fig. 2 and results in less abrupt changes in sedimentation rates. The core was sampled with a ~2 kyr resolution, covering the last ~150 kyr. In total, 74 sediment samples were analyzed for bulk and organic geochemistry.

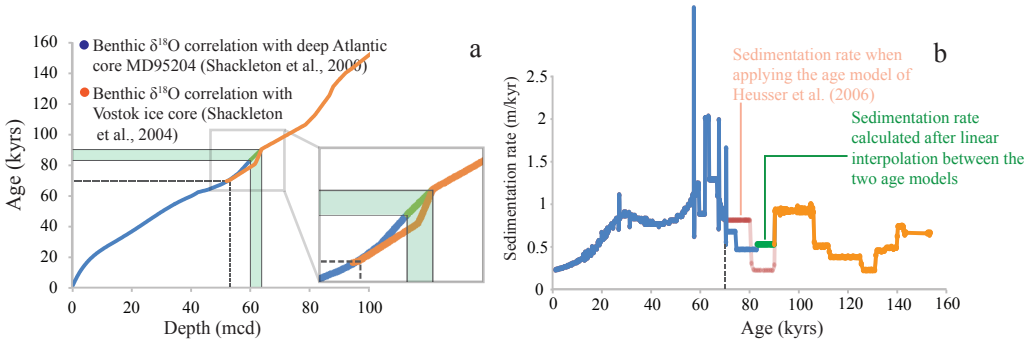

Fig. 2 Age-depth relations for ODP 1234 derived from Heusser et al. (2006). **(a)** Age-depth constrains based on the correlation of benthic $\delta^{18}O$ with Atlantic core MD95204 (dark blue; upper half) and the Vostok ice core chronology (orange; lower half). Heusser et al. (2006) switched between the two different age models at ~69 ka/~53 mcd (dashed line). However, we used the full upper age model and then linearly interpolated between the age models from ~ 60 to 64 mcd, as indicated by the connecting green line. **(b)** Sedimentation rates calculated after linear interpolation between the age-depth tie-points of the two age models. The sedimentation rates calculated after the linear interpolation between the age models are presented in green. In transparent red, the sedimentation rates are plotted when applying the dating strategy of Heusser et al. (2006).

2.3 Elemental analysis

All 74 sediment samples were freeze-dried and homogenized. Small aliquots (ca. 50–100 mg) were used for elemental analysis. For this purpose, all aliquots were acidified with 2 M hydrochloric acid (HCl) to remove all carbonates, and rinsed with distilled water to remove salts. Subsequently, the decalcified sediment samples were analyzed for total organic carbon (TOC), total nitrogen (TN) and stable carbon isotope ratios ($\delta^{13}C$) by means of a Thermo Scientific Flash 2000 Elemental Analyzer coupled to a Thermo Scientific Delta V Advantage Isotope Ratio Mass Spectrometer. Total nitrogen (TN) was measured on aliquots which were not acidified. Results are expressed in standard δ-notation relative to Vienna Pee Dee Belemnite (VPDB) for $\delta^{13}C$. The precision as determined using laboratory standards calibrated to certified international reference standards, were in all cases <0.2 ‰. TOC mass accumulation rates ARs (MAR_{TOC}) were calculated by multiplication of the sedimentation rate (linear interpolation between depth points of the age-depth model; see above) with an estimated bulk density of 1.6 g cm^{-3} (Mix et al., 2003) and subsequent multiplication with the TOC percentage.

2.4 Foraminiferal stable isotope analysis

Benthic stable isotope data were previously published, and were generated using standard techniques in laboratories at Oregon State University and the Woods Hole Oceanographic Institution (McManus et al., 1999, 2002, 2003; Heusser et al., 2006). Oxygen isotope ratios in *Cibicidoides* and *Uvigerina* were adjusted to each other by 0.64 ‰ (Shackleton, 1974). Additional data on the planktonic species *Globigerina bulloides* were generated at Lamont Doherty Earth Observatory (LDEO) of Columbia University using a Thermo Delta V Plus gas-source isotope ratio mass spectrometer (IRMS) equipped with a Kiel IV automated individual acid bath sample-preparation device. Although a recent study found no size-related influence on *G. bulloides* $\delta^{18}O$ (Costa et al., 2017) specimens were generally picked from the 250–300 μm size range, with 8–12 individuals selected for analysis. Samples were replicated at ~5–10 % frequency and measured isotope ratios were calibrated to the VPDB isotope scale with NBS-19 and NBS-18. Reproducibility of the in-house standard (1 sigma) is ±0.06 ‰ ($\delta^{18}O$) and ±0.04 ‰ ($\delta^{13}C$).

2.5 Lipid extraction and organic geochemical analysis

The sediment samples (ca. 15 g dry weight) were extracted using accelerated solvent extraction (ASE) using a DIONEX 200, at 100 °C, a pressure of $7–8\times10^6$ Pa, and a mixture of dichloromethane (DCM) and methanol (MeOH) (9:1; vol./vol.). The total lipid extracts (TLEs) were dried under a stream of nitrogen (N_2) using a Caliper TurboVap LV. All TLEs were desulfurized using copper granules activated with 1M HCL. The copper turnings were added to the TLEs and stirred overnight and subsequently dried over anhydrous sodium sulfate (Na_2SO_4), in order to remove precipitate and water, and dried down under N_2. For quantification purposes, three internal standards were added to the TLEs: 10-nonadecanone ($C_{19:0}$ ketone) for long-chain alkenones, C_{22} 7,16-diol for LCDs (Rodrigo-Gámiz et al., 2015) and the C_{46} GDGT for GDGTs (Huguet et al., 2006). The TLEs (aliquots of ~4.5 mg) were separated into apolar, ketone (containing alkenones) and polar (containing LCDs and GDGTs) fractions, by separation over activated (2h at 150 °C) Al_2O_3 and elution with hexane/DCM (9:1; vol./vol.), hexane/DCM (1:1; vol./vol.) and DCM/MeOH (1:1; vol./vol.), respectively. Polar fractions were split for GDGT (25 %) and LCD (75 %) analysis.

2.5.1 GDGTs

Aliquots of the polar fractions were dissolved in hexane:isopropanol (99:1, vol./vol.) to a concentration of ca. 2 mg mL^{-1}. The fractions were then filtered through 0.45 μm polytetrafluoroethylene (PTFE) filters. GDGTs were analyzed by means of Ultra High Performance Liquid Chromatography Mass Spectrometry (UHPLC-MS), on an Agilent 1260 HPLC, equipped with automatic injector, coupled to a 6130 Agilent MSD and HP Chemstation software according to Hopmans et al. (2016). The injection volume was 10 μL.

Separation of the GDGTs was achieved in normal phase using 2 silica BEH HILIC columns in series (150 mm × 2.1 mm; 1,7 µm; Waters Acquity) at a temperature of 25 °C. The mobile phases are hexane (A) and hexane:isopropanol (9:1, vol./vol.) (B). Compounds were isocratically eluted for 25 minutes with 18 % B, followed by a linear gradient to 35 % B in 25 minutes and a linear gradient to 100 % B in the 30 min thereafter. The flow rate was kept constant (0.2 mL min^{-1}) during the analysis. The conditions for the APCI-MS were identical to Hopmans et al. (2016). GDGTs were detected in single ion monitoring (SIM) mode of the protonated molecules ($[M+H]^+$) of the various GDGTs. A standard mixture of C_{46} GDGT (internal standard) and crenarchaeol was analyzed to determine the relative response factor (RFF) between these two compounds (c.f. Huguet et al., 2006), and thereby quantify GDGTs in the sediments.

For reconstruction of past SST we used the TEX_{86}^{H} index as proposed by Kim et al. (2010), which is defined as the logarithmic function of the original TEX_{86} (Schouten et al., 2002):

$$TEX_{86}^{H} = \log([GDGT\text{-}2+GDGT\text{-}3+cren´]/[GDGT\text{-}1+GDGT\text{-}2+GDGT\text{-}3+cren´]) \quad (1)$$

where the numbers correspond to the amount of cyclopentane moieties in the isoprenoid GDGTs and where Cren´ refers to the later eluting isomer of crenarchaeol (Sinninghe Damsté et al., 2002). We have discarded 13 samples for the TEX_{86} calculation due to the partial co-elution of GDGT-2 with an unknown compound.

The TEX_{86}^{H} values were converted to SSTs applying the global core top calibration of Kim et al. (2010):

$$SST = 68.4 \times TEX_{86}^{H} + 38.6 \quad (2)$$

There is also a regional TEX_{86}^{H} calibration available, based on Chilean surface sediments between 25 and 50°S (Kaiser et al., 2015):

$$SST = 59.6 \times TEX_{86}^{H} + 33.0 \quad (3)$$

This calibration has a similar slope compared to the global core-top calibration of Kim et al. (2010) but a lower intercept, which results in SSTs that were ca. 2.4 °C lower compared to the TEX_{86}^{H}-SSTs calculated after Kim et al. (2010). Although the outcomes are relatively similar, the calibration of Kim et al. (2010) resulted in SSTs that agreed better with the $U_{37}^{K´}$ and LDI records, and therefore we have used this calibration. In Appendix A, the TEX_{86}^{H} temperatures based on the calibration of Kaiser et al. (2015) are plotted (Fig. A1). Additionally, we plotted TEX_{86} temperatures calculated after the Bayesian calibration of Tierney and Tingley (2014, 2015) in Fig A1. These SSTs are on average 4 °C lower compared to the TEX_{86}^{H}-derived temperatures after Kim et al. (2010), which might be due to the relative large number of high latitude core tops on which in this case the BAYSPAR calibration is based (Tierney and Tingley, 2014; 2015), whereas the TEX_{86}^{H} calibration of Kim et al. (2010) excludes (sub)polar core-top data. However, both reconstructions show the same trend.

To assess continental organic matter input into the marine realm, we calculated the Branched Isoprenoid Tetraether (BIT) index, as proposed by Hopmans et al. (2004), including the 6-methyl brGDGTs as described by de Jonge et al. (2014a; 2015):

$$BIT = [brGDGT\ Ia+brGDGT\ IIa+IIa'+brGDGT\ IIIa+IIIa']/[brGDGT\ Ia+brGDGT\ IIa+IIa'+brGDGT\ IIIa+IIIa'+Cren] \quad (4)$$

where the numbers correspond to different branched GDGTs (Hopmans et al., 2004).

Additionally, we calculated the Methane Index (MI), as a proxy for dissociation of marine gas hydrates conducive to anaerobic oxidation of methane (AOM), as proposed by Zhang et al. (2011):

$$MI = [GDGT\text{-}1+GDGT\text{-}2+GDGT\text{-}3]/[GDGT\text{-}1+GDGT\text{-}2+GDGT\text{-}3+Cren+Cren'] \quad (5)$$

The archaea living in hydrate-impacted environments mainly contain GDGT-1, -2 and -3 as their membrane lipids. Therefore, relative high abundances of these GDGTs might indicate these types of environments in the past, and potentially explain erroneous TEX_{86}^{H} results due to high GDGT-1, -2 and/or -3 abundances. For all samples, this index was < 0.3, except for one data point (MI = 0.6), which was therefore removed from further discussion. Additionally, to assess other potential influence on the TEX_{86}^{H}, we determined the %GDGT-0 and Ring Index for all sediments. All values were below the advised thresholds, implying no substantial biases on the TEX_{86} (Zhang et al., 2011; Sinninghe Damsté et al., 2012b; Zhang et al., 2016).

2.5.2 Long-chain alkenones

Ketone fractions were dissolved in ethyl acetate to a concentration of ~1 mg mL^{-1}, and analyzed on an Agilent 6890N gas chromatograph (GC) with flame ionization detection (FID). Separation was achieved on a fused silica column with a length of 50 m and diameter of 0.32 mm, coated with a CP Sil-5 (thickness = 0.12 µm). Helium was used as carrier gas. The flow mode was a constant pressure of 100 kPa. Alkenones were injected on-column at 70 °C at the start of the analysis, increased by 20 °C min^{-1} to 200 °C followed by 3 °C min^{-1} until the final temperature of 320 °C. This end temperature was held for 25 min. Quantification of the alkenones was achieved by means of the $C_{19:0}$ ketone internal standard. Identification of the long-chain alkenones was done on an Agilent 7890B GC system interfaced with an Agilent 5977A MS. Separation was achieved on a CP Sil-5 column with an identical diameter and film thickness as that of the GC-FID, but a length of 25 m. Helium was the carrier gas, maintaining a constant flow rate of 2 mL min^{-1}. The MS operated at 70 eV. For both systems, the injection volume was 1 µL. The long-chain alkenones were identified in full scan, scanning between *m*/*z* 50 and 850, and comparison with literature (de Leeuw et al., 1980; Volkman et al., 1980b; Marlowe et al., 1984a).

The $U_{37}^{K'}$ index was calculated according to Prahl and Wakeham (1987):

$$U_{37}^{K'} = [C_{37:2} \text{ alkenone}]/[C_{37:2}+C_{37:3} \text{ alkenones}] \quad (6)$$

The $U_{37}^{K'}$ values were converted to SSTs using the calibration of Müller et al. (1998):

$$SST = (U_{37}^{K'}–0.044)/0.033 \quad (7)$$

There is also a Bayesian calibration available for the $U_{37}^{K'}$, called the BAYSPLINE (Tierney and Tingley, 2018), but below ~24 °C temperature estimates are similar to that of the calibration of Müller et al. (1998). Since our temperatures are well below 24 °C, we have applied the calibration of Müller et al. (1998).

2.5.3 LCDs

The LCDs were silylated prior to analysis. Polar fractions were dissolved in 25 µL of pyridine and 25 µL of N,O-bis(trimethylsilyl)trifluoroacetamide (BSTFA) and heated at 60 °C for 20 min. Prior to injection, 450 µL ethyl acetate was added. GC-MS analysis was carried out on an Agilent 7890B gas chromatograph coupled to an Agilent 5977A mass spectrometer. Samples were injected at 70 °C. The oven temperature was programmed to 130 °C by 20 °C min^{-1}, and subsequently to 320 °C by 4 °C min^{-1}; this final temperature was held for 25 min. The GC was equipped with an on-column injector and fused silica column (25 m × 0.32 mm) coated with CP Sil-5 (film thickness 0.12 µm). The carrier gas was helium at a constant flow of 2 mL min^{-1}. The mass spectrometer operated with an ionization energy of 70 eV. The injection volume was 1 µL. Identification of the LCDs was achieved in full scan, scanning between *m*/*z* 50 to 850, and on basis of their characteristic fragmentation (Versteegh et al., 1997). Quantification of the LCDs and proxy computation was done by analysis in SIM mode of the characteristic fragments (*m*/*z* 299, 313, 327 and 341; Rampen et al., 2012; *m*/*z* 187 for C_{22} 7,16-diol internal standard). We applied the following correction factors for the relative contribution of the selected fragment ions during SIM to the total ion counts: 16 % for all saturated diols, 9 % for all unsaturated diols and 25 % for the C_{22} 7,16-diol internal standard.

Past SST was reconstructed by means of the LDI index (Rampen et al., 2012):

$$LDI = [C_{30} \text{ 1,15-diol}]/[C_{28} \text{ 1,13-diol}+C_{30} \text{ 1,13-diol}+C_{30} \text{ 1,15-diol}] \quad (8)$$

Subsequently, LDI values were converted to SST values via the following equation:

$$SST = (LDI–0.095)/0.033 \quad (9)$$

Three samples were discarded for the calculation of the LDI due to partial co-elution of the C_{28} 1,13-diol with another unknown compound.

For the reconstruction of past upwelling conditions, the Diol Index as proposed by Willmott et al. (2010) was applied:

$$\text{Diol Index} = [C_{28}+C_{30}\ 1,14\text{-diol}]/[C_{28}+C_{30}\ 1,14\text{-diol}+C_{28}+C_{30}\ 1,13\text{-diol}] \quad (10)$$

The Diol Index according to Rampen et al. (2008) was shown to be also affected by variations in SST due to the inclusion of the C_{30} 1,15-diol in the ratio (Rampen et al., 2014a; Zhu et al., 2018), and since on a glacial-interglacial timescale we expect substantial SST differences, we consider the Willmott et al. (2010) ratio more appropriate.

Possible fluvial input of LCDs was assessed by the fractional abundance of the C_{32} 1,15-diol which is potentially derived from rivers (de Bar et al., 2016; Lattaud et al., 2017a; 2017b):

$$F C_{32}\ 1,15\text{-diol} = [C_{32}\ 1,15\text{-diol}]/[C_{28}\ 1,13\text{-diol}+C_{30}\ 1,13\text{-diol}+C_{30}\ 1,15\text{-diol}+C_{32}\ 1,15\text{-diol}] \quad (11)$$

The NDI index, a proposed proxy for PO_4^{3-} and NO_3^- concentrations, was calculated following Gal et al. (2018):

$$\text{NDI} = [C_{28}\ 1,14\text{-diol}+C_{28:1}\ 1,14\text{-diol}]/[C_{28}\ 1,14\text{-diol}+C_{28:1}\ 1,14\text{-diol}+C_{30}\ 1,14\text{-diol}+C_{30:1}\ 1,14\text{-diol}+C_{28}\ 1,13\text{-diol}+C_{30}\ 1,13\text{-diol}+C_{30}\ 1,15\text{-diol}] \quad (12)$$

The NDI was then translated to $[PO_4^{3-}]$ and $[NO_3^-]$ concentrations by using the following equations (Gal et al., 2018):

$$[PO_4^{3-}] = (\text{NDI}–0.015)/0.413 \quad (13)$$

$$[NO_3^-] = (\text{NDI}–0.075)/0.026 \quad (14)$$

Finally, loliolide, an indicator of diatom abundance (Klok et al., 1984; Repeta, 1989), and dinosterol, a biomarker for dinoflagellates (Boon et al., 1979; Volkman et al., 1998), were identified by GC-MS analysis (simultaneously with the LCDs) of the silylated polar fraction and quantified using the C_{22} 7,16-diol standard in full scan, correcting for the molecular weights of the compounds.

3. Results

3.1 Bulk parameters and sedimentation rates

The TOC content varies between 0.4 and 2.6 %. The TOC content is significantly higher during the interglacial periods (MIS 1, 3 and 5) compared to glacial periods (MIS 2, 4 and 6; two-tailed $p < 0.001$): the average TOC concentration is 1.4 % for the interglacial periods and 0.7 % for the glacial intervals (Fig. 3d), although TOC levels for MIS 3 are quite similar to those of MIS 1 and 2. Similarly, the average TN levels are 0.2 % and 0.1 % during the interglacial and glacial intervals, respectively (Fig. 3d). During Termination 2, both the TOC

and TN contents increase rapidly (within < 2 kyr) towards interglacial values, and the highest TOC and TN values are observed around 78 ka (2.6 and 0.3 %, respectively). The atomic C/N ratio (Fig. 3b) varies from 4.3 to 10.5 and is on average higher during the interglacial periods (7.2) as compared to glacial times (6.2). The organic matter $\delta^{13}C$ record ($\delta^{13}C_{OM}$) also reveals a glacial-interglacial variation (Fig. 3c), corresponding to slightly ^{13}C-enriched values during interglacial times ($\delta^{13}C$average = –21.2 ‰) as compared to the glacials ($\delta^{13}C$average = –21.8‰). Although small, these changes are statistically significant (5% significance level, two-tailed $p < 0.001$).

Using the age model modified from Heusser et al. (2006), we estimated sedimentation rates that varied between ca. 0.2 and 1.7 mm yr^{-1} (Fig. 3a). Sedimentation rates were highest in MIS 4, during which the sedimentation rate reaches values of around 2 mm yr^{-1}. Sedimentation rates were lowest during the warmest periods (MIS 1 and 5e; ca. 0.3–0.4 mm yr^{-1}). The MAR_{TOC} varied between ca. 2 and 32 g m^{-2} yr^{-1} and shows a relatively similar pattern as the sedimentation rate, implying that the sedimentation rate strongly controls the AR of TOC (Fig. 3a). Around ca. 100 ka there is a pronounced maximum in the TOC AR, reaching ca. 32 g m^{-2} yr^{-1}.

3.2 Lipid biomarker concentrations and ARs

In all sediments, long-chain alkenones, GDGTs and LCDs were present above the quantification limit. The total concentration of crenarchaeol, a specific biomarker for marine Thaumarchaeota (Schouten et al., 2002; 2003), varies between ca. 2 and 16 µg g^{-1}, with highest values during MIS 5, after MIS 5e (Eemian Interglacial; Fig. 4a). Accumulation rates (ARs) range from 1 to 25 mg m^{-2} yr^{-1} (Fig. 4a). The summed concentration of the di- and tri-unsaturated C_{37} alkenones, a productivity proxy for alkenone-producing haptophytes (e.g., Prahl et al., 1988; Prahl and Muehlhausen, 1989; Rostek et al., 1997; Villanueva et al., 1997), varies between ca. 0.5 and 10 µg g^{-1}. Highest concentrations are observed for MIS 5e (126–116 ka; Fig. 4b). Around the boundary of MIS 4 and 5, concentrations decrease from ca. 6 to 2 µg g^{-1} sediment, however the alkenone AR does not show this decrease. During the Late Holocene, C_{37} alkenone concentrations increase again. The alkenone AR record resembles that of the MAR_{TOC} with a peak around 100 ka of ca. 10 mg m^{-2} yr^{-1} (Fig. 4b).

Dinosterol shows highest abundance during the Last Interglacial (MIS 5), peaking just after the Eemian Interglacial (between ca. 116 and 110 ka; Fig. 4c) with concentrations of ca. 4 µg g^{-1}. This peak is followed by a gradual decrease towards the LGM with values near 1 µg g^{-1} sediment. The AR record of dinosterol highly resembles the concentration record but peaks somewhat later, i.e., between ca. 105 and 98 ka. The loliolide concentration shows one maximum during the Late Holocene of ca. 2.3 µg g^{-1} sediment (Fig. 4d). Its AR varies between ca. 0 and 1 mg m^{-2} yr^{-1}, throughout the record, with one pronounced peak around 100 ka of around 2 mg m^{-2} yr^{-1}.

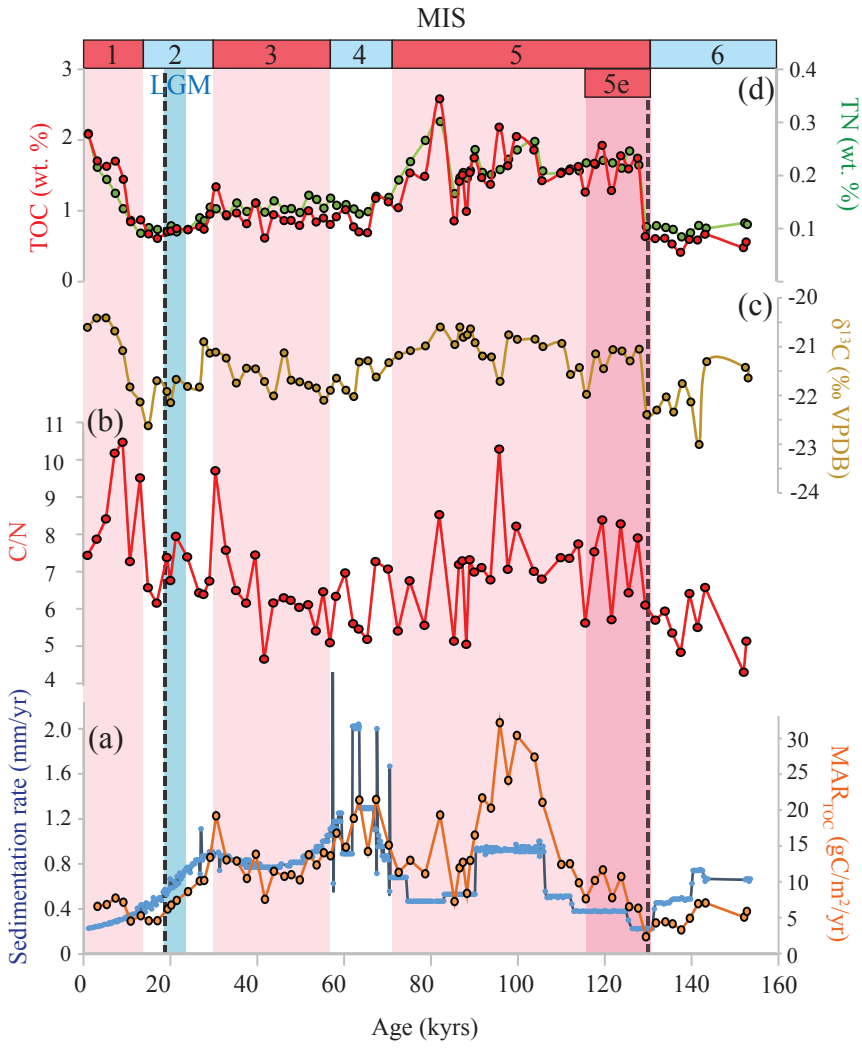

Fig. 3 Geochemical bulk records for the studied interval of ODP 1234. **(a)** sedimentation rate (blue) and MAR_{TOC} (orange), **(b)** atomic C/N ratio, **(c)** Bulk organic $\delta^{13}C$, **(d)** TOC (red) and TN (green) concentrations. The different color bands indicate different time periods: interglacial stages MIS 1, 3 and 5 in pink, including the MIS 5e in dark pink. The LGM is highlighted in blue. MIS ages are according to Lisiecki and Raymo (2005). The dashed lines indicate the onset ages of Terminations 1 (Pacific age of Stern and Lisiecki, 2014) and 2 (approximate age).

The main LCDs detected throughout the core are the C_{28} and C_{30} 1,13-, C_{28}, C_{30} and $C_{30:1}$ 1,14- and the C_{30} and C_{32} 1,15-diols. We did not detect the C_{32} 1,14-diol (characteristic for *Apedinella radians*), but we did identify the $C_{30:1}$ 1,14 diol and C_{29} 12-OH fatty acid, which

are typical biomarkers for *Proboscia* diatoms (Sinninghe Damsté et al., 2003), implying that *Proboscia* diatoms are most likely the source of the 1,14-diols detected in the sediments. The profile of the summed concentration of 1,14-diols shows four distinct sharp peaks during the MIS 5 (Fig 4f), reaching concentrations up to 1.2 µg g^{-1}. The 1,14-diol AR shows one distinct peak at 94 ka of ca. 1.7 mg m^{-2} yr^{-1}, whereas throughout the rest of the record the AR varies between 0 and 0.6 mg m^{-2} yr^{-1}. Figure 4h shows the ARs of the summed 1,13- and 1,15-diols. The AR of the 1,13-diols ranges between ca. 0.1 and 0.8 mg m^{-2} yr^{-1} throughout MIS 6 and 5, and peaks (ca. 1.2 mg m^{-2} yr^{-1}) at the end of MIS 5 revealing highest ARs during MIS 4, followed by a subsequent gradual decrease towards Holocene values of around 0.2 mg m^{-2} yr^{-1}. The AR record of the 1,15-diols is highly similar to that of the 1,13-diols for MIS 1 to 4, as well as for MIS 6, but shows higher values during the second half of MIS 5 with maxima around 94, 104 and 122 ka of between ca. 1 and 1.3 mg m^{-2} yr^{-1}.

3.3 Foraminiferal stable isotopic composition

We generated a $\delta^{18}O$ record of *G. bulloides* for MIS 5, from ca. 70 to 142 ka, as well as for a short interval within MIS 3, from ca. 36 to 41 ka, plotted in Fig. 5b. The $\delta^{18}O$ of *G. bulloides* varied between ca. 0.3 and 4.2 ‰ and are most depleted during the Eemian Interglacial around 123 ka ($\delta^{18}O$ = 0.3 ‰), and enriched values are observed for MIS 6 and 3.

3.4 Organic proxy records

The Diol Index record shows several maxima, of which the most evident one is during MIS 5 (Fig. 4g). During MIS 5e, the Diol Index reveals two peaks around 126 and 116 ka (up to 0.7), followed by a sharp drop and a subsequent increase around 110 ka, reaching a maximum value at ~ 86 ka (up to 0.8). After 86 ka, the index gradually decreases. During MIS 2–4 the Diol Index varies between ca. 0.1 and 0.5. During MIS 1, the Diol Index shows a gradual increase from ca. 0.15 to 0.35.

We did not detect the mono-unsaturated C_{28} 1,14-diol ($C_{28:1}$ 1,14-diol), and therefore this diol could not be included in the calculation of the NDI index. In ~64 % of the surface sediments of the datasets of Rampen et al. (2014a) and de Bar et al. (2016) on which the NDI calibration of Gal et al. (2018) is based, the $C_{28:1}$ 1,14 was also not detected. The NDI record reveals similar variations as the Diol Index, although more pronounced. During MIS 6 the NDI is close to zero, followed by a small peak at the end of the Eemian Interglacial (NDI = 0.4), coincident with the peak in the Diol Index at 116 ka. NDI-derived [NO_3^-] and [PO_4^{3-}] concentrations around 116 ka are 11 and 0.8 µmol L^{-1}, respectively (Fig. 4h). Similar to the Diol Index, the ratio then decreases after which the NDI shows a broad peak (~ 100–80 ka) with a maximum at 88 ka (NDI = 0.6), which gives concentrations of 20 and 1.4 µmol L^{-1} when translated to [NO_3^-] and [PO_4^{3-}], respectively (Fig. 4h). Between 80 and 0 ka (i.e., MIS

4–1), the NDI index does not reveal any distinct maxima, and the ratio varies between ca. 0 and 0.2.

Overall the organic SST proxy records broadly follow the same trend, clearly revealing glacial-interglacial temperature variability (Fig. 5b). Indeed, when we cross-correlate the three proxies, all combinations display significant positive correlations ($p < 0.001$; Fig. 6) albeit with some scatter. Additionally, the SST trends show good correspondence with the planktonic $\delta^{18}O$ record of *G. bulloides* (Fig. 5c), as well as with the benthic oxygen isotope record for ODP Site 1234 (Heusser et al., 2006; Fig 5a), and the global stack of benthic $\delta^{18}O$ values (e.g., Lisiecki and Raymo, 2005; Fig. 5d). Termination 2 (around 130 ka) is clearly expressed in all three organic proxy SST records, showing a rise in temperature of approximately 4 °C within ca. 2 kyr. During MIS 5e, SSTs were between ca. 16 and 18 °C, based on the three temperature proxies. Then, during MIS 5, the interglacial substages representing alternating cold and warm periods are clearly reflected in all three proxy records. The three records show temperature drops between ca. 4 and 6 °C during MIS 5a (ca. 70 ka). During MIS 4, 3 and 2, all SST records show a gradual decrease towards the LGM, during which $U_{37}^{K'}$ and TEX_{86}^{H} reveal temperatures between 9 to 10 °C, and the LDI between 7 and 8 °C. Around 25 ka, $U_{37}^{K'}$ and TEX_{86}^{H} temperatures show a similar steady rise to Holocene temperatures of around 16 and 18 °C. The LDI reveals an approximate 7 °C warming over Termination 1, starting slightly later at around 22 ka. During the last ~20 kyr, LDI-derived SSTs are ~3–4 °C lower as compared to the $U_{37}^{K'}$ and TEX_{86}^{H}-derived SSTs.

Fig. 4 Biomarker proxy and accumulations records for ODP 1234. **(a)** Crenarchaeol concentrations and MARs. **(b)** C_{37} alkenone concentrations and MARs. **(c)** Dinosterol concentrations and MARs. **(d)** Loliolide concentrations and MARs. **(e)** 1,13- and 1,15-diol MARs. **(f)** 1,14-diol concentration and MARs. **(g)** Diol Index (blue) and biogenic opal concentrations (green; Muratli et al., 2010b) for the last ~28 kyr. **(h)** Phosphate and nitrate concentrations calculated after the NDI index. **(i)** Total diatom counts (purple) and *Chaetoceros* diatom counts (blue) (Mix et al., 2003). The thick smoothed lines reflects 2-point running averages of the diatom records. The counts are descriptive: F = few; C = common; A = abundant; VA = very abundant. **(j)** Mass AR of TOC. For panels **(a)** – **(d)** and **(f)**: concentrations are in grey and MARs are in black. The different color bands indicate different time periods: interglacial stages MIS 1, 3 and 5 in pink, including the MIS 5e, in dark pink. The LGM is highlighted in blue. The purple band indicates the period of presumed enhanced upwelling. MIS ages are according to Lisiecki and Raymo (2005). The dashed lines indicate the onset ages of Terminations 1 (Pacific age of Stern and Lisiecki, 2014) and 2 (approximate age).

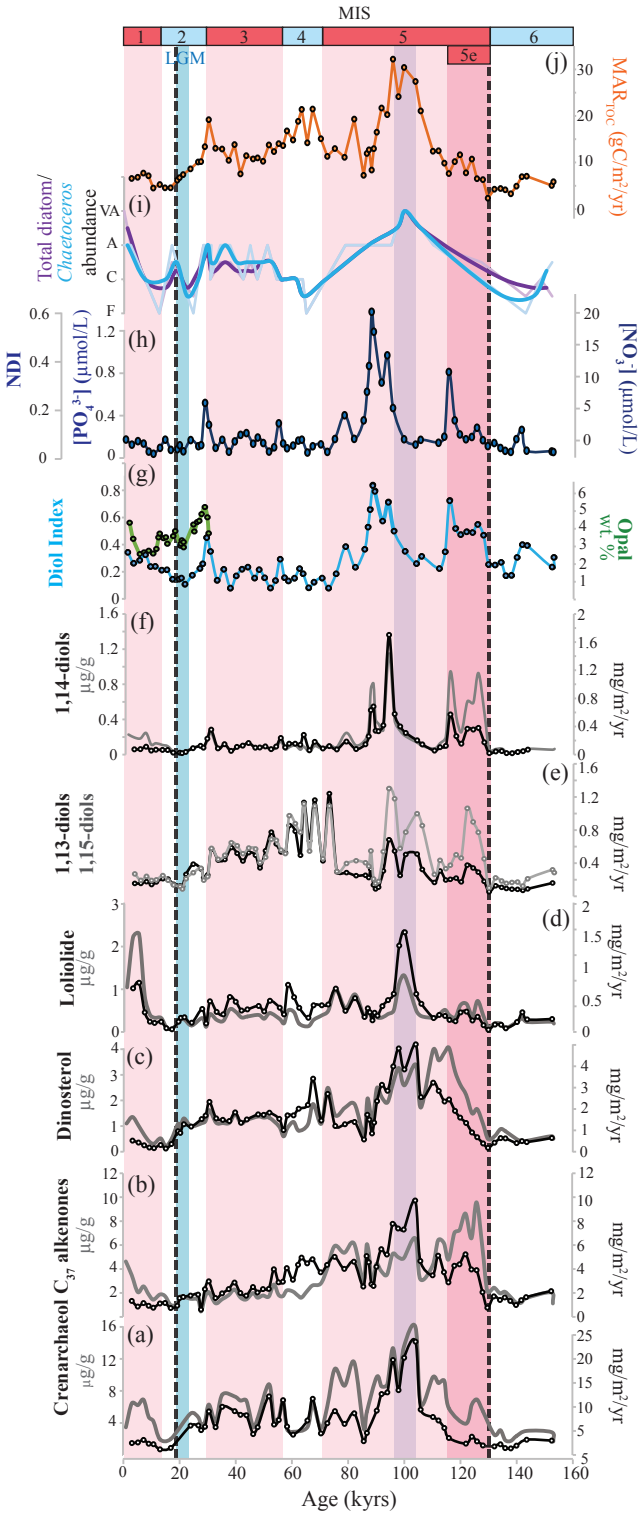
MIS
1
2
3
4
5
6
5e
LGM
(j)
MAR$_{TOC}$ (gC/m^2/yr)
(i)
Total diatom/ *Chaetoceros* abundance
VA
A
C
F
(h)
NDI
[PO_4^{3-}] (µmol/L)
[NO_3^-] (µmol/L)
(g)
Diol Index
Opal wt.%
(f)
1,14-diols µg/g
mg/m^2/yr
(e)
1,13-diols 1,15-diols
(d)
Lolioldide µg/g
(c)
Dinosterol µg/g
(b)
Crenarchaeol C_{37} alkenones µg/g
(a)
0
20
40
60
80
100
120
140
160
Age (kyrs)

4. Discussion

4.1 Productivity

The average bulk organic carbon $\delta^{13}C$ over the last 150 kyr is –21.4 (±0.6; s.dev.) ‰, and the atomic C/N ratio displays an average value of 6.8 (±1.3), both implying a dominant marine organic carbon source (Bordovskiy, 1965; Emerson and Hedges, 1988; Meyers, 1997). Today, the amount of sedimentary organic carbon is a good indicator of export production along the Chilean margin (Hebbeln et al., 2000). Hence, higher TOC levels during the interglacial intervals in the ODP 1234 record may suggest enhanced marine productivity during these intervals for this site. However, enhanced interglacial productivity is in contrast with previous studies that state that coastal productivity on the Peru Margin was highest during the LGM and diminished during the Holocene (e.g., Thomas et al., 1994; Marchant et al., 1999; Thomas, 1999; Hebbeln et al., 2000, 2002; Lamy et al., 2002, 2004; Romero & Hebbeln, 2003; Mohtadi & Hebbeln, 2004). These studies suggest that during the LGM the ACC migrated northward, supplying nutrients (particularly nitrate and phosphate; Levitus et al., 1994), together with a northward shift of the Southern Westerly belt as main precipitation source onshore, resulting in enhanced micronutrient supply via continental runoff. This combined effect would have stimulated productivity along the Chilean coast during the LGM. Upon deglaciation the climate zones propagated southward resulting in a lowering of productivity, as indicated by pollen, sedimentological and continental studies (e.g., Heusser, 1990; Lamy et al., 1998, 1999, 2001, 2004; Brathauer & Abelmann, 1999; Haberle & Bennett, 2004; Stuut & Lamy, 2004; Kaiser et al., 2005; Heusser et al., 2006). These studies suggest a 5° to 6°Northward movement of the Southern Westerly belt during the LGM.

In contrast to the hypothesis of stimulated productivity during the LGM, and lower productivity during the Holocene, two studies suggested low paleoproductivity during the LGM for core sites at the same latitude as that of our core (35–36°S) (Romero et al., 2006; Mohtadi et al., 2008). Mohtadi et al. (2008) hypothesized that if the climate zones shifted 5 to 6°Northward during the LGM, the SWW would be just above the core site (35–36°S), blowing directly onshore thereby preventing coastal upwelling. In turn, during the Early Holocene the subtropical high pressure would have become the dominant atmospheric player according to Romero et al. (2006), favouring upwelling. However, Muratli et al. (2010b), who reconstructed paleoproductivity over the last ~30 kyr for ODP 1234, suggested that the rise in TOC after the LGM is probably not the result of increased productivity, but of a lower oxygen availability due to decreased Antarctic Intermediate Water ventilation, and thus increased preservation. The authors based these suggestions on the fact that neither opal concentrations nor opal or TOC MARs increased simultaneously with TOC concentrations. Chase et al. (2014) support this hypothesis based on the Th normalized organic carbon fluxes. Our (unnormalized) MAR_{TOC} support these findings as well since although TOC levels show a steady rise after the LGM, we do not observe this increase in the accumulation of organic carbon, and the MAR_{TOC} is higher during the LGM as compared to the Holocene, suggesting higher glacial productivity. In summary, our findings seem consistent with previous studies

which suggested that higher TOC levels during the Holocene likely not result from increased productivity, but rather from increased preservation.

Interestingly, during MIS 3, 4 and 5 we observe even higher MAR_{TOC} values, reaching a pronounced maximum around 100 ka during MIS 5, i.e., during an interglacial period. Hence, this record suggests that the general productivity over the last ~150 kyr was highest around 100 ka. This interpretation is supported by most of the AR records of the individual lipid biomarkers peaking around 100 ka. The C_{37} alkenone, crenarchaeol and dinosterol ARs are all at their maximum between ca. 105 and 95 ka (Fig. 4b, 4a and 4c, respectively), simultaneous with maximal MAR_{TOC} (Fig. 4j). The AR of loliolide (indicating diatom abundance) peaks at 100 ka (Fig. 4d), coincident with a maximum in total diatoms and *Chaetoceros* diatom counts (Mix et al., 2003; Fig 4c), and concurrent with the peak in MAR_{TOC}. *Chaetoceros* diatoms are generally associated with upwelling (e.g., Abrantes, 1988; Abrantes and Moita, 1999), and also for the Peru-Chile upwelling system, the diatom genus *Chaetoceros* is thought to dominate the diatom community during upwelling conditions (e.g., Anabalón et al., 2007; Schrader and Sorknes, 1991; Romero et al., 2001; Vargas et al., 2004; Abrantes et al., 2007; González et al., 2007; Sanchez et al., 2012). Therefore, the high abundance of *Chaetoceros* diatoms at ~100 ka suggests that there was a peak in upwelling intensity around this time. This upwelling would have introduced macronutrients from deeper colder waters into the euphotic zone, stimulating several phytoplankton communities, including haptophytes, dinoflagellates and diatoms. During MIS 4 we also observe a peak in MAR_{TOC} (Fig. 3a) but there is no corresponding peak in *Chaetoceros* abundance (Fig. 4i). However, the high MAR_{TOC} during MIS 4 is linked to high sedimentation rates (Fig. 3c), whereas the peak in MAR_{TOC} during MIS 5 is not, confirming that the MAR_{TOC} maximum during MIS 5 indeed likely resulted from increased primary productivity, whereas during MIS 4 the high MAR_{TOC} did not.

4.2 1,14-diols as past upwelling and nutrient indicators

Interestingly, peaks in the Diol Index and 1,14-diol concentrations and accumulation rates occur before and after (around 116 and 88 ka; Fig. 4a and 4j), but not during the time interval with enhanced upwelling (i.e., around 100 ka; purple band in Fig. 3). Contreras et al. (2010) also reported high abundances of the C_{28} 1,14-diol around 120 ka near the coast of Peru (11°S). This suggests that *Proboscia* diatoms were more abundant before and after this period of intense upwelling, and is in agreement with observations that in the present-day Chile-Peru upwelling region, *Proboscia alata* is more dominant when upwelling is less intense (Tarazona et al., 2003; Herrera and Escribano, 2006). Although the recent time scale is quite different from our long-time record, which represents an integrated signal of several hundreds to thousands of years, it suggests that over the time period 120–80 kyr, on average, upwelling became stronger, reaching a maximum at 100 ka before subsequently decreasing. Shortly before and after the period of maximum upwelling, the conditions (averaged over multiple

years) were apparently optimal for *Proboscia* diatoms. As previously suggested by Rampen et al. (2014a), this indicates that the Diol Index should perhaps be considered as a specific indicator for *Proboscia* productivity, rather than upwelling strength generally, as the environmental conditions determining *Proboscia* abundance likely differ from region to region.

Recently, the NDI was introduced as a quantitative paleonutrient proxy. The Diol Index, the 1,14-diols AR and the NDI are low during the time of most intense upwelling (around 100 ka), suggesting a minimum in annual mean nitrate and phosphate concentrations, which is highly unlikely. The NDI is based on the saturated and mono-unsaturated C_{28} 1,14-diol relative to other diols. Whereas we observe a strong correlation between the ARs of the mono-unsaturated and saturated C_{30} 1,14-diol ($R^2 = 0.70$), the correlations between the C_{28} 1,14 and C_{30} 1,14-diol ($R^2 = 0.32$), and the C_{28} 1,14 and $C_{30:1}$ 1,14-diol ($R^2 = 0.36$) are weak, indicating different source organisms for the C_{28} and C_{30} 1,14-diols, in agreement with previous studies (Rampen et al., 2014a; de Bar et al., 2016; Gal et al., 2018). In fact, Sinninghe Damsté et al. (2003) found that 98 % of the diols in *P. alata* consisted of the saturated and mono-unsaturated C_{28} 1,14-diol, whereas *P. indica* produces similar amounts of the C_{30} and C_{28} 1,14-diol and *P. inermis* mainly produced the C_{28} 1,14-diol (Rampen et al., 2007). *P. alata* is the *Proboscia* species detected along the modern coast of Chile and Peru (Tarazona et al., 2003; Herrera and Escribano, 2006), and, therefore, it is likely that *P. alata* is the predominant producer of the C_{28} 1,1,4-diol detected in the ODP 1234 sediments. Consequently, the NDI record likely reflects variations in the abundance of *P. alata* over the last 150 kyr in the Chilean margin, whereas the Diol Index (which also includes the C_{30} 1,14-diol) more likely reflects the abundance of multiple species of *Proboscia*.

Previous studies showed that *P. alata* preferentially blooms over other diatoms when nutrients are high but silica concentrations are low (as *P. alata* needs little Si to build its frustule) (Haake et al., 1993; Sakka et al., 1999; Koning et al., 2001; Smith, 2001). In fact, although *P. alata* is often observed in high-nutrient and/or upwelling regions (Hernández-Becerril, 1995; Lange et al., 1998; Koning et al., 2001; Smith, 2001), the conditions in which the species is abundant, is often described as post-bloom, stratification, early upwelling season and/or the oceanic side of the upwelling front (e.g., Hart, 1942; Takahashi et al., 1994; Katsuki et al., 2003; Moita et al., 2003; Tarazona et al., 2003; Herrera and Escribano, 2006; Sukhanova et al., 2006; see references in Table 1 of Rampen et al., 2014a). Moreover, sediment trap studies from the Arabian Sea showed that the maximum flux of *Proboscia* lipids was at the start of the upwelling season (Prahl et al., 2000; Wakeham et al., 2002; Sinninghe Damsté et al., 2003; Rampen et al., 2007). When silicate concentrations increase (i.e., during upwelling), *P. alata* is likely outcompeted by more heavily silicified diatoms (such as *Chaetoceros*; e.g., Riegman et al., 1996). This suggests that the C_{28} 1,14-diol likely reflects early- or post-upwelling nutrient conditions. Hence, the dip in reconstructed [PO_4^{3-}] and [NO_3^-] concentrations at ~ 100 ka is not realistic and likely due to the low abundance of *P. alata* at this time of intense upwelling. In other regions, the C_{28} 1,14-diol might be

produced by other *Proboscia* species (e.g, *P. inermis*) and the NDI might thus not reflect solely *P. alata* productivity. In summary, we suggest that the NDI at the Chilean Margin likely reflects *Proboscia* productivity, and may therefore not be suitable as paleo-nutrient tracer.

4.3 Sea surface temperature evolution

The three organic proxy-based SST records broadly follow the trend of the planktonic oxygen isotope record for MIS 5, as well as the benthic oxygen isotope record for ODP Site 1234 (Heusser et al., 2006; Fig 5), and the global stack of benthic $\delta^{18}O$ (e.g., Lisiecki and Raymo, 2005) for the entire record, suggesting that the evolution of SST at our study location generally follows global climate patterns. The resolution of our record is not high enough to recognize possible millennial-scale SST variations related to climatic events such as the Antarctic Cold Reversal. Nevertheless, the overall SST patterns are similar to other Southern Hemisphere records (e.g., Kaiser et al., 2005; Kaiser and Lamy, 2010; Caniupán et al., 2011; Lopes dos Santos et al., 2013) and Antarctic ice-core stable isotope records (e.g., Blunier & Brook, 2001). The three temperature proxies are all significantly positively correlated and present a coherent view of regional climate variability (Fig. 6).

In principle, we would expect similar reconstructed temperatures from the LDI and $U_{37}^{K'}$ indices, since both proxies are based on biomarkers produced by photosynthetic algae (Prahl and Wakeham, 1987; Rampen et al., 2012). Indeed, Kim et al. (2002) showed that for surface sediments off Chile $U_{37}^{K'}$-derived temperatures strongly correlated with annual mean temperatures of the sea surface mixed layer. The linear regression for the $U_{37}^{K'}$ vs. the LDI is close to the 1:1 line, suggesting the LDI is reflecting SST. Interestingly, the LDI reveals a greater amplitude over the record as compared to the $U_{37}^{K'}$ and TEX_{86}^{H}, with a maximum temperature difference between the coldest (LGM) and warmest (Eemian Interglacial) temperature of ca. 10 °C, whereas this is ca. 7 and 8 °C, for the $U_{37}^{K'}$ and TEX_{86}^{H}, respectively. Other LDI and $U_{37}^{K'}$ applications on glacial-interglacial timescales also show somewhat greater amplitudes for the LDI compared to the $U_{37}^{K'}$, (Rampen et al., 2012; Lopes dos Santos et al., 2013; Rodrigo-Gámiz et al., 2014; Jonas et al., 2017). This might potentially suggest that the surface sediment calibration of the LDI requires some modification, such as a lower slope. Further analysis of surface sediments should reveal this.

For the TEX_{86}, it has been shown to potentially reflect subsurface rather than surface water temperatures (Huguet et al., 2007; Kim et al., 2010; 2015; Schouten et al., 2013b; Chen et al., 2014) due to the production of isoprenoid GDGTs below the surface mixed layer. Overall, the TEX_{86}^{H} record agrees reasonably well with the $U_{37}^{K'}$ record for ODP 1234, suggesting that it mainly reflects SST. Also, Kaiser et al. (2015) who established a regional TEX_{86}^{H} calibration suggested that this proxy mainly reflects SST. However, all cross-correlations still reveal relatively large scatter, reflecting the multiple different constraints on the respective proxies,

as each one is affected by different parameters and can reflect different seasonal temperatures. Nevertheless, for the largest part of the record, the absolute temperature differences between the three temperature proxies is smaller than the maximal possible discrepancy that can be explained by the combined calibration errors (calibration errors of $U_{37}^{K'}$, TEX_{86}^{H} and LDI are 1.5 °C, 2.5 °C and 2.0 °C, respectively; Müller et al., 1998; Kim et al., 2010; Rampen et al., 2012, respectively).

The only period during which the offsets are larger than calibration errors, is the last ~25 kyr, i.e., from the LGM to the Holocene, and the relatively brief interval between 52 and 56 ka. During these timespans, the LDI-derived temperatures are ca. 3 to 6 °C lower than those derived from $U_{37}^{K'}$ or TEX_{86}^{H}. This offset could potentially be related to terrestrial input, however, we have assessed the relative contribution of terrestrial derived organic carbon, by means of the BIT index (Hopmans et al., 2004) and the fractional abundance of the C_{32} 1,15-diol (de Bar et al., 2016; Lattaud et al., 2017a; 2017b), which were both always <0.2, implying that there was no substantial riverine input from terrigenous organic matter. Alternatively, the LDI might be compromised by high input of 1,14-diols (Rodrigo-Gámiz et al. 2015), however, we do not observe a correlation between the LDI (or the SST offset between the LDI and $U_{37}^{K'}$ or TEX_{86}^{H}) and the fractional abundance of the summed 1,14-diols. Potentially, the production of the 1,13- and 1,15-diols shifted to a colder season due to regional climatic change associated with the southward migration of the ACC and SWW upon the deglacial warming. Finally, wo observe an early onset of the deglacial warming for the LDI compared to the $U_{37}^{K'}$ and TEX_{86}^{H} (ca. 6 kyr; Fig. 5b), the reasons for which are elusive.

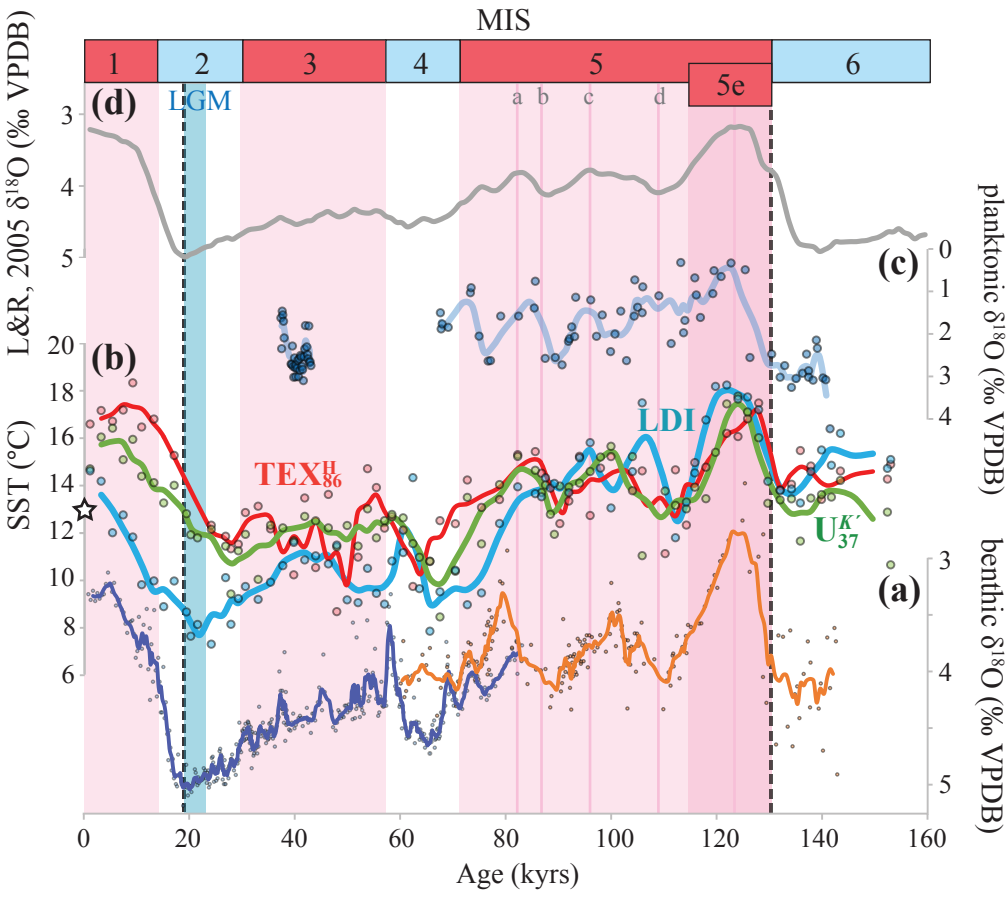

Fig. 5 Foraminiferal oxygen isotope and organic temperature proxy records for ODP 1234. **(a)** The benthic stable oxygen isotope records for ODP Site 1234 of Heusser et al. (2006), where the blue data reflect the benthic $\delta^{18}O$ dated by correlation to Atlantic core MD95204, and the orange data represent the $\delta^{18}O$ data correlated to the Vostok ice core chronology. **(b)** The organic geochemical seawater surface temperature records: $U^{K'}_{37}$ (green), TEX^{H}_{86} (red) and LDI (blue). The thick lines reflect 3-point running averages. **(c)** Planktonic foraminiferal $\delta^{18}O$ of the species *Globigerina bulloides* with the 3-point running average. **(d)** Global compilation of benthic stable oxygen isotopes (Lisiecki and Raymo, 2005). The pink colored bands reflect the interglacial periods (MIS 1, 3 and 5). The pink lines within MIS 5 reflect the different substage $\delta^{18}O$ minima and maxima. MIS (substage) ages are according to Lisiecki and Raymo (2005). The blue band reflects the Last Glacial Maximum, and the star symbol represents the present-day SST (World Ocean Atlas 2013 version 2). The dashed lines indicate the onset ages of Terminations 1 (Pacific age of Stern and Lisiecki, 2014) and 2 (approximate age).

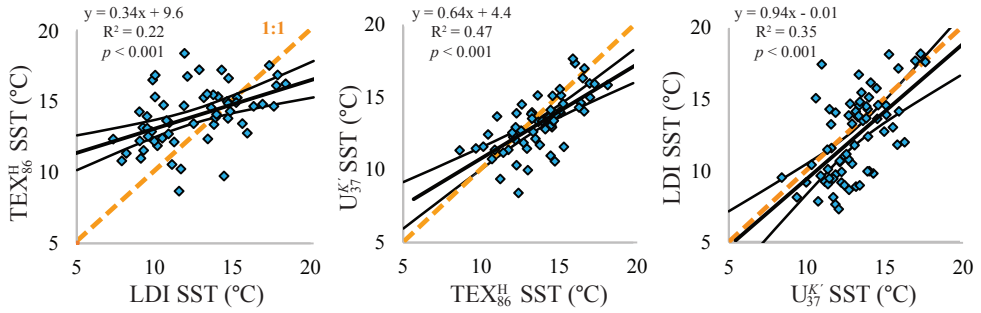

Fig. 6 Cross-correlations of sea surface temperature estimates based on the TEX^{H}_{86}, $U^{K'}_{37}$ and LDI indices. Linear regressions are indicated by the black solid lines, together with the 95 % confidence intervals. All correlations are significant ($p < 0.001$). The orange dashed line represents the 1:1 line.

We can compare our SST records of ODP Site 1234 with those of other SST records along the coast of South America, in particular those generated by the $U^{K'}_{37}$, which has been used the most often (Fig. 7). Our $U^{K'}_{37}$ temperature record agrees well with other records in the vicinity of ODP 1234, both in terms of absolute temperature as well as in glacial-interglacial temperature amplitude. Our $U^{K'}_{37}$ SST record shows an approximate 7 °C warming over Termination 1, which is in agreement with other past SST records for the central and Southern Chilean margin (Kim et al., 2002; Lamy et al., 2002; 2004; Kaiser et al., 2005; Romero et al., 2006; Kaiser and Lamy, 2010). Although the timing of deglacial warming associated with Termination 2 is comparable to other records, the last deglaciation (Termination 1) reveals an early start (around 26 ka) at Site 1234 as compared to neighboring sites. The TEX^{H}_{86} record reveals this same timing, whereas the LDI suggests a timing more comparable to other records in the vicinity (around 20 ka). Regional differences in timing of deglacial warming have previously been related to the southward shift of the SWW, which directly and indirectly influences local paleoproductivity and upwelling intensity, and thereby potentially leaving site-dependent, unique signatures in the SST records (Mohtadi et al., 2008). This may partially explain the discrepancies that we observe between our $U^{K'}_{37}$ record and the other records. For instance, site GeoB 3327-5 is located at the northern extent of the ACC, and thus largely influenced by its latitudinal movement which is closely related to the migration of the SWW (Ho et al., 2012), whereas for ODP 1234 this influence might be less. Furthermore, the combined regional records show an increase in the magnitude of $U^{K'}_{37}$ temperature variations over glacial-interglacial timescales towards the south (Fig. 7), which agrees with the idea of greater glacial-interglacial temperature differences at high latitudes as compared to low latitudes (e.g., CLIMAP, 1976; Mohtadi & Hebbeln, 2004; Mohtadi et al., 2008).

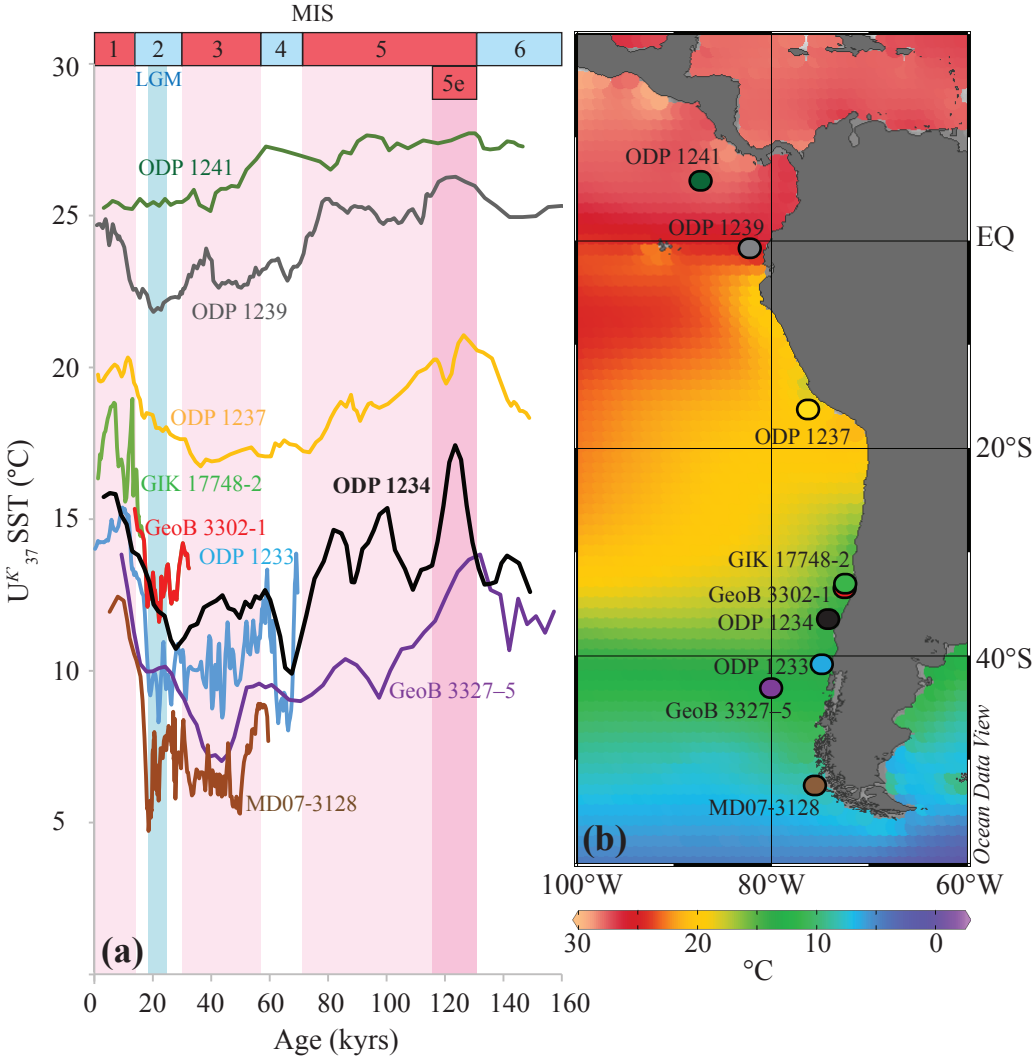

Fig. 7 **(a)** Pacific $U^{K'}_{37}$ SST reconstructions off South America for the last ~160 kyr (3-point running averages). **(b)** Sea surface temperature (°C) map for the region. The colors of the records correspond to the colors of the site symbols in the map. Alkenone-based SST data is from Caniupán et al. (2011) (MD07-3128; 53°S), Ho et al. (2012) (GeoB 3327-5; 43°S), Kaiser et al. (2005) (ODP1233; 41°S), this study (ODP 1234; 36°S), Kim et al., 2002 (GeoB 3302-1 and GIK 17748-2; 33°S), Bin Shaari (2013a) (ODP 1237; 16°S), Bin Shaari et al. (2013b) (ODP 1239; 1°S) and Bin Shaari et al. (2014) (ODP 1241; 6°N). Surface temperature data derived from the World Ocean Atlas 2013; map is drawn in Ocean Data View (Schlitzer, 2015), and modified manually.

5. Conclusions

We have applied long-chain diols as tracers for past SST (using the LDI index), upwelling and nutrient conditions (Diol Index), and [PO_4^{3-}] and [NO_3^-] (NDI index) at ODP 1234, located within the Peru-Chile upwelling system. The LDI agrees with the TEX_{86}^H and $U_{37}^{K'}$ sea surface temperature records, as well as with the planktonic $\delta^{18}O$, suggesting that the LDI reflects past SSTs. During the Last Interglacial (MIS 5), increased accumulation of TOC and phytoplankton lipid biomarkers centered around 100 ka indicate enhanced primary productivity. Concurrently, there is a peak abundance in preserved *Chaetoceros* diatoms, suggesting a peak in upwelling intensity. The Diol Index peaks before and after this peak in upwelling, agreeing with present-day diatom distributions along the Chile-Peru margin, with *Chaetoceros* diatoms being dominant during upwelling, and *Proboscia alata* thriving in more stable waters. The NDI (based primarily on the C_{28} 1,14-diol) shows the same trend as the Diol Index (based on both the C_{28} and C_{30} 1,14-diols), i.e., also showing a dip around 100 ka, suggesting low mean annual nitrate and phosphate concentrations during this upwelling interval, which is not realistic. Likely *P. alata* is the main C_{28} 1,14-diol producer at ODP 1234 suggesting that the NDI likely reflects *P. alata* productivity at the core site, and is therefore not suitable as paleo-nutrient tracer, since the species is generally outcompeted when Si concentrations increase, i.e., during upwelling (potentially explaining the minimum in NDI around 100 ka). Overall, these data suggest that the NDI and the Diol Index should perhaps be considered indicators for *Proboscia* productivity, rather than nutrient concentrations or general upwelling conditions.

Acknowledgements

We thank Phil Rumford for sampling of core ODP 1234. Ronald van Bommel is thanked for analytical support. Linda Heusser and Alan Mix are thanked for providing the age model. Dr. Alberto Reyes and three anonymous reviewers are thanked for their constructive comments which improved the manuscript. This research has been funded by the European Research Council (ERC) under the European Union's Seventh Framework Program (FP7/2007-2013) ERC grant agreement [339206] to S.S. S.S. and J.S.S.D. receive funding from the Netherlands Earth System Science Center (NESSC) through a gravitation grant from the Dutch ministry for Education, Culture and Science (grant number 024.002.001). The contribution of J.F.M. to this work was supported in part by funding from the United States National Science Foundation.

Fig. A1 TEX_{86} records for ODP 1234 applying different calibrations, i.e., the global core-top calibration of Kim et al. (2010) in red (TEX_{86}^{H}), the local core-top calibration of Kaiser et al. (2015) in purple and the Bayesian model of Tierney and Tingley (2014; 2015) in green applying the BAYSPAR tool (http://bayspar.geo.arizona.edu/). For the BAYSPAR calculation we have assumed a prior mean 13 °C and a search tolerance of 0.2 TEX_{86} units. The calculated values are based on TEX_{86} values from 62 20° by 20° latitude-longitude grid boxes.

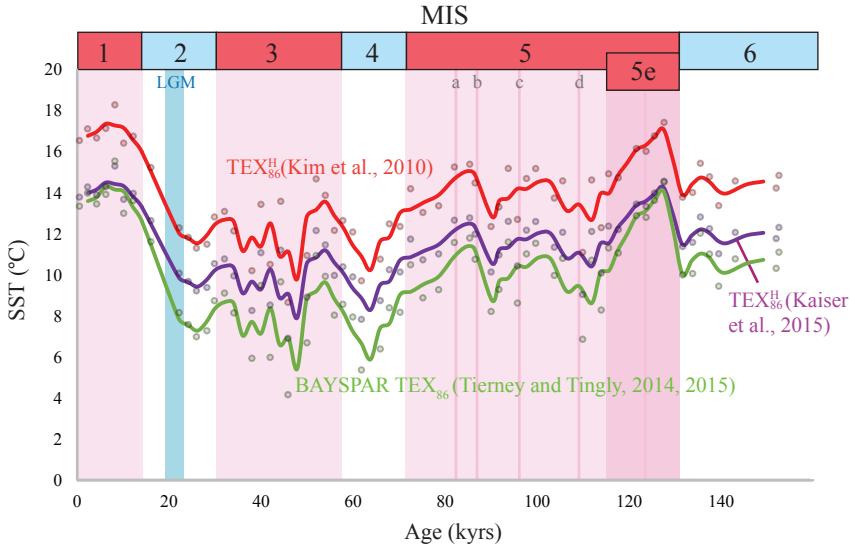

Chapter 8

Constraining the applicability of organic paleotemperature proxies for the last 90 Myrs

Marijke W. de Bar, Sebastiaan W. Rampen, Ellen C. Hopmans, Jaap S. Sinninghe Damsté and Stefan Schouten

Organic Geochemistry 128 (2019)

DOI: 10.1016/j.orggeochem.2018.12.005

Abstract

We evaluated changes in the distributions of long-chain alkenones, long-chain diols and GDGTs, lipids commonly used for paleothermometry, over the last 90 Myrs for sediments deposited on the New Jersey shelf (the Bass River site) and assessed potential effects of different ancestral producers and diagenesis on their distributions and their impact on the associated temperature proxies. As reported before, the Paleogene distributions of alkenones are generally similar to those in haptophytes, but unusual alkenone distributions, characterized by a dominant di-unsaturated C_{40} alkenone, are observed for Late Cretaceous sediments, suggesting different ancestral source organisms for alkenones in this interval. The isoprenoid GDGT distributions remained comparable to modern-day distributions, suggesting that the TEX_{86} can be applied up to ca. 90 Ma. The Miocene long-chain diol distributions are similar to modern-day distributions, but the older sediments reveal unusual distributions, dominated by the C_{28} 1,12- and C_{26} 1,13-diols, suggesting different source organisms before ~30 Ma. Accordingly, the LDI does not match other paleotemperature proxies, suggesting its applicability might be compromised for sediments older than the Miocene. Our results indicate that of the three proxies, the TEX_{86} seems to be the most applicable for deep time temperature reconstructions.

1. Introduction

Lipid biomarkers have become popular tools in paleoclimate and paleoceanographic studies. Several proxies have been proposed for the reconstruction of past seawater temperature and salinity, terrestrial organic matter input into the marine realm, and continental vegetation changes (see Brocks and Pearson, 2005; Schouten et al., 2013b; Luo et al., 2018 for reviews). The most important reconstructed climate parameter is probably sea surface temperature (SST), for which different lipid proxies have been developed. First, the $U^{K'}_{37}$ index (Brassell et al., 1986; Prahl and Wakeham, 1987) based on the unsaturation of long-chain alkenones (LCAs; see Supplementary Fig. S1 for lipid structures), which in modern systems are mainly produced in the open ocean by the haptophytes *Emiliania huxleyi* and *Gephyrocapsa oceanica* (Conte et al. 1995; Volkman et al., 1995). LCAs observed in marine sediments are typically composed of C_{37} – C_{39} alkyl chains, with two, three or four unsaturations and a keto group at the C2 (methyl ketone) or C3 (ethyl ketone) position. The first alkenone unsaturation index was established by Brassell et al. (1986), which included the relative abundance of the di-, tri- and tetra-unsaturated C_{37} LCAs (U^{K}_{37}), followed by the $U^{K'}_{37}$ index proposed by Prahl and Wakeham (1987), which excluded the tetra-unsaturated C_{37} LCA since this LCA did not correlate well with temperature. $U^{K'}_{37}$ values in surface sediments exhibit a strong relationship with SST (Müller et al., 1998; Conte, 2006). LCAs are relatively simple to analyze and occur often abundant in marine sediments, and hence, the proxy is regularly applied in paleoclimate reconstructions over the last decades. Evidently, there are also certain issues associated with the $U^{K'}_{37}$ proxy, such as the effect of lateral transport (Ohkouchi et al., 2002; Mollenhauer et al., 2008; Kim et al., 2009b), postdepositional oxic degradation (Hoefs et al., 1998) and its upper temperature limit of 29 °C (Prahl and Wakeham, 1987).

The second temperature proxy is TEX_{86} (Schouten et al., 2002; 2013) which is based on the ratio of isoprenoidal glycerol dialkyl glycerol tetraethers (iGDGTs) containing different numbers of cyclopentane moieties (see Supplementary Fig. S1 for example of lipid structures). These compounds are membrane lipids produced by a range of Archaea (Koga and Morii, 2007, Schouten et al., 2013b). In the marine environment the main producers of isoprenoidal GDGTs are thought to be Thaumarchaeota (Schouten et al., 2013b), and a strong correlation between this index and annual mean SST has been observed for marine surface sediments from all over the world (Schouten et al., 2002; Kim et al., 2008; 2010; Ho et al., 2014; Tierney and Tingley, 2014). Due to the preservation of iGDGT core lipids up to at least the Jurassic, the TEX_{86} proxy has been widely used over these timescales (e.g., Schouten et al., 2004; Forster et al., 2007a; 2007b; Bijl et al., 2009; Littler et al., 2011; Linnert et al., 2014) and its utility has been demonstrated for sediments where other proxies were compromised by diagenesis or associated lipid biomarkers were absent (e.g., Bijl et al, 2009; Liu et al, 2009; Hollis et al., 2012; Schouten et al., 2013b and references cited therein). Also, whereas the upper limit of the $U^{K'}_{37}$ is around 29 °C, the TEX_{86} paleothermometer can record higher temperature as it has not reached unity yet at modern day tropical temperatures, although extrapolation above 30 °C is relatively uncertain and should therefore be done with

caution (e.g., Schouten et al., 2003; Tierney and Tingley, 2014 and references cited therein). However, iGDGTs used in TEX_{86} may not solely derive from the surface mixed layer, but also from deeper living archaea, affecting the TEX_{86} signal, evidenced for both core GDGTs (e.g., Huguet et al., 2007; Lee et al., 2008; Kim et al., 2010; 2012; 2016; Lopes dos Santos et al., 2010; Schouten et al., 2013b; Taylor et al., 2013; Chen et al., 2014), as well as for intact polar lipids (IPLs; e.g., Basse et al., 2014; Zhu et al., 2016; Hurley et al., 2018). Additionally, there are several non-thermal biological factors which can potentially affect the TEX_{86}. For instance, it has been shown that the lipid composition of Thaumarchaeota can markedly differ with growth phase (Elling et al., 2014), oxygen concentrations, and ammonia oxidation rates as well as between different species (Qin et al., 2015; Elling et al., 2017; Hurley et al., 2016; 2018). In contrast, pH and salinity variations likely have minimal effect on the intact polar GDGT composition (Wuchter et al., 2004; Elling et al., 2015). GDGTs produced by archaea other than marine Thaumarchaeota can also affect the TEX_{86}, and several indices have been proposed to assess these affects, such as the %GDGT-0 index and the Methane Index reflecting methanogenic or methanotrophic archaeal GDGT production, and the $\%GDGT_{RS}$ index as tool to identify Red Sea-type GDGT distributions (Zhang et al., 2011; Sinninghe Damsté et al., 2012avol; Inglis et al., 2015). Furthermore, it has been shown that input from the terrestrial environment can potentially affect the TEX_{86} proxy, which can be monitored by the branched isoprenoid tetraether (BIT) index (Hopmans et al., 2004), which is based upon the ratio of crenarchaeol, predominantly produced by marine Thaumarchaeota, and branched GDGTs (brGDGTs), which predominantly derive from the continent. Typically, BIT values < 0.3 are considered to reflect marine conditions (e.g., Weijers et al., 2006; Zhu et al., 2011; Sinninghe Damsté, 2016).

The most recent lipid-based proxy for SST is the Long-chain Diol Index (LDI) based on the relative abundances of specific long-chain alkyl diols (LCDs), i.e., those with alcohol groups positioned at C1 and at C13 or C15 (Supplementary Fig. S1). Analysis of marine surface sediments from all over the world, showed a strong correlation of the LDI with SST (Rampen et al., 2012). Although this proxy has been applied successfully in several studies (e.g., Naafs et al., 2012; Lopes dos Santos et al., 2013; Smith et al., 2013; Plancq et al., 2015; Jonas et al., 2017), a lack of understanding still complicates the application of this proxy. For instance, the source organisms are not well known. Whereas 1,13- and 1,15-diols have been observed in cultures of (marine) eustigmatophyte algae (e.g., Volkman et al., 1992; 1999; Méjanelle et al., 2003; Rampen et al., 2014b), the observed LCD distributions are dissimilar to those observed in marine sediment, and therefore their role as LCD producers remains highly uncertain (Versteegh et al., 1997; 2000; Rampen et al., 2012; 2014b). Furthermore, riverine input into the marine realm might compromise the LDI (de Bar et al., 2016; Lattaud et al., 2017a; 2017b), while Rodrigo-Gámiz et al. (2015) obtained unrealistic LDI-derived SSTs due to high abundances of 1,14-diols, which are produced by *Proboscia* diatoms (Sinninghe Damsté et al., 2003; Rampen et al., 2014a), which also produce minor amounts of 1,13- and 1,15-diols. Saturated C_{28}, C_{30} and C_{32} 1,14-diols have also been observed in the marine Dictyochophyte *Apedinella radians* (Rampen et al., 2011), however, its importance as 1,14-

diol producer in the marine realm is unknown. In addition to LCDs, structurally corresponding long-chain keto-ols are also often observed and it has been proposed that these keto-ols are intermediate products of the oxidation of LCDs (Ferreira et al., 2001), although the chain length and positional isomer distributions for LCDs and keto-ols are not always similar (e.g., ten Haven et al., 1992; Yamamoto et al., 1996; Versteegh et al., 1997; 2000).

The TEX_{86}, $U_{37}^{K'}$ and LDI temperature proxies are all based upon the assumption that growth temperature is the main factor affecting the composition of the lipids on which they are based. However, many other factors, such as salinity, nutrient availability, inter- and intraspecies variation, may affect these proxies (e.g., Herbert, 2003; Liu et al., 2007; Qin et al., 2015; Elling et al., 2017). Importantly, application of these proxies in deep time, in particular the Cenozoic, implicitly assumes that the biological sources of these compounds have remained the same and that evolutionary ancestors of the modern day organisms producing these biomarkers responded in a similar way to temperature. However, for the $U_{37}^{K'}$ it has already been shown that its application is limited to the last ca. 55 Ma, due to the absence of tri-unsaturated LCAs in older sediments (Brassell, 2014 and references therein). Moreover, LCA distributions deviating from those in modern day sediments have been observed for Cretaceous and Paleocene sediments (Farrimond et al., 1986; Yamamoto et al., 1996; Brassell et al., 2004). Brassell (2014) assessed distributional variations in LCAs preserved in the sedimentary record with respect to changes in preserved calcareous nannoplankton over time, and linked the alkenone distributions to evolutionary adaptations of the source organisms in response to climate change. However, this evaluation was done on sediments from multiple sites covering relatively short time periods and regions covering different climate zones. More importantly, proxies like the TEX_{86} and LDI have not been evaluated in a similar fashion, i.e., to assess the impact of (evolutionary) changes in the producers of GDGTs and LCDs, respectively, on the TEX_{86} and LDI proxies. In addition to evolutionary adaptations, diagenetic alterations may also influence lipids used for deriving paleoclimatic information.

In this study we investigate the lipid biomarker distributions in a sediment core from the New Jersey Shelf, USA, which covers the last 90 Myrs. These sediments were previously investigated by de Bar et al. (accepted) for different temperature proxies, i.e., benthic foraminiferal stable oxygen isotopes ($\delta^{18}O$), Mg/Ca, clumped isotopes (Δ_{47}), MAT_{mrs} and TEX_{86} which showed that temperature reconstructions were consistent with each other. In this study we have examined in detail variations in distributions of LCAs, GDGTs and LCDs, which can give clues about changes in sources of these lipids compared to modern day contributors. In particular, when biomarker lipids are encountered with e.g. unusual chain lengths compared to modern day distributions in extant organisms and environments, this may hint at contributions of ancestral species which are different than today, although it is possible that different lipid distributions derive from the same species. Our results shed new light on the applicability of the biomarker lipids used for temperature reconstructions across the Mid- to Late Cretaceous and Cenozoic.

2. Materials and methods

2.1 Study site and age model

Lipid biomarkers were analyzed in sediments of the Bass River core (Ocean Drilling Program Leg 174AX, New Jersey Coastal Plain; 39°36´42´´N, 74°26´12´´W). A complete description of the core is provided by Miller et al. (1998). Nine sediment intervals spanning a time period of ca. 80 million years (Late Cretaceous to Late Miocene) were subject of study, dated at ca. 91, 78, 74, 60, 50, 41, 33, 18 and 11 Ma, based on biostratigraphy, magnetostratigraphy, isotope stratigraphy and specific paleoclimatic events (for detailed description, see de Bar et al., accepted). Note that the age uncertainties are relatively large (in the order of millions of years), due to the coarse resolution of the age model. For every sediment interval, 10–15 subsamples (95 in total) were obtained, covering shorter time intervals (in the order of ten to hundreds of thousands of years) to assess short-term versus long-term variability.

2.2 Lipid extraction and analysis

Extracts of the sediments obtained by de Bar et al. (accepted) were re-analyzed (see Supplementary Table S2 for the subsamples which were analyzed). In short, sediments were extracted via Accelerated Solvent Extraction (ASE) with dichloromethane (DCM)/methanol (MeOH) (9:1, vol./vol.) and separated over Al_2O_3 into apolar, ketone and polar fractions, using *n*-hexane/DCM (9:1, vol./vol.), *n*-hexane/DCM (1:1, vol./vol.) and DCM/methanol (1:1, vol./vol.), respectively. Fractions containing elemental sulfur were desulfurized using copper granules activated with 1M HCL. Polar fractions were purified by polytetrafluoroethylene (PTFE) filtration (0.45 μm). A selection of alkenone fractions was further purified by chromatographic separation on silica impregnated with Ag^+, whereby DCM and ethyl acetate was used as eluents to purify the ketone fraction by removing saturated hydrocarbons (in the DCM fraction).

2.2.1 Long-chain alkenones

We analyzed the ketone fractions of between 2 and 13 samples per age interval for LCAs, depending on the presence of these compounds. The ketone fractions were redissolved in ethyl acetate prior to analysis. Quantification of the LCAs was achieved on an Agilent 6890N gas chromatograph (GC) with flame ionization detection (FID). Separation was achieved on a fused silica column with a length of 50 m and diameter of 0.32 mm, coated with a CP Sil-5 (thickness = 0.12 μm). Helium was used as carrier gas. The oven program was as follows: 70 °C at injection, increased by 20 °C min^{-1} to 200 °C followed by 3 °C min^{-1} until the final temperature of 320 °C. This end temperature was held for 30 min. The flow mode was a constant pressure of 100 kPa. Identification of the LCAs was performed on an Agilent 7890A GC coupled to an Agilent 5975C mass spectrometer (MS). The column, carrier gas, flow rate and oven program were identical to those described for GC–FID analysis but the end temperature was kept for 25 min, and the length of the column was 25 m instead of 50 m.

The MS was operated at 70 eV, with an ion source temperature of 250 °C and an interface temperature of 320 °C. For both systems, injection was done on-column, with an injection volume of 1 µL. The mass spectra of the LCAs were obtained in full scan mode, scanning between *m*/*z* 50 and 600 and compared with literature data (de Leeuw et al., 1980; Marlowe et al., 1984a; Volkman et al., 1980b). For the $C_{42:2}$ ketone, we could not detect the molecular ion mass (*m*/*z* 600), but its identification is based on the presence of the M^+–29 ion and its relative retention time. Since the $C_{38:2}$ methyl (Me) and ethyl (Et) ketones were not sufficiently separated on a CP Sil-5 column, complicating identification by GC–MS, one sample containing both isomers was also analyzed on an Agilent 7890B GC system equipped with a RTX200 column (mid-polarity) (cf. Longo et al., 2013) and FID. The RTX200 column had a length of 60 m, a diameter of 0.32 mm and a film thickness of 0.5 µm. The carrier gas was helium and the system was operated at a constant flow of 1.5 mL min^{-1}. The oven was programmed at 70 °C at injection, which was increased with a rate of 15 °C min^{-1} to 250 °C, followed by a linear gradient to 320 °C by 1.5 °C min^{-1}. This end temperature was held for 25 min. The injection volume was 1 µL. Comparison of the retention time with a sample containing $C_{38:2}$ Me confirmed the identity of this LCA in the Bass River sediment.

The $\delta^{13}C$ composition for the $C_{37:2}$ and $C_{38:2}$ LCAs of a sediment from the 41.2 Ma age interval, and of the $C_{40:2}$ LCA for the 77.8 Ma age interval was analyzed, by means of gas chromatography–isotope ratio mass spectrometry (GC–IRMS). Analyses were performed on a Thermo Delta V isotope ratio monitoring mass spectrometer coupled to a Thermo Trace 1310 GC. Separation was achieved on a column identical to that of the GC–FID but with a length of 25 m. The oven temperature at injection was 70 °C, which was then increased by 20 °C min^{-1} to 130 °C, followed by 4 °C min^{-1} to the end temperature of 320 °C at which it was held for 20 min. The $\delta^{13}C$ data represent averaged values of replicate analyses, and are reported in delta notation relative to the VPDB standard using CO_2 reference gas calibrated to the NBS-22 reference material. The instrumental reproducibility was monitored by co-injection of deuterated *n*-alkane standards (C_{20} and C_{24} perdeuterated *n*-alkanes) with the samples. Injection volumes of the samples varied between 2 and 3 µL; injection volume for the *n*-alkane standards was 0.4 µL. Based on the quadruplicate injection of the *n*-alkane standards, the instrumental error is < 0.4 ‰.

2.2.2 Glycerol dialkyl glycerol tetraethers

The polar fractions, containing the GDGTs and related lipids, were redissolved in hexane/isopropanol (99:1, vol./vol.) and analyzed using high performance liquid chromatography–atmospheric pressure chemical ionization / mass spectrometry (HPLC-APCI/MS) on an Agilent 1260 HPLC, equipped with automatic injector, coupled to a 6130 Agilent MSD and HP Chemstation software according to Hopmans et al. (2016). Separation of the GDGTs was achieved in normal phase using 2 silica BEH HILIC columns in series (150 mm × 2.1 mm; 1,7 µm; Waters Acquity) at a temperature of 25 °C. Compounds were

isocratically eluted with 82 % A and 18 % B for the first 25 min, followed by a gradient to 35 % B in 25 min and a linear gradient to 100 % B in 30 min. A = hexane and B = hexane/isopropanol (90:10, vol./vol.) and the flow rate was 0.2 mL min^{-1}. The conditions for the APCI–MS were identical to Schouten et al. (2007) and Hopmans et al. (2016). We assessed the distributions of GDGTs and related glycerol ether lipids by monitoring *m*/*z* 900 to 1400 rather than single ion monitoring as performed previously (de Bar et al., accepted) to investigate the distribution of ether lipids other than those used in the TEX_{86} and BIT proxies. The injection volume was 10 µL. For each age interval we analyzed three polar fractions (27 samples in total) on single quadrupole UHPLC–MS and integrated the extracted ion chromatograms of the protonated molecules for the ether lipids, with exception of the hydroxy GDGTs (OH-GDGTs) for which the $[M+H]^+ - H_2O$ ions were integrated (Liu et al., 2012b, 2012c). The integrated peak area of iGDGT-4 was corrected for the contribution of the isotope peak of crenarchaeol by subtracting 45 % of the crenarchaeol peak (Hopmans et al., 2000; Pitcher et al., 2011). We report fractional abundances based on peak areas which were not corrected for possible differences in response factors between the various glycerol ether lipids.

For identity confirmation of the ether lipids, we performed UHPLC–high resolution MS (HRMS) on 1 to 2 samples per age interval, using an Agilent 1290 Infinity I equipped with thermostatted auto-injector and column compartment coupled to a Q Exactive (Quadrupole Orbitrap hybrid MS) MS equipped with ion max source with APCI probe (Thermo Fisher Scientific, USA). Positive-ion APCI setting were as follows: capillary temperature 200 °C, sheath gas (N_2) 50 arbitrary units (AU); vaporizer temperature 400 °C; auxiliary gas (N_2) 5 AU, corona current 2.5 µA, APCI heater temperature 400 °C; S-lens 100 V. Chromatography was identical as described above for the UHPLC–MS analyses (i.e., 2 silica BEH HILIC columns in series according to Hopmans et al., 2016). Ether lipids were analyzed with a mass range of *m*/*z* 600 to 2000 (resolution 70,000), followed by data dependent MS^2 (resolution 17,500), in which the ten most abundant masses in the mass spectrum (with the exclusion of isotope peaks) were fragmented successively (stepped normalized collision energy 15, 20, 25; isolation window 1.0 *m*/*z*). A dynamic exclusion window of 6 sec, with a mass tolerance of 3 ppm, was applied. In addition, an inclusion list was used with a mass tolerance of 3 ppm, comprehensively targeting ether lipids described in literature. Identification was achieved by comparison of exact mass and fragmentation spectra to literature (e.g., Knappy et al., 2009; Liu et al., 2012a, 2012b, 2012c, Zhu et al., 2014; Naafs et al. 2018).

To assess the sources of branched GDGTs we calculated the $\#rings_{tetra}$ index for the two youngest time intervals characterized by a BIT index > 0.3, according to Sinninghe Damsté et al. (2016):

$$\#rings_{tetra} = [brGDGT\ Ib+2\times brGDGT\ Ic]/[brGDGT\ Ia+brGDGT\ Ib+brGDGT\ Ic] \quad (1)$$

We have calculated the ring index of OH-GDGTs (Lü et al., 2015) based on the peak areas of the $[M+H]^+ - H_2O$ ions of OH-GDGTs:

$$RI\text{-}OH = [OH\text{-}GDGT\text{-}1+2\times OH\text{-}GDGT\text{-}2]/[OH\text{-}GDGT\text{-}1+OH\text{-}GDGT\text{-}2] \quad (2)$$

To assess Red Sea-type GDGT contributions we calculated the $\%GDGT_{RS}$ ratio according to Inglis et al. (2015):

$$\%GDGT_{RS} = ([Cren']/[GDGT\text{-}0+Cren'])\times 100 \quad (3)$$

Lastly, we calculated the $f_{Cren':Cren'+Cren}$ as proposed by O'Brien et al. (2017) to identify anomalous GDGT distributions in Cretaceous sediments:

$$f_{Cren':Cren'+Cren} = [Cren']/[Cren+Cren'] \quad (4)$$

2.2.3 Long-chain diols and keto-ols

Polar fractions were dried in inserts under a stream of nitrogen and silylated by addition of BSTFA (N,O-bis(trimethylsilyl)trifluoroacetamide) and pyridine, and subsequent heating at 60 °C for 35 min. Subsequently, LCDs and corresponding keto-ols were analyzed on an Agilent 7890B GC system interfaced to a 7000C GC Triple Quadudropole MS operated in single MS mode, and a selection of samples was analyzed on an Agilent 7890 B gas chromatograph coupled to an Agilent 5977A mass spectrometer. We analyzed on average 5 samples per age interval. The oven was programmed with a starting temperature of 70 °C, increased to 130 °C with a 20 °C min^{-1} rate, followed by a gradient of 4 °C min^{-1} to the end temperature of 320 °C, which was held for 15 min. Fractions were injected on-column with an injection volume of 1 µL. The GC was equipped with a fused silica column (25 m × 0.32 mm) coated with CP Sil-5 (film thickness 0.12 µm). The flow rate was 2mL min^{-1}; the carrier gas was helium, and the mass spectrometer operated at 70 eV. The ion source had a temperature of 250 °C, and the interface temperature was 330 °C. Identification of all the LCDs and keto-ols was performed in full scan mode (*m*/*z* 50–800) by comparison with published mass spectra (e.g., Volkman et al., 1992; Versteegh et al., 1997). To assess distributional changes over time, ion chromatograms (EICs) with *m*/*z* 271, 285, 299, 313, 327, 341, 355 and 369, which are characteristic ion fragments formed by cleavage adjacent to the OTMSi groups (silylated hydroxyl groups) (Versteegh et al., 1997) were integrated. Similarly, for the long-chain keto-ols, distribution changes were assessed in full scan, i.e., quantification using mass chromatograms of their M^+–15 ions, i.e., *m*/*z* 453, 481, 509, 537, 565 and 593, as these were typically the most abundant characteristic fragment ions. Corrections for the relative contributions of the fragment ions to the total ion counts were made (9 % and 3 % for the LCDs and keto-ols, respectively). Typically, the LCDs and keto-ols were present in trace amounts in the older sediments.

LCDs are easier to identify than keto-ols since the characteristic fragments resulting from cleavage adjacent to the mid-chain OTMSi group are abundant, and hence, are relatively easily recognized in mass spectra. For long-chain keto-ols, the characteristic fragments associated with the position of the keto-group are much less dominant in the mass spectra,

and therefore suffer more from background noise (de Leeuw et al., 1981; Versteegh et al., 1997). For mass spectral identification of the keto-ols we used the diagnostic mid-chain cleavage fragments (Versteegh et al., 1997), the M^+–15 ions, as well as *m*/*z* 130, which is a typical fragment for long-chain keto-ols, possibly formed after steps of TMSi rearrangement and subsequent McLafferty rearrangement (de Leeuw et al., 1981).

The LDI index and the fractional abundance of the C_{32} 1,15-diol were computed by using peak areas obtained by integration of appropriate peaks in SIM analysis (cf. Rampen et al., 2012; de Bar et al., 2016):

$$LDI = [C_{30}\ 1,15\text{-diol}]/[C_{28}\ 1,13\text{-diol}+C_{30}\ 1,13\text{-diol}+C_{30}\ 1,15\text{-diol}] \quad (5)$$

LDI values were converted to SST values via the following equation:

$$SST = (LDI–0.095)/0.033 \quad (6)$$

$$FC_{32}\ 1,15\text{-diol} = [C_{32}\ 1,15\text{-diol}]/[C_{28}\ 1,13\text{-diol}+C_{30}\ 1,13\text{-diol}+C_{30}\ 1,15\text{-diol}+C_{32}\ 1,15\text{-diol}] \quad (7)$$

Due to the higher sensitivity of SIM compared to full scan, LCDs which were below the limit of detection in full scan mode in some samples (and are thus not shown in Fig. 6), were just above quantification limit in SIM, and could therefore be used for proxy calculation. For these proxy calculations, all sediment subsamples (on average 10 per age interval) were analyzed in SIM. The identities of the LCD isomers were affirmed by selected MRM analyses (de Bar et al., 2017), confirming that the fragments originate from LCDs.

3. Results and discussion

3.1 Long-chain alkenone distributions

We detected LCAs in sediments for the age intervals of 91, 78, 50, 41 and 33 Ma (e.g., Fig. 1) but not in the sediments of 74, 60, 18 and 11 Ma. The sediments for the intervals of 91, 50 and 33 Ma contain the di-unsaturated C_{37} methyl (Me) and C_{38} ethyl (Et) ketones (Fig. 2), and the sediments of 50 Ma also contain the $C_{38:2}$ Me alkenone. The LCA abundance in these sediments is generally low, and particularly for the sediments of 33 and 91 Ma, the signal is around the detection limit. For the sediments of 78 Ma we observed the $C_{40:2}$ Et ketone as a dominant LCA in addition to the more commonly observed LCAs. In the sediments of 41 Ma the largest variety in LCAs was detected, i.e., the C_{37} Me, C_{38} Et and Me, C_{39} Et and Me, C_{40} Et, C_{41} Me and C_{42} Et di-unsaturated ketones (Fig. 2).

The absence of LCAs in the youngest sediment intervals, i.e., 11 and 18 Ma, can probably be explained by the nearshore depositional setting of the core site at that time, as revealed by the high BIT index (> 0.8; de Bar et al., accepted), and thus the absence of marine LCA producers. One remarkable observation is that tri- or tetra-unsaturated LCAs were not

detected in any of the studied sediments, indicating that the value for $U_{37}^{K'}$ was always 1. Brassell (2014) observed that tri-unsaturated LCAs, as well as the C_{38} di-unsaturated methyl ketone, only appeared in the sedimentary record after the Early Eocene Climatic Optimum (EECO; ± 52 Ma) in the sedimentary record. The first evidence of tri-unsaturated LCAs in the sedimentary record was found in the Arctic Ocean immediately after the EECO (± 52 Ma; Weller and Stein, 2008). With time, there seems to be an equatorward migration of haptophytes able to produce tri-unsaturated LCAs, linked to reduced ocean warmth (Brassell, 2014), and the first occurrence of tri-unsaturated LCAs for the mid latitudes was around 45 Ma. Hence, for the Bass River site, we would expect the presence of tri-unsaturated LCAs for the age intervals of 33 and 41 Ma. Accordingly, the absence of the C_{37} tri-unsaturated LCAs in these sediments likely indicates SSTs > 27 °C as above this temperature no tri-unsaturated LCAs are produced (e.g., Prahl and Wakeham, 1987; Volkman et al., 1995) rather than the absence of haptophyte populations producing tri-unsaturated LCAs. Indeed, for the time slice of 41 Ma, TEX_{86}^{H} indicates a temperature of 27 °C (de Bar et al., accepted), which would agree with a value of the $U_{37}^{K'}$ of 1. However, for the age interval of 33 Ma, the TEX_{86}^{H}-derived SST was 22 °C, which is inconsistent with the absence of tri-unsaturated LCAs. The reason for this is unclear, but one possibility is that TEX_{86}^{H} reflects subsurface temperatures (de Bar et al., accepted) and SST might have been much higher such that $U_{37}^{K'}$ nears unity. An alternative explanation for the absence of tri- and tetra-unsaturated LCAs may be diagenesis leading to selective degradation of LCAs with more double bonds (Hoefs et al., 1998).

Overall, the distributions observed for 33, 41 and 50 Ma are typical for marine haptophytes, such as the present-day *E. huxleyi* and *G. oceanica* (Volkman et al., 1980a; 1980b; Conte et al., 1995). However, present-day producers, i.e., *E. huxleyi* and *G. oceanica* evolved only 290 kyrs and 1.85 Myrs ago, respectively (Pujos-Lamy, 1977; Thierstein et al., 1977; Raffi et al., 2006) and cannot be the source for the detected sedimentary LCAs. Since LCA distributions are similar to modern distributions up to the Eocene, it has been suggested that the most probable Cenozoic LCA producers are in the *Reticulofenestra* genus, which is part of the Noelaerhabdaceae family (like *Emiliania* and *Geohyrocapsa*) (Marlowe et al., 1990). However, it is plausible that LCAs were also produced by any species within the three genera of Noelaerhabdaceae, i.e., *Reticulofenestra*, *Dictyococcites* and *Cyclicargolithus* (Beltran et al., 2011; Plancq et al., 2012; Furota et al., 2016). In fact, for the late Oligocene-early Miocene it was suggested that *Cyclicargolithus* was the main producer (Plancq et al., 2012).

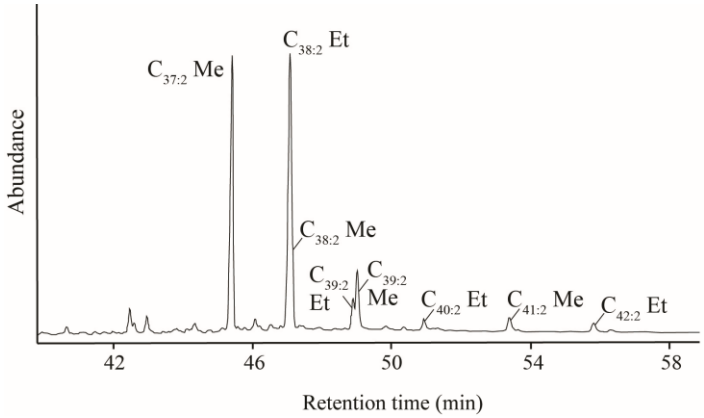

Fig. 1 Partial chromatogram of a ketone fraction of the extract from a sediment (ODP Leg 174AX) of ca. 41 Ma, illustrating the distribution of LCAs in the Bass River sediments. Separation was achieved using a CP Sil-5 column. Key: Et = ethyl ketone; Me = methyl ketone.

The identification of the C_{38} Me ketone at 41 and 50 Ma is remarkable since it is not frequently reported (Brassell, 2014). For the Paleocene and Eocene, this LCA has only been detected in high-latitude sediments of the Arctic (ca. 44 Ma) (Weller and Stein, 2008) and the Iceland-Faeroe Ridge and Falkland Plateau (between ca. 39 and 28 Ma) (Dzvonik, 1996). In the sediments of 60 and 74 Ma, LCAs were not detected despite good preservation conditions for organic matter as evidenced by the presence of GDGTs and LCDs in the same sediments (see below). This potentially suggest that LCA producers were not present in the depositional environment.

At 78 Ma (Campanian), we observe an unusual LCA distribution with a highly dominant $C_{40:2}$ Et ketone. This LCA has solely been reported in Cretaceous (Farrimond et al., 1986; Brassell et al., 2004) and Danian sediments (Yamamoto et al., 1996). This unusual distribution suggests a different source organism for the LCAs as compared to those in younger sediments, or alternatively, a separate biological source for the $C_{40:2}$ LCA. However, the stable carbon isotopic composition of the $C_{40:2}$ LCA (–32.0 ± 0.2 ‰) is identical to the $\delta^{13}C$ values of the $C_{37:2}$ and $C_{38:2}$ LCAs (–32.5 ± 0.4 ‰ and –32.2 ± 0.1 ‰, respectively) measured for the age interval of 41 Ma. Factors which can impact the $\delta^{13}C$ of LCAs include growth rate, cell geometry and pCO_2 (Pagani, 2014 and references therein). Since pCO_2 was similar around 41 and 78 Ma (Foster et al., 2017) and environmental conditions were not dramatically different at our site, our results suggest that the $C_{40:2}$ LCA at 78 Ma was produced by haptophytes with similar cell dimensions and biosynthetic pathways as those producing C_{37} and C_{38} LCAs, but from a different family than Noelaerhabdaceae. Nevertheless, the unusual Mesozoic LCA distributions suggests care should be taken in applying the $U^{K'}_{37}$ index in the early Cenozoic.

3.2 GDGTs and other ether lipids

In addition to the iGDGTs and brGDGTs used for the TEX_{86} and BIT indices, we have assessed distributional changes of all other ether lipids which were visible by scanning between *m*/*z* 900 and 1400, to evaluate potential relations between these lipids and the GDGTs used in the proxies. For instance, transformation of iGDGTs into diagenetic products might potentially affect the applicability of the TEX_{86}. The ether lipid distributions revealed the presence of predominantly iGDGTs (15–67 % of the total ether lipid assemblage) and brGDGTs (1–70 %; Fig. 3). The two youngest time intervals (11 and 18 Ma) are characterized by relatively high amounts of brGDGTs (40–70 %). To constrain the sources of these branched GDGTs we calculated the $\#rings_{tetra}$ index (Eq. (1)), the average number of cyclopentane moieties of the tetramethylated brGDGTs, which when > 0.7 indicates that sources other than soil and rivers must contribute to the branched GDGT pool (Sinninghe Damsté et al., 2016). The $\#rings_{tetra}$ index for these sediments range between 0.08 and 0.20, suggesting that the brGDGTs derive from a soil/riverine source, and not from in-situ production in the shelf sediments (Sinninghe Damsté, 2016; Fig. 3). Accordingly, the BIT index indicates a mostly terrestrial signal for the two youngest time intervals (BIT index > 0.8).

The sediments of >33 Ma are dominated by iGDGTs, reflecting a mostly marine signal (BIT index < 0.3; de Bar et al., accepted). However, since the BIT index is a ratio, it is unclear whether this is due to reduced terrestrial input or increased archaeal productivity (e.g., Fietz et al., 2011). In addition to the commonly detected iGDGTs, GDGT-0-4, crenarchaeol (Sinninghe Damsté et al., 2002), and its isomer (Cren′), trace amounts of GDGT-5 were tentatively identified in one of the sediments of the 18 Ma age interval (Fig. 3). Additionally, we detected a suite of other classes of ether lipids (see Supplementary Fig. S2 for lipid structures), some of which may derive from GDGTs by diagenesis.

Hydroxylated analogues of the iGDGTs (i.e., OH-GDGT-0, -1 and -2; Liu et al., 2012b, 2012c), were detected in the sediments of the time slices 18, 33 and 41 Ma, albeit in low relative abundances (0–1.1 % fractional abundance; Fig. 3). Liu et al. (2012b, 2012c) showed the presence of OH-GDGTs in marine sediments, also solely 0-2 cyclopentane moieties, whereas the iGDGT distributions comprise members with 0-3 cyclopentane moieties and crenarchaeol. Therefore, it was suggested that this potentially indicates different sources or different environmental conditions affecting the production of both groups of GDGTs.

The presence of, and number of rings in, OH-GDGTs in sediments has previously been linked to SST (Fietz et al., 2013) with relatively low amounts of OH-GDGTs at high SST, which is in agreement with our data. Lü et al. (2015) also observed a positive correlation between the weighted average number of cyclopentane moieties in OH-GDGT-1 and -2 (the RI-OH index; Eq. (2)) and SST. We obtain average RI-OH values of 1.4 and 1.7 for the time intervals of 33 and 41 Ma, respectively, corresponding to annual mean SSTs of ca. 17 and 29 °C, which compare reasonably well with the average TEX_{86}^{H}-derived SSTs of ca. 22 and 27 °C (de Bar et al., accepted).

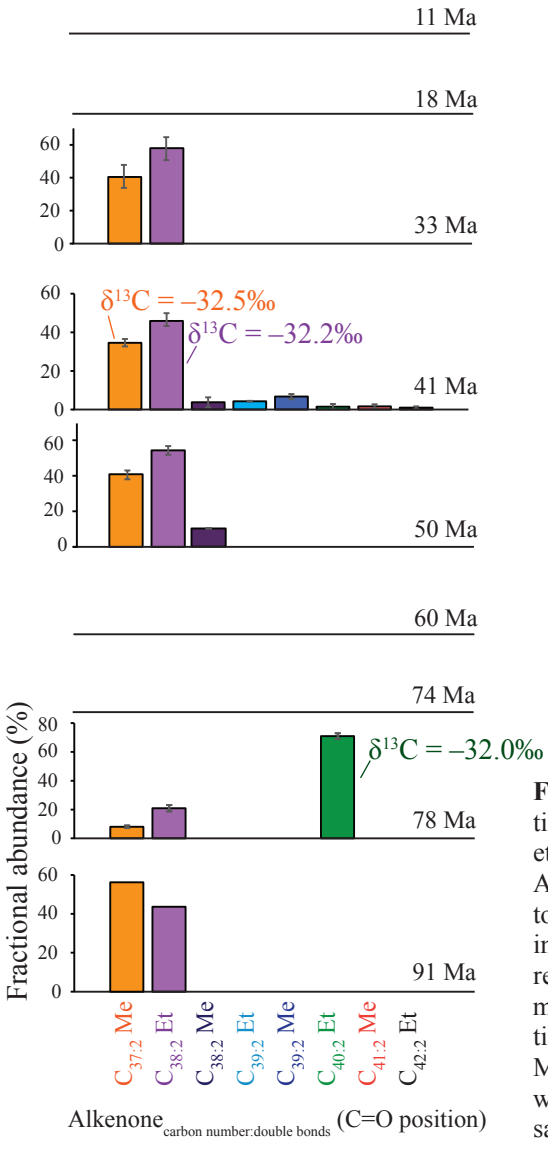

Fig. 2 LCA distributions through time for the Bass River record. Key: Et = ethyl ketone; Me = methyl ketone. Average fractional abundances (based on total summed LCAs for the specified time interval) are plotted, with error bars reflecting ± 1σ standard deviations of the multiple sediments (n = 3–8) from one time slice analyzed. For the time slice 91 Ma, no error bars are provided since LCAs were only detected in one sediment sample.

We observe positive correlations (although not significant; $R^2 = 0.84$ and 0.85) between the relative abundance of OH-GDGT-0 and -1 and iGDGT-0, suggesting related sources for these lipids at this site, while there is no correlation between the OH-GDGTs and the other iGDGTs.

Glycerol monoalkyl glycerol tetraethers (GMGTs; "H-shaped" GDGTs, Supplementary Fig. S2) are another group of glycerol ether lipids detected. The only iGMGT detected was iGMGT-0, present in low relative abundance (0.2–1.9 %). iGMGTs have been reported in thermophilic archaea (e.g., Morii et al., 1998; Sugai et al., 2004; Schouten et al., 2008a; Knappy et al., 2009, 2011, 2015), the methanogenic archaeon *Methanothermus* (Koga and Morii, 2005), environmental samples (Schouten et al., 2008b; Liu et al., 2012c; Lincoln et al., 2013; Jaeschke et al., 2014), and recently also in peat bogs (Naafs et al., 2018). Schouten et al. (2008b) suggested that benthic archaea possibly produce this compound. BrGMGTs, the GMGT homologues of brGDGTs Ia, IIa and IIIa, were sometimes present in much higher relative abundances (0–19 %). BrGMGT Ia was reported in several marine sediments (Liu et al., 2012c) and in the oxygen minimum zone of the Eastern Tropical North Pacific Ocean (Xie et al., 2014). Recently, Naafs et al. (2018) reported these three brGMGTs in peat bogs. The fractional abundances of the brGMGTs correlate (R^2 = 0.3–0.8) with those of the associated brGDGTs, indicating a terrestrial origin like the brGDGTs (Fig. 3), in agreement with the results of Naafs et al. (2018).

Glycerol dialkanol diether (GDD; Knappy and Keely, 2012; Liu et al., 2012a, 2012c) derivatives, i.e., GDGTs that have lost one glycerol unit (Supplementary Fig. S2), were also identified throughout the entire record (Fig. 3). The predominant GDDs are derivatives of the major GDGTs (iGDGT-0, crenarchaeol, brGDGT Ia), i.e., iGDD-0, iGDD-crenarchaeol (0–9 % fractional abundance) and brGDD Ia (0–4 %). Liu et al. (2012a, 2012c) observed that iGDDs and iGDGTs have similar ring distributions compared to each other, suggesting similar origins, either indicating a biosynthetic relationship or due to diagenetic transformation. GDDs are observed both in their core lipid form as well as in their IPL form in archaeal cultures (Meador et al., 2014; Elling et al., 2014; 2015; 2017), suggesting a biosynthetic origin. However, Yang et al. (2014) observed an exponential decrease in the GDGT/(GDGT+GDD) ratio with depth in a Chinese loess-paleosol sequence, which indicates that GDDs have a diagenetic origin. In agreement, we observe a significant positive relation between the fractional abundance of iGDD-0 and iGDGT-0, and iGDD-Cren and Crenarchaeol (R^2 = 0.64 and 0.41, respectively; p-values < 0.001), as well as between the branched GDD Ia and branched GDGT Ia (R^2 = 0.69; p-value < 0.001).
Interestingly, the isoprenoidal glycerol monoalkanediol diether-0 (iGMD-0; Bauersachs and Schwark, 2016; Liu et al., 2016) is present in all studied time intervals except for the youngest interval. If indeed iGDD-0 and iGDD-Cren (partially) result from the diagenetic transformation of GDGT-0 and crenarchaeol, respectively, this could potentially compromise the TEX_{86} proxy. Therefore, we cross-correlated the ratio of crenarchaeol over the sum of crenarchaeol and iGDGT-0 with the same ratio for their iGDD counterparts, shown in Fig. 4. The evidently strong positive correlation between these two ratios (R^2 = 0.98; slope ~1 and intercept ~0; p < 0.001; n = 23) suggests that, if indeed the iGDDs are degradation products, the diagenetic conversion of iGDGT-0 and crenarchaeol into iGDD-0 and iGDD-Cren is proportional. Assuming similar degradation dynamics hold for the iGDGTs used in the

TEX_{86}, this suggests that degradation does not affect the distribution of iGDGTs and, hence, of TEX_{86} values.

Some less common tetraethers, where one of the glycerol moieties is replaced by another group, were also detected; butanetriol dibiphytanyl glycerol tetraether-0, -1 and -2 (iBDGT-0, -1, -2; between 0 and 5.8 % fractional abundance) and the pentanetriol dibiphytanyl glycerol tetraether-0 (iPDGT-0; between 0 and 2.6 %). These lipids were recently identified in marine and estuarine sediments (Zhu et al., 2014) as well as in the methanogenic archaeon *Methanomassiliicoccus luminyensis* (Becker et al., 2016). The iBDGTs were detected in relatively low abundance (0–6 %) throughout the entire Bass River record with exception of the youngest sediment interval (11 Ma; Fig. 3). iPDGT-0 was present in relatively small amounts (0–3 %), except for the youngest and oldest time interval (11 and 91 Ma; Fig. 3). It showed a relatively high abundance (1.6 %) in the time interval of 50 Ma (Fig. 3), together with a novel tentatively identified ether lipid (Supplementary Fig. S3), the isoprenoidal pentanetriol monoalkyl glycerol tetraether-0 (iPMGT-0; 3.9 %).
Similarly, we tentatively identified (Supplementary Fig. S4) the isoprenoidal butanetriol monoalkyl glycerol tetraether-0 and -1 (iBMGT-0 and -1; between 0 and 2.2 %; Fig. 3), which were detected in the same sediments as where iBDGTs occur. These tentative identifications were based on retention times, the exact protonated molecular mass obtained by HRMS and its MS^2 fragmentation pattern (Supplementary Fig. S3 and S4). The fractional abundances of iBMGT-1 and iGMGT-0 reveal a very strong positive relation with each other ($R^2 = 0.83$; $p < 0.001$). iBMGT-0 strongly correlates with iPDGT-0, iPMGT-0 and iGMD-0 ($R^2 = 0.76$, 0.83 and 0.76, respectively; p-values < 0.001), suggesting similar sources. Interestingly, the fractional abundance of the iBDGTs does not correlate with the abundance of these lipids.

Overall, despite the wide structural variety in glycerol ether lipids detected throughout Bass River over the last ca. 90 Myrs, the distributions of the main iGDGTs stayed relatively similar from 33 to 91 Ma and they remained the most abundant glycerol ether lipids (Fig. 3). This suggests a similar biological source throughout this time interval and no major diagenetic transformations. iGDDs were encountered in the record but they remain minor relative to the iGDGTs and their formation seems not to affect the iGDGT distribution. Potential secondary effects on the TEX_{86}^{H} were assessed by de Bar et al. (accepted) by means of calculation of the Methane Index, the %GDGT-0 and Ring Index, which were all below recommended threshold values. Additionally, we calculated here the $\%GDGT_{RS}$ (Eq. (3)) to identify Red Sea-type GDGT distributions, since it is known to differ from other modern ocean settings (Inglis et al., 2015). For the time intervals where TEX_{86} SST < 30 °C, the $\%GDGT_{RS}$ is always below the threshold, i.e. < 30. Additionally, we applied the $f_{Cren':Cren'+Cren}$ as proposed by O'Brien et al. (2017) (Eq. (4)), to identify anomalous GDGT distributions in Cretaceous sediments, associated with $f_{Cren':Cren'+Cren}$ values of > 0.25. However, all values for the Bass River are below 0.16.

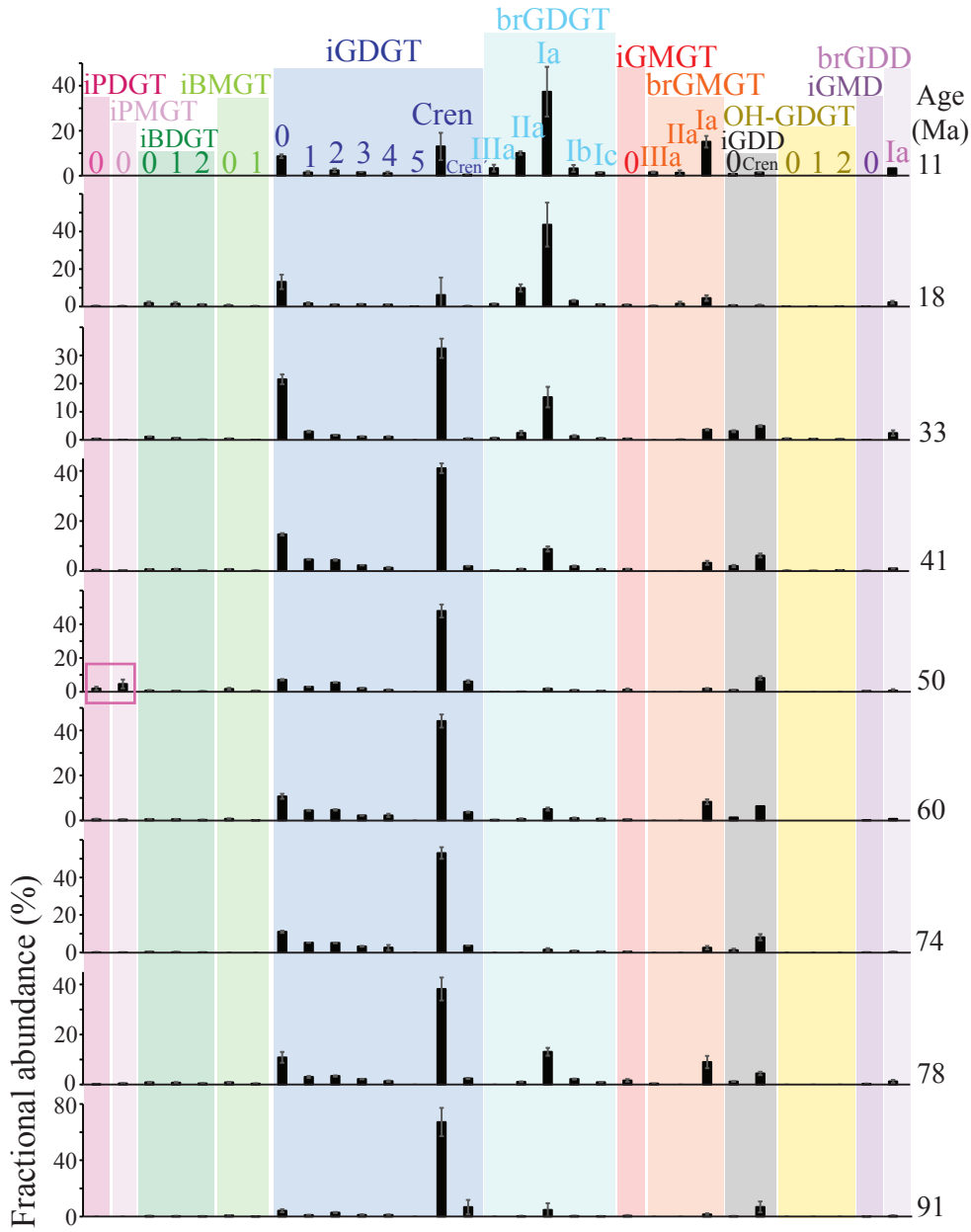

Fig. 3 Glycerol ether lipid distributions through time for the Bass River record. The bars reflect the fractional abundances of the glycerol ether lipids (based on total summed glycerol ether lipids for the specified time interval); the error bars reflect ± 1σ standard deviation of three sediment samples analyzed per time interval. The pink box in the 50 Ma age interval highlights the occurrence of iPDGT-0 and iPMGT-0.

The observed distributional changes of the iGDGTs appear to relate to temperature changes as TEX_{86}-derived SSTs correlate well with SST estimates based on other temperature proxies determined on the same sediments (de Bar et al., accepted), as well as with the global benthic oxygen isotopic compilation (Zachos et al., 2008; Friedrich et al. 2012). This indicates that the fundamental principles underlying the TEX_{86} proxy relationship with temperature potentially remained the same over the last ca. 90 Myrs. iGDGTs have been found in sediments up to 140 Ma (Kuypers et al., 2001; Carillo-Hernandez et al., 2003; Jenkyns et al., 2012), and recently even in Early Jurassic sediments (ca. 191 Ma; Robinson et al., 2017), and based on genetic analysis it was estimated that Thaumarchaeota already originated more than 1 Gyr ago (Blank, 2009; Spang et al., 2010). Moreover, the same temperature adaptation, i.e., an increase in the number of cyclopentane rings with increasing temperature, as observed with the TEX_{86} has also been evidenced for distantly related hyperthermophilic archaea (see Schouten et al., 2013b and references therein), signifying that this adaptation mechanism is shared by more archaeal phyla and thus likely also the ancestors of modern day Thaumarchaeota.

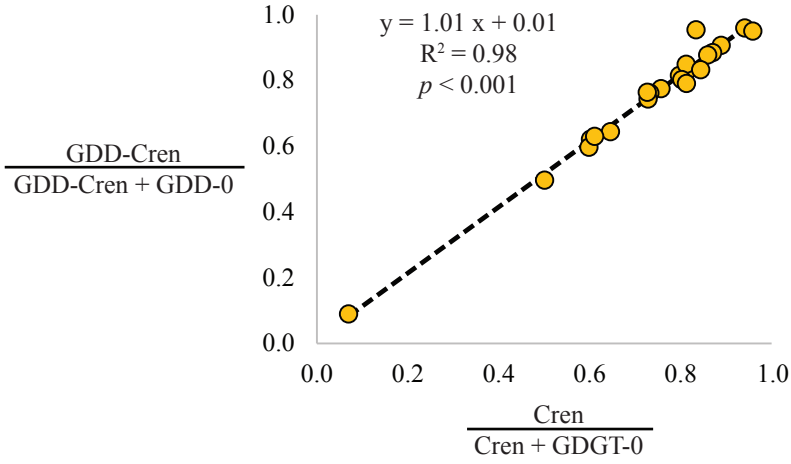

Fig. 4 Cross-correlation of the ratio of crenarchaeol over the sum of crenarchaeol and GDGT-0 versus the same ratio for the GDD-counterparts for the examined sediments from the Bass River record.

3.3 Long-chain diol and keto-ol distributions

All sediment intervals contained LCDs (e.g., Fig. 5 for a sediment of 50 Myrs old), albeit generally in low amounts. Particularly, for the age intervals of 11, 60, 74 and 91 Ma, the LCDs identified were often near the detection limit. The two youngest time intervals investigated (i.e., ca. 11 and 18 Ma) reveal C_{30} and C_{32} 1,15-diols as dominant LCDs (Fig. 6; Supplementary Table S1). Sediments with the ages of 33, 41 and 50 Ma reveal different LCD

distributions with the dominant isomers being the C_{26} 1,13-, C_{28} 1,12-, C_{30} 1,15-, C_{32} 1,15- and C_{34} 1,17-diol. Plancq et al. (2014) reported similar LCD distributions for Eocene-Oligocene (ca. 31–37 Ma) sediments of DSDP Site 511 in the South Atlantic as observed here for the 33 and 41 Ma age intervals (i.e., the C_{26} 1,12- 1,13- and 1,14-diol, C_{28} 1,12-, 1,13-, 1,14-diol and C_{30} 1,13- and 1,14-diol). In the sediments of 60 Ma, the C_{28} 1,12-diol, C_{30} 1,15-diol and the C_{30} 1,12-diol were detected of which the C_{28} 1,12-diol occurs in the highest abundance. For the interval of 74 Ma the C_{26} 1,13-, C_{28} 1,12-, 1,13- and 1,14-diols and the C_{30} 1,15-diol were detected, of which the C_{26} 1,13-diol is most abundant. In the sediments of 78 and 91 Ma, we solely detected the C_{26} 1,13-diol. Through time, there is a clear gradual shift in chain length dominance towards shorter chain lengths from C_{32} to C_{26} (Fig. 6).

We also quantified long-chain keto-ols, suspected diagenetic products of LCDs (e.g., Ferreira et al., 2001). The concentrations in the youngest time interval (11 Ma) were too low for unambiguous identification of keto-ols. For the interval of 18 Ma, we detected the C_{30} and C_{32} 1,15-keto-ols in addition to the C_{34} 1,15-keto-ol, and trace abundances the C_{36} 1,19-keto-ol (Fig. 6). The polar fractions of the sediments of 33 Ma generally contained higher backgrounds, complicating identifications of keto-ols, and consequently we solely unambiguously identified the C_{32} 1,15-keto-ol. Further back in time, the presence of the C_{28} 1,12- and C_{26} 1,13-keto-ols was established (Fig. 6).
Overall, the long-chain keto-ols show a gradual shift in chain length through time, similar as observed for the LCDs (from C_{32} to C_{26}) (Fig. 6), which would agree with the idea that long-chain keto-ols result from oxidation of the mid-chain alcohol group of the LCDs (Ferreira et al., 2001). Another possibility is that the keto-ols are biosynthesized by the same algae producing LCDs, but evidence for this is lacking. We did not recognize keto-ols for all corresponding LCDs, but keto-ols were generally present in trace amounts, and the characteristic fragment ions related to the position of the keto-group, on which the identification of the keto-ols are based, have relatively low abundances (de Leeuw et al., 1981) which prohibited unambiguous identifications of all keto-ols.

Particularly interesting are the C_{28} 1,12- and C_{26} 1,13- and 1,14- LCDs, which become more dominant in the older sediment intervals. The C_{28} 1,12-diol has been previously observed in lake sediments (Shimokawara et al., 2010; Rampen et al., 2014b), in trace amounts in cultures of the eustigmatophyte freshwater algae *Vischeria* spp. (Volkman et al., 1999a; Rampen et al., 2014b), and the marine *Proboscia* diatoms (Rampen et al., 2007). Additionally, low abundances were observed in marine sediments from the Bransfield Basin (Holocene; Antarctic Peninsula; Willmott et al., 2010), the Arabian Sea (recent; Rampen et al., 2007), the Oman margin (Pliocene; ten Haven and Rullkötter, 1991), and the Chilean margin (Late Quaternary; de Bar et al., 2018). Interestingly, all these sediments were deposited under upwelling conditions, and contained high relative abundances of 1,14-diols (produced by *Proboscia* diatoms; Sinninghe Damsté et al., 2003; Rampen et al., 2014a).

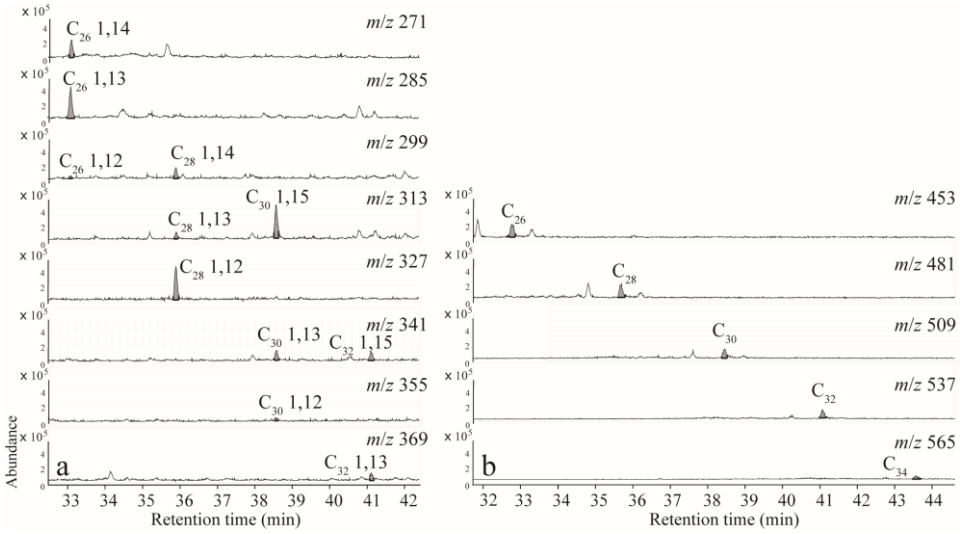

Fig. 5 Partial extracted ion chromatograms revealing the presence of LCDs **(a)** and long-chain keto-ols **(b)** present in a Bass River sediment of 50 Ma (ODP Leg 174AX). For quantification of the LCDs, the fragment ions formed by cleavage adjacent to the OTMSi groups (silylated hydroxyl groups) were integrated, whereas for keto-ols the M^+–15 ions (M^+–CH_3) were used.

Since the C_{28} 1,12-diol has also been detected in *Proboscia* cultures, albeit in relatively low abundances, the *Proboscia* diatoms are likely to be the present-day producer of the C_{28} 1,12-diol in the marine realm. The relative high abundance of the C_{28} 1,12-diol in the sediments from ca. 33 to 74 Ma, may therefore indicate the dominance of a diatom population closely related to *Proboscia*. In addition to the C_{28} 1,12-diol, the C_{26} 1,14 and 1,13-diols are relatively dominant between 91 and 33 Ma. In the two oldest sediment intervals (91 and 78 Ma) solely the C_{26} 1,13-diol was detected. Similar to the C_{28} 1,12-diol, these LCDs are generally not observed in high abundance in recent marine sediments. Moreover, to the best of our knowledge, they have only been reported for sediments of Lake Baikal (Japan; Shimokawara et al., 2010), Holocene sapropels in the Mediterranean (ten Haven et al., 1987) and, in trace amounts, in *Proboscia* cultures (Rampen et al., 2007). Accordingly, this latter observation might indicate that these LCDs were (similar as for the C_{28} 1,12-diol) produced by a group of diatoms, closely related to *Proboscia*. However, the observed co-occurrence of the C_{28} 1,12-/C_{26} 1,13-diols with their corresponding -keto-ols would imply that *Proboscia*, or related diatoms, are not the source of these lipids, since 1,14-keto-ols are generally not detected in modern sediments in contrast to 1,13- and 1,15-keto-ols (e.g., Versteegh et al., 1997; Sinninghe Damsté et al., 2003). Similarly, for this site, we did not detect 1,14-keto-ols. Sinninghe Damsté et al. (2003) hypothesized that because *Proboscia* diatoms sink relatively fast to the seafloor, and the lipids are protected by a silica frustule, the 1,14-diols are much

less exposed to oxygen in the water column, preventing the oxidation of 1,14-diols. In contrast, 1,13- and 1,15-diols are likely longer exposed to oxygen and therefore degraded to 1,13- and 1,15-keto-ols. In agreement with this idea, we have not detected the C_{29} 12-hydroxy methyl alkanoate in the Bass River sediments, a typical biomarker for *Proboscia* and potentially formed from common precursors (C_{28} 12-hydroxy fatty acid) as the 1,14-diols (Sinninghe Damsté et al., 2003).

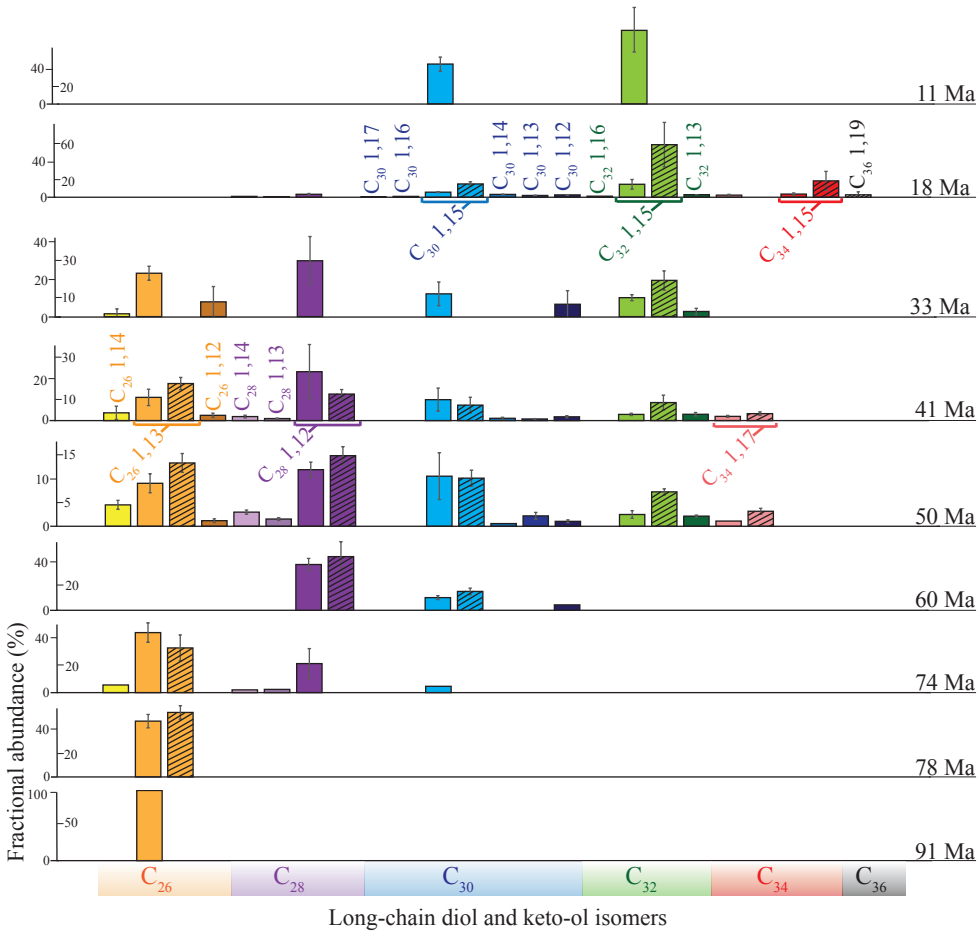

Fig. 6 LCD and keto-ol distributions through time for the Bass River record. Keto-ols are plotted right next to the associated LCD isomers, highlighted by a dashed pattern. Bars represent average fractional abundances (based on summed LCD and long-chain keto-ol abundance) for the specified time intervals. Error bars reflect ± 1σ standard deviations of the different sediments of a particular age interval. When there is no error bar, the LCD or keto-ol was identified in solely one sediment sample for that time interval.

Interestingly, Yamamoto et al. (1996) observed similar LCD distributions for Danian sediments (Geulhemmerberg; the Netherlands; ca. 65 Ma): the C_{26} 1,13-, C_{28} 1,12- and 1,13-, C_{30} 1,13- and 1,15- and C_{32} 1,15-diols, suggesting that the rarely reported C_{26} 1,13- and C_{28} 1,12-diols may have been more common in the early Cenozoic. However, they observed different keto-ol distributions, i.e., the C_{32} 1,15-, C_{34} 1,13- and 1,15- and C_{36} 1,15-keto-ols. This discrepancy in LCD and keto-ol distribution might be the result of different settling speeds of material with which the LCDs are associated, due to different producers, and thus different oxygen exposure times. The authors did detect the C_{28} 12-hydroxy fatty acid at their site, which is an indication, that in contrast to the Bass River, the C_{28} 1,12- and C_{26} 1,13-diols were potentially produced by diatoms closely related to *Proboscia*.

Integrating these long-term LCD distribution changes with fossil distributions or molecular phylogenic data, which can give insight in the evolution of organisms, could potentially shed light on the source organisms of LCDs. However, little is known on the evolutionary history of the present-day LCD producers, i.e., the eustigmatophytes (1,13- and 1,15-diols), *Proboscia* diatoms (1,14-diols) and the dictyochophyte *Apedinella radians* (1,14-diols). Molecular clock analysis estimated the divergence of different genera within the Eustigmatophyceae and Dictyochophyceae families to have most likely occurred around 120 and 280 Ma, respectively (Brown and Sorhannus, 2010), i.e., predating our oldest sedimentary LCD occurrence (± 91 Ma).
Proboscia taxa originate from a centric diatom lineage which likely evolved between approximately 149 and 125 Ma (Sorhannes, 2007). Indeed, a number of fossil *Proboscia* species has been reported for the Cenozoic and the Late Cretaceous despite their weak preservation potential (Jordan and Priddle, 1991; Koç et al., 2001; Jordan and Ito, 2002). The oldest reported occurrences of preserved *Proboscia* is for Late Cretaceous sediments, for which in total six species were described (Hajós, 1975; Harwood and Nikolaev, 1995; Jordan and Ito, 2002), suggesting that diversification within the *Proboscia* genus already occurred prior to the Late Cretaceous. Jordan and Ito (2002) argued, based on morphological grounds and the absence of *Proboscia* fossils in Early Cretaceous sediments (Gersonde and Harwood, 1990), that a possible ancestor would be the *Kreagra* diatom genus, observed in Early Cretaceous sediments. Thus, the present-day producers of the most dominant LCDs all evolved prior to our oldest LCD occurrence. The observed trends may therefore be predominantly explained by shifting populations of *Proboscia*, causing a shift to shorter chain lengths with increasing sediment deposition age.

Values for the LDI (Eq. (5)), the paleothermometer based on LCDs, could be calculated for the youngest five time intervals (i.e., 11, 18, 33, 41 and 50 Ma; Fig. 7a). For sediments older than 50 Ma, solely the C_{28} 1,13-diol was tentatively identified in trace amounts in a sediment from 74 Ma, but the C_{30} 1,13-diol could not be unambigously identified anymore, implying that for this site, the applicability of the LDI is restricted to the last ± 50 Myrs. However, Yamamoto et al. (1996) reported low amounts of the C_{30} 1,13-diol for Danian sediments (± 66 Ma) suggesting that the LDI might be applicable in older sediments at other sites. The

LDI-derived SSTs vary between ca. 15 and 22 °C (Fig. 7a). The SST trend does not agree with that of the other temperature records for this site (i.e., $\delta^{18}O$ bottom water temperature (BWT), the TEX_{86}^{H} SST and MAT_{mrs} mean air temperatures (MAT) as reported by de Bar et al. accepted; Fig. 7a). LDI-derived SSTs are ca. 2 and 14 °C lower as compared to the TEX_{86}^{H}-derived SSTs and they show only a subtle increase in SST from 50 to 41 Ma (ca. 1.5 °C), whereas other proxy records, as well as the global benthic $\delta^{18}O$ compilation, show a strong cooling after the Early Eocene Climatic Optimum (EECO).
Rodrigo-Gámiz et al. (2015) previously reported LDI values for surface sediments around Iceland, in which the 1,13- and 1,15-diols were relatively low compared to the 1,14-diols. They obtained LDI-SSTs which were significantly lower compared to satellite SSTs, and they proposed that the *Proboscia* diatoms might be at least a partial source of the 1,13-diols in that region, affecting the LDI. Likely, the LDI signal we obtained for the Bass River site is similarly affected by 1,13- and 1,15-diols produced by unknown organisms producing the more abundant C_{28} 1,12- and C_{26} 1,13-diols.

We also determined the fractional abundance of the C_{32} 1,15-diol (Eq. (7)), which is a potential indicator of riverine organic matter input (de Bar et al., 2016; Lattaud et al., 2017a; 2017b). We observe a good correlation between the BIT index, a proxy for soil and riverine input (e.g., Weijers et al., 2007; Zell et al., 2014; de Jonge et al., 2015), and the fractional abundance of the C_{32} 1,15-diol ($R^2 = 0.72$, *p*-value < 0.001; n = 38; Fig. 7b), suggesting a contribution of terrestrial derived organic carbon, potentially providing an alternative explanation for the erroneous LDI SSTs (cf. de Bar et al., 2016). So far, the C_{32} 1,15-diol as tracer for contribution of riverine organic carbon has only been tested for Late Quaternary records (Lattaud et al., 2017b; Jonas et al., 2017; Warnock et al., 2017). The agreement between the fractional abundance of the C_{32} 1,15-diol and the BIT index determined for the Bass River site over the last ca. 50 Myrs suggests that this proxy might also be applicable over longer timescales.

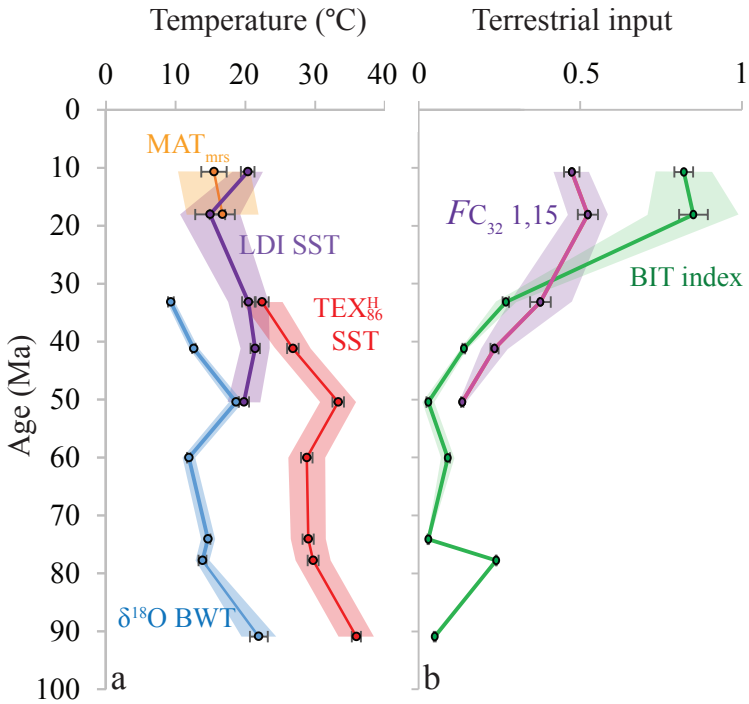

Fig. 7 Proxy records for the Bass River site based on LCDs. (a) The LDI SST record plotted together with TEX_{86}^{H}-derived SSTs, MAT_{mrs} air temperatures and $\delta^{18}O$-derived BWTs adapted from de Bar et al. (accepted). The transparent envelopes represent propagations of short term variability within the age interval and calibration errors of the proxies. The error bars reflect the standard errors ($\sigma/\sqrt{n}$, where σ = standard deviation, reflecting the short-term variability and n = number of sediment samples); when not visible, the error bars are smaller than the symbol size. (b) The BIT index (from de Bar et al., accepted) and the fractional abundance of the C_{32} 1,15-diol. Transparent envelopes here reflect standard deviation from the mean for the respective age intervals; the error bars reflect the standard errors.

4. Conclusions

In this study we have assessed changes in lipid biomarker distributions (LCAs, GDGTs, LCDs, keto-ols) in the Bass River core (New Jersey shelf, North Atlantic) from the late Cretaceous to the Pliocene to gain insight into the long-term evolution of sources of these lipid biomarkers and associated temperature proxies and potential effects of diagenesis. Tri-unsaturated LCAs were absent, and consequently the $U_{37}^{K'}$ results in reconstructed SSTs > 27 °C for the Mid-Eocene and later. At 78 Ma, we observed a highly dominant $C_{40:2}$ Et ketone, potentially suggesting different ancestors and thereby limiting the applicability of the $U_{37}^{K'}$ to the Cenozoic. However, the stable carbon isotopic composition is highly similar to that of the $C_{37:2}$ and $C_{38:2}$ LCAs of the age interval of 41 Ma, potentially suggesting similar sources.

We have encountered a wide variety of glycerol ether lipids, and tentatively identified three new GMGT homologues of previously reported isoprenoid PDGTs and BDGTs, i.e., iPMGT-0 and iBMGT-0 and -1. The iGDGT distributions observed throughout the core are highly comparable to distributions typically observed in marine Thaumarchaeota and in present-day sediments, suggesting that the fundamental principles underlying the relation of the TEX_{86}^{H} proxy to temperature remained consistent back to ± 91 Ma. We also detected GDDs, which have a diagenetic or biosynthetic origin. If they are formed by diagenetic coversion of GDGTs, this conversion appears to be constant through time, implying there is no effect of degradation on the TEX_{86} proxy. The LDI could solely be calculated for sediments up to ca. 50 Ma, due to the absence of 1,13-diols in the older sediment intervals and calculated temperatures and trend did not agree with other records. Changing LCD distributions were observed with time, revealing the dominant C_{28} 1,12-diol and C_{26} 1,13-diol between 33 and 91 Ma which may have impacted the LDI. Good agreement between the fractional abundance of the C_{32} 1,15-diol and the BIT index over the last 50 Myrs suggesting that this proxy for riverine input is potentially applicable up to the Eocene. Long-chain keto-ols had the same isomer distributions as the LCDs suggesting a diagenetic link.

Acknowledgements

The Ocean Drilling Project (ODP) is acknowledged for providing sediment samples. We thank Gabriella Weiss and Marcel van der Meer for help with alkenone analyses and Jan de Leeuw for stimulating discussions. Dr. Ann Pearson and two anonymous reviewers are thanked for their constructive comments which improved the manuscript. This research has been funded by the European Research Council (ERC) under the European 555 Union's Seventh Framework Program (FP7/2007-2013) ERC grant agreement [339206] to S.S. S.S. and J.S.S.D. receive funding from the Netherlands Earth System Science Center (NESSC) through a Gravitation grant from the Dutch ministry for Education, Culture and Science (grant number 024.002.001).

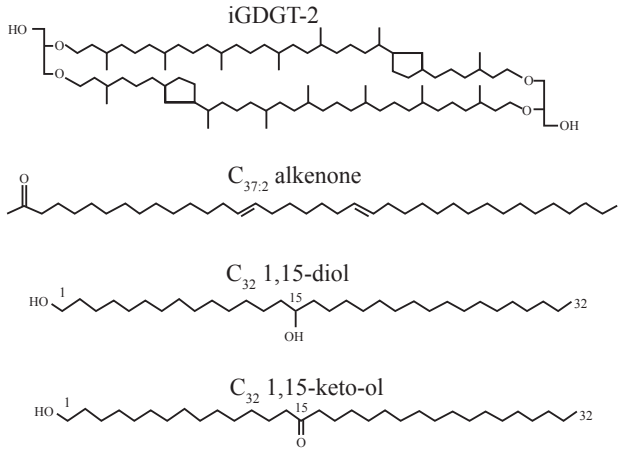

Fig. S1 Structure of an isoprenoid GDGT, long-chain alkenone, LCD and keto-ol.

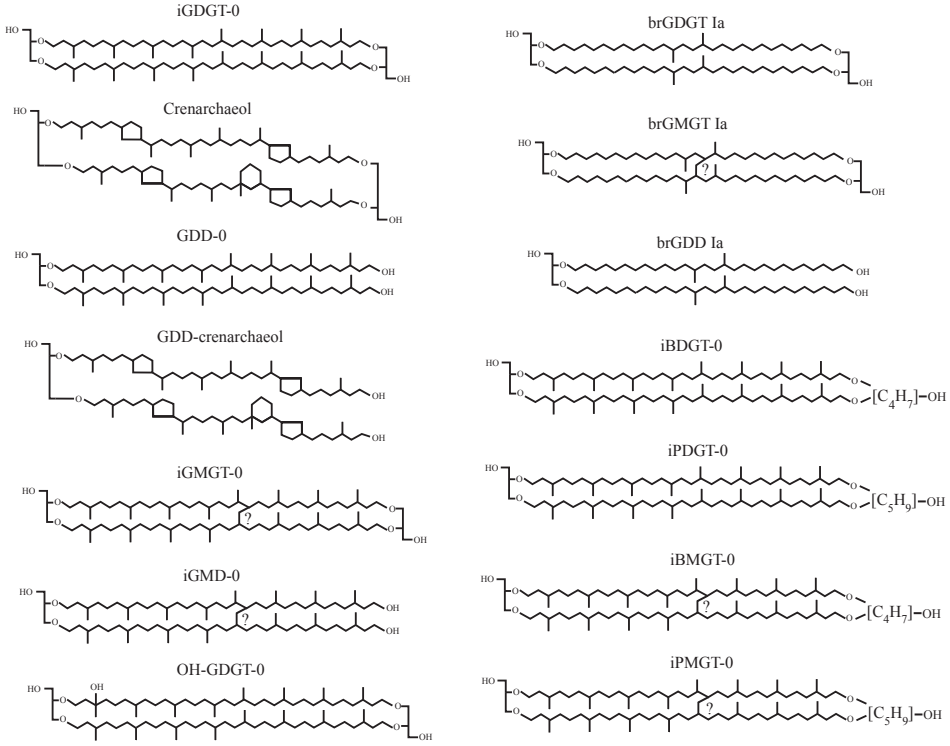

Fig. S2 Structures of glycerol ether lipids detected in the Bass River sediments. The position of the covalent bond in the GMGTs is tentative (Morii et al. 1998), indicated by the question mark.

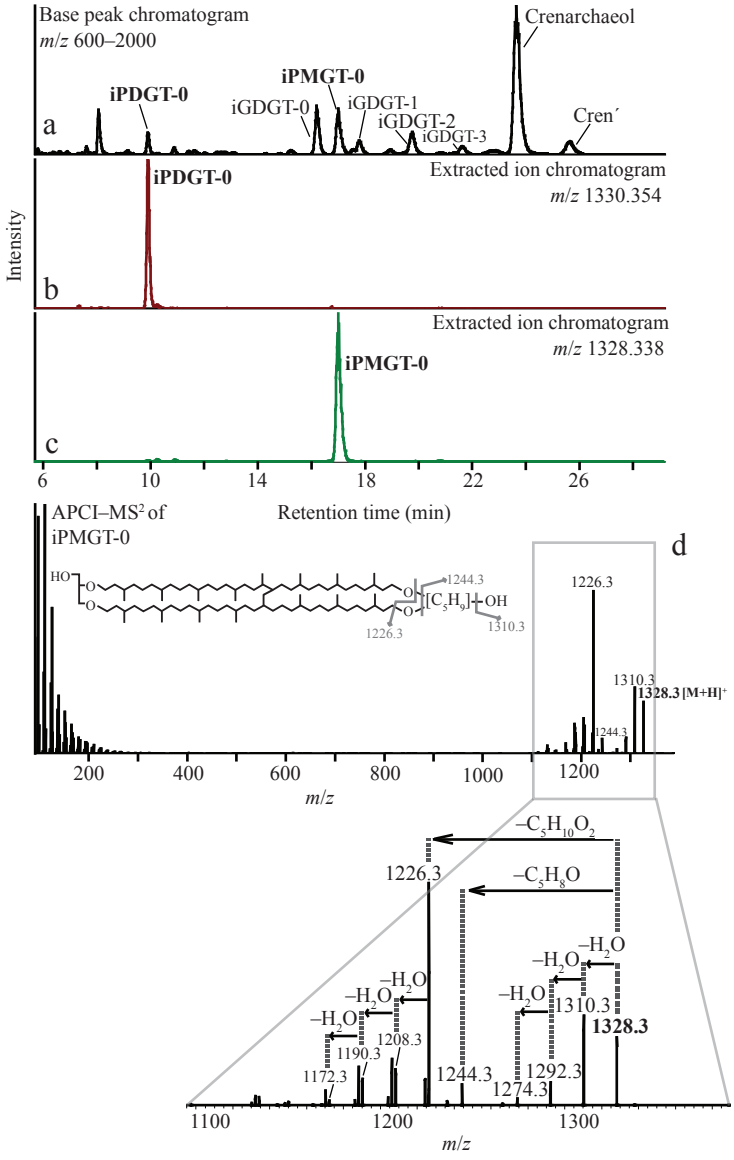

Fig. S3 Partial base peak **(a)** and **(b** and **c)** extracted ion chromatograms (within 5 ppm mass accuracy) revealing the presence of iPDGT-0 and the tentatively identified iPGMT-0 for a sediment (ODP Leg 174AX) of the 50 Ma time slice. Panel **(d)** shows the HPLC–APCI/MS^2 fragmentation spectrum of iPMGT-0, revealing the absence of fragments associated with the hydrocarbon chains, since it is assumed that the covalent C-C bond remains intact during dissociation (cf. Knappy et al., 2009). The *m/z* 1226.3 ion reflects the loss of the pentatriol unit ($C_5H_{10}O_2$; 102.1 Da) as described by Zhu et al. (2014).

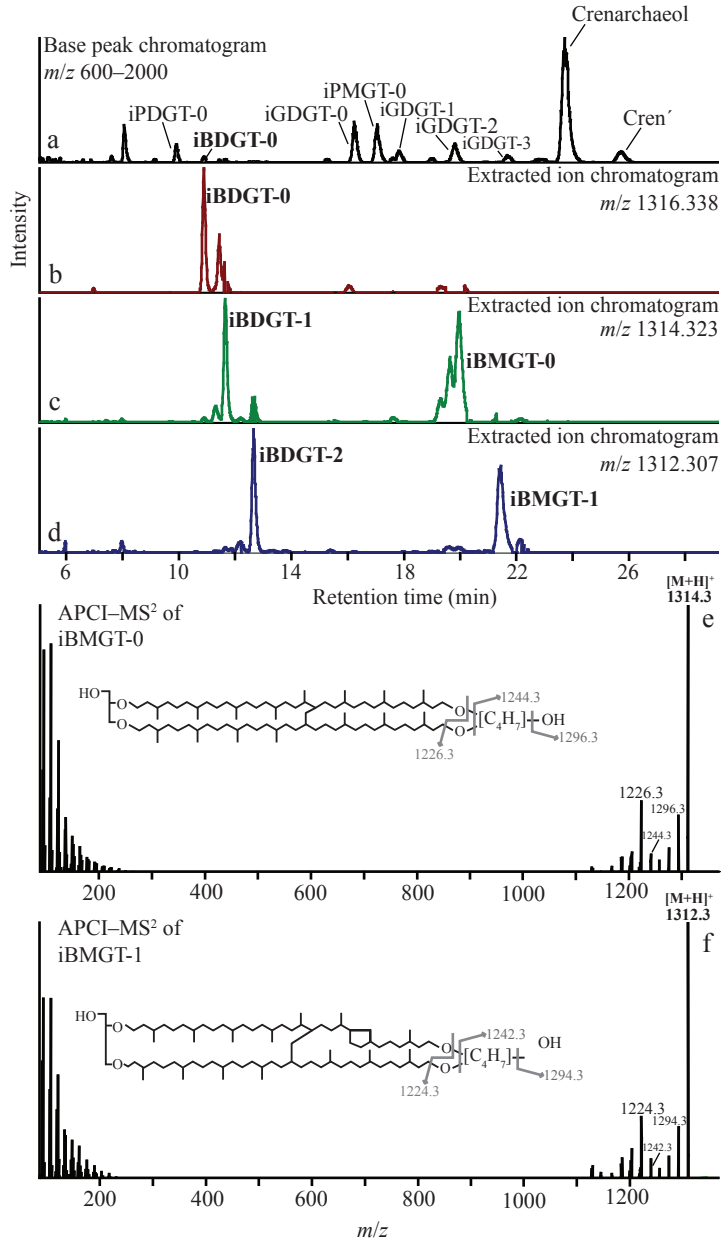

Fig. S4 Partial base peak **(a)** and extracted ion chromatograms **(b, c** and **d**; within 5 ppm mass accuracy) for iBDGT-0, -1 and -2 and iBGMT-0 and -1 for a sediment of the 50 Ma time slice, showing the elution order of the iBDGTs, iBMGTs and iGDGTs. Panel **(e)** and **(f)** show the HPLC–APCI/MS^2 fragmentation spectra of iBMGT-0 and -1, respectively. The *m/z* 1226.3 and 1224.3 fragment ions associated with iBMGT-0 and -1, respectively, reflect the loss of the butanetriol units ($C_4H_8O_2$; 88.1 Da) as described by Zhu et al. (2014).

Table S1 Fractional abundances of the LCDs and keto-ols for the 9 age intervals. Note that these fractional abundances are corrected for the relative contribution of the ion fragments which were integrated, i.e. the characteristic ion fragments formed by cleavage adjacent to the OTMSi groups for the LCDs (correction factor 9 %) and the M^+–15 ions for the keto-ols (correction factor 3 %).

		Fractional abundances long-chain diols																	*Fractional abundances long-chain keto-ols*						
Age	**Depth**	**C_{26}**			**C_{28}**			**C_{30}**							**C_{32}**			**C_{34}**		**C_{26}**	**C_{28}**	**C_{30}**	**C_{32}**	**C_{34}**		**C_{36}**
(Ma)	**(m)**	**1,14**	**1,13**	**1,12**	**1,14**	**1,13**	**1,12**	**1,17**	**1,16**	**1,15**	**1,14**	**1,13**	**1,12**	**1,16**	**1,15**	**1,13**	**1,17**	**1,15**	**1,13**	**1,12**	**1,15**	**1,15**	**1,15**	**1,17**	**1,19**
10.7	22.75														1.00										
	21.11									0.45					0.55										
	21.44									0.35					0.65										
	22.14														1.00										
	23.06									0.43					0.57										
17.7	114.92						0.04			0.05	0.03	0.02	0.02		0.10	0.02	0.00	0.04			0.14	0.43	0.10		
	114.38														0.19							0.81			
	115.47				0.01	0.01	0.02	0.00	0.01	0.04	0.03	0.02	0.02	0.01	0.09	0.02	0.01	0.02			0.10	0.43	0.12		0.03
	116.02						0.03			0.05					0.11		0.03				0.13	0.34	0.26		0.06
33.4	177.44		0.30	0.19			0.51																		
	174.51	0.03	0.23	0.03			0.21			0.21					0.10	0.04						0.15			
	176.34		0.22	0.04			0.32			0.12					0.12							0.20			
	178.78	0.03	0.20	0.12			0.19			0.07			0.01		0.11							0.26			
	179.45		0.21	0.05			0.27			0.09			0.12		0.08	0.02						0.17			
41.2	265.01		0.16	0.04			0.45			0.20												0.15			
	264.47	0.08	0.12	0.02	0.03	0.01	0.14			0.08	0.01	0.01	0.01		0.03	0.02			0.20	0.10	0.08	0.08			
	264.67	0.03	0.11	0.03	0.02	0.01	0.16			0.08	0.01	0.01	0.02		0.04	0.03	0.02		0.20	0.13	0.02	0.07		0.03	
	264.73	0.02	0.11	0.02	0.02	0.01	0.23			0.08		0.01	0.02		0.03	0.04			0.17	0.13	0.08	0.06			
	264.95	0.02	0.05	0.02	0.01	0.01	0.19			0.06	0.02	0.01	0.02		0.03	0.04	0.02		0.14	0.15	0.11	0.08		0.04	
50.2	303.41	0.04	0.06	0.01	0.03	0.01	0.09			0.12	0.01	0.02	0.01		0.02	0.02	0.01		0.13	0.19	0.14	0.08		0.04	
	303.6	0.04	0.09	0.01	0.03	0.02	0.14			0.16		0.03			0.03	0.02			0.11	0.13	0.09	0.07		0.03	
	303.75	0.04	0.09	0.01	0.03	0.01	0.12			0.13		0.02	0.01		0.02	0.02			0.15	0.15	0.10	0.07		0.03	
	303.93	0.04	0.09	0.02	0.02	0.02	0.12			0.10		0.02	0.01		0.02	0.02			0.16	0.16	0.10	0.07		0.03	
	304.11	0.04	0.10	0.01	0.03	0.02	0.13			0.13		0.02	0.01		0.03	0.02			0.12	0.14	0.10	0.08		0.03	
	304.88	0.06	0.11	0.01	0.03	0.02	0.11			0.11		0.03	0.01		0.03	0.02			0.14	0.13	0.08	0.07		0.04	

		Fractional abundances long-chain diols																	*Fractional abundances long-chain keto-ols*						
Age	**Depth**	**C_{26}**			**C_{28}**			**C_{30}**						**C_{32}**			**C_{34}**		**C_{26}**	**C_{28}**	**C_{30}**	**C_{32}**	**C_{34}**		**C_{36}**
(Ma)	**(m)**	**1,14**	**1,13**	**1,12**	**1,14**	**1,13**	**1,12**	**1,17**	**1,16**	**1,15**	**1,14**	**1,13**	**1,12**	**1,16**	**1,15**	**1,13**	**1,17**	**1,15**	**1,13**	**1,12**	**1,15**	**1,15**	**1,15**	**1,17**	**1,19**
60.1	379.98						0.40													0.60					
	379.89						0.44													0.56					
	379.25						0.38			0.09			0.05							0.35	0.13				
	379.34						0.38			0.11										0.32	0.18				
	380.04						0.30			0.12										0.41	0.16				
74.1	396.47		0.47				0.28												0.25						
	396.19		0.45				0.31												0.23						
	396.83		0.48				0.10												0.42						
	396.93	0.05	0.35		0.02	0.02	0.21			0.05									0.30						
77.8	481.6		0.52																0.48						
	482		0.40																0.60						
	481.51		0.47																0.53						
	481.42		0.51																0.49						
	481.9		0.42																0.58						
90.9	568.13		1.00																						
	569.78		1.00																						
	571.39		1.00																						
	568.95		1.00																						
	571.21		1.00																						
	571.82		1.00																						
	570.78		1.00																						

Table S2 Sample list where indicated which samples were analyzed for long-chain alkenones, GDGTs and long-chain diols and keto-ols.

			Long-chain alkenones		Glycerol ether lipids		Long-chain diols and keto-ols		
Depth	**Depth**	**Age**	**GC-FID**	**GC-MS**	**UHPLC-MS**	**UHPLC-HRMS**	**GC-MS**	**GC-MS**	**GC-MS/MS**
(ft)	(m)	(Ma)		full scan	full scan		full scan	SIM	MRM
69.25	21.11	10.7	×				×	×	×
70.35	21.44				×	×	×	×	
71.65	21.84							×	
72.65	22.14						×	×	
73.65	22.45							×	×
74.65	22.75		×	×	×		×	×	×
75.65	23.06				×	×	×	×	
79.15	24.12		×					×	
80.05	24.40					×		×	
364.65	111.15	17.7			×	×	×	×	
366.25	111.63				×			×	×
367.95	112.15							×	
369.85	112.73							×	×
371.65	113.28		×				×	×	
373.15	113.74							×	×
375.25	114.38		×				×	×	
377.05	114.92					×	×	×	×
378.85	115.47				×		×	×	×
380.65	116.02						×	×	
572.55	174.51	33.4					×	×	
574.55	175.12		×			×		×	×
576.55	175.73		×		×			×	
578.55	176.34		×		×	×	×	×	
580.55	176.95		×					×	
582.15	177.44						×	×	×
584.95	178.29		×					×	×
586.55	178.78			×			×	×	×
588.75	179.45		×		×		×	×	
590.55	180.00							×	
867.45	264.40	41.2						×	
867.70	264.47		×				×	×	
867.95	264.55		×					×	×
868.15	264.61		×			×		×	
868.35	264.67		×	×			×	×	
868.55	264.73			×	×		×	×	
868.75	264.80		×					×	
869.05	264.89		×	×	×			×	
869.25	264.95		×		×	×	×	×	×
869.45	265.01		×				×	×	×

995.45	303.41	50.2	×				×	×		
996.05	303.60		×	×			×	×		
996.55	303.75		×				×	×		
997.15	303.93		×		×		×	×		
997.75	304.11		×			×	×	×		
998.35	304.30		×					×		
998.95	304.48				×	×		×	×	
999.55	304.66		×		×			×		
1000.25	304.88						×	×		
1000.75	305.03		×					×	×	
1243.95	379.16	60.1	×	×				×		
1244.25	379.25						×	×	×	
1244.55	379.34						×	×		
1244.95	379.46				×	×		×	×	
1245.25	379.55		×					×		
1245.55	379.64		×		×			×		
1245.85	379.74		×				×	×		
1246.35	379.89		×				×	×	×	
1246.65	379.98						×	×	×	
1246.85	380.04		×		×		×	×		
1299.85	396.19	74.1	×	×			×	×		
1300.15	396.29							×		
1300.45	396.38			×	×			×		
1300.75	396.47		×		×	×	×	×		
1301.05	396.56									
1301.35	396.65		×					×		
1301.65	396.74							×		
1301.95	396.83		×	×				×		
1302.25	396.93						×	×		
1302.55	397.02				×		×	×		
1578.85	481.23	77.8	×					×		
1579.15	481.32		×			×		×		
1579.45	481.42		×				×	×		
1579.75	481.51		×	×			×	×		
1580.05	481.60		×		×		×	×		
1580.25	481.66		×	×	×		×	×		
1580.55	481.75		×	×				×		
1580.85	481.84		×				×	×		
1581.05	481.90		×				×	×		
1581.35	482.00				×					
1863.95	568.13	90.9	×	×		×	×			
1865.35	568.56		×					×		
1866.05	568.77		×							
1866.65	568.95		×				×			
1867.35	569.17		×							
1868.05	569.38		×							
1869.35	569.78		×				×			
1870.15	570.02		×							
1870.65	570.17		×					×		
1871.35	570.39			×						
1872.65	570.78		×				×	×		
1874.05	571.21		×		×	×	×			
1874.65	571.39		×		×		×			
1876.05	571.82		×		×		×			
1876.65	572.00									

References

Abrantes, F., 1988. Diatom assemblages as upwelling indicators in surface sediments off Portugal. Marine Geology 85, 15-39.

Abrantes, F., Moita, M.T., 1999. Water column and recent sediment data on diatoms and coccolithophorids, off Portugal, confirm sediment record of upwelling events. Oceanologica acta 22, 318-336.

Abrantes, F., Lopes, C., Mix, A., Pisias, N., 2007. Diatoms in Southeast Pacific surface sediments reflect environmental properties. Quaternary Science Reviews 26, 155-169.

Ahmed, M., Schouten, S., Baas, M., de Leeuw, J.W., 2000. Bound lipids in kerogens from the Monterey formation, Naples Beach, California, The Monterey Formation from Rocks to Molecules. Colombia University Press, New York, pp. 189-205.

Allard, B., Templier, J., 2001. High molecular weight lipids from the trilaminar outer wall (TLS)-containing microalgae *Chlorella emersonii, Scenedesmus communis* and *Tetraedron minimum*. Phytochemistry 57, 459-467.

Alt-Epping, U., 2008. Late Quaternary sediment processes and sediment accumulation changes off Portugal, Dissertation Universität Bremen, 161 pp.

Alt-Epping, U., Mil-Homens, M., Hebbeln, D., Abrantes, F., Schneider, R.R., 2007. Provenance of organic matter and nutrient conditions on a river- and upwelling influenced shelf: A case study from the Portuguese margin. Marine Geology 243, 169-179.

Alvarez-Salgado, X.A., Figueiras, F.G., Perez, F.F., Groom, S., Nogueira, E., Borges, A., Chou, L., Castro, C.G., Moncoiffe, G., Rios, A.F., Miller, A.E.J., Frankignoulle, M., Savidge, G., Wollast, R., 2003. The Portugal coastal counter current off NW Spain: new insights on its biogeochemical variability. Progress in Oceanography. 56, 281-321.

Anabalón, V., Morales, C.E., Escribano, R., Angélica Varas, M., 2007. The contribution of nano- and micro-planktonic assemblages in the surface layer (0–30m) under different hydrographic conditions in the upwelling area off Concepción, central Chile. Progress in Oceanography 75, 396-414.

Anagnostou, E., John, E.H., Edgar, K.M., Foster, G.L., Ridgwell, A., Inglis, G.N., Pancost, R.D., Lunt, D.J., Pearson, P.N., 2016. Changing atmospheric CO_2 concentration was the primary driver of early Cenozoic climate. Nature 533, 380.

Araújo, M.F., Dias, J.M.A., Jouanneau, J.M., 1994. Chemical characterisation of the main fine sedimentary deposit at the northwestern Portuguese shelf. Gaia 9, 59-65.

Araujo, M., Noriega, C., Hounsou-gbo, G.A., Veleda, D., Araujo, J., Bruto, L., Feitosa, F., Flores-Montes, M., Lefevre, N., Melo, P., Otsuka, A., Travassos, K., Schwamborn, R., Neumann-Leitao, S., 2017. A Synoptic Assessment of the Amazon River-Ocean Continuum during Boreal Autumn: From Physics to Plankton Communities and Carbon Flux. Frontiers in Microbiology 8.

Atwood, A.R., Volkman, J.K., Sachs, J.P., 2014. Characterization of unusual sterols and long chain diols, triols, keto-ols and *n*-alkenols in El Junco Lake, Galapagos. Organic Geochemistry 66, 80-89.

Balzano, S., Abs, E., Leterme, S.C., 2015. Protist diversity along a salinity gradient in a coastal lagoon. Aquatic Microbial Ecology 74, 263-277.

Balzano, S., Lattaud, J., Villanueva, L., Rampen, S.W., Brussaard, C.P.D., van Bleijswijk, J., Bale, N., Sinninghe Damsté, J.S., Schouten, S., 2018. A quest for the biological sources of long chain alkyl diols in the western tropical North Atlantic Ocean. Biogeosciences 15, 5951-5968.

Balzano, S., Sarno, D., Kooistra, W.H.C.F., 2011. Effects of salinity on the growth rate and morphology of ten Skeletonema strains. Journal of Plankton Research 33, 937-945.

Balzano, S., Villanueva, L., de Bar, M.W., Sinninghe Damsté, J.S., Schouten, S., 2017. Impact of culturing conditions on the abundance and composition of long chain alkyl diols in species of the genus *Nannochloropsis*. Organic Geochemistry 108, 9-17.

Barrington, D.J., Ghadouani, A., 2008. Application of hydrogen peroxide for the removal of toxic Cyanobacteria and other phytoplankton from wastewater. Environmental Science & Technology 42, 8916-8921.

Bartels-Jónsdóttir, H.B., Voelker, A.H.L., Knudsen, K.L., Abrantes, F., 2009. Twentieth-century warming and hydrographical changes in the Tagus Prodelta, eastern North Atlantic. Holocene 19, 369-380.

Basse, A., Zhu, C. , Versteegh, G. J. , Fischer, G. , Hinrichs, K.-U., Mollenhauer, G., 2014. Distribution of intact and core tetraether lipids in water column profiles of suspended particulate matter off Cape Blanc, NW Africa , Organic Geochemistry 72, 1-13.

Bauersachs, T., Schwark, L., 2016. Glycerol monoalkanediol diethers: a novel series of archaeal lipids detected in hydrothermal environments. Rapid Communications in Mass Spectrometry 30, 581 54–60.

Becker, K.W., Elling, F.J., Yoshinaga, M.Y., Söllinger, A., Urich, T., Hinrichs, K.-U., 2016. Unusual Butane- and Pentanetriol-Based Tetraether Lipids in *Methanomassiliicoccus luminyensis*, a Representative of the Seventh Order of Methanogens. Applied and Environmental Microbiology 82, 4505–4516.

Becker, K.W., Lipp, J.S., Versteegh, G.J.M., Wormer, L., Hinrichs, K.-U., 2015. Rapid and simultaneous analysis of three molecular sea surface temperature proxies and application to sediments from the Sea of Marmara. Organic Geochemistry 85, 42-53.

Becker, K.W., Lipp, J.S., Zhu, C., Liu, X.L., Hinrichs, K.-U., 2013. An improved method for the analysis of archaeal and bacterial ether core lipids. Organic Geochemistry 61, 34-44.

Beltran, C., Flores, J.A., Sicre, M.A., Baudin, F., Renard, M., de Rafelis, M., 2011. Long chain alkenones in the Early Pliocene Sicilian sediments (Trubi Formation - Punta di Maiata section): Implications for the alkenone paleothermometry. Palaeogeography, Palaeoclimatology, Palaeoecology 308, 253-263.

Bemis, B.E., Spero, H.J., Bijma, J., Lea, D.W., 1998. Reevaluation of the oxygen isotopic composition of planktonic foraminifera: Experimental results and revised paleotemperature equations. Paleoceanography 13, 150-160.

Berger, W.H., Fischer, K., Lai, C., and Wu., G., 1987. Ocean productivity and organic carbon flux. Part I. Overview and maps of primary production and export productivity, University of California, San Diego, La Jolla, Calif.

Biastoch, A., Krauss, W., 1999. The Role of Mesoscale Eddies in the Source Regions of the Agulhas Current. Journal of Physical Oceanography 29, 2303-2317.

Bijl, P.K., Schouten, S., Sluijs, A., Reichart, G.-J., Zachos, J.C., Brinkhuis, H., 2009. Early Palaeogene temperature evolution of the southwest Pacific Ocean. Nature 461, 776-779.

Bin Shaari, H., 2013a. Hydrological evolution of the eastern tropical Pacific during the last 430,000 years, PhD Thesis, Hokkaido University, http://doi.org/10.14943/doctoral.r6891.

Bin Shaari, H., Yamamoto, M., Irino, T., 2013b. Enhanced upwelling in the eastern equatorial Pacific at the last five glacial terminations. Palaeogeography Palaeoclimatology Palaeoecology 386, 8-15.

Bin Shaari, H., Yamamoto, M., Irino, T., Oba, T., 2014. Nutricline shoaling in the eastern Pacific warm pool during the last two glacial maxima. Journal of Oceanography 70, 25-34.

Blank, C.E., 2009. Not so old Archaea - the antiquity of biogeochemical processes in the archaeal domain of life. Geobiology 7, 495–514.

Blokker, P., Schouten, S., de Leeuw, J.W., Sinninghe Damsté, J.S., van den Ende, H., 1999. Molecular structure of the resistant biopolymer in zygospore cell walls of *Chlamydomonas monoica*. Planta 207, 539-543.

Blokker, P., Schouten, S., Van den Ende, H., de Leeuw, J.W., Hatcher, P.G., Sinninghe Damsté, J.S., 1998. Chemical structure of algaenans from the fresh water algae *Tetraedron minimum, Scenedesmus communis* and *Pediastrum boryanum*. Organic Geochemistry 29, 1453-1468.

Blunier, T., Brook, E.J., 2001. Timing of millennial-scale climate change in Antarctica and Greenland during the last glacial period. Science 291, 109-112.

Bogus, K.A., Zonneveld, K.A.F., Fischer, D., Kasten, S., Bohrmann, G., Versteegh, G.J.M., 2012. The effect of meter-scale lateral oxygen gradients at the sediment-water interface on selected organic matter based alteration, productivity and temperature proxies. Biogeosciences 9, 1553-1570.

Boon, J.J., Rijpstra, W.I.C., Delange, F., Deleeuw, J.W., Yoshioka, M., Shimizu, Y., 1979. Black Sea sterol – molecular fossil for dinoflagellate blooms. Nature 277, 125-127.

Boyer, T.P., J. I. Antonov, O. K. Baranova, C. Coleman, H. E. Garcia, A. Grodsky, D. R. Johnson, R. A. Locarnini, A. V. Mishonov, T.D. O'Brien, C.R. Paver, J.R. Reagan, D. Seidov, I. V. Smolyar, and M. M. Zweng, 2013. World Ocean Database 2013, NOAA Atlas NESDIS 72, S. Levitus, Ed., A. Mishonov, Technical Ed.; Silver Spring, MD, 209 pp., http://doi.org/10.7289/V5NZ85MT

Bordovskiy O. K., 1965. Accumulation of organic matter in bottom sediments, Marine Geology, 3, 33-82.

Brassell, S.C., 2014. Climatic influences on the Paleogene evolution of alkenones. Paleoceanography 29, 255-272.

Brassell, S.C., Dumitrescu, M., Party, O.D.P.L.S.S., 2004. Recognition of alkenones in a lower Aptian porcellanite from the west-central Pacific. Organic Geochemistry 35, 181–188.

Brassell, S.C., Eglinton, G., Marlowe, I.T., Pflaumann, U., Sarnthein, M., 1986. Molecular stratigraphy: A new tool for climatic assessment. Nature 320, 129-133.

Brathauer, U., Abelmann, A., 1999. Late Quaternary variations in sea surface temperatures and their relationship to orbital forcing recorded in the Southern Ocean (Atlantic sector). Paleoceanography 14, 135-148.

Brocks, J.J., Pearson, A., 2005. Building the biomarker tree of life. In: Banfield, J.E., CerviniSilva, J., Nealson, K.H. (Ed.), Molecular Geomicrobiology, pp. 233–258.

Brown, J.W., Sorhannus, U., 2010. A Molecular Genetic Timescale for the Diversification of Autotrophic Stramenopiles (Ochrophyta): Substantive Underestimation of Putative Fossil Ages. Plos One 5

Caimi, R.J., Brenna, J.T., 1997. Quantitative evaluation of carbon isotopic fractionation during reversed-phase high-performance liquid chromatography. Journal of Chromatography A 757, 307-310.

Caniupán, M., Lamy, F., Lange, C.B., Kaiser, J., Arz, H., Kilian, R., Urrea, O.B., Aracena, C., Hebbeln, D., Kissel, C., Laj, C., Mollenhauer, G., Tiedemann, R., 2011. Millennial-scale sea surface temperature and Patagonian Ice Sheet changes off southernmost Chile (53°S) over the past ~60 kyr. Paleoceanography 26.

Carr, M.E., Kearns, E.J., 2003. Production regimes in four Eastern Boundary Current systems. Deep-Sea Research Part Ii-Topical Studies in Oceanography 50, 3199-3221.

Carrillo-Hernandez, T., Schaeffer, P., Adam, P., Albrecht, P., Derenne, S., Largeau, C., 200. Remarkably well-preserved archaeal and bacterial membrane lipids in 140 million years old sediment from the Russian platform (Kasphpir oil shales, upper Jurrassic). In: 21st International Meeting on Organic Geochemistry (IMOG 2003) Krakow Part 1, pp. 77–78 (Abstract).

Castañeda, I.S., Schouten, S., 2011. A review of molecular organic proxies for examining modern and ancient lacustrine environments. Quaternary Science Reviews 30, 2851-2891.

Castañeda, I.S., Werne, J.P., Johnson, T.C., 2009. Influence of climate change on algal community structure and primary productivity of Lake Malawi (East Africa) from the Last Glacial Maximum to present. Limnology and Oceanography 54, 2431-2447.

Chaler, R., Grimalt, J.O., Pelejero, C., Calvo, E., 2000. Sensitivity effects in $U_{37}^{K'}$ paleotemperature estimation by chemical ionization mass spectrometry. Analytical Chemistry 72, 5892-5897.

Chaler, R., Villanueva, J., Grimalt, J.O., 2003. Non-linear effects in the determination of paleotemperature $U_{37}^{K'}$ alkenone ratios by chemical ionization mass spectrometry. Journal of Chromatography A 1012, 87-93.

Chase, Z., McManus, J., Mix, A.C., Muratli, J., 2014. Southern-ocean and glaciogenic nutrients control diatom export production on the Chile margin. Quaternary Science Reviews 99, 135-145.

Chen, W.W., Mohtadi, M., Schefuss, E., Mollenhauer, G., 2014. Organic-geochemical proxies of sea surface temperature in surface sediments of the tropical eastern Indian Ocean. Deep Sea Research Part I: Oceanographic Research Papers 88, 17-29.

Chivall, D., M'boule, D., Sinke-Schoen, D., Sinninghe Damsté, J.S., Schouten, S., van der Meer, M.T.J., 2014. Impact of salinity and growth phase on alkenone distributions in coastal haptophytes. Organic Geochemistry 67, 31-34.

CLIMAP, 1976. The Surface of the Ice-Age Earth, Science, 191, 1131-1137.

Coles, V.J., Brooks, M.T., Hopkins, J., Stukel, M.R., Yager, P.L., Hood, R.R., 2013. The pathways and properties of the Amazon River Plume in the tropical North Atlantic Ocean. Journal of Geophysical Research-Oceans 118, 6894-6913.

Conte, M.H., Sicre, M.A., Rühlemann, C., Weber, J.C., Schulte, S., Schulz-Bull, D., Blanz, T., 2006. Global temperature calibration of the alkenone unsaturation index ($U_{37}^{K'}$) in surface waters and comparison with surface sediments. Geochemistry Geophysics Geosystems 7, 1-22.

Conte, M.H., Thompson, A., Eglinton, G., 1994. Primary production of lipid biomarker compounds by Emiliania Huxleyi – Results from an experimental mesocosm study in fjords of southwestern Norway. Sarsia 79, 319-331.

Conte, M.H., Thompson, A., Eglinton, G., 1995. Lipid biomarker diversity in the coccolithophorid *Emiliania huxleyi* (Prymnesiophyceae) and the related species *Gephyrocapsa oceanica*. Journal of Phycology 31, 272-282.

Conte, M.H., Thompson, A., Lesley, D., Harris, R.P., 1998. Genetic and physiological influences on the alkenone/alkenoate versus growth temperature relationship in *Emiliania huxleyi* and *Gephyrocapsa oceanica*. Geochimica et Cosmochimica Acta 62, 51-68.

Conte, M.H., Weber, J.C., King, L.L., Wakeham, S.G., 2001. The alkenone temperature signal in western North Atlantic surface waters. Geochimica et Cosmochimica Acta 65, 4275-4287.

Contreras, S., Lange, C.B., Pantoja, S., Lavik, G., Rincon-Martinez, D., Kuypers, M.M.M., 2010. A rainy northern Atacama Desert during the last interglacial. Geophysical Research Letters 37, L23612.

Costa, K.M., McManus, J.F., Anderson, R.F., 2018. Radiocarbon and Stable Isotope Evidence for Changes in Sediment Mixing in the North Pacific Over the Past 30 kyr. Radiocarbon 60, 113-135.

Cranwell, P.A., Eglinton, G., Robinson, N., 1987. Lipids of aquatic organisms as potential contributors to lacustrine sediments .II. Organic Geochemistry 11, 513-527.

Cropper, T.E., Hanna, E., Bigg, G.R., 2014. Spatial and temporal seasonal trends in coastal upwelling off Northwest Africa, 1981-2012. Deep-Sea Research Part I-Oceanographic Research Papers 86, 94-111.

Crosta, X., Romero, O.E., Ther, O., Schneider, R.R., 2012. Climatically-controlled siliceous productivity in the eastern Gulf of Guinea during the last 40 000 yr. Climate of the Past 8, 415-431.

Daneri, G., Dellarossa, V., Quinones, R., Jacob, B., Montero, P., Ulloa, O., 2000. Primary production and community respiration in the Humboldt Current System off Chile and associated oceanic areas. Marine Ecology Progress Series 197, 41-49.

de Baar, H.J.W., Dejong, J.T.M., Bakker, D.C.E., Loscher, B.M., Veth, C., Bathmann, U., Smetacek, V., 1995. Importance of iron for plankton blooms and carbon-dioxide drawdown in the Southern-Ocean. Nature 373, 412-415.

de Bar, M.W., de Nooijer, L.J., Schouten, S., Ziegler, M., Sluijs, A., Reichart, G.-J., accepted. Comparing sea water temperature proxy records for the past 90 Myrs from the shallow shelf record Bass River, New Jersey, Paleoceanography and Paleoclimatology.

de Bar, M.W., Dorhout, D.J.C., Hopmans, E.C., Rampen, S.W., Sinninghe Damsté, J.S., Schouten, S., 2016. Constraints on the application of long chain diol proxies in the Iberian Atlantic margin. Organic Geochemistry 101, 184-195.

de Bar, M.W., Dorhout, D.J.C., Hopmans, E.C., Rampen, S.W., Sinninghe Damsté, J.S., Schouten, S., 2019b. Corrigendum to "Constraints on the application of long chain diol proxies in the Iberian Atlantic margin". Organic Geochemistry 130, 51-52.

de Bar, M.W., Hopmans, E.C., Verweij, M., Dorhout, D.J.C., Sinninghe Damsté, J.S., Schouten, S., 2017. Development and comparison of chromatographic methods for the analysis of long chain diols and alkenones in biological materials and sediment. Journal of Chromatography A 1521, 150–160.

de Bar, M.W., Rampen, S.W., Hopmans, E.C., Sinninghe Damsté, J.S., Schouten, S., 2019a. Constraining the applicability of organic paleotemperature proxies fort he last 90 Myrs. Organic Geochemistry 128, 122-136.

de Bar, M.W., Stolwijk, D.J., McManus, J.F., Sinninghe Damsté, J.S., Schouten, S., 2018. A Late Quaternary climate record based on long-chain diol proxies from the Chilean margin. Climate of the Past 14, 1783-1803.

de Jonge, C., Hopmans, E.C., Zell, C.I., Kim, J.H., Schouten, S., Sinninghe Damsté, J.S., 2014b. Occurrence and abundance of 6-methyl branched glycerol dialkyl glycerol tetraethers in soils: Implications for palaeoclimate reconstruction. Geochimica Et Cosmochimica Acta 141, 97-112.

de Jonge, C., Stadnitskaia, A., Hopmans, E.C., Cherkashov, G., Fedotov, A., Sinninghe Damsté, J.S., 2014a. In situ produced branched glycerol dialkyl glycerol tetraethers in suspended particulate matter from the Yenisei River, Eastern Siberia. Geochimica et Cosmochimica Acta 125, 476-491.

de Jonge, C., Stadnitskaia, A., Hopmans, E.C., Cherkashov, G., Fedotov, A., Streletskaya, I.D., Vasiliev, A.A., Sinninghe Damsté, J.S., 2015. Drastic changes in the distribution of branched tetraether lipids in suspended matter and sediments from the Yenisei River and Kara Sea (Siberia): Implications for the use of brGDGT-based proxies in coastal marine sediments. Geochimica Et Cosmochimica Acta 165, 200-225.

de Leeuw, J.W., Rijpstra, W.I.C., Mur, L.R., 1992. The absence of long-chain alkyl diols and alkyl keto-1-ols in cultures of the cyanobacterium *Aphanizomenon flos-aquae*. Org. Geochem 18, 575-578.

de Leeuw, J.W., Rijpstra, W.I.C., Schenck, P.A., 1981. The occurrence and identification of C_{30}, C_{31} and C_{32} alkan 1,15-diols and alkan 15-one 1-ols in Unit I and Unit II Black Sea sediments. Geochimica et Cosmochimica Acta 45, 2281-2285.

de Leeuw, J.W., Rijpstra, W.I.C., Schenck, P.A., Volkman, J., 1983. Free, esterified and residual sterols in Black Sea Unit I sediments. Geochimica et Cosmochimica Acta 47, 455-465.

de Leeuw, J.W., v.d. Meer, F.W., Rijpstra, W.I.C., Schenck, P.A., 1980. On the occurrence and structural identification of long chain unsaturated ketones and hydrocarbons in sediments. Physics and Chemistry of the Earth 12, 211-217.

de Vargas, C., Audic, S., Henry, N., Decelle, J., Mahe, F., Logares, R., Lara, E., Berney, C., Le Bescot, N., Probert, I., Carmichael, M., Poulain, J., Romac, S., Colin, S., Aury, J.-M., Bittner, L., Chaffron, S., Dunthorn, M., Engelen, S., Flegontova, O., Guidi, L., Horak, A., Jaillon, O., Lima-Mendez, G., Lukes, J., Malviya, S., Morard, R., Mulot, M., Scalco, E., Siano, R., Vincent, F., Zingone, A., Dimier, C., Picheral, M., Searson, S., Kandels-Lewis, S., Acinas, S.G., Bork, P., Bowler, C., Gorsky, G., Grimsley, N., Hingamp, P., Iudicone, D., Not, F., Ogata, H., Pesant, S., Raes, J., Sieracki, M.E., Speich, S., Stemmann, L., Sunagawa, S., Weissenbach, J., Wincker, P., Karsenti, E., Tara Oceans, C., 2015. Eukaryotic plankton diversity in the sunlit ocean. Science 348, 6237.

Derenne, S., Largeau, C., Casadevall, E., Tegelaar, E., de Leeuw, J.W., 1988. Characterization of coal pyrolysis products relationships between algal coals and resistant cell wall biopolymers of extant algae as revealed by Py-GC-MS. Fuel Processing Technology 20, 93-101.

Dias, J.M.A., Jouanneau, J.M., Gonzalez, R., Araujo, M.F., Drago, T., Garcia, C., Oliveira, A., Rodrigues, A., Vitorino, J., Weber, O., 2002. Present day sedimentary processes on the northern Iberian shelf. Progress in Oceanography 52, 249-259.

Dias, J.M.A., Nittrouer, C.A., 1984. Continental shelf sediments of northern Portugal. Continen Doi, T., Tozuka, T., Yamagata, T., 2009. Interannual variability of the Guinea Dome and its possible link with the Atlantic Meridional Mode. Climate Dynamics 33, 985-998.tal Shelf Research 3, 147–165.

Dickens, G.R., Castillo, M.M., Walker, J.C., 1997. A blast of gas in the latest Paleocene: simulating first-order effects of massive dissociation of oceanic methane hydrate. Geology 25, 259-262.

Doi, T., Tozuka, T., Yamagata, T., 2009. Interannual variability of the Guinea Dome and its possible link with the Atlantic Meridional Mode. Climate Dynamics 33, 985-998.

Drabkova, M., Admiraal, W., Marsalek, B., 2007. Combined exposure to hydrogen peroxide and light. Selective effects on Cyanobacteria, green algae, and diatoms. Environmental Science & Technology 41, 309-314.

Drago, T., Araújo, F., Valério, P., Weber, O., Jouanneau, J. M., 1999. Geomorphological control of fine sedimentation on the northern Portuguese shelf. Boletin Instituto Espagnol Oceanografia 15, 111–122.

Drago, T., Oliveira, A., Magalhães, F., Cascalho, J., Jouanneau, J.M., Vitorino, J., 1998. Some evidence of the northward fine sediment transport in the northern Portuguese continental shelf. Oceanologica Acta 21, 223–231.

Duce, R.A., Liss, P.S., Merrill, J.T., Atlas, E.L., Buat-Menard, P., Hicks, B.B., Miller, J.M., Prospero, J.M., Arimoto, R., Church, T.M., Ellis, W., Galloway, J.N., Hansen, L., Jickells, T.D., Knap, A.H., Reinhardt, K.H., Schneider, B., Soudine, A., Tokos, J.J., Tsunogai, S., Wollast, R., Zhou, M., 1991. The Atmospheric Input of Trace Species to the World Ocean. Global Biogeochemical Cycles 5, 193-259.

Dunstan, G.A., Volkman, J.K., Barrett, S.M., Garland, C.D., 1993. Changes in the lipid composition and maximization of the polyunsaturated fatty acid content of 3 microalgae grown in mass culture. Journal of Applied Phycology 5, 71-83.

Dzvonik, J.P., 1996. Alkenones as records of oceanic paleotemperatures; studies of Eocene and Oligocene sediments from the North, South, and Equatorial Atlantic. Indiana University at Bloomington, Bloomington, IN, United States, p. 21.

Elling, F.J., Könneke, M., Lipp, J.S., Becker, K.W., Gagen, E.J., Hinrichs, K.-U., 2014. Effects of growth phase on the membrane lipid composition of the thaumarchaeon *Nitrosopumilus* maritimus and their implications for archaeal lipid distributions in the marine environment. Geochimica Et Cosmochimica Acta 141, 579-597.

Elling, F.J., Könneke, M., Mussmann, M., Greve, A., Hinrichs, K.-U., 2015. Influence of temperature, pH, and salinity on membrane lipid composition and TEX_{86} of marine planktonic thaumarchaeal isolates. Geochimica Et Cosmochimica Acta 171, 238-255.

Elling, F.J., Könneke, M., Nicol, G.W., Stieglmeier, M., Bayer, B., Spieck, E., de la Torre, J.R., Becker, K.W., Thomm, M., Prosser, J.I., Herndl, G.J., Schleper, C., Hinrichs, K.-U., 2017. Chemotaxonomic characterisation of the thaumarchaeal lipidome. Environmental Microbiology 19, 2681-2700.

Emerson, S., Hedges, J.I., 1988. Processes controlling the organic carbon content of open ocean sediments. Paleoceanography 3, 621-634.

Emiliani, C., 1955. Pleistocene Temperatures. The Journal of Geology 63, 538-578.

Escala, M., Fietz, S., Rueda, G., Rosell-Melé, A., 2009. Analytical Considerations for the Use of the Paleothermometer Tetraether Index(86) and the Branched vs Isoprenoid Tetraether Index Regarding the Choice of Cleanup and Instrumental Conditions. Analytical Chemistry 81, 2701-2707.

European Commission, Joint Research Centre (2016): EMIS - SeaWiFS Monthly sea surface Chlorophyll-*a* concentration (2km) in mg m^{-3}. European Commission, Joint Research Centre (JRC). Dataset accessed on 25/08/2016.

Fabregas, J., Maseda, A., Dominguez, A., Otero, A., 2004. The cell composition of *Nannochloropsis* sp. changes under different irradiances in semicontinuous culture. World Journal of Microbiology & Biotechnology 20, 31-35.

Fallet, U., Brummer, G.J., Zinke, J., Vogels, S., Ridderinkhof, H., 2010. Contrasting seasonal fluxes of planktonic foraminifera and impacts on paleothermometry in the Mozambique Channel upstream of the Agulhas Current. Paleoceanography 25, 12.

Fallet, U., Castaneda, I.S., Aneurin, H.E., Richter, T.O., Boer, W., Schouten, S., Brummer, G.J., 2012. Sedimentation and burial of organic and inorganic temperature proxies in the Mozambique Channel, SW Indian Ocean. Deep-Sea Research Part I-Oceanographic Research Papers 59, 37-53.

Fallet, U., Ullgren, J.E., Castaneda, I.S., van Aken, H.M., Schouten, S., Ridderinkhof, H., Brummer, G.J.A., 2011. Contrasting variability in foraminiferal and organic paleotemperature proxies in sedimenting particles of the Mozambique Channel (SW Indian Ocean). Geochimica et Cosmochimica Acta 75, 5834-5848.

Farrimond, P., Eglinton, G., Brassell, S.C., 1986. Alkenones in Cretaceous black shales, Blake-Bahama Basin, western North Atlantic, Organic Geochemistry 10, 897–903.

Fernández, E., Bode, A., 1994. Succession of phytoplankton assemblages in relation to the hydrography in the southern Bay of Biscay: a multivariate approach. Scientia Marina 58, 191-205.

Ferreira, A.M., Miranda, A., Caetano, M., Baas, M., Vale, C., Sinninghe Damsté, J.S., 2001. Formation of mid-chain alkane keto-ols by post-depositional oxidation of mid-chain diols in Mediterranean sapropels. Organic Geochemistry 32, 271-276.

Fietz, S., Bleiss, W., Hepperle, D., Koppitz, H., Krienitz, L., Nicklisch, A., 2005. First record of *Nannochloropsis limnetica* (Eustigmatophyceae) in the autotrophic picoplankton from Lake Baikal. Journal of Phycology 41, 780-790.

Fietz, S., Martinez-Garcia, A., Huguet, C., Rueda, G., Rosell-Melé, A., 2011. Constraints in the application of the Branched and Isoprenoid Tetraether index as a terrestrial input proxy. Journal of Geophysical Research – Oceans 116.

Fietz, S., Huguet, C., Rueda, G., Hambach, B., Rosell-Melé, A., 2013. Hydroxylated isoprenoidal GDGTs in the Nordic Seas. Marine Chemistry 152, 1–10.

Fiúza, A., 1983. Upwelling patterns off Portugal. In: Suess, E., Thide, J. (Eds.) Coastal upwelling, its sediment record: Responses of sedimenta¬ry regime to present coastal upwelling. Nato Conference Series 10B, Springer, 58–89.

Fiuza, A.F.D., Demacedo, M.E., Guerreiro, M.R., 1982. Climatological space and time-variation of the Portuguese coastal upwelling. Oceanologica acta 5, 31-4

Forster, A., Schouten, S., Baas, M., Sinninghe Damsté, J.S., 2007a. Mid-Cretaceous (Albian-Santonian) sea surface temperature record of the tropical Atlantic Ocean. Geology 35, 919–922.

Forster, A., Schouten, S., Moriya, K., Wilson, P.A., Sinninghe Damsté, J.S., 2007b. Tropical warming and intermittent cooling during the Cenomanian/Turonian oceanic anoxic event 2: Sea surface temperature records from the equatorial Atlantic. Paleoceanography 22.

Foster, G.L., Royer, D.L., Lunt, D.J., 2017. Future climate forcing potentially without precedent in the last 420 million years. Nature Communications 8.

Friedrich, O., Norris, R.D., Erbacher, J., 2012. Evolution of middle to Late Cretaceous oceans – A 55 m.y. record of Earth's temperature and carbon cycle. Geology 40, 107–110.

Frouin, R., Franz, B. A., Werdell, P. J., 2003. The SeaWiFS PAR product., In: S.B. Hooker and E.R. Firestone, Algorithm Updates for the Fourth SeaWiFS Data Reprocessing, NASA Tech.

Memo. 2003–206892, Volume 22, NASA Goddard Space Flight Center, Greenbelt, Maryland, 46-50. The SeaWiFS PAR product.

Furota, S., Nakamura, H., Sawada, K., 2016. Long-chain alkenones and related distinctive compounds in the late Miocene and Pliocene sediments from the Gulf of Cadiz, eastern North Atlantic. Organic Geochemistry 101, 166-175.

Gal, J.-K., Kim, J.-H., Shin, K.-H., 2018. Distribution of long chain alkyl diols along a south-north transect of the northwestern Pacific region: Insights into a paleo sea surface nutrient proxy. Organic Geochemistry 119, 80-90.

Garcia, H.E., Locarnini, R.A., Boyer, T.P., Antonov, J.I., Baranova, O.K., Zweng, M.M., Reagan, J.R., Johnson, D.R., 2013. World Ocean Atlas 2013. Vol. 4: Dissolved Inorganic Nutrients (phosphate, nitrate, silicate). Levitus, S., Ed.; Mishonov, A., Technical Ed. NOAA Atlas NESDIS 76, 25 pp.

Gelin, F., Boogers, I., Noordeloos, A.A.M., Sinninghe Damsté, J.S., Hatcher, P.G., deLeeuw, J.W., 1996. Novel, resistant microalgal polyethers: An important sink of organic carbon in the marine environment? Geochimica Et Cosmochimica Acta 60, 1275-1280.

Gelin, F., Boogers, I., Noordeloos, A.A.M., Sinninghe Damsté, J.S., Riegman, R., de Leeuw, J.W., 1997a. Resistant biomacromolecules in marine microalgae of the classes Eustigmatophyceae and Chlorophyceae: Geochemical implications. Organic Geochemistry 26, 659-675.

Gelin, F., Volkman, J.K., deLeeuw, J.W., Sinninghe Damsté, J.S., 1997b. Mid-chain hydroxy long-chain fatty acids in microalgae from the genus *Nannochloropsis*. Phytochemistry 45, 641-646.

Gelin, F., Volkman, J.K., Largeau, C., Derenne, S., Sinninghe Damsté, J.S., de Leeuw, J.W., 1999. Distribution of aliphatic, nonhydrolyzable biopolymers in marine microalgae. Organic Geochemistry 30, 147-159.

Gersonde, R., Harwood, D. M. 1990. Lower Cretaceous diatoms from ODP Leg 113, Site 693 (Weddell Sea). Part 1: vegetative cells. In: Barker, P. F., Kennett, J. P. et al. (Ed). Proceedings of the Ocean Drilling Program, Scientific Results, vol. 113. Ocean Drilling Program, College Station, Texas, pp. 365–402.

Gibbons, J. D. & Chakraborty, S., 2003. Nonparametric Statistical Inference. Fourth Edition. Marcel Dekker Inc., New York, 645 pp. ISBN: 0-8247-4052-1.

Goddard Earth Sciences Data and Information Services Center, 2016. TRMM (TMPA-RT) Near Real-Time Precipitation L3 1 day 0.25 degree × 0.25 degree V7, Greenbelt, MD, Goddard Earth Sciences Data and Information Services Center (GES DISC), http://disc.gsfc.nasa.gov/datacollection/TRMM_3B42RT_Daily_7.html.

Goñi, M.A., Woodworth, M.P., Aceves, H.L., Thunell, R.C., Tappa, E., Black, D., Muller-Karger, F., Astor, Y., Varela, R., 2004. Generation, transport, and preservation of the alkenone-based $U_{37}^{K'}$ sea surface temperature index in the water column and sediments of the Cariaco Basin (Venezuela). Global Biogeochemical Cycles 18, GB2001-2001-GB2001-2021.

Gonzalez, H.E., Menschel, E., Aparicio, C., Barria, C., 2007. Spatial and temporal variability of microplankton and detritus, and their export to the shelf sediments in the upwelling area off Concepcion, Chile (~36°S), during 2002-2005. Progress in Oceanography 75, 435-451.

Gordon, A.L., 1986. Inter-ocean exchange of thermocline water. Journal of Geophysical Research-Oceans 91, 5037-5046.

Goudie, A.S., Middleton, N.J., 2001. Saharan dust storms: nature and consequences. Earth-Science Reviews 56, 179-204.

Grimalt, J.O., Calvo, E., Pelejero, C., 2001. Sea surface paleotemperature errors in $U_{37}^{K'}$ estimation due to alkenone measurements near the limit of detection. Paleoceanography 16, 226-232.

Guerreiro, C.V., Baumann, K.H., Brummer, G.J.A., Fischer, G., Korte, L.F., Merkel, U., Sa, C., de Stigter, H., Stuut, J.B.W., 2017. Coccolithophore fluxes in the open tropical North Atlantic: influence of thermocline depth, Amazon water, and Saharan dust. Biogeosciences 14, 4577-4599.

Guerreiro, C. V., Baumann, K.-H., Brummer, G.-J. A., Fischer, G., Korte, L. F., Sá, C. and Stuut, J.-B. W., 2018. Wind-forced transatlantic gradients in coccolithophore species fluxes, Submitted to Progess in Oceanography (in revision).

Guillard, R.R.L., 1975. Culture of phytoplankton for feeding marine invertebrates, in: Smith, W.L., Chanley, M.H. (Eds.), Culture of marine invertebrate animals. Plenum Book Publication Corporation, New York, pp. 29-60.

Gutteridge, J.M.C., Wilkins, S., 1983. Copper salt-dependent hydroxyl radical formation. Damage to proteins acting as anti-oxidant. Biochimica Et Biophysica Acta 759, 38-41.

Haake, B., Ittekkot, V., Rixen, T., Ramaswamy, V., Nair, R.R., Curry, W.B., 1993. Seasonality and interannual variability of particle fluxes to the deep Arabian Sea. Deep-Sea Research Part I-Oceanographic Research Papers 40, 1323-1344.

Haberle, S.G., Bennett, K.D., 2004. Postglacial formation and dynamics of North Patagonian Rainforest in the Chonos Archipelago, southern Chile. Quaternary Science Reviews 23, 2433-2452.

Hajós, M., Stradner, H., 1975. Late Cretaceous Archaeomonadaceae, Diatomaceae, and Silicoflagellatae from the South Pacific Ocean, Deep Sea Drilling Project, Leg 29, Site 275. Initial Reports of the Deep Sea Drilling Project, 29, 913–1009.

Harlander, U., Ridderinkhof, H., Schouten, M.W., de Ruijter, W.P.M., 2009. Long-term observations of transport, eddies, and Rossby waves in the Mozambique Channel. Journal of Geophysical Research-Oceans 114.

Hart, J. T., 1942. Phytoplankton periodicity in Antarctic surface waters, Disc. Rep., 21, 261–356.

Hartnett, H.E., Keil, R.G., Hedges, J.I., Devol, A.H., 1998. Influence of oxygen exposure time on organic carbon preservation in continental margin sediments. Nature 391, 572-574.

Harwood, D., Nikolaev, V., 1995. Cretaceous Diatoms: Morphology, Taxonomy, Biostratigraphy. In: Blome, C. D., Whalen, P. M. and Reed, K. M. (Ed.). Siliceous Microfossils: Paleontological Society Short Courses in Paleontology, 8. Paleontology Society, University of Tennessee, Knoxville, Tennessee, pp 81–106.

Hebbeln, D., Marchant, M., Freudenthal, T., Wefer, G., 2000. Surface sediment distribution along the Chilean continental slope related to upwelling and productivity. Marine Geology 164, 119-137.

Hebbeln, D., Marchant, M., Wefer, G., 2002. Paleoproductivity in the southern Peru-Chile Current through the last 33 000 yr. Marine Geology 186, 487-504.

Hedges, J.I., Sheng Hu, F., Devol, A.H., Hartnett, H.E., Tsamakis, E., Keil, R.G., 1999. Sedimentary organic matter preservation: a test for selective degradation under oxic conditions. American Journal of Science 299, 529-555.

Hefter, J., 2008. Analysis of alkenone unsaturation indices with fast gas chromatography/time-of-flight mass spectrometry. Analytical Chemistry 80, 2161-2170.

Herbert, T.D., 2003. Alkenone Paleotemperature Determinations. In: Turekian, K.K., Holland, H.D. (Ed.), Treatise on Geochemistry. Elsevier-Pergamon, Oxford, pp. 391-432.

Hernández-Becerril, D.U., 1995. Planktonic diatoms from the Gulf of California and coasts off Baja California: The genera *Rhizosolenia*, *Proboscia*, *Pseudosolenia*, and former *Rhizosolenia* species. Diatom Research 10, 251-267.

Herndl, G.J., Reinthaler, T., Teira, E., van Aken, H., Veth, C., Pernthaler, A., Pernthaler, J., 2005. Contribution of Archaea to total prokaryotic production in the deep Atlantic Ocean. Applied and Environmental Microbiology 71, 2303-2309.

Herrera, L., Escribano, R., 2006. Factors structuring the phytoplankton community in the upwelling site off El Loa River in northern Chile. Journal of Marine Systems 61, 13-38.

Heusser, C.J., 1990. Ice-age vegetation and climate subtropical Chile. Palaeogeography Palaeoclimatology Palaeoecology 80, 107-127.

Heusser, L., Heusser, C., Mix, A., McManus, J., 2006. Chilean and Southeast Pacific paleoclimate variations during the last glacial cycle: directly correlated pollen and $\delta^{18}O$ records from ODP Site 1234. Quaternary Science Reviews 25, 3404-3415.

Hibberd, D.J., 1981. Notes on the taxonomy and the nomenclature of the algal class Eustigmatophyceae and Tribophyceae (synonym Xanthophyceae). Botanical Journal of the Linnean Society 82, 93-119.

Hinrichs, K.-U., Schneider, R.R., Muller, P.J., Rullkötter, J., 1999. A biomarker perspective on paleoproductivity variations in two Late Quaternary sediment sections from the Southeast Atlantic Ocean. Organic Geochemistry 30, 341-366.

Ho, S.L., Mollenhauer, G., Lamy, F., Martínez-Garcia, A., Mohtadi, M., Gersonde, R., Hebbeln, D., Nunez-Ricardo, S., Rosell-Melé, A., Tiedemann, R., 2012. Sea surface temperature variability in the Pacific sector of the Southern Ocean over the past 700 kyr. Paleoceanography 27.

Hoefs, M.J.L., Versteegh, G.J.M., Rijpstra, W.I.C., de Leeuw, J.W., Sinninghe Damsté, J.S., 1998. Postdepositional oxic degradation of alkenones: Implications for the measurement of palaeo sea surface temperatures. Paleoceanography 13, 42-49.

Hollis, C.J., Taylor, K.W.R., Handley, L., Pancost, R.D., Huber, M., Creech, J.B., Hines, B.R., Crouch, E.M., Morgans, H.E.G., Crampton, J.S., Gibbs, S., Pearson, P.N., Zachos, J.C., 2012. Early Paleogene temperature history of the Southwest Pacific Ocean: Reconciling proxies and models. Earth and Planetary Science Letters 349, 53–66.

Honjo, S., Doherty, K.W., 1988. Large aperture time-series sediment traps; design objectives, construction and application. Deep Sea Research Part A. Oceanographic Research Papers 35, 133-149.

Hopmans, E.C., Schouten, S., Pancost, R.D., van der Meer, M.T.J., Sinninghe Damsté, J.S., 2000. Analysis of intact tetraether lipids in archaeal cell material and sediments by high performance liquid chromatography/atmospheric pressure chemical ionization mass spectrometry. Rapid Communications in Mass Spectrometry 14, 585-589.

Hopmans, E.C., Schouten, S., Sinninghe Damsté, J.S., 2016. The effect of improved chromatography on GDGT-based palaeoproxies. Organic Geochemistry 93, 1-6.

Hopmans, E.C., Weijers, J.W.H., Schefuss, E., Herfort, L., Sinninghe Damsté, J.S., Schouten, S., 2004. A novel proxy for terrestrial organic matter in sediments based on branched and isoprenoid tetraether lipids. Earth and Planetary Science Letters 224, 107-116.

Huang, Y., Murray, M., Eglinton, G., Metzger, P., 1995. Sacredicene, a novel monocyclic C_{33} hydrocarbon from sediments of Sacred Lake, a tropical freshwater lake, Mount Kenya. Tetrahedron Letters 36, 5973-5976.

Huffman, G.J., Adler, R.F., Bolvin, D.T., Gu, G., Nelkin, E.J., Bowman, K.P., Hong, Y., Stocker, E.F., Wolff, D.B., 2007. The TRMM Multi-satellite Precipitation Analysis: Quasi- Global, Multi-Year, Combined-Sensor Precipitation Estimates at Fine Scale. J. Hydrometeor. 8 (1), 38-55.

Hughen, K.A., Overpeck, J.T., Lehman, S.J., Kashgarian, M., Southon, J., Peterson, L.C., Alley, R., Sigman, D.M., 1998. Deglacial changes in ocean circulation from an extended radiocarbon calibration. Nature 391, 65-68.

Hughen, K.A., Overpeck, J.T., Peterson, L.C., Anderson, R.F., 1996. The nature of varved sedimentation in the Cariaco Basin, Venezuela, and its palaeoclimatic significance. Geological Society, London, Special Publications 116, 171-183.

Huguet, C., Hopmans, E.C., Febo-Ayala, W., Thompson, D.H., Sinninghe Damsté, J.S., Schouten, S., 2006. An improved method to determine the absolute abundance of glycerol dibiphytanyl glycerol tetraether lipids. Organic Geochemistry 37, 1036-1041.

Huguet, C., Schimmelmann, A., Thunell, R., Lourens, L.J., Sinninghe Damsté, J.S., Schouten, S., 2007. A study of the TEX_{86} paleothermometer in the water column and sediments of the Santa Barbara Basin, California. Paleoceanography 22.

Hurley, S.J., Elling, F.J., Könneke, M., Buchwald, C., Wankel, S.D., Santoro, A.E., Lipp, J.S., Hinrichs, K.-U., Pearson, A., 2016. Influence of ammonia oxidation rate on thaumarchaeal lipid

composition and the TEX_{86} temperature proxy. Proceedings of the National Academy of Sciences of the United Stated of America 113, 7762-7767.

Hurley, S.J., Lipp, J.S., Close, H.G., Hinrichs, K.-U., Pearson, A., 2018. Distribution and export of isoprenoid tetraether lipids in suspended particulate matter from the water column of the Western Atlantic Ocean. Organic Geochemistry 116, 90-102.

Inglis, G.N., Farnsworth, A., Lunt, D., Foster, G.L., Hollis, C.J., Pagani, M., Jardine, P.E., Pearson, P.N., Markwick, P., Galsworthy, A.M.J., Raynham, L., Taylor, K.W.R., Pancost, R.D., 2015. Descent toward the Icehouse: Eocene sea surface cooling inferred from GDGT distributions. Paleoceanography 30, 1000-1020.

IPCC, 2014. Climate Change 2014: Synthesis Report. Contribution of Working Groups I, II and III to the Fifth Assessment Report of the Intergovernmental Panel on Climate Change [Core Writing Team, R.K. Pachauri and L.A. Meyer (eds.)]. IPCC, Geneva, Switzerland, 151 pp.

Jaeschke, A., Eickmann, B., Lang, S.Q., Bernasconi, S.M., Strauss, H., Fruh-Green, G.L., 2014. Biosignatures in chimney structures and sediment from the Loki's Castle low-temperature hydrothermal vent field at the Arctic Mid-Ocean Ridge. Extremophiles 18, 545–560.

Jenkyns, H.C., Schouten-Huibers, L., Schouten, S., Sinninghe Damsté, J.S., 2012. Warm Middle Jurassic-Early Cretaceous high-latitude sea-surface temperatures from the Southern Ocean. Climate of the Past 8, 215–226.

Jia, J., Han, D., Gerken, H.G., Li, Y., Sommerfeld, M., Hu, Q., Xu, J., 2015. Molecular mechanisms for photosynthetic carbon partitioning into storage neutral lipids in *Nannochloropsis oceanica* under nitrogen-depletion conditions. Algal Research-Biomass Biofuels and Bioproducts 7, 66-77.

Jiang, H.M., Gao, K.S., 2004. Effects of lowering temperature during culture on the production of polyunsaturated fatty acids in the marine diatom *Phaeodactylum tricornutum* (Bacillariophyceae). Journal of Phycology 40, 651-654.

Jiang, Y., Chen, F., 2000. Effects of temperature and temperature shift on docosahexaenoic acid production by the marine microalga *Crypthecodinium cohnii*. Journal of the American Oil Chemists Society 77, 613-617.

Jiang, S., O'Leary, T., Volkman, J.K., Zhang, H., Jia, R., Yu, S., Wang, Y., Luan, Z., Sun, Z., Jiang, R., 1994. Origins and simulated thermal alteration of sterols and keto-alcohols in deep-sea marine-sediments of the Okinawa Trough. Organic Geochemistry 21, 415-422.

Jonas, A.S., Schwark, L., Bauersachs, T., 2017. Late Quaternary water temperature variations of the Northwest Pacific based on the lipid paleothermometers TEX^{H}_{86}, $U^{K'}_{37}$ and LDI. Deep Sea Research Part I: Oceanographic Research Papers 125, 81-93.

Jordan, R.W., Priddle, J., 1991. Fossil members of the diatom genus *Proboscia*. Diatom Research 6, 55–61.

Jordan, R., Ito, R., 2002. Observations on *Proboscia* species from Late Cretaceous sediments, and their possible evolution from Kreagra. In: John, J. (Ed.), Proceedings of the 15th International Diatom Symposium, ARG Gantner Verlag KG Ruggell, Liechtenstein, pp. 313–329.

Jouanneau, J.M., Garcia, C., Oliveira, A., Rodrigues, A., Dias, J.A., Weber, O., 1998. Dispersal and deposition of suspended sediment on the shelf off the Tagus and Sado estuaries, SW Portugal. Progress in Oceanography 42, 233-257.

Kaiser, J., Lamy, F., 2010. Links between Patagonian Ice Sheet fluctuations and Antarctic dust variability during the last glacial period (MIS 4-2). Quaternary Science Reviews 29, 1464-1471.

Kaiser, J., Lamy, F., Hebbeln, D., 2005. A 70-kyr sea surface temperature record off southern Chile (Ocean Drilling Program Site 1233). Paleoceanography 20.

Kaiser, J., Schouten, S., Kilian, R., Arz, H.W., Lamy, F., Sinninghe Damsté, J.S., 2015. Isoprenoid and branched GDGT-based proxies for surface sediments from marine, fjord and lake environments in Chile. Org. Geochem. 89-90, 117-127.

Karner, M.B., DeLong, E.F., Karl, D.M., 2001. Archaeal dominance in the mesopelagic zone of the Pacific Ocean. Nature 409, 507-510.

Katsuki, K., Takahashi, K., Okada, M., 2003. Diatom assemblage and productivity changes during the last 340,000 years in the subarctic Pacific. Journal of Oceanography 59, 695-707.

Kim, J.-H., Buscail, R., Bourrin, F., Palanques, A., Sinninghe Damsté, J.S., Bonnin, J., Schouten, S., 2009a. Transport and depositional process of soil organic matter during wet and dry storms on the Têt inner shelf (NW Mediterranean). Paleogeography, Paleoclimatology, Paleoecology 273, 228-238.

Kim, J.-H., Crosta, X., Michel, E., Schouten, S., Duprat, J., Sinninghe Damsté, J.S., 2009b. Impact of lateral transport on organic proxies in the Southern Ocean. Quat. Res. 71, 246-250.

Kim, J.-H., Crosta, X., Willmott, V., Renssen, H., Bonnin, J., Helmke, P., Schouten, S., Sinninghe Damsté, J.S., 2012a. Holocene subsurface temperature variability in the eastern Antarctic continental margin. Geophysical Research Letters 39.

Kim, J.-H., Huguet, C., Zonneveld, K.A.F., Versteegh, G.J.M., Roeder, W., Sinninghe Damsté, J.S., Schouten, S., 2009c. An experimental field study to test the stability of lipids used for TEX_{86} and $U^{K'}_{37}$ palaeothermometry. Geochimica et Cosmochimica Acta 73, 2888-2898.

Kim, S.-T., O'Neil, J.R., 1997. Equilibrium and nonequilibrium oxygen isotope effects in synthetic carbonates. Geochimica et Cosmochimica Acta 61, 3461-3475.

Kim, J.-H., Romero, O.E., Lohmann, G., Donner, B., Laepple, T., Haam, E., Sinninghe Damsté, J.S., 2012b. Pronounced subsurface cooling of North Atlantic waters off Northwest Africa during Dansgaard–Oeschger interstadials. Earth and Planetary Science Letters 339-340, 95-102.

Kim, J.-H., Schneider, R.R., Hebbeln, D., Müller, P.J., Wefer, G., 2002. Last deglacial sea-surface temperature evolution in the Southeast Pacific compared to climate changes on the South American continent. Quaternary Science Reviews 21, 2085-2097.

Kim, J.-H., Schouten, S., Hopmans, E.C., Donner, B., Sinninghe Damsté, J.S., 2008. Global sediment core-top calibration of the TEX_{86} paleothermometer in the ocean. Geochimica et Cosmochimica Acta 72, 1154-1173.

Kim, J.-H., Schouten, S., Rodrigo-Gámiz, M., Rampen, S., Marino, G., Huguet, C., Helmke, P., Buscail, R., Hopmans, E.C., Pross, J., Sangiorgi, F., Middelburg, J.B.M., Sinninghe Damsté, J.S., 2015. Influence of deep-water derived isoprenoid tetraether lipids on the TEX^{H}_{86} paleothermometer in the Mediterranean Sea. Geochimica Et Cosmochimica Acta 150, 125-141.

Kim, J.-H., van der Meer, J., Schouten, S., Helmke, P., Willmott, V., Sangiorgi, F., Koc, N., Hopmans, E.C., Sinninghe Damsté, J.S., 2010. New indices and calibrations derived from the distribution of crenarchaeal isoprenoid tetraether lipids: Implications for past sea surface temperature reconstructions. Geochimica et Cosmochimica Acta 74, 4639-4654.

Kim, J.H., Villanueva, L., Zell, C., Sinninghe Damsté, J.S., 2016. Biological source and provenance of deep-water derived isoprenoid tetraether lipids along the Portuguese continental margin. Geochimica et Cosmochimica Acta 172, 177-204.

Klok, J., Cox, H.C., Deleeuw, J.W., Schenck, P.A., 1984. Loliolides and dihydroactinidiolide in a recent marine sediment probably indicate a major transformation pathway of carotenoids. Tetrahedron Letters 25, 5577-5580.

Knappy, C.S., Chong, J.P.J., Keely, B.J., 2009. Rapid Discrimination of Archaeal Tetraether Lipid Cores by Liquid Chromatography–Tandem Mass Spectrometry. Journal of the American Society for Mass Spectrometry 20, 51–59.

Knappy, C.S., Nunn, C.E.M., Morgan, H.W., Keely, B.J., 2011. The major lipid cores of the archaeon Ignisphaera aggregans: implications for the phylogeny and biosynthesis of glycerol monoalkyl glycerol tetraether isoprenoid lipids. Extremophiles 15, 517–528.

Knappy, C.S., Keely, B.J., 2012. Novel glycerol dialkanol triols in sediments: transformation products of glycerol dibiphytanyl glycerol tetraether lipids or biosynthetic intermediates? Chemical Communications 48, 841–843.

Knappy, C., Barillà, D., Chong, J., Hodgson, D., Morgan, H., Suleman, M., Tan, C., Yao, P., Keely, B., 2015. Mono-, di- and trimethylated homologues of isoprenoid tetraether lipid cores in archaea and environmental samples: mass spectrometric identification and significance. Journal of Mass Spectrometry 50, 1420–1432.

Koç, N., Labeyrie, L., Manthé, S., Flower, B.P., Hodell, D.A., Aksu, A., 2001. The last occurrence of *Proboscia curvirostris* in the North Atlantic marine isotope stages 9–8. Marine Micropaleontology 41, 9–23.

Koga, Y., Morii, H., 2005. Recent advances in structural research on ether lipids from archaea including comparative and physiological aspects. Bioscience Biotechnology and Biochemistry 69, 2019–2034.

Koga, Y., Morii, H., 2007. Biosynthesis of Ether-Type Polar Lipids in Archaea and Evolutionary Considerations. Microbiology and Molecular Biology Reviews 71, 97–120.

Koning, E., van Iperen, J.M., van Raaphorst, W., Helder, W., Brummer, G.J.A., van Weering, T.C.E., 2001. Selective preservation of upwelling-indicating diatoms in sediments off Somalia, NW Indian Ocean. Deep Sea Research Part I: Oceanographic Research Papers 48, 2473-2495.

Konneke, M., Bernhard, A.E., de la Torre, J.R., Walker, C.B., Waterbury, J.B., Stahl, D.A., 2005. Isolation of an autotrophic ammonia-oxidizing marine archaeon. Nature 437, 543-546.

Korte, L.F., Brummer, G.J.A., van der Does, M., Guerreiro, C.V., Hennekam, R., van Hateren, J.A., Jong, D., Munday, C.I., Schouten, S., Stuut, J.B.W., 2017. Downward particle fluxes of biogenic matter and Saharan dust across the equatorial North Atlantic. Atmos. Chem. Phys. 17, 6023-6040.

Kuypers, M.M.M., Blokker, P., Erbacher, J., Kinkel, H., Pancost, R.D., Schouten, S., Sinninghe Damsté, J.S., 2001. Massive expansion of marine archaea during a mid-Cretaceous oceanic anoxic event. Science 293, 92–94.

Lamy, F., Hebbeln, D., Rohl, U., Wefer, G., 2001. Holocene rainfall variability in southern Chile: a marine record of latitudinal shifts of the Southern Westerlies. Earth Planet. Sci. Lett. 185, 369-382.

Lamy, F., Hebbeln, D., Wefer, G., 1998. Late quaternary precessional cycles of terrigenous sediment input off the Norte Chico, Chile (27.5°S) and palaeoclimatic implications. Paleogeogr. Paleoclimatol. Paleoecol. 141, 233-251.

Lamy, F., Hebbeln, D., Wefer, G., 1999. High-resolution marine record of climatic change in mid-latitude Chile during the last 28,000 years based on terrigenous sediment parameters. Quat. Res. 51, 83-93.

Lamy, F., Kaiser, J., Ninnemann, U., Hebbeln, D., Arz, H.W., Stoner, J., 2004. Antarctic timing of surface water changes off Chile and Patagonian ice sheet response. Science 304, 1959-1962.

Lamy, F., Ruhlemann, C., Hebbeln, D., Wefer, G., 2002. High- and low-latitude climate control on the position of the southern Peru-Chile Current during the Holocene. Paleoceanography 17.

Lange, C.B., Romero, O.E., Wefer, G., Gabric, A.J., 1998. Offshore influence of coastal upwelling off Mauritania, NW Africa, as recorded by diatoms in sediment traps at 2195 m water depth. Deep Sea Research Part I: Oceanographic Research Papers 45, 985-1013.

Lattaud, J., Dorhout, D., Schulz, H., Castañeda, I.S., Schefuß, E., Sinninghe Damsté, J.S., Schouten, S., 2017b. The C_{32} alkane-1,15-diol as a proxy of late Quaternary riverine input in coastal margins. Climate of the Past 13, 1049-1061.

Lattaud, J., Kirkels, F., Peterse, F., Freymond, C.V., Eglinton, T.I., Hefter, J., Mollenhauer, G., Balzano, S., Villanueva, L., van der Meer, M.T.J., Hopmans, E.C., Sinninghe Damsté, J.S., Schouten, S., 2018a. Long-chain diols in rivers: distribution and potential biological sources. Biogeosciences 15, 4147-4161.

Lattaud, J., Kim, J.-H., de Jonge, C., Zell, C., Sinninghe Damsté, J.S., Schouten, S., 2017a. The C_{32} alkane-1,15-diol as a tracer for riverine input in coastal seas. Geochimica et Cosmochimica Acta 202, 146-158.

Lattaud, J., Lo, L., Huang, J.-J., Chou, Y.-M., Gorbarenko, S.A., Sinninghe Damsté, J.S., Schouten, S., 2018b. A Comparison of Late Quaternary Organic Proxy-Based Paleotemperature Records of the Central Sea of Okhotsk. Paleoceanography and Paleoclimatology 33, 732-744.

Lee, K.E., Kim, J.-H., Wilke, I., Helmke, P., Schouten, S., 2008. A study of the alkenone, TEX_{86}, and planktonic foraminifera in the Benguela Upwelling System: Implications for past sea surface temperature estimates. Geochemistry Geophysics Geosystems 9.

Lee, T., Lagerloef, G., Gierach, M.M., Kao, H.-Y., Yueh, S., Dohan, K., 2012. Aquarius reveals salinity structure of tropical instability waves, Geophys. Res. Lett., 39, L12610.

Lefevre, N., Moore, G., Aiken, J., Watson, A., Cooper, D., 1998. Variability of pCO_2 in the tropical Atlantic in 1995. Journal of Geophysical Research C3, 5623-5634.

Levitus, S., Burgett, R., and Boyer, T. B., 1994. World Ocean Atlas 1994, vol. 3, Nutrients, NOAA, U.S. Dept. of Comm., Washington, D. C.

Li, J., Han, D., Wang, D., Ning, K., Jia, J., Wei, L., Jing, X., Huang, S., Chen, J., Li, Y., Hu, Q., Xu, J., 2014. Choreography of transcriptomes and lipidomes of *Nannochloropsis* reveals the mechanisms of oil synthesis in microalgae. Plant Cell 26, 1645-1665.

Lincoln, S.A., Bradley, A.S., Newman, S.A., Summons, R.E., 2013. Archaeal and bacterial glycerol dialkyl glycerol tetraether lipids in chimneys of the Lost City Hydrothermal Field. Organic Geochemistry 60, 45–53.

Linnert, C., Robinson, S.A., Lees, J.A., Bown, P.R., Pérez-Rodríguez, I., Petrizzo, M.R., Falzoni, F., Littler, K., Arz, J.A., Russell, E.E., 2014. Evidence for global cooling in the Late Cretaceous. Nature Communications 5.

Lisiecki, L. E. and Raymo, M. E., 2005. A Pliocene-Pleistocene stack of 57 globally distributed benthic $\delta^{18}O$ records, Paleoceanography, 20.

Littler, K., Robinson, S.A., Bown, P.R., Nederbragt, A.J., Pancost, R.D., 2011. High sea-surface temperatures during the Early Cretaceous Epoch. Nature Geoscience 4, 169–172.

Liu, Z.H., Pagani, M., Zinniker, D., DeConto, R., Huber, M., Brinkhuis, H., Shah, S.R., Leckie, R.M., Pearson, A., 2009. Global Cooling During the Eocene-Oligocene Climate Transition. Science 323, 1187–1190.

Liu, X.-L., Lipp, J.S., Schröder, J.M., Summons, R.E., Hinrichs, K.-U., 2012a. Isoprenoid glycerol dialkanol diethers: A series of novel archaeal lipids in marine sediments. Organic Geochemistry 43, 50–55.

Liu, X.-L., Lipp, J.S., Simpson, J.H., Lin, Y.-S., Summons, R.E., Hinrichs, K.-U., 2012b. Mono- and dihydroxyl glycerol dibiphytanyl glycerol tetraethers in marine sediments: Identification of both core and intact polar lipid forms. Geochimica et Cosmochimica Acta 89, 102–115.

Liu, X.L., Summons, R.E., Hinrichs, K.-U., 2012c. Extending the known range of glycerol ether lipids in the environment: structural assignments based on tandem mass spectral fragmentation patterns. Rapid Communications in Mass Spectrometry 26, 2295–2302.

Liu, X.L., Birgel, D., Elling, F.J., Sutton, P.A., Lipp, J.S., Zhu, R., Zhang, C., Könneke, M., Peckmann, J., Rowland, S.J., Summons, R.E., Hinrichs, K.-U., 2016. From ether to acid: A plausible degradation pathway of glycerol dialkyl glycerol tetraethers. Geochimica Et Cosmochimica Acta 183, 138-152.

Ljung, G. M., & Box, G. E., 1978. On a measure of lack of fit in time series models. Biometrika, 65(2), 297-303.

Locarnini R. A., Mishonov A. V., Antonov J. I., Boyer T. P., Garcia H. E., Baranova O. K., Zweng M. M., Paver C. R., Reagan J. R., Johnson D. R., Hamilton M., Seidov D., 2013. World Ocean Atlas 2013, Volume 1: temperature. Levitus S, Ed.; Mishonov A, Technical Ed.; NOAA Atlas NESDIS 73, 40 pp.

Longo, W.M., Dillon, J.T., Tarozo, R., Salacup, J.M., Huang, Y.S., 2013. Unprecedented separation of long chain alkenones from gas chromatography with a poly(trifluoropropylmethylsiloxane) stationary phase. Organic Geochemistry 65, 94-102.

Lopes dos Santos, R.A., Prange, M., Castañeda, I.S., Schefuß, E., Mulitza, S., Schulz, M., Niedermeyer, E.M., Sinninghe Damsté, J.S., Schouten, S., 2010. Glacial-interglacial variability in Atlantic meridional overturning circulation and thermocline adjustments in the tropical North Atlantic. Earth and Planetary Science Letters 300, 407-414.

Lopes dos Santos, R.A., Spooner, M.I., Barrows, T.T., De Deckker, P., Sinninghe Damsté, J.S., Schouten, S., 2013. Comparison of organic ($U^{K'}_{37}$, TEX^{H}_{86}, LDI) and faunal proxies (foraminiferal assemblages) for reconstruction of late Quaternary sea surface temperature variability from offshore southeastern Australia. Paleoceanography 28, 377-387.

Lopes dos Santos, R.A.L., Wilkins, D., De Deckker, P., Schouten, S., 2012. Late Quaternary productivity changes from offshore Southeastern Australia: A biomarker approach. Paleogeogr. Paleoclimatol. Paleoecol. 363, 48-56.

Lopezescobar, L., Frey, F.A., Vergara, M., 1977. Andesites and high-alumina basalts from central south Chile high Andes – geochemical evidence bearing on their petrogenesis. Contrib. Mineral. Petrol. 63, 199-228.

Loureiro, J.J.M., Macedo, M.E., 1986. Bacia Hidrografica do Rio Tejo. Monografias Hidrologicas dos Principais Cursos de Agua de Portugal continental, Servico Hidraulico (DGRAH), Lisbon, 281-335.

Loureiro, J.J., Machado, M.L., Macedo, M.E., Nunes, M.N., Botelho, O.F., Sousa, M.L., Almeida, M.C., Martins, J.C., 1986. Direcção Geral dos Serviços Hidraulicos. Monografias hidrológi¬cas dos principais cursos de água de Portugal Continental., Lisboa, p. 569.

Lü, X.X., Liu, X.L., Elling, F.J., Yang, H., Xie, S.C., Song, J.M., Li, X.G., Yuan, H.M., Li, N., Hinrichs, K.-U., 2015. Hydroxylated isoprenoid GDGTs in Chinese coastal seas and their potential as a paleotemperature proxy for mid-to-low latitude marginal seas. Organic Geochemistry 89-90, 31-43.

Luo, G., Yang, H., Algeo, T.J., Hallmann, C., Xie, S., 2018. Lipid biomarkers for the reconstruction of deep-time environmental conditions. Earth-Science Reviews.

Lutjeharms, J. R. E., 2006. The Agulhas Current, 330 pp., Springer, Berlin.

Malauene, B.S., Shillington, F.A., Roberts, M.J., Moloney, C.L., 2014. Cool, elevated chlorophyll-a waters off northern Mozambique. Deep-Sea Research Part Ii-Topical Studies in Oceanography 100, 68-78.

Marchant, M., Hebbeln, D., Wefer, G., 1999. High resolution planktic foraminiferal record of the last 13,300 years from the upwelling area off Chile. Mar. Geol. 161, 115-128.

Marie, D., Partensky, F., Vaulot, D., Brussaard, C., 2001. Enumeration of phytoplankton, bacteria, and viruses in marine samples, Current protocols in cytometry John Wiley & Sons, New York.

Marlowe, I.T., Brassell, S.C., Eglinton, G., Green, J.C., 1984a. Long chain unsaturated ketones and esters in living algae and marine sediments. Org. Geochem. 6, 135-141.

Marlowe, I.T., Green, J.C., Neal, A.C., Brassell, S.C., Eglinton, G., Course, P.A., 1984b. Long-Chain (n-C_{37}–C_{39}) alkenones in the Prymnesiophyceae. Distribution of alkenones and other lipids and their taxonomic significance. British Phycological Journal 19, 203-216.

Martin, M.W., Kato, T.T., Rodriguez, C., Godoy, E., Duhart, P., McDonough, M., Campos, A., 1999. Evolution of the late Paleozoic accretionary complex and overlying forearc-magmatic arc, south central Chile (38°–41°S): Constraints for the tectonic setting along the southwestern margin of Gondwana. Tectonics 18, 582-605.

Martinez-Roldan, A.J., Perales-Vela, H.V., Canizares-Villanueva, R.O., Torzillo, G., 2014. Physiological response of *Nannochloropsis* sp. to saline stress in laboratory batch cultures. Journal of Applied Phycology 26, 115-121.

Martin, J.H., Fitzwater, S.E., 1988. Iron-deficiency limits phytoplankton growth in the Northeast Pacific Subarctic. Nature 331, 341-343.

Martins, C.S., Hamann, M., Fiuza, A.F.G., 2002. Surface circulation in the eastern North Atlantic, from drifters and altimetry. Journal of Geophysical Research 107, 3217.

Mazeika, P.A., 1967. Thermal domes in the Eastern Tropical Atlantic Ocean. Limnology and Oceanography 12, 537-539.

McCave, I.N., 1972. Transport and escape of fine-grained sediment from shelf areas. In: Swift, D. J. P., Duane, D. B., Pilkey, O. H. (Eds). Shelf sediment transport: processes and patterns. Stroudsburg, PA: Dowden, Hutchinson & Ross, pp 225-248.

McKersie, B.D., Leshem, Y.Y., 1995. Oxidative stress, in: McKersie, B.D., Leshem, Y.Y. (Eds.), Stress and Stress Coping in Cultivated Plants, pp. 15-54.

McManus, J.F., Oppo, D.W., Cullen, J.L., 1999. A 0.5-million-year record of millennial-scale climate variability in the North Atlantic. Science 283, 971-975.

McManus, J. F., Oppo, D. W., Cullen, J. L., Healey, S. L., 2003. Marine Isotope Stage 11 (MIS 11): Analog for Holocene and future climate? In "Geophysical Monograph 137, Earth's Climate and Orbital Eccentricity: The Marine Isotope Stage 11 Question." (A. Droxler, R. Poore, L. Burckle, and L. Osterman, Eds.), pp. 69-85. AGU.

McManus, J.F., Oppo, D.W., Keigwin, L.D., Cullen, J.L., Bond, G.C., 2002. Thermohaline circulation and prolonged interglacial warmth in the North Atlantic. Quat. Res. 58, 17-21.

Meador, T.B., Zhu, C., Elling, F.J., Könneke, M., Hinrichs, K.-U., 2014. Identification of isoprenoid glycosidic glycerol dibiphytanol diethers and indications for their biosynthetic origin. Organic Geochemistry 69, 70-75.

Méjanelle, L., Sanchez-Gargallo, A., Bentaleb, I., Grimalt, J.O., 2003. Long chain *n*-alkyl diols, hydroxy ketones and sterols in a marine eustigmatophyte, *Nannochloropsis gaditana*, and in *Brachionus plicatilis* feeding on the algae. Organic Geochemistry 34, 527-538.

Meyers, P.A., 1997. Organic geochemical proxies of paleoceanographic, paleolimnologic, and paleoclimatic processes. Organic Geochemistry 27, 213-250.

Miller, K. G., Sugarman, P. J., Browning, J. V., Olsson, R. K., Pekar, S. F., Reilly, T. J., Cramer, B.S., Aubry, M.-P., Lawrence, R.P., Curran, J., Stewart, M., Metzger, J.M., Uptegrove, J., Bukry, D., Burckle, L.H., Wright, J.D., Feigenson, M.D., Brenner, G.J., Dalton, R.F., 1998. Bass River Site. Proceedings of the Ocean Drilling Program, Initial Reports, 915 Vol. 174AX: College Station, TX (Ocean Drilling Program).

Mitra, M., Patidar, S.K., George, B., Shaha, F., Mishra, S., 2015. A euryhaline Nannochloropsis gaditana with potential for nutraceutical (EPA) and biodiesel production. Algal Research-Biomass Biofuels and Bioproducts 8, 161-167.

Mix, A.C., Tiedemann, R., Blum, P., et al., 2003. Proc. ODP, Init. Repts., 202: College Station, TX (Ocean Drilling Program).. doi:10.2973/odp.proc.ir.202.2003.

Mohtadi, M., Hebbeln, D., 2004. Mechanisms and variations of the paleoproductivity off northern Chile (24°S–33°S) during the last 40,000 years. Paleoceanography 19.

Mohtadi, M., Rossel, P., Lange, C.B., Pantoja, S., Boning, P., Repeta, D.J., Grunwald, M., Lamy, F., Hebbeln, D., Brumsack, H.J., 2008. Deglacial pattern of circulation and marine productivity in the upwelling region off central-south Chile. Earth Planet. Sci. Lett. 272, 221-230.

Moita, M.T., Oliveira, P.B., Mendes, J.C., Palma, A.S., 2003. Distribution of chlorophyll a and *Gymnodinium catenatum* associated with coastal upwelling plumes off central Portugal. Acta Oecologica 24, S125-S132.

Mollenhauer, G., Eglinton, T.I., Hopmans, E.C., Sinninghe Damsté, J.S., 2008. A radiocarbon-based assessment of the preservation characteristics of crenarchaeol and alkenones from continental margin sediments. Org. Geochem. 39, 1039–1045.

Morii, H., Eguchi, T., Nishihara, M., Kakinuma, K., König, H., Koga, Y., 1998. A novel ether core lipid with H-shaped C80-isoprenoid hydrocarbon chain from the hyperthermophilic methanogen Methanothermus fervidus. Biochimica Et Biophysica Acta - Lipids and Lipid Metabolism 1390, 339–345.

Morris, R.J., Brassell, S.C., 1988. Long-chain alkanediols: biological markers for cyanobacterial contributions to sediments. Lipids 23, 256-258.

Mougenot, D., 1988. Géologie de la marge portugaise. These Doct. d'Etat. Univ. Paris VI.

Muller-Karger, F.E., McClain, C.R., Richardson, P.L., 1988. The dispersal of the Amazon´s water. Nature 333, 56-59.

Muller-Karger, F.E., Richardson, P.L., McGillicuddy, D., 1995. On the offshore dispersal of the Amazon´s Plume in the North Atlantic: Comments on the paper by A. Longhurst, "Seasonal cooling and blooming in tropical oceans". Deep-Sea Research I 42, 2127-2137.

Muller-Karger, F., Varela, R., Thunell, R., Astor, Y., Zhang, H.Y., Luerssen, R., Hu, C.M., 2004. Processes of coastal upwelling and carbon flux in the Cariaco Basin. Deep-Sea Research Part Ii-Topical Studies in Oceanography 51, 927-943.

Muller-Karger, F., Varela, R., Thunell, R., Scranton, M., Bohrer, R., Taylor, G., Capelo, J., Astor, Y., Tappa, E., Ho, T.Y., Walsh, J.J., 2001. Annual cycle of primary production in the Cariaco Basin: Response to upwelling and implications for vertical export. Journal of Geophysical Research-Oceans 106, 4527-4542

Müller, P.J., Fischer, G., 2001. A 4-year sediment trap record of alkenones from the filamentous upwelling region off Cape Blanc, NW Africa and a comparison with distributions in underlying sediments. Deep-Sea Research Part I-Oceanographic Research Papers 48, 1877-1903.

Müller, P.J., Kirst, G., Ruhland, G., von Storch, I., Rosell-Melé, A., 1998. Calibration of the alkenone paleotemperature index $U^{K'}_{37}$ based on core-tops from the eastern South Atlantic and the global ocean (60°N-60°S). Geochimica et Cosmochimica Acta 62, 1757-1772.

Muratli, J.M., Chase, Z., Mix, A.C., McManus, J., 2009. Increased glacial-age ventilation of the Chilean margin by Antarctic Intermediate Water. Nature Geoscience 3, 23.

Muratli, J.M., Chase, Z., McManus, J., Mix, A., 2010. Ice-sheet control of continental erosion in central and southern Chile (36°–41°S) over the last 30,000 years. Quaternary Science Reviews 29, 3230-3239.

Naafs, B.D.A., Hefter, J., Stein, R., 2012. Application of the long chain Diol Index (LDI) paleothermometer to the early Pleistocene (MIS 96). Organic Geochemistry 49, 83-85.

NASA Aquarius project, 2015a. Aquarius Official Release Level 3 Sea Surface Salinity Standard Mapped Image Daily Data V4.0. Ver. 4.0. PO.DAAC, CA, USA.

NASA Aquarius project, 2015b Aquarius Official Release Level 3 Wind Speed Standard Mapped Image Daily Data V4.0. Ver. 4.0. PO.DAAC, CA, USA, 2015b.

Nehring, D., Hagen, E., Jorge da Silva, A., Schemainda, R., Wolf, G., Michelchen, N., Kaiser, W., Postel, L., Gosselk, F., Brenning, U., 1984. The oceanological conditions in the western part of the Mozambique Channel in February-March 1980.

Nieto-Moreno, V., Martínez-Ruiz, F., Gallego-Torres, D., Giralt, S., García-Orellana, J., Masqué, P., Sinninghe Damsté, J.S., Ortega-Huertas, M., 2015. Palaeoclimate and palaeoceanographic conditions in the westernmost Mediterranean over the last millennium: an integrated organic and inorganic approach. Journal of the Geological Society 172, 264-271.

Nürnberg, D., Bijma, J., Hemleben, C., 1996. Assessing the reliability of magnesium in foraminiferal calcite as a proxy for water mass temperatures. Geochimica et Cosmochimica Acta 60, 803-814.

Oba, M., Sakata, S., Tsunogai, U., 2006. Polar and neutral isopranyl glycerol ether lipids as biomarkers of archaea in near-surface sediments from the Nankai Trough. Organic Geochemistry 37, 1643-1654.

O'Brien, C.L., Robinson, S.A., Pancost, R.D., Sinninghe Damsté, J.S., Schouten, S., Lunt, D.J., Alsenz, H., Bomemann, A., Bottini, C., Brassell, S.C., Farnsworth, A., Forster, A., Huber, B.T., Inglis, G.N., Jenkyns, H.C., Linnert, C., Littler, K., Markwick, P., McAnena, A., Mutterlose, J., Naafs, B.D.A., Puttmann, W., Sluijs, A., van Helmond, N., Vellekoop, J., Wagner, T., Wrobel, N.E., 2017. Cretaceous sea-surface temperature evolution: Constraints from TEX_{86} and planktonic foraminiferal oxygen isotopes. Earth-Science Reviews 172, 224-247.

Ohkouchi, N., Eglinton, T.I., Keigwin, L.D., Hayes, J.M., 2002. Spatial and temporal offsets between proxy records in a sediment drift. Science 298, 1224–1227.

Olofsson, M., Lamela, T., Nilsson, E., Berge, J.P., del Pino, V., Uronen, P., Legrand, C., 2012. Seasonal variation of lipids and fatty acids of the microalgae *Nannochloropsis oculata* grown in outdoor large-scale photobioreactors. Energies 5, 1577-1592.

Pagani, M., 2014. 12.13 - Biomarker-Based Inferences of Past Climate: The Alkenone pCO_2 Proxy. A2 – Holland, Heinrich D. In: Turekian, K.K. (Ed.), Treatise on Geochemistry (Second Edition). Elsevier, Oxford, pp. 361-378.

Pal, D., Khozin-Goldberg, I., Cohen, Z., Boussiba, S., 2011. The effect of light, salinity, and nitrogen availability on lipid production by *Nannochloropsis* sp. Applied Microbiology and Biotechnology 90, 1429-1441.

Pancost, R.D., Boot, C.S., Aloisi, G., Maslin, M., Bickers, C., Ettwein, V., Bale, N., Handley, L., 2009. Organic geochemical changes in Pliocene sediments of ODP Site 1083 (Benguela Upwelling System). Paleogeogr. Paleoclimatol. Paleoecol. 280, 119-131.

Pearson, A., McNichol, A.P., Benitez-Nelson, B.C., Hayes, J.M., Eglinton, T.I., 2001. Origins of lipid biomarkers in Santa Monica Basin surface sediment: A case study using compound-specific $\delta^{14}C$ analysis. Geochimica et Cosmochimica Acta 65, 3123-3127.

Peeters, F.J.C., Acheson, R., Brummer, G.J.A., de Ruijter, W.P.M., Schneider, R.R., Ganssen, G.M., Ufkes, E., Kroon, D., 2004. Vigorous exchange between the Indian and Atlantic oceans at the end of the past five glacial periods. Nature 430, 661-665.

Peterson, L.C., Overpeck, J.T., Kipp, N.G., Imbrie, J., 1991. A high-resolution Late Quaternary upwelling record from the anoxic Cariaco Basin. Paleoceanography 6, 99-119.

Pitcher, A., Hopmans, E.C., Mosier, A.C., Park, S.-J., Rhee, S.-K., Francis, C.A., Schouten, S., Sinninghe Damsté, J.S., 2011. Core and Intact Polar Glycerol Dibiphytanyl Glycerol Tetraether Lipids of Ammonia-Oxidizing Archaea Enriched from Marine and Estuarine Sediments. Applied and Environmental Microbiology 77, 3468–3477.

Pitcher, A., Hopmans, E.C., Schouten, S., Sinninghe Damsté, J.S., 2009. Separation of core and intact polar archaeal tetraether lipids using silica columns: Insights into living and fossil biomass contributions. Organic Geochemistry 40, 12-19.

Plancq, J., Grossi, V., Henderiks, J., Simon, L., Mattioli, E., 2012. Alkenone producers during late Oligocene-early Miocene revisited. Paleoceanography 27, PA1202.

Plancq, J., Grossi, V., Pittet, B., Huguet, C., Rosell-Melé, A., Mattioli, E., 2015. Multi-proxy constraints on sapropel formation during the late Pliocene of central Mediterranean (southwest Sicily). Earth and Planetary Science Letters 420, 30-44.

Plancq, J., Mattioli, E., Pittet, B., Simon, L., Grossi, V., 2014. Productivity and sea-surface temperature changes recorded during the late Eocene-early Oligocene at DSDP Site 511 (South Atlantic). Palaeogeography, Palaeoclimatology, Palaeoecology 407, 34–44.

Prahl, F.G., Dymond, J., Sparrow, M.A., 2000. Annual biomarker record for export production in the central Arabian Sea. Deep-Sea Research II 47, 1581-1604.

Prahl, F.G., Muehlhausen, L.A., 1989. Lipid biomarkers as geochemical tools for paleoceanographic study. John Wiley.

Prahl, F.G., Muehlhausen, L.A., Zahnle, D.B., 1988. Further evaluation of long-chain alkenones as indicators of paleoceanographic conditions. Geochimica et Cosmochimica Acta 52, 2303-2310.

Prahl, F.G., Wakeham, S.G., 1987. Calibration of unsaturation patterns in long-chain ketone compositions for palaeotemperature assessment. Nature 330, 367-369.

Pribyl, P., Elias, M., Cepak, V., Lukavsky, J., Kastanek, P., 2012. Zoosporogenesis, morphology, ultrastructure, pigment composition, and phylogenetic position of *Trachydiscus minutus* (Eustigmatophyceae, Heterokontophyta) Journal of Phycology 48, 231-242.

Pujos-Lamy, A., 1977. Essai d'établissement d'une biostratigraphie du nannoplancton calcaire dans le Pleistocéne de l'Atlantique Nord-oriental. Boreas 6, 323–331.

Qin, W., Carlson, L.T., Armbrust, E.V., Devol, A.H., Moffett, J.W., Stahl, D.A., Ingalls, A.E., 2015. Confounding effects of oxygen and temperature on the TEX_{86} signature of marine Thaumarchaeota. Proceedings of the National Academy of Sciences of the United States of America 112, 10979-10984.

Raffi, I., Backman, J., Fornaciari, E., Palike, H., Rio, D., Lourens, L.J., Hilgen, F., 2006. A review of calcareous nannofossil astrobiochronology encompassing the past 25 million years. Quaternary Science Reviews 25, 3113–3137.

Rampen, S.W., Datema, M., Rodrigo-Gámiz, M., Schouten, S., Reichart, G.-J., Sinninghe Damsté, J.S., 2014b. Sources and proxy potential of long chain alkyl diols in lacustrine environments. Geochimica Et Cosmochimica Acta 144, 59-71.

Rampen, S.W., Schouten, S., Koning, E., Brummer, G.J.A., Sinninghe Damsté, J.S., 2008. A 90 kyr upwelling record from the northwestern Indian Ocean using a novel long-chain Diol Index. Earth and Planetary Science Letters 276, 207-213.

Rampen, S.W., Schouten, S., Schefuss, E., Sinninghe Damsté, J.S., 2009. Impact of temperature on long chain diol and mid-chain hydroxy methyl alkanoate composition in *Proboscia* diatoms: Results from culture and field studies. Organic Geochemistry 40, 1124-1131.

Rampen, S.W., Schouten, S., Sinninghe Damsté, J.S., 2011. Occurrence of long chain 1,14-diols in *Apedinella radians*. Organic Geochemistry 42, 572-574.

Rampen, S.W., Schouten, S., Wakeham, S.G., Sinninghe Damsté, J.S., 2007. Seasonal and spatial variation in the sources and fluxes of long chain diols and mid-chain hydroxy methyl alkanoates in the Arabian Sea. Organic Geochemistry 38, 165-179.

Rampen, S.W., Willmott, V., Kim, J.H., Rodrigo-Gámiz, M., Uliana, E., Mollenhauer, G., Schefuss, E., Sinninghe Damsté, J.S., Schouten, S., 2014a. Evaluation of long chain 1,14-alkyl diols in marine sediments as indicators for upwelling and temperature. Organic Geochemistry 76, 39-47.

Rampen, S.W., Willmott, V., Kim, J.H., Uliana, E., Mollenhauer, G., Schefuss, E., Sinninghe Damsté, J.S., Schouten, S., 2012. Long chain 1,13-and 1,15-diols as a potential proxy for palaeotemperature reconstruction. Geochimica Et Cosmochimica Acta 84, 204-216.

Reiche, S., Rampen, S.W., Dorhout, D.J.C., Sinninghe Damsté, J.S., Schouten, S., 2018. The impact of oxygen exposure on long-chain alkyl diols and the long chain Diol Index (LDI) – a long-term incubation study. Organic Geochemistry 124, 238-246.

Repeta, D.J., 1989. Carotenoid diagenesis in recent marine sediments: II. Degradation of fucoxanthin to loliolide. Geochimica Et Cosmochimica Acta 53, 699-707.

Richards, F. A., 1975. The Cariaco Basin (Trench). Oceanogr. Mar. Biol. Ann. Rev. 13: 11–67.

Richardson, P.L., Reverdin, G., 1987. Seasonal cycle of velocity in the Atlantic North Equatorial Countercurrent as measured by surface drifters, current meters, and ship drifts. Journal of Geophysical Research-Oceans 92, 3691-3708.

Ridderinkhof, H., van der Werf, P.M., Ullgren, J.E., van Aken, H.M., van Leeuwen, P.J., de Ruijter, W.P.M., 2010. Seasonal and interannual variability in the Mozambique Channel from moored current observations. Journal of Geophysical Research-Oceans 115.

Riegman, R., deBoer, M., Domis, L.D., 1996. Growth of harmful marine algae in multispecies cultures. Journal of Plankton Research 18, 1851-1866.

Rieley, G., 1994. Derivatization of organic-compounds prior to gas-chromatographic combustion-isotope ratio mass-spectrometric analysis - identification of isotope fractionation processes. Analyst 199, 915-919.

Robinson, N., Cranwell, P.A., Eglinton, G., Brassell, S.C., Sharp, C.L., Gophen, M., Pollingher, U., 1986. Lipid geochemistry of Lake Kinneret. Org. Geochem 10, 733-742.

Robinson, S.A., Ruhl, M., Astley, D.L., Naafs, B.D.A., Farnsworth, A.J., Bown, P.R., Jenkyns, H.C., Lunt, D.J., O'Brien, C., Pancost, R.D., Markwick, P.J., 2017. Early Jurassic North Atlantic sea-surface temperatures from TEX86 palaeothermometry. Sedimentology 64, 215–230.

Rodrigo-Gámiz, M., Martinez-Ruiz, F., Rampen, S., Schouten, S., Sinninghe Damsté, J., 2014. Sea surface temperature variations in the western Mediterranean Sea over the last 20 kyr: A dual-organic proxy ($U^{K'}_{37}$ and LDI) approach. Paleoceanography 29, 87-98.

Rodrigo-Gámiz, M., Rampen, S.W., de Haas, H., Baas, M., Schouten, S., Sinninghe Damsté, J.S., 2015. Constraints on the applicability of the organic temperature proxies $U^{K'}_{37}$, TEX_{86} and LDI in the subpolar region around Iceland. Biogeosciences 12, 6573-6590.

Rodrigo-Gámiz, M., Rampen, S.W., Schouten, S., Sinninghe Damsté, J.S., 2016. The impact of oxic degradation on long chain alkyl diol distributions in Arabian Sea surface sediments. Organic Geochemistry 100, 1-9.

Rodrigues, A., Matos, M. (1994). Distribuçao sedimentar do plataforma continentale portuguese entre Sines e Ericeira. 1st Symposio Margem Continental Iberica Atlantica. Abstract, 48.

Romero, O., Hebbeln, D., 2003. Biogenic silica and diatom *thanatocoenosis* in surface sediments below the Peru-Chile Current: controlling mechanisms and relationship with productivity of surface waters. Marine Micropaleontology 48, 71-90.

Romero, O.E., Hebbeln, D., Wefer, G., 2001. Temporal and spatial variability in export production in the SE Pacific Ocean: evidence from siliceous plankton fluxes and surface sediment assemblages. Deep-Sea Res. Part I-Oceanogr. Res. Pap. 48, 2673-2697.

Romero O. E., Lange C. B., Fischer G., Treppke U. F., Wefer G., 1999. Variability in Export Production Documented by Downward Fluxes and Species Composition of Marine Planktic Diatoms: Observations from the Tropical and Equatorial Atlantic. In: Fischer G., Wefer G. (eds) Use of Proxies in Paleoceanography. Springer, Berlin, Heidelberg.

Romero-Viana, L., Kienel, U., Sachse, D., 2012. Lipid biomarker signatures in a hypersaline lake on Isabel Island (Eastern Pacific) as a proxy for past rainfall anomaly (1942-2006 AD). Paleogeography, Paleoclimatology, Paleoecology 350, 49-61.

Romero-Viana, L., Kienel, U., Wilkes, H., Sachse, D., 2013. Growth-dependent hydrogen isotopic fractionation of algal lipid biomarkers in hypersaline Isabel Lake (México). Geochimica Et Cosmochimica Acta 106, 490-500.

Rontani, J.F., Marty, J.C., Miquel, J.C., Volkman, J.K., 2006a. Free radical oxidation (autoxidation) of alkenones and other microalgal lipids in seawater. Organic Geochemistry 37, 354-368.

Rontani, J.F., Prahl, F.G., Volkman, J.K., 2006b. Characterization of unusual alkenones and alkyl alkenoates by electron ionization gas chromatography/mass spectrometry. Rapid Communications in Mass Spectrometry 20, 583-588.

Rosell-Melé, A., Emeis, K.-C., Grimalt, J.O., Müller, P., Schneider, R., Bouloubassi, I., Epstein, B.L., Fahl, K., Fluegge, A., Freeman, K., Goñi, M., Günter, U., Hartz, d., Hellebust, S., Herbert, T., Ikehara, M., Ishiwatari, R., Kawamura, K., Kenig, F., de Leeuw, J.W., Lehman, S.J., Méjanelle, L., Onkouchi, N., Pancost, R.D., Pelejero, C., Prahl, F., Quinn, J.G., Rontani, J.-F., Rostek, F., Rullkötter, J., Sachs, J.P., Blanz, T., Sawada, K., Schulz-Bull, D.E., Sikes, E.L., Sonzogni, C., Ternois, Y., Versteegh, G.J.M., Volkman, J.K., Wakeham, S.G., 2001. Precision of the current methods to measure the alkenone proxy $U^{K'}_{37}$ and the absolute alkenone abundance in sediments: Results of an interlaboratory comparison study. Geochemistry Geophysics Geosystems 2, 1-28.

Rosell-Melé, A., Carter, J.F., Parry, A.T., Eglinton, G., 1995. Determination of the $U^{K'}_{37}$ index in geological samples. Analytical Chemistry 67, 1283-1289.

Rosenthal, Y., Boyle, E.A., Slowey, N., 1997. Temperature control on the incorporation of magnesium, strontium, fluorine, and cadmium into benthic foraminiferal shells from Little Bahama Bank: Prospects for thermocline paleoceanography. Geochimica Et Cosmochimica Acta 61, 3633-3643.

Rossignol, M., and Meyruis, A.M., 1964. Campagnes océanographiques du Gérard-Tréca, 53 pp., Cent. Oceanogr. Dakar-Thiaroye, ORSTOM, Dakar, Senegal.

Rostek, F., Bard, E., Beaufort, L., Sonzogni, C., Ganssen, G., 1997. Sea surface temperature and productivity records for the past 240 kyr in the Arabian Sea. Deep Sea Research Part II: Topical Studies in Oceanography 44, 1461-1480.

Sætre, R., and Da Silva, A. J., 1984. The circulation of the Mozambique channel, Deep Sea Res., 31, 485-508.

Sakka, A., Legendre, L., Gosselin, M., Leblanc, B., Delesalle, B., Price, N., 1999. Nitrate, phosphate, and iron limitation of the phytoplankton assemblage in the lagoon of Takapoto Atoll (Tuamotu Archipelago, French Polynesia).

Salgueiro, E., Voelker, A., Abrantes, F., Meggers, H., Pflaumann, U., Loncaric, N., Gonzalez-Alvarez, R., Oliveira, P., Bartels-Jonsdottir, H.B., Moreno, J., Wefer, G., 2008. Planktonic foraminifera from modern sediments reflect upwelling patterns off Iberia: Insights from a regional transfer function. Marine Micropaleontology 66, 135-164.

Samanta, B., Bhadury, P., 2014. Analysis of diversity of chromophytic phytoplankton in a mangrove ecosystem using rbcL gene sequencing. Journal of Phycology 50, 328-340.

Sanchez, G.E., Lange, C.B., Gonzalez, H.E., Vargas, G., Munoz, P., Cisternas, C., Pantoja, S., 2012. Siliceous microorganisms in the upwelling center off Concepcion, Chile (36°S): Preservation in surface sediments and downcore fluctuations during the past similar to 150 years. Prog. Oceanogr. 92-95, 50-65.

Schlitzer, R., 2015. Data Analysis and Visualization with Ocean Data View, CMOS Bulletin SCMO, 43, 9–13, available at: https://odv.awi.de/.

Schmidt, F., Hinrichs, K.-U., Elvert, M., 2010. Sources, transport, and partitioning of organic matter at a highly dynamic continental margin. Marine Chemistry 118, 37-55.

Scholz, M.J., Weiss, T.L., Jinkerson, R.E., Jing, J., Roth, R., Goodenough, U., Posewitz, M.C., Gerken, H.G., 2014. Ultrastructure and composition of the Nannochloropsis gaditana cell wall. Eukaryotic Cell 13, 1450-1464.

Schott, F., Koltermann, K.P., Stramma, L., SY, A., Zahn, R., Zenk, W., 1998. North Atlantic, cruise 39, 18 April - 14 September 1997. METEOR-Berichte, Universität Hamburg, 197 pp.

Schouten, S., Baas, M., Hopmans, E.C., Reysenbach, A.-L., Sinninghe Damsté, J.S., 2008a. Tetraether membrane lipids of *Candidatus* "*Aciduliprofundum boonei*", a cultivated obligate thermoacidophilic euryarchaeote from deep-sea hydrothermal vents. Extremophiles 12, 119–124.

Schouten, S., Baas, M., Hopmans, E.C., Sinninghe Damsté, J.S., 2008b. An unusual isoprenoid tetraether lipid in marine and lacustrine sediments. Organic Geochemistry 39, 1033–1038.

Schouten, M.W., de Ruijter, W.P.M., van Leeuwen, P.J., Ridderinkhof, H., 2003. Eddies and variability in the Mozambique Channel. Deep-Sea Research Part Ii-Topical Studies in Oceanography 50, 1987-2003.

Schouten, S., Forster, A., Panoto, F.E., Sinninghe Damsté, J.S., 2007. Towards calibration of the TEX_{86} palaeothermometer for tropical sea surface temperatures in ancient greenhouse worlds. Organic Geochemistry 38, 1537-1546.

Schouten, S., C. Hopmans, E., Forster, A., van Breugel, Y., M. M. Kuypers, M., Sinninghe Damsté, J.S., 2003. Extremely high sea-surface temperatures at low latitudes during the middle Cretaceous as revealed by archaeal membrane lipids.

Schouten, S., Hopmans, E.C., Rosell-Melé, A., Pearson, A., Adam, P., Bauersachs, T., Bard, E., Bernasconi, S.M., Bianchi, T.S., Brocks, J.J., Carlson, L.T., Castañeda, I.S., Derenne, S., Selver, A.D., Dutta, K., Eglinton, T., Fosse, C., Galy, V., Grice, K., Hinrichs, K.-U., Huang, Y.S., Huguet, A., Huguet, C., Hurley, S., Ingalls, A., Jia, G., Keely, B., Knappy, C., Kondo, M., Krishnan, S., Lincoln, S., Lipp, J., Mangelsdorf, K., Martinez-Garcia, A., Menot, G., Mets, A., Mollenhauer, G., Ohkouchi, N., Ossebaar, J., Pagani, M., Pancost, R.D., Pearson, E.J., Peterse, F., Reichart, G.-J., Schaeffer, P., Schmitt, G., Schwark, L., Shah, S.R., Smith, R.W., Smittenberg, R.H., Summons, R.E., Takano, Y.,

Talbot, H.M., Taylor, K.W.R., Tarozo, R., Uchida, M., van Dongen, B.E., Van Mooy, B.A.S., Wang, J.X., Warren, C., Weijers, J.W.H., Werne, J.P., Woltering, M., Xie, S.C., Yamamoto, M., Yang, H., Zhang, C.L., Zhang, Y.G., Zhao, M.X., Sinninghe Damsté, J.S., 2013a. An interlaboratory study of TEX_{86} and BIT analysis of sediments, extracts, and standard mixtures. Geochemistry Geophysics Geosystems 14, 5263-5285.

Schouten, S., Hopmans, E.C., Schefuß, E., Sinninghe Damsté, J.S., 2002. Distributional variations in marine crenarchaeotal membrane lipids: a new tool for reconstructing ancient sea water temperatures? Earth and Planetary Science Letters 204, 265-274.

Schouten, S., Hopmans, E.C., Sinninghe Damsté, J.S., 2004. The effect of maturity and depositional redox conditions on archaeal tetraether lipid palaeothermometry. Organic Geochemistry 35, 567-571.

Schouten, S., Hopmans, E.C., Sinninghe Damsté, J.S., 2013b. The organic geochemistry of glycerol dialkyl glycerol tetraether lipids: A review. Organic Geochemistry 54, 19-61.

Schouten, S., Huguet, C., Hopmans, E.C., Kienhuis, M.V.M., Sinninghe Damsté, J.S., 2007. Analytical methodology for TEX_{86} paleothermometry by high-performance liquid chromatography/atmospheric pressure chemical ionization-mass spectrometry. Analytical Chemistry 79, 2940–2944.

Schrader, H., Sorknes, R., 1991. Peruvian coastal upwelling – Late Quaternary productivity changes revealed by diatoms. Marine Geology 97, 233-249.

Schreuder, L.T., Stuut, J.-B.W., Korte, L.F., Sinninghe Damsté, J.S., Schouten, S., 2018a. Aeolian transport and deposition of plant wax *n*-alkanes across the tropical North Atlantic Ocean. Organic Geochemistry 115, 113-123.

Schreuder, L.T., Hopmans, E.C., Stuut, J.-B.W., Sinninghe Damsté, J.S., Schouten, S., 2018b. Transport and deposition of the fire biomarker levoglucosan across the tropical North Atlantic Ocean. Geochimica et Cosmochimica Acta 227, 171-185.

Schwab, V.F., Sachs, J.P., 2009. The measurement of D/H ratio in alkenones and their isotopic heterogeneity. Organic Geochemistry 40, 111-118.

Seki, O., Schmidt, D.N., Schouten, S., Hopmans, E.C., Sinninghe Damsté, J.S., Pancost, R.D., 2012. Paleoceanographic changes in the Eastern Equatorial Pacific over the last 10 Myr. Paleoceanography 27.

Shackleton, N.J., 1967. Oxygen Isotope Analyses and Pleistocene Temperatures Re-assessed. Nature 215, 15.

Shackleton, N. J., 1974. Attainment of isotopic equilibrium between ocean water and the benthonic foraminifera genus *Uvigerina*: isotopic changes in the ocean during the last glacial, England, Colloques Internationaux du C.N.R.S.

Shackleton, N.J., Hall, M.A., Vincent, E., 2000. Phase relationships between millennial-scale events 64,000-24,000 years ago. Paleoceanography 15, 565-569.

Shackleton, N.J., Fairbanks, R.G., Chiu, T.C., Parrenin, F., 2004. Absolute calibration of the Greenland time scale: implications for Antarctic time scales and for Delta C-14. Quaternary Science Reviews 23, 1513-1522.

Shimokawara, M., Nishimura, M., Matsuda, T., Akiyama, N., Kawai, T., 2010. Bound forms, compositional features, major sources and diagenesis of long chain, alkyl mid-chain diols in Lake Baikal sediments over the past 28,000 years. Organic Geochemistry 41, 753-766.

Shiratake, T., Sato, A., Minoda, A., Tsuzuki, M., Sato, N., 2013. Air-drying of cells, the novel conditions for stimulated synthesis of triacylglycerol in a green alga, *Chlorella kessleri*. Plos One 8.

Siedler, G., Zangenberg, N., Onken, R., 1992. Seasonal Changes in the Tropical Atlantic Circulation – Observation and Simulation of the Guinea Dome. Journal of Geophysical Research-Oceans 97, 703-715.

Sinninghe Damsté, J.S., 2016. Spatial heterogeneity of sources of branched tetraethers in shelf systems: The geochemistry of tetraethers in the Berau River delta (Kalimantan, Indonesia). Geochimica et Cosmochimica Acta 186, 13–31.

Sinninghe Damsté, J.S., Ossebaar, J., Schouten, S., Verschuren, D., 2012a. Distribution of tetraether lipids in the 25-ka sedimentary record of Lake Challa: extracting reliable TEX_{86} and MBT/CBT palaeotemperatures from an equatorial African lake. Quaternary Science Reviews 50, 43-54.

Sinninghe Damsté, J.S., Rampen, S., Rijpstra, W.I.C., Abbas, B., Muyzer, G., Schouten, S., 2003. A diatomaceous origin for long-chain diols and mid-chain hydroxy methyl alkanoates widely occurring in Quaternary marine sediments: Indicators for high-nutrient conditions. Geochimica et Cosmochimica Acta 67, 1339-1348.

Sinninghe Damsté, J.S., Rijpstra, W.I.C., Hopmans, E.C., den Uijl, M.J., Weijers, J.W.H., Schouten, S., 2018. The enigmatic structure of the crenarchaeol isomer. Organic Geochemistry 124, 22-28.

Sinninghe Damsté, J.S., Rijpstra, W.I.C., Hopmans, E.C., Jung, M.-Y., Kim, J.-G., Rhee, S.-K., Stieglmeier, M., Schleper, C., 2012b. Intact Polar and Core Glycerol Dibiphytanyl Glycerol Tetraether Lipids of Group I.1a and I.1b Thaumarchaeota in Soil. Applied and Environmental Microbiology 78, 6866–6874.

Sinninghe Damsté, J.S., Rijpstra, W.I.C., Hopmans, E.C., Prahl, F.G., Wakeham, S.G., Schouten, S., 2002. Distribution of membrane lipids of planktonic Crenarchaeota in the Arabian Sea. Applied and Environmental Microbiology 68, 2997-3002.

Sinninghe Damsté, J.S., Rijpstra, W.I.C., Reichart, G.-J., 2002. The influence of oxic degradation on the sedimentary biomarker record II. Evidence from Arabian Sea sediments. Geochimica et Cosmochimica Acta 66, 2737-2754.

Sluijs, A., Schouten, S., Pagani, M., Woltering, M., Brinkhuis, H., Sinninghe Damsté, J.S., Dickens, G.R., Huber, M., Reichart, G.-J., Stein, R., Matthiesen, J., Lourens, L.J., Pedentchouk, N., Backman, J., Moran, K., Scientists, t.E., 2006. Subtropical Arctic Ocean temperatures during the Palaeocene/Eocene thermal maximum. Nature 441, 610-612.

Smith, S. L., 2001. Understanding the Arabian Sea: Reflections on the 1994-1996 Arabian Sea Expedition, Deep-Sea Res. Pt. II, 48, 1385-1402.

Smith, M., de Deckker, P., Rogers, J., Brocks, J., Hope, J., Schmidt, S., Lopes dos Santos, R., Schouten, S., 2013. Comparison of $U^{K'}_{37}$, TEX^{H}_{86}, and LDI temperature proxies for reconstruction of south-east Australian ocean temperatures. Organic Geochemistry 64, 94-104.

Smith, D.J., Eglinton, G., Morris, R.J., 1983. Occurrence of Long-Chain Alkan-Diols and Alkan-15-One-1-Ols in A Quaternary Sapropel from the Eastern Mediterranean. Lipids 18, 902-905.

Sorhannus, U., 2007. A nuclear-encoded small-subunit ribosomal RNA timescale for diatom evolution. Marine Micropaleontology 65, 1–12.

Spang, A., Hatzenpichler, R., Brochier-Armanet, C., Rattei, T., Tischler, P., Spieck, E., Streit, W., Stahl, D.A., Wagner, M., Schleper, C., 2010. Distinct gene set in two different lineages of ammonia-oxidizing archaea supports the phylum Thaumarchaeota. Trends in Microbiology 18, 331–340.

Stern, J.V., Lisiecki, L.E., 2014. Termination 1 timing in radiocarbon-dated regional benthic $\delta^{18}O$ stacks. Paleoceanography 29, 1127-1142.

Stramma, L., Schott, F., 1999. The mean flow field of the tropical Atlantic Ocean. Deep-Sea Research Part Ii-Topical Studies in Oceanography 46, 279-303.

Strub, T. P., Mesias, M. J., Montecino, V., Rutland, J., and Salinas, S., 1998. Coastal ocean circulation off western South America. In: Robinson, R.A., Brink, H.K. (Eds.), The Global Coastal Ocean – Regional Studies and Synthesis. The Sea, Ideas and Observations on Progress in the Study of the Seas. John Wiley & Sons, Inc, New York, 273-313.

Stuut, J.B.W., Lamy, F., 2004. Climate variability at the southern boundaries of the Namib (Southwestern Africa) and Atacama (northern Chile) coastal deserts during the last 120,000 yr. Quat. Res. 62, 301-309.

Stuut, J.-B., Marchant, M., Kaiser, J., Lamy, F., Mohtadi, M., Romero, O., and Hebbeln, D., 2006. The late quaternary paleoenvironment of Chile as seen from marine archives, Geographica Helvetica, 61, 135-151.

Stuut, J.-B., Zabel, M., Ratmeyer, V., Helmke, P., Schefuß, E., Lavik, G., Schneider, R., 2005. Provenance of present-day eolian dust collected off NW Africa. Journal of Geophysical Research-Atmospheres 110, D04202- 04201-D04202-04214.

Sugai, A., Uda, I., Itoh, Y.H., Itoh, T., 2004. The Core Lipid Composition of the 17 Strains of Hyperthermophilic Archaea, Thermococcales. Journal of Oleo Science 53, 41–44.

Sukenik, A., Carmeli, Y., 1990. Lipid synthesis and fatty acid composition in *Nannochloropsis* sp. (Eustigmatophyceae) grown in a light dark cycle Journal of Phycology 26, 463-469.

Sukhanova, I.N., Flint, M.V., Whitledge, T.E., Stockwell, D.A., Rho, T.K., 2006. Mass development of the planktonic diatom *Proboscia alata* over the Bering Sea shelf in the summer season. Oceanology 46, 200-216.

Takahashi, K., Jordan, R., Priddle, J., 1994. The diatom genus *Proboscia* in Subantarctic waters. Diatom Research 9, 411-428.

Tarazona, J., Gutiérrez, D., Paredes, C., Indacochea, A., 2003. Overview and challenges of Marine Biodiversity Research in Peru. Gayana (Concepción).

Taylor, K.W.R., Huber, M., Hollis, C.J., Hernandez-Sanchez, M.T., Pancost, R.D., 2013. Re-evaluating modern and Palaeogene GDGT distributions: Implications for SST reconstructions. Global and Planetary Change 108, 158–174.

Taylor, R.L., Rand, J.D., Caldwell, G.S., 2012. Treatment with algae extracts promotes flocculation, and enhances growth and neutral lipid content in *Nannochloropsis oculata*, a candidate for biofuel production. Marine Biotechnology 14, 774-781.

Tegelaar, E.W., de Leeuw, J.W., Saizjimenez, C., 1989. Possible origin of aliphatic moieties in humic substances Science of the Total Environment 81-2, 1-17.

ten Haven, H.L., Baas, M., de Leeuw, J.W., Schenck, P.A., Brinkhuis, H., 1987. Late Quaternary Mediterranean sapropels II. Organic geochemistry and palynology of S1 sapropels and associated sediments. Chemical Geology 64, 149–167.

ten Haven, H.L., Eglinton, G., Farrimond, P., Kohnen, M.E.L., Poynter, J.G., Rullkötter, J., Welte, D.H., 1992. Variations in the content and composition of organic matter in sediments underlying active upwelling regimes: a study from ODP Legs 108, 112, and 117. Geological Society, London, Special Publications 64, 229–246.

ten Haven, H.L., Rullkötter, J., 1991. Preliminary lipid analyses of sediments recovered during leg 117 1., Proceedings of the Ocean Drilling Program, Scientific Results, pp. 561-569.

Thierstein, H.R., Geitzenauer, K.R., Molfino, B., 1977. Global synchroneity of Late Quaternary coccolith datum levels – validation by oxygen isotopes. Geology 5, 400–404.

Thomas, A.C., 1999. Seasonal distributions of satellite-measured phytoplankton pigment concentration along the Chilean coast. J. Geophys. Res.-Oceans 104, 25877-25890.

Thomas, A.C., Huang, F., Strub, P.T., James, C., 1994. omparison of the seasonal and interannual variability of phytoplankton pigment concentrations in the Peru and California Current systems. Journal of Geophysical Research - Oceans 99, 7355-7370.

Thunell, R., Benitez-Nelson, C., Varela, R., Astor, Y., Muller-Karger, F., 2007. Particulate organic carbon fluxes along upwelling-dominated continental margins: Rates and mechanisms. Global Biogeochemical Cycles 21.

Thunell, R.C., Varela, R., Llano, M., Collister, J., Muller-Karger, F., Bohrer, R., 2000. Organic carbon fluxes, degradation, and accumulation in an anoxic basin: Sediment trap results from the Cariaco Basin. Limnology and Oceanography 45, 300-308.

Tierney, J.E., Sinninghe Damsté, J.S., Pancost, R.D., Sluijs, A., Zachos, J.C., 2017. Eocene temperature gradients. Nature Geoscience 10, 538-539.

Tierney, J.E., Tingley, M.P., 2014. A Bayesian, spatially-varying calibration model for the TEX_{86} proxy. Geochimica Et Cosmochimica Acta 127, 83-106.

Tierney, J.E., Tingley, M.P., 2015. A TEX_{86} surface sediment database and extended Bayesian calibration. Scientific Data 2, 150029.

Tierney, J.E., Tingley, M.P., 2018. BAYSPLINE: A New Calibration for the Alkenone Paleothermometer. Paleoceanography and Paleoclimatology 33, 281-301.

Tonon, T., Harvey, D., Larson, T.R., Graham, I.A., 2002. Long chain polyunsaturated fatty acid production and partitioning to triacylglycerols in four microalgae. Phytochemistry 61, 15-24.

Torrence, C., Compo, G. P., 1998. A practical guide to wavelet analysis. Bull. Am. Meteorol. Soc.79, 61–78.

Treppke, U. F., Lange, C. B., and Wefer, G., 1996. Vertical fluxes of diatoms and silicoflagellates in the eastern equatorial Atlantic, and their contribution to the sedimentary record, Marine Micropaleontology 28, 73-96.

Turich, C., Schouten, S., Thunell, R.C., Varela, R., Astor, Y., Wakeham, S.G., 2013. Comparison of TEX_{86} and $U^{K'}_{37}$ temperature proxies in sinking particles in the Cariaco Basin. Deep-Sea Research Part I-Oceanographic Research Papers 78, 115-133.

Ullgren, J. E., van Aken, H. M., Ridderinkhof, H. and de Ruijter, W. P. M., 2012. The hydrography of the Mozambique Channel from six years of continuous temperature, salinity, and velocity observations. Deep-Sea Res. Pt. I, 69, 36 – 50.

Urey, H.C., 1947. The Thermodynamic Properties of Isotopic Substances. Journal of the Chemical Society, 562-581.

Vale, C., Sundby, B., 1987. Suspended sediment fluctuations in the Tagus estuary on semi-diurnal and fortnightly time scales. Estuarine, Coastal and Shelf Science 25, 495-508.

Vargas, G., Ortlieb, L., Pichon, J.J., Bertaux, J., Pujos, M., 2004. Sedimentary facies and high resolution primary production inferences from laminated diatomacous sediments off northern Chile (23°S). Mar. Geol. 211, 79-99.

van der Does, M., Korte, L.F., Munday, C.I., Brummer, G.J.A., Stuut, J.B.W., 2016. Particle size traces modern Saharan dust transport and deposition across the equatorial North Atlantic. Atmospheric Chemistry and Physics 16, 13697-13710.

Van der Leeden, F., 1975. Water resources of the world: selected statistics. Water Information Center, Port Washington, N.Y., 808.

Vanney, J.R., Mougenot, D., 1981. La plate-forme continentale de Portugal et les prov¬inces adjacentes: Analyse geomorphologique. Memoriás dos Serviçios Geológicos de Portugal 28, 86.

van Soelen, E.E., Lammertsma, E.I., Cremer, H., Donders, T.H., Sangiorgi, F., Brooks, G.R., Larson, R.A., Sinninghe Damsté, J.S., Wagner-Cremer, F., Reichart, G.-J., 2010. Late Holocene sea-level rise in Tampa Bay: Integrated reconstruction using biomarkers, pollen, organic-walled dinoflagellate cysts, and diatoms. Estuarine Coastal and Shelf Science 86, 216-224.

Verleye, T.J., Louwye, S., 2010. Late Quaternary environmental changes and latitudinal shifts of the Antarctic Circumpolar Current as recorded by dinoflagellate cysts from offshore Chile (41°S). Quaternary Science Reviews 29, 1025-1039.

Versteegh, G.J.M., Bosch, H.J., de Leeuw, J.W., 1997. Potential palaeoenvironmental information of C_{24} to C_{36} mid-chain diols, keto-ols and mid-chain hydroxy fatty acids; a critical review. Organic Geochemistry 27, 1-13.

Versteegh, G.J.M., Jansen, J.H.F., de Leeuw, J.W., Schneider, R.R., 2000. Mid-chain diols and keto-ols in SE Atlantic sediments: A new tool for tracing past sea surface water masses? Geochimica Et Cosmochimica Acta 64, 1879-1892.

Vieler, A., Wu, G., Tsai, C.-H., Bullard, B., Cornish, A.J., Harvey, C., Reca, I.-B., Thornburg, C., Achawanantakun, R., Buehl, C.J., Campbell, M.S., Cavalier, D., Childs, K.L., Clark, T.J., Deshpande, R., Erickson, E., Ferguson, A.A., Handee, W., Kong, Q., Li, X., Liu, B., Lundback, S., Peng, C., Roston, R.L., Sanjaya, Simpson, J.P., TerBush, A., Warakanont, J., Zaeuner, S., Farre, E.M., Hegg, E.L., Jiang, N., Kuo, M.-H., Lu, Y., Niyogi, K.K., Ohlrogge, J., Osteryoung, K.W., Shachar-Hill, Y., Sears, B.B., Sun, Y., Takahashi, H., Yandell, M., Shiu, S.-H., Benning, C., 2012. Genome, functional gene annotation, and nuclear transformation of the heterokont oleaginous alga *Nannochloropsis oceanica* CCMP1779. Plos Genetics 8.

Villanueva, L., Besseling, M., Rodrigo-Gámiz, M., Rampen, S.W., Verschuren, D., Sinninghe Damsté, J.S., 2014. Potential biological sources of long chain alkyl diols in a lacustrine system. Organic Geochemistry 68, 27-30.

Villanueva, J. and Grimalt, J.O., 1997. Gas chromatographic tuning of the $U_{37}^{K'}$ paleothermometer, Analytical Chemistry 69, 3329-3332.

Villanueva, J., Grimalt, J.O., Cortijo, E., Vidal, L., Labeyriez, L., 1997. A biomarker approach to the organic matter deposited in the North Atlantic during the last climatic cycle. Geochimica Et Cosmochimica Acta 61, 4633-4646.

Villanueva, J., Pelejero, C., Grimalt., J.O., Clean-up procedures for the unbiased estimation of C_{37} alkenone sea surface temperatures and terrigenous *n*-alkane inputs in paleoceanography. Journal of Chromatography A 757, 145-151.

Vinogradova, O.M., Darienko, T.M., 2008. Terrestrial algae of hypersaline environments of the Central Syvash islands (Kherson Region, Ukraine). Biologia 63, 813-823.

Vitorino, J., Oliveira, A., Jouanneau, J.M., Drago, T., 2002. Winter dynamics on the northern Portuguese shelf. Part 2: bottom boundary layers and sediment dispersal. Progress in Oceanography 52, 155-170.

Voituriez, B., 1981. Les sous-courants 6quatoriaux nord et sud et la formation des dômes thermiques tropicaux, Oceanol. Acta, 4,497-506.

Volkman, J.K., Barrett, S.M., Blackburn, S.I., 1999a. Eustigmatophyte microalgae are potential sources of C_{29} sterols, C_{22}–C_{28} *n*-alcohols and C_{28}–C_{32} *n*-alkyl diols in freshwater environments. Organic Geochemistry 30, 307-318.

Volkman, J.K., Barrett, S.M., Blackburn, S.I., 1999b. Fatty acids and hydroxy fatty acids in three species of freshwater eustigmatophytes. Journal of Phycology 35, 1005-1012.

Volkman, J.K., Barrett, S.M., Blackburn, S.I., Mansour, M.P., Sikes, E.L., Gelin, F., 1998. Microalgal biomarkers: A review of recent research developments. Organic Geochemistry 29, 1163-1179

Volkman, J.K., Barrett, S.M., Blackburn, S.I., Sikes, E.L., 1995. Alkenones in *Gephyrocapsa oceanica*: Implications for studies of paleoclimate. Geochimica et Cosmochimica Acta 59, 513-520.

Volkman, J.K., Barrett, S.M., Dunstan, G.A., Jeffrey, S.W., 1992. C_{30}–C_{32} alkyl diols and unsaturated alcohols in microalgae of the class Eustigmatophyceae. Organic Geochemistry 18, 131-138.

Volkman, J.K., Brown, M.R., Dunstan, G.A., Jeffrey, S.W., 1993. The biochemical composition of marine microalgae from the class Eustigmatophyceae. Journal of Phycology 29, 69-78.

Volkman, J.K., Eglinton, G., Corner, E.D.S., Forsberg, T.E.V., 1980a. Long-chain alkenes and alkenones in the marine coccolithophorid *Emiliania huxleyi*. Phytochemistry 19, 2619-2622.

Volkman, J.K., Eglinton, G., Corner, E.D.S., Sargent, J.R., 1980b. Novel unsaturated straight-chain C_{37}-C_{39} methyl and ethyl ketones in marine sediments and a coccolithophore *Emiliania huxleyi*. Physics and Chemistry of the Earth 12, 219-227.

Volkman, J.K., Revill, A.T., Holdsworth, D.G., Fredericks, D., 2008. Organic matter sources in an enclosed coastal inlet assessed using lipid biomarkers and stable isotopes. Organic Geochemistry 39, 689-710.

Wakeham, S.G., Peterson, M.L., Hedges, J.I., Lee, C., 2002. Lipid biomarker fluxes in the Arabian Sea, with a comparison to the equatorial Pacific Ocean. Deep-Sea Research Part II 49, 2265-2301.

Walsh, E.M., Ingalls, A.E., Keil, R.G., 2008. Sources and transport of terrestrial organic matter in Vancouver Island fjords and the Vancouver-Washington Margin: A multiproxy approach using $\delta^{13}C_{org}$, lignin phenols, and the ether lipid BIT index. Limnology and Oceanography 53, 1054-1063.

Warnock, J.P., Bauersachs, T., Kotthoff, U., Brandt, H.T., Andren, E., 2018. Holocene environmental history of the Angermanalven Estuary, northern Baltic Sea. Boreas 47, 593-608.

Weijer, W., de Ruiter, W. P. M., Dijkstra, H. A., and van Leeuwen, P. J., 1999. Impact of interbasin exchange on the Atlantic overturning circulation, J. Phys. Oceanogr., 29, 2266-2284.

Weijers, J.W.H., Schouten, S., Schefuß, E., Schneider, R.R., Sinninghe Damsté, J.S., 2009. Disentangling marine, soil and plant organic carbon contributions to continental margin sediments: A multi-proxy approach in a 20,000 year sediment record from the Congo deep-sea fan. Geochimica et Cosmochimica Acta 73, 119-132.

Weijers, J.W.H., Schouten, S., Spaargaren, O.C., Sinninghe Damsté, J.S., 2006. Occurrence and distribution of tetraether membrane lipids in soils: Implications for the use of the TEX_{86} proxy and the BIT index. Organic Geochemistry 37, 1680-1693.

Weijers, J.W.H., Schouten, S., van den Donker, J.C., Hopmans, E.C., Sinninghe Damsté, J.S., 2007. Environmental controls on bacterial tetraether membrane lipid distribution in soils. Geochimica ét Cosmochimica Acta 71, 703–713.

Welch, B.L., 1947. The generalisation of Students problem with several different population variances are involved. Biometrika 34, 28-35.

Weller, P., Stein, R., 2008. Paleogene biomarker records from the central Arctic Ocean (Integrated Ocean Drilling Program Expedition 302): Organic carbon sources, anoxia, and sea surface temperature. Paleoceanography 23.

Willmott, V., Rampen, S.W., Domack, E., Canals, M., Sinninghe Damsté, J.S., Schouten, S., 2010. Holocene changes in *Proboscia* diatom productivity in shelf waters of the north-western Antarctic Peninsula. Antarctic Science 22, 3-10.

Wuchter, C., Abbas, B., Coolen, M.J.L., Herfort, L., van Bleijswijk, J., Timmers, P., Strous, M., Teira, E., Herndl, G.J., Middelburg, J.J., Schouten, S., Sinninghe Damsté, J.S., 2006a. Archaeal nitrification in the ocean. Proceedings of the National Academy of Sciences U. S. A. 103, 12317-12322.

Wuchter, C., Schouten, S., Wakeham, S.G., Sinninghe Damsté, J.S., 2005. Temporal and spatial variation in tetraether membrane lipids of marine Crenarchaeota in particulate organic matter: Implications for TEX_{86} paleothermometry. Paleoceanography 20, PA3013-3011-PA3013- 3011.

Wuchter, C., Schouten, S., Wakeham, S.G., Sinninghe Damsté, J.S., 2006b. Archaeal tetraether membrane lipid fluxes in the northeastern Pacific and the Arabian Sea: Implications for TEX_{86} paleothermometry. Paleoceanography 21, PA4208-4201-PA4208-4209.

Xenopoulos, M.A., Bird, D.F., 1997. Effect of acute exposure to hydrogen peroxide on the production of phytoplankton and bacterioplankton in a mesohumic lake. Photochemistry and Photobiology 66, 471-478.

Xiao, Y., Zhang, J., Cui, J., Feng, Y., Cui, Q., 2013. Metabolic profiles of N*annochloropsis oceanica* IMET1 under nitrogen-deficiency stress. Bioresource Technology 130, 731-738.

Xie, P. and Arkin, P.A., 1997. Global precipitation: A 17-year monthly analysis based on gauge observations, satellite estimates, and numerical model outputs. Bull. Am. Meteor. Soc., 78, 2539 – 2558.

Xie, S.T., Liu, X.L., Schubotz, F., Wakeham, S.G., Hinrichs, K.-U., 2014. Distribution of glycerol ether lipids in the oxygen minimum zone of the Eastern Tropical North Pacific Ocean. Organic Geochemistry 71, 60-71.

Xu, L., Reddy, C.M., Farrington, J.W., Frysinger, G.S., Gaines, R.B., Johnson, C.G., Nelson, R.K., Eglinton, T.I., 2001. Identification of a novel alkenone in Black Sea sediments. Organic Geochemistry. 32, 633-645.

Xu, Y.P., Simoneit, B.R.T., Jaffe, R., 2007. Occurrence of long chain *n*-alkenols, diols, keto-ols and sec-alkanols in a sediment core from a hypereutrophic, freshwater lake. Organic Geochemistry 38, 870-883.

Yamagata, T., and Iizuka, S., 1995. Simulation of the Tropical Thermal Domes in the Atlantic – A Seasonal Cycle, Journal of Physical Oceanography 25, 2129-2140.

Yamamoto, M., Ficken, K., Baas, M., Bosch, H.J., de Leeuw, J.W., 1996. Molecular palaeontology of the earliest Danian at Geulhemmerberg (the Netherlands). Geologie En Mijnbouw 75, 255-267.

Yamamoto, M., Shimamoto, A., Fukuhara, T., Tanaka, Y., Ishizaka, J., 2012. Glycerol dialkyl glycerol tetraethers and TEX_{86} index in sinking particles in the western North Pacific. Organic Geochemistry 53, 52-62.

Yang, H., Pancost, R.D., Tang, C.Y., Ding, W.H., Dang, X.Y., Xie, S.C., 2014. Distributions of isoprenoid and branched glycerol dialkanol diethers in Chinese surface soils and a loess-paleosol sequence: Implications for the degradation of tetraether lipids. Organic Geochemistry 66, 70-79.

Zachos, J.C., Dickens, G.R., Zeebe, R.E., 2008. An early Cenozoic perspective on greenhouse warming and carbon-cycle dynamics. Nature 451, 279–283.

Zell, C., Kim, J.H., Balsinha, M., Dorhout, D., Fernandes, C., Baas, M., Sinninghe Damsté, J.S., 2014. Transport of branched tetraether lipids from the Tagus River basin to the coastal ocean of the Portuguese margin: consequences for the interpretation of the MBT'/CBT paleothermometer. Biogeosciences 11, 5637-5655.

Zell, C., Kim, J.H., Dorhout, D., Baas, M., Sinninghe Damsté, J.S., 2015. Sources and distributions of branched tetraether lipids and crenarchaeol along the Portuguese continental margin: Implications for the BIT index. Continental Shelf Research 96, 34-44.

Zell, C., Kim, J.H., Moreira-Turcq, P., Abril, G., Hopmans, E.C., Bonnet, M.P., Sobrinho, R.L., Sinninghe Damsté, J.S., 2013. Disentangling the origins of branched tetraether lipids and crenarchaeol in the lower Amazon River: Implications for GDGT-based proxies. Limnology and Oceanography 58, 343-353.

Zhang, Y.G., Liu, X.Q., 2018. Export Depth of the TEX_{86} Signal. Paleoceanography and Paleoclimatology 33, 666-671.

Zhang, Z.H., Metzger, P., Sachs, J.P., 2011. Co-occurrence of long chain diols, keto-ols, hydroxy acids and keto acids in recent sediments of Lake El Junco, Galapagos Islands. Organic Geochemistry 42, 823-837.

Zhang, Y.G., Pagani, M., Wang, Z., 2016. Ring Index: A new strategy to evaluate the integrity of TEX_{86} paleothermometry. Paleoceanography 31, 220-232.

Zhang, Z., Volkman, J.K., 2017. Algaenan structure in the microalga *Nannochloropsis oculata* characterized from stepwise pyrolysis. Organic Geochemistry 104, 1-7.

Zhang, Y.G., Zhang, C.L., Liu, X.-L., Li, L., Hinrichs, K.-U., Noakes, J.E., 2011. Methane Index: A tetraether archaeal lipid biomarker indicator for detecting the instability of marine gas hydrates. Earth Planet. Sci. Lett. 307, 525-534.

Zhu, X.W., Jia, G.D., Mao, S.Y., Yan, W., 2018. Sediment records of long chain alkyl diols in an upwelling area of the coastal northern South China Sea. Org. Geochem. 121, 1-9.

Zhu, C., Lipp, J.S., Wormer, L., Becker, K.W., Schroder, J., Hinrichs, K.-U., 2013. Comprehensive glycerol ether lipid fingerprints through a novel reversed phase liquid chromatography-mass spectrometry protocol. Organic Geochemistry 65, 53-62.

Zhu, C., Meador, T.B., Dummann, W., Hinrichs, K.-U., 2014. Identification of unusual butanetriol dialkyl glycerol tetraether and pentanetriol dialkyl glycerol tetraether lipids in marine sediments. Rapid Communications in Mass Spectrometry 28, 332–338.

Zhu, C., Wakeham, S.G., Elling, F.J., Basse, A., Mollenhauer, G., Versteegh, G.J.M., Könneke, M., Hinrichs, K.-U., 2016. Stratification of archaeal membrane lipids in the ocean and implications for adaptation and chemotaxonomy of planktonic archaea. Environmental Microbiology 18, 4324-4336.

Zhu, C., Weijers, J.W.H., Wagner, T., Pan, J.-M., Chen, J.-F., Pancost, R.D., 2011. Sources and distributions of tetraether lipids in surface sediments across a large river-dominated continental margin. Organic Geochemistry 42, 376–386.

Zweng, M.M., Reagan, J.R., Antonov, J.I., Locarnini, R.A., Mishonov, A.V., Boyer, T.P., Garcia, H.E., Baranova, O.K., Johnson, D.R., Seidov, D., Biddle, M.M., 2013. World Ocean Atlas 2013, Volume 2: Salinity: Salinity. Levitus, S., Ed.; Mishonov, A., Technical Ed.; NOAA Atlas NESDIS 74, 39 pp.

Summary

The prediction of future global warming and its impact on the Earth's climate relies on the simulations of climate models, which extrapolate long term climate trends related to the interactions between ocean, atmosphere and land. These models need to be validated against continuous time series of instrumental climate data. However, instrumental records only extend back to the last century inhibiting the validation of long-term (i.e. thousands to millions of years) climate modelling experiments. Instead, climate archives are used to reconstruct past climates of thousands to millions of years ago, and marine sediment is one of the climate archives paleoclimatologists frequently turn to. In these marine sediments so-called climate proxies, preserved entities holding information of the depositional environment, are measured. One of the most frequently reconstructed climate parameters is sea surface temperature (SST), and various independent methods exist to reconstruct SST, amongst which the analysis of stable oxygen isotopes ($\delta^{18}O$) or Mg/Ca ratios in the calcitic shells of fossilized foraminifera. In contrast to such inorganic proxies, organic proxies are based on fossilized lipids, so-called biomarkers. Two frequently applied organic SST proxies are the $U^{K'}_{37}$, based on long-chain alkenones produced by haptophytes, and the TEX_{86}, based on glycerol dialkyl glycerol tetraethers (GDGTs) produced by archaea. Over the last years, long-chain diols (LCDs) have also gained much interest as paleoclimate indicators. These LCDs have hydroxy groups attached to the first carbon atom and at a mid-chain position and are most often encountered in marine sediments as 1,13-, 1,14- and 1,15-diols with carbon chain lengths generally ranging from C_{28} to C_{32}. In the marine environment the 1,14-diols are often produced by *Proboscia* diatoms, and since these diatoms are typically associated with upwelling regions, it was proposed that the relative abundance of the 1,14-diols, expressed as the Diol Index, could be used as an indirect tracer for past upwelling. The producers of 1,13- and 1,15-diols in the marine realm are unknown, but the relative abundance of the C_{30} 1,15-diol with respect to the C_{28} 1,13-, C_{30} 1,13- and C_{30} 1,15-diols showed a strong empirical relationship with annual mean SST. Accordingly, a ratio based on these diols called the Long-chain Diol Index (LDI) was proposed as a new proxy for SST. This thesis focuses on testing and validating the applicability of these proxies, and on the significance of long-chain diols as paleoenvironmental indicators.

Long-chain diols are generally measured by means of gas chromatography coupled to a mass spectrometer (GC-MS) using selected ion monitoring (SIM), long-chain alkenones by means of GC flame ionization detection (FID) and GDGTs by means of ultra high performance liquid chromatography – MS (UHPLC-MS) in SIM mode. Accordingly, to determine the three temperature proxies based on these lipids (i.e., LDI, $U^{K'}_{37}$ and TEX_{86}, respectively) three types of analyses have to be carried out. To streamline these analyses we tested the possibility to analyze the three lipid classes by means of UHPLC-MS in SIM mode. We have assessed detection and quantification limits for alkenones and diols for this method

and other methods by serial dilutions of culture extracts containing these compounds. The results showed that this UHPLC-MS method was 2–3 orders more sensitive regarding the detection of long-chain alkenones when compared to the traditional GC-FID analysis, but was less sensitive for long-chain diols when compared to GC-MS analysis. However, UHPLC with high resolution MS (HRMS) revealed a similar sensitivity regarding LCD detection when compared to GC-MS analysis, as well as the best reproducibility. Thus UHPLC-HRMS seems to be an excellent method for the simultaneous analysis of all three lipid classes, although standard mixtures are needed to monitor the relative responses of these compounds. Another newly developed method for the measurement of LCDs, i.e. GC-MS/MS in multiple reaction monitoring (MRM), revealed a slightly lower limit of quantification than the traditional method, and improved reproducibility. However, here too, authentic standards are needed, which poses a limitation to the method.

Long-chain diols have been observed in several eustigmatophyte algae, in particular *Nannochloropsis* species, but the biochemical factors regulating LCD synthesis, as well as their biological function, is unknown. We have cultured *Nannochloropsis* under different conditions (i.e., light irradiance, salinity, nitrogen depletion, desiccation, cold shock and oxidative stress) to identify their impact on the production of long-chain diols. In all experiments, the diol concentrations remained relatively stable, supporting the hypothesis that long-chain diols are part of the cell wall, and that the abundance of long-chain diols in the marine environment may be used as indicator of the abundance of diol-producing algae.

The quantification of long-chain diols, long-chain alkenones and GDGTs in surface sediments in the tropical Atlantic and in overlying sediment traps showed that generally less than 2 % of these lipid biomarkers was preserved in the sediments, implying significant degradation at the seafloor. However, the LDI, $U_{37}^{K'}$ and TEX_{86}-derived temperatures in the sediments are very similar to the LDI, $U_{37}^{K'}$ and TEX_{86}-derived temperatures obtained from sediment traps, and the actual annual mean SST. A sediment trap time-series in the Cariaco Basin reveals a seasonal imprint on the LDI, probably caused by seasonal upwelling. During summer stratification the LDI reflects temperatures of up to ca. 30 m water depth, whereas during the upwelling season the LDI reflects SST, suggesting that during upwelling the diol producers were closer to the surface, in agreement with shoaling of the nutri- and thermocline. The Diol Index shows excellent agreement with primary productivity rates in the Cariaco Basin, signifying that the Diol Index is a good indicator of upwelling intensity at this location, where upwelling is the main driver of overall productivity.

To further investigate the relationship between the LDI and SST, the initial core-top calibration was re-evaluated and extended, by considering 733 marine surface sediments from all over the world. We observed a similar relationship between the LDI and temperature as reported previously, but with increased scatter. Inspection of the data and with the related environmental parameters showed that this scatter can largely be explained by the influence of fresh water, and long-chain diol contribution of *Proboscia* diatoms. Accordingly, the

exclusion of core-tops from regions with low salinity, as well as core-tops with high *Proboscia*-derived diol abundances (as signified by high C_{28} 1,12-diol contributions), significantly increased the quality of correlation between the LDI and SST. Despite a larger calibration error, the final LDI calibration is statistically similar to the original calibration, confirming the robustness of the LDI as SST proxy.

To assess the impact of fresh water input on the applicability of the LDI, the LDI and individual long-chain diol abundances were measured along five transects off the coast of Portugal impacted by the outflow of several rivers. In the prodelta of the largest river, the river Tagus, the LDI severely underestimates annual mean SST (up to ca. –7 °C), whereas offshore the LDI accurately reflects SST. This implies that fluvial input can indeed compromise the LDI. Interestingly, relatively high abundances of the C_{32} 1,15-diol were detected in front of the major river mouths, and the fractional abundances of this diol showed an excellent correlation with the BIT index, a proxy for the input of continental organic carbon to the marine environment based on GDGTs. Moreover, its fractional abundance was even higher in the suspended particulate matter of the Tagus river water. Hence, this suggests that the C_{32} 1,15-diol predominantly derives from rivers, and might be a suitable tracer for river outflow.

In order to further validate the applicability of the LDI and Diol Index, a sediment core off the coast of Chile covering several glacial-interglacial cycles was investigated. The LDI-based SST reconstruction was in good agreement with the $U^{K'}_{37}$ and TEX_{86} temperature reconstructions, as well as with the planktonic foraminiferal $\delta^{18}O$ data, implying that the LDI reflects past SST variations at this location. The Diol Index, and a recently proposed proxy for nutrient concentrations called the Nutrient Diol Index, or NDI, determined from this sediment core, showed disagreement with other paleo-upwelling and/or –productivity indicators. Where other records (based on diatom counts, total organic carbon or other lipid biomarkers) indicated a peak in upwelling intensity around 100 thousand years ago, the Diol Index and NDI showed a minimum around this time, suggesting diminished upwelling and very low nutrient concentrations. These data suggest that the Diol Index and NDI may be considered as *Proboscia* productivity indicators, rather than indicators for upwelling conditions or nutrient concentrations.

Several applications of the LDI have shown that the proxy is highly promising as a proxy for past SST. However, most applications have focused on Quaternary timescales (up to ca. 3 million years ago), whereas it is also timely to know whether the LDI might be applicable to longer timescales. Accordingly, we have evaluated lipid biomarker distributions (diols, alkenones and GDGTs) over the last ca. 90 million years, in a core of the New Jersey Shelf. Whereas the GDGTs showed distributions comparable to modern-day distributions, we observed unusual alkenone distributions for the Late Cretaceous (ca. 78 million years old), suggesting different ancestral organisms for these biomarkers. The long-chain diol distributions in sediments older than ca. 30 million years were very different when compared

to modern-day distributions, also suggesting that the source organisms were different than those today. The LDI could be calculated up to ca. 50 million years ago, because of the absence of LDI-diols in older sediments. Furthermore, the LDI temperature trend disagrees with other organic and inorganic temperature proxy records, suggesting that the LDI might be compromised for sediments older than ca. 30 million years.

The results in this thesis provide new insights in the environmental controls determining the long-chain diol distributions observed in marine sediments and show that long-chain diols can serve as valuable paleoenvironmental proxies, though several constraints have to be considered before application.

Nederlandse samenvatting

Het voorspellen van klimaatopwarming en de invloed daarvan op de aarde gaat aan de hand van complexe klimaatmodellen, die de langetermijnvariatie in klimaatverandering extrapoleren naar de toekomst, en daarbij rekening houden met processen in en tussen de atmosfeer, oceaan en land. De betrouwbaarheid van deze modellen wordt gevalideerd met behulp van langetermijnobservaties van bijvoorbeeld temperatuur. Echter, instrumentele klimaatmetingen bestaan alleen voor ongeveer de laatste 150 jaar, wat op geologische tijdschaal maar een hele korte periode is en het dus niet mogelijk maakt om klimaatmodellen te testen op langere tijdschalen (duizenden tot miljoenen jaren). Als alternatief gebruiken paleoklimatologen klimaatarchieven, en diepzeesedimenten zijn één van de meest gebruikte archieven. In deze sedimenten worden zogenoemde klimaatproxy's gemeten. Dit zijn indirecte gegevens die bewaard zijn gebleven in het sediment en iets zeggen over het klimaat in de tijd dat het sediment is afgezet op de zeebodem. Eén van de belangrijkste klimaatparameters die paleoklimatologen proberen te reconstrueren, is zeewateroppervlaktetemperatuur (ZOT). Er bestaan momenteel verschillende onafhankelijke methoden voor de reconstructie van ZOT, waaronder de chemische samenstelling van de kalkschelpjes van gefossiliseerde foraminiferen, en in het bijzonder de zuurstofisotopensamenstelling ($\delta^{18}O$) of de Mg/Ca verhoudingen van deze kalkskeletjes. Deze proxy's worden vaak als anorganisch bestempeld. Voorbeelden van organische ZOT proxy's zijn de $U_{37}^{K'}$ en de TEX_{86}. De eerste is gebaseerd op alkenonen met lange koolstofketens geproduceerd door haptofyte algen, en de TEX_{86} is gebaseerd op glycerol dialkyl glycerol tetraethers (GDGTs), die worden gemaakt door archaea. De laatste jaren hebben langeketendiolen steeds meer aandacht gekregen omdat ook deze moleculen waarschijnlijk veel informatie bevatten over het klimaat van vroeger. Deze diolen hebben alcoholgroepen die vastzitten aan het eerste koolstofatoom, en aan een koolstofatoom in het midden van het molecuul. De meest voorkomende diolen in mariene sedimenten zijn de 1,13-, 1,14- en 1,15-diolen met ketenlengtes tussen de C_{28} en C_{32}. 1,14-diolen worden in de oceaan over het algemeen geproduceerd door *Proboscia*-diatomeeën, die vaak voorkomen in gebieden met opwelling. Dit laatste is een oceanografisch fenomeen waarbij koud, mineraalrijk water vanaf de zeebodem opstijgt en voedingsstoffen levert aan het fytoplankton, en daarmee algengroei stimuleert. Omdat *Proboscia*-diatomeeën vaak voorkomen in deze gebieden wordt de relatieve concentratie van 1,14-diolen gebruikt als indicatie voor opwellingsintensiteit, uitgedrukt in de Diol Index. Welke micro-organismen de 1,13- en 1,15-diolen produceren in de oceaan is onbekend, maar de relatieve hoeveelheid van de C_{30} 1,15-diol (ten opzichte van de C_{28} 1,13-, C_{30} 1,13- en C_{30} 1,15-diol) heeft wereldwijd een sterke empirische positieve correlatie met de jaarlijks gemiddelde zeewateroppervlaktetemperatuur. Zodoende werd de verhouding van deze diolen voorgesteld als nieuwe ZOT-proxy, met de naam LDI (Langeketen Diol Index). In dit proefschrift testen

we de toepassing van de diol-proxy's in mariene milieus, en onderzoeken we de potentie van diolen als paleoklimaatindicatoren in het algemeen.

Langeketendiolen worden over het algemeen gemeten door middel van gaschromatografie gekoppeld aan massaspectrometrie (GC-MS) met selectieve iondetectie (SIM). Alkenonen worden doorgaans geanalyseerd op een GC met een vlamionisatiedetector (FID), en GDGTs worden gemeten met hoge-prestatie-vloeistofchromatografie gekoppeld aan massaspectrometrie (UHPLC-MS) met SIM-detectie. We hebben getest of we deze drie molecuulgroepen, en de daarbij horende temperatuurproxy's (LDI, $U^{K'}_{37}$ en TEX_{86}), in één keer kunnen analyseren door middel van UHPLC-MS met SIM detectie. We hebben de detectie- en kwantificeringslimieten voor deze methode en andere methoden bepaald door middel van verdunningsreeksen van algenextracten. De UHPLC-MS was twee tot drie ordes van grootte gevoeliger in alkenonendetectie dan de traditionele GC-FID methode, maar was minder gevoelig in dioldetectie vergeleken met de GC-MS. Daarentegen, UHPLC met hoge-resolutie-massaspectrometrie (HRMS) had een vergelijkbare gevoeligheid als GC-MS wat betreft de diolen, en een betere reproduceerbaarheid. UHPLC-HRMS is dus potentieel een goede methode voor de simultane analyse van de drie groepen verbindingen, maar standaarden zijn nodig om de relatieve MS-responsen van de lipiden te bepalen. We hebben ook een nieuwe analytische methode ontwikkeld voor diolen, namelijk GC-MS/MS met MRM ('Multiple Reaction Monitoring')-detectie waarbij de geselecteerde ionen twee keer gefragmenteerd worden. Deze methode was iets gevoeliger dan de traditionele GC-MS methode, en had een betere reproduceerbaarheid. Echter, ook voor deze methode zijn synthetische standaarden nodig.

Langeketendiolen zijn gevonden in verschillende eustigmatofyte algen, met name in *Nannochloropsis*, maar de factoren die ten grondslag liggen aan de biosynthese van diolen en hun biologische functie is onbekend. Wij hebben *Nannochloropsis*-microalgen gekweekt onder verschillende groeiomstandigheden (lichtintensiteit, zoutgehalte, stikstoflimitatie, koude schok, en oxidatieve stress) en de lipiden geëxtraheerd, om de invloed van deze kweekcondities op de productie van diolen te bepalen. De diolconcentraties bleven relatief constant in alle experimenten, wat overeenkomt met de hypothese dat diolen onderdeel zijn van de celwand, en dat diolen in de oceaan indicatief zijn voor de hoeveelheid diol-producerende algen.

De concentratie van diolen, alkenonen en GDGTs in zeebodemsedimenten in de tropische Atlantische Oceaan is twee tot drie ordes van grootte lager dan de concentratie in sedimentvallen die zich direct boven deze sedimenten in de waterkolom bevinden. Met andere woorden, minder dan 2 % van deze lipiden geproduceerd in de waterkolom wordt uiteindelijk bewaard in de zeebodem, wat betekent dat er degradatie plaatsvindt op en in de zeebodem. Deze degradatie lijkt echter geen invloed te hebben op de proxy's, want de proxy-temperaturen in het sediment zijn zeer vergelijkbaar met zowel de proxy-temperaturen in de sedimentvallen, als de daadwerkelijke gemiddelde oppervlaktetemperatuur van het zeewater.

Een sedimentval-tijdreeks in het Cariaco Bassin laat zien dat de LDI temperatuurvariaties van de verschillende seizoenen vastlegt, wat waarschijnlijk in verband staat met seizoensgebonden opwelling. Tijdens de zomer, wanneer het bassin gestratificeerd is, reflecteert de LDI namelijk watertemperaturen overeenkomstig met een maximale diepte van ca. 30 m, terwijl tijdens het opwellingsseizoen de LDI-temperaturen meer overeenkomen met oppervlaktetemperaturen, wat suggereert dat tijdens opwelling de diol-producerende algen zich dichter bij het zeeoppervlak bevinden. De Diol Index laat dezelfde variaties zien als de primaire productiviteit, wat betekent dat de Diol Index een goede proxy is voor opwellingsintensiteit in dit bassin, omdat opwelling hier de belangrijkste drijfveer is voor primaire productiviteit.

Om de relatie tussen de LDI en ZOT beter te begrijpen hebben we de originele kalibratie, gebaseerd op 161 zeebodemsedimenten, gerevalueerd en uitgebreid waarbij we in totaal 733 diepzeesedimenten hebben beschouwd. De relatie tussen de LDI en ZOT was vergelijkbaar met de oorspronkelijke relatie, maar met meer ruis. Vergelijking van de data met verschillende milieufactoren wees uit dat een groot deel van de ruis verklaard kon worden door de invloed van zoet water en diolproductie door *Proboscia*-diatomeeën. Het verwerpen van LDI data van de sedimenten uit gebieden met zoet water en grote hoeveelheden *Proboscia*-diolen (gekenmerkt door hoge C_{28} 1,12-diol hoeveelheden), versterkte dan ook duidelijk de empirische correlatie tussen de LDI en ZOT. De kalibratie-afwijking is uiteindelijk groter dan die van de originele kalibratie, maar de regressie is statistisch gezien gelijk aan de originele formule, wat de relatie tussen de LDI en ZOT bevestigt.

We hebben de invloed van zoet water op de LDI bestudeerd langs de kust van Portugal waar verschillende rivieren uitmonden in de zee. Langs vijf zeebodemtransecten hebben we de LDI en individuele diolen gemeten in het sediment. Ver weg van de kust/riviermondingen (open oceaan) geeft de LDI redelijke ZOT-schattingen, maar in de monding van de grootste rivier, de Taag, onderschat de LDI de ZOT, met afwijkingen tot wel -7 °C. Dit suggereert dat de LDI inderdaad beïnvloed wordt door zoet water, in dit geval rivierwater. Opmerkelijk is de relatief hoge hoeveelheid van de C_{32} 1,15-diol in de zeebodemsedimenten in de riviermondingen, die eenzelfde soort distributie laat zien als de BIT index, een proxy voor de bijdrage van organisch koolstof afkomstig van land. Bovendien is de relatieve hoeveelheid van de C_{32} 1,15-diol het hoogst in het rivierwater van de Taag, wat suggereert dat deze diol voornamelijk uit rivieren afkomstig is, en wellicht dus bruikbaar is als een tracer voor rivierinvloed.

De toepassing van de LDI en Diol Index is getest in een sedimentkern voor de kust van Chili, die meerdere glacialen en interglacialen omvat. De op de LDI gebaseerde ZOT-reconstructie was erg vergelijkbaar met de temperatuurreconstructies gebaseerd op de $U^{K'}_{37}$ en TEX_{86}, maar ook met de $\delta^{18}O$ variaties gemeten aan planktonische foraminiferen. Dat betekent dat de LDI inderdaad variaties in de ZOT vastlegt op deze locatie. De Diol Index,

en een onlangs geïntroduceerde proxy voor nutriëntconcentraties (de Nutriënt Diol Index of NDI), komen niet overeen met andere proxy's voor opwelling/primaire productiviteit: waar proxy's als diatomeeëntellingen, totaal organisch koolstof of andere biomarkers een piek in opwellingsintensiteit suggereren (ca. 100 duizend jaar geleden), laten de Diol Index en NDI een minimum zien, wat zwakkere opwelling en lagere nutriëntconcentraties zou suggereren. Dit lijkt onrealistisch, en laat zien dat de Diol Index en NDI misschien beter beschouwd kunnen worden als proxy's voor de productiviteit van *Proboscia*, in plaats van proxy's specifiek voor opwelling of nutriëntconcentraties.

Hoewel verschillende studies de LDI nu hebben toegepast, en de LDI veelbelovend lijkt als ZOT-proxy, zijn toepassingen over het algemeen niet ouder dan het Kwartair (ongeveer laatste 3 miljoen jaar). Het is echter belangrijk om te onderzoeken of de LDI bruikbaar is verder terug in de tijd. Daarom hebben we diolen, alkenonen en GDGTs bestudeerd over de laatste 90 miljoen jaar, in een sedimentkern dichtbij New Jersey. De GDGT-distributies in de kern zijn vergelijkbaar met moderne GDGT-distributies in diepzeesedimenten. Echter, de alkenonen in sedimenten uit het Krijt (ongeveer 78 miljoen jaar oud) zijn anders dan de alkenonen in de jongere en moderne sedimenten. Dit suggereert dat in het Krijt alkenonen werden geproduceerd door andere typen organismen. De sedimenten ouder dan ongeveer 30 miljoen jaar bevatten dioldistributies die verschillen van typische dioldistributies in hedendaagse diepzeesedimenten, wat ook suggereert dat deze door een ander soort organisme werden gemaakt. De 1,13- en 1,15-diolen waarop de LDI is gebaseerd, zijn gevonden tot ongeveer 50 miljoen jaar geleden. Echter, de temperatuurreconstructie gebaseerd op de LDI komt niet overeen met andere reconstructies voor deze kern, hetgeen suggereert dat de LDI wellicht is beïnvloed door de onbekende organismen die verantwoordelijk zijn voor de afwijkende dioldistributies in de sedimenten ouder dan 30 miljoen jaar.

De resultaten gepresenteerd in dit proefschrift geven nieuwe inzichten in de milieufactoren die bepalend zijn voor welke diolen we aantreffen in diepzeesedimenten, en laten zien dat langeketendiolen goede milieuproxy's zijn, maar ook dat er restricties zijn op hun toepassing.

Dankwoord

Van dit 254-pagina-tellende proefschrift wordt dit hoofdstuk waarschijnlijk het meest gelezen. Ik ben dan ook dank verschuldigd aan veel collega's en vrienden zonder wiens hulp ik niet op dit punt was beland.

De grootste dank ben ik verschuldigd aan Stefan. Zonder jouw hulp en toewijding was dit proefschrift niet geworden tot wat het nu is. Het is ongelofelijk hoe kalm jij altijd bleef wanneer ik met de zoveelste (paniek)vraag je kantoor binnenkwam, en hoe je manuscripten binnen een dag terugstuurde met commentaar. Bedankt voor al je hulp, je inzichten en discussies, ik heb veel van je geleerd.

Jaap, bedankt voor je altijd constructieve commentaar op mijn manuscripten. Ik ben je heel erg dankbaar voor al je hulp.

Sebastiaan, bedankt dat je altijd de tijd nam om al mijn vragen te beantwoorden. Ik heb heel veel van je geleerd. Bedankt voor al je hulp en je vriendschap.

I want to thank the members of the reading committee for reviewing my thesis.

I am grateful to my co-authors from outside the NIOZ: Jenny Ullgren, Stuart Wakeham, Jerry McManus, Jung-Hyun Kim, Hartmut Schulz, Jochen Knies, Andreas Lückge and Barbara Donner.

Ook dank aan alle technische en analytische ondersteuning. Ellen, bedankt voor alle LC-MS kennis die je met me hebt gedeeld. Maar ook bedankt voor onze niet-wetenschappelijke gesprekken op de boot of 's ochtends om acht uur bij de koffie. Je hebt me regelmatig opgebeurd als ik het even niet meer zag zitten. Denise, je hebt me zo vaak gerustgesteld als ik me drukt maakte om iets, bedankt. Ik kijk uit naar nog veel avondjes zwemmen en samen eten. Marcel, bedankt voor onze vele gesprekken over wetenschap, milieu, en nog zo veel meer. Ik hoop dat we elkaar nog vaak zullen spreken. Caglar, wij zijn pas gaan samenwerken in het laatste jaar van mijn PhD, maar je hebt me heel veel geholpen. Bedankt voor je ondersteuning in het lab, en onze data discussies. Ik wens je alle geluk in je carriere, en ik kijk uit naar je eerste wetenschappelijke publicatie! Monique, bedankt voor al je hulp met de GC-MS, ik heb veel van je geleerd.

Dave, mijn master-student, bedankt voor het opwerken en analyseren van een enorme set sedimentmonsters. Ik mocht mij gelukkig prijzen met je inzet!

Jort en Sharyn, bedankt voor jullie vriendschap de afgelopen vier jaar. Bedankt voor de ontelbare therapeutische filmavondjes (en wijntjes). Laten we deze traditie vooral voortzetten!

Karsten en Melvin, bedankt voor alle leuke koffiepauzes! Melvin, ik ga je echt missen als kantoorgenoot!

Jan, bedankt voor je commentaar op mijn wetenschappelijke en populair-wetenschappelijke artikelen! Irene, bedankt voor onze leuke gesprekken tijdens de lunch.

En dan alle andere MMB collega's en vrienden: Julie (thank you for all the lovely dinners and your friendship), Gabriella (I'm glad we got to know each other better in Florence!), Zeynep (thank you for our nice scientific and non-scientific conversations), Sophie, Marianne, Michel (bedankt voor de Bob Ross koffiemok!), Sergio, Caitlyn, Nicole, Marc, Darci, Clara, Sigrid, Saara, Laura, Douwe, Diana, Alejandro, Nadine, Jessica, Philip, Anchelique, Ronald. Bedankt voor de leuke tijden in het lab, pauzes, congressen, en buiten het werk. Ook van de OCS afdeling en andere afdelingen natuurlijk niet te vergeten: Wim (bedankt voor de muziek!), Laura (I'm so glad we became friends at EGU!), Karin (bedankt voor je hulp met de vertaling), Lennart, Gert-Jan, Jan-Berend, Geert-Jan, Bob, Henko, Piet, Esmee, Rick, Alice, Michelle, Furu, Evaline, Jolanda. Bedankt voor de leuke gesprekken in de pauzes, congressen, feestjes, etc.

En dan natuurlijk mijn paranimfen, Laura en Inge.
Laura, mijn congres-maatje! We zijn naar Praag, Tokyo, Urbino, Florence, en Wenen geweest, en deze ervaringen ga ik nooit vergeten. Ik ben blij dat we zo goed bevriend zijn geworden.
Inge, ik ken je sinds het begin van mijn master, en je bent echt m'n beste vriendinnetje geworden. Je bent er altijd voor me, en ik voor jou.

Dan mijn vrienden van buiten het NIOZ, en in het bijzonder Giselijne, Viola, Roos en Joanne. Bedankt voor de welkome afleiding de agelopen jaren, en jullie vriendschap.

Tenslotte mijn familie en schoonfamilie, bedankt dat ik altijd op jullie kan rekenen, en voor jullie onvoorwaardelijke steun.

Als allerlaatste: Wiebe bedankt voor je steun en liefde, voor alles.

About the author

Marijke Wilhelmina de Bar was born on the 22nd of March 1991 in Doetinchem, the Netherlands. After secondary school, she started studying Earth Sciences at the University of Utrecht in 2009 where she received her Bachelor of Science degree in 2012. Subsequently, she specialized in climate reconstruction investigating past sea water temperature proxies over the last 90 million years for the Bass River site (New Jersey, USA) combining organic and inorganic geochemistry for her Master research project. This research was carried out at the Royal Netherlands Institute for Sea Research (NIOZ) where she graduated with a Master of Science distinction in 2014. Directly afterwards, she started a PhD project at the NIOZ, focusing on long-chain diols as environmental proxies, under the supervision of Prof. dr. ir. Stefan Schouten and Prof. dr. ir. Jaap Sinninghe Damsté, which has resulted in this thesis.

Bibliography

de Bar, M.W., Dorhout, D.J.C., Hopmans, E.C., Rampen, S.W., Sinninghe Damsté, J.S., Schouten, S., 2016. Constraints on the application of long chain diol proxies in the Iberian Atlantic margin. Organic Geochemistry 101, 184-195.

Balzano, S., Villanueva, L., de Bar, M.W., Sinninghe Damsté, J.S., Schouten, S., 2017. Impact of culturing conditions on the abundance and composition of long chain alkyl diols in species of the genus Nannochloropsis. Organic Geochemistry 108, 9-17.

de Bar, M.W., Hopmans, E.C., Verweij, M., Dorhout, D.J.C., Sinninghe Damsté, J.S., Schouten, S., 2017. Development and comparison of chromatographic methods for the analysis of long chain diols and alkenones in biological materials and sediment. Journal of Chromatography A 1521, 150–160.

de Bar, M.W., Stolwijk, D.J., McManus, J.F., Sinninghe Damsté, J.S., Schouten, S., 2018. A Late Quaternary climate record based on long-chain diol proxies from the Chilean margin. Climate of the Past 14, 1783-1803.

de Bar, M.W., Rampen, S.W., Hopmans, E.C., Sinninghe Damsté, J.S., Schouten, S., 2019. Constraining the applicability of organic paleotemperature proxies fort he last 90 Myrs. Organic Geochemistry 128, 122-136.

de Bar, M.W., Dorhout, D.J.C., Hopmans, E.C., Rampen, S.W., Sinninghe Damsté, J.S., Schouten, S., 2019. Corrigendum to "Constraints on the application of long chain diol proxies in the Iberian Atlantic margin". Organic Geochemistry 130, 51-52.

de Bar, M.W., de Nooijer, L.J., Schouten, S., Ziegler, M., Sluijs, A., Reichart, G.-J., accepted. Comparing sea water temperature proxy records for the past 90 Myrs from the shallow shelf record Bass River, New Jersey, Paleoceanography and Paleoclimatology.

de Bar, M.W., Ullgren, J.E., Thunnel, R.C., Wakeham, S.G., Brummer, G.-J.A., Stuut, J.-B.W., Sinninghe Damsté, J.S., Schouten, S., 2019. Long chain diols in settling particles in tropical oceans: insights into sources, seasonality and proxies. Biogeosciences (discussion paper).

Balzano, S., Villanueva, L., de Bar, M.W., Sahonero Canavesi, D.X., Yildiz, C., Engelmann, J.C., Marechal, E., Lupette, J., Sinninghe Damsté, J.S., Schouten, S., in revision. Biosynthesis of long chain alkyl diols and long chain alkenols in *Nannochloropsis* spp. (Eustigmatophyceae). Plant and Cell Physiology.

Weiss, G.M., de Bar, M.W., Stolwijk, D.J., Schouten, S., Sinninghe Damsté, J.S., van der Meer, M.T.J., under review. Paleosensitivity of hydrogen isotope ratios of long-chain alkenones to salinity changes at the Chile Margin. Paleoceanography and Paleoclimatology.

de Bar, M.W., Weiss, G.M., Yildiz, C. Rampen, S.W., Lattaud, J., Bale, N.J., Mienis, F., Brummer, G.-J.A., Schulz, H., Rush, D., Kim, Y.-H., Donner, B., Knies, J., Lückge, A., Stuut, J.-B.W., Sinninghe Damsté, J.S., Schouten, S., submitted. Global temperature calibration of the Long chain Diol Index in marine surface sediments. Paleoceanography and Paleoclimatology.